Andrea Gruber

Direct Numerical Simulation Of Turbulent Combustion Near Solid Surfaces

Doctoral thesis
for the degree Doktor ingeniør

Trondheim, January 2006

Norwegian University of Science and Technology
Faculty of Engineering Science and Technology
Department of Energy and Process Engineering

NTNU
Norwegian University of Science and Technology
Doctoral thesis
for the degree of Doktor ingeniør
Faculty of Engineering Science and Technology
Department of Energy and Process Engineering

ISBN 82-471-7767-6 (printed version)
ISBN 82-471-7766-8 (electronic version)
ISSN 1503-8181

Doctoral theses at NTNU, 2006:14

Printed by NTNU-trykk

Abstract

This study uses Direct Numerical Simulation of turbulent reacting compressible plane channel flow at low Reynolds number in order to understand the physics of the interaction of a flame with the turbulent boundary layer near a solid inert surface.

Better insight into the process of flame quenching near a solid surface, of the influence of turbulence on this process, and of its relation to the maximum and average wall heat fluxes, pollutant formation and incomplete fuel consumption is crucial to obtain improved prediction capabilities about combustor lifetime and pollutant emissions in complex engineering problems both at low Reynolds numbers (micro and nano gas turbines) and high Reynolds numbers (conventional gas turbines, internal combustion engines).

A fuel-rich mixture (characterized by an equivalence ratio of 1.5) of hydrogen and air is chosen for the direct simulations resulting in high turbulent flame speed, thereby allowing high centerline average fluid velocity which in turn results in relatively short channel transit times. Because of the high centerline average flow velocity the flame is anchored at the channel centerline and assumes a characteristic V-shape. The detailed chemical kinetics mechanism describing hydrogen combustion in air (NO_x formation reactions are neglected) is relatively *"light"* from the computational point of view. Additionally, the possibility of using hydrogen as fuel in conventional combustion equipment has been under investigation in late years and this study hopes to contribute to the amount of knowledge available about (premixed) hydrogen-flames behaviour.

As a first step the near-wall behaviour of a planar pre-mixed laminar flame is examined in a one-dimensional head-on quenching (HOQ) setup: very useful information is obtained about the impact of the physio-chemical assumptions used to model the combustion process on the flame-wall interaction. A detailed chemical kinetics mechanism is adopted because it is well known from the literature that one-step simplified chemistry is not able to accurately capture the spatial nor the temporal evolution of the quenching process that takes place when the flame approaches the solid *"cold"* surface. The results compare well with the existing literature on pla-

nar one-dimensional laminar flame-wall interaction.

As a second step, the near-wall behaviour of the anchored v-shaped turbulent flame is studied both in two- and three-dimensional turbulent plane channel flow providing detailed insight of the side wall quenching (SWQ) configuration. Large differences in 2-D versus 3-D boundary layer turbulence characteristics, especially important at the wall, lead to large differences in near-wall flame behaviour and maximum wall heat fluxes for the two configurations: intense near-wall streamwise vorticity present in the 3-D simulation *"pushes"* the flame closer to the wall increasing the maximum wall heat flux by a factor of two in respect to the 2-D simulation. The average spatial spacing in the spanwise direction of the maximum wall heat flux *"hotspots"* is found to be close to 100 wall units while their characteristic temporal frequency is close to time scales between 10 and 30 wall or "inner" time units. The above mentioned spatial and temporal scalings correlate well with the mean spanwise spacing of the near-wall streamwise vorticity structures and with their characteristic longitudinal time scale. Three-dimensional direct simulations are very expensive computationally and, at the time of the writing of this document, the computation is still running. Only few channel transit times are considered in the statistical analysis included in this report, statistical data from a larger number of samples will be reported in a later publication.

Contents

1 Introduction

1.1 Turbulent Combustion

Combustion processes in which some species of reactants are burned into products to generate heat by chemical reaction are almost ubiquitous in our modern world. According to the International Energy Agency (IEA): "Continued economic growth is expected to result in increased use of fossil fuels with likely increases in the emissions of local and global pollutants. In the next twenty years, fossil fuels will account for almost all new electric power generating capacity, 78% in the developing world, as much as 97% in transition economies, and 89% in the developed world" IEA (2004). This means that more than 90% of the energy consumed today by mankind is generated by means of combustion processes in their various form and with various efficiencies, moreover, also according to the IEA, more than 95% of the atmospheric pollution is created by the very same combustion processes that provide us with energy. Renewable energy is important to achieve sustainable energy development, but clean fossil energy is also needed since energy needs will exceed the practical capacity of renewable energy supply. Therefore, fossil energy must overcome its environmental difficulties, as it is crucial for sustainable development to maintain access to fossil energy resources.

Ample margin still exists to reduce the adverse impact of combustion processes on the environment. Combustion generated pollution can be greatly reduced following two main strategies: the one consists in burning reactants that are less prone to generate polluting products, the other implies redesigning the existing combustion equipment to improve thermal efficiency (so that less fuel has to be oxidised to produce the desired amount of energy) and reduce pollutant formation (NO_x, PAH, soot). The optimal result is certainly obtained by combining these two approaches. The choice of fuel and oxidiser to be burned in order to reduce pollutant emissions is relatively straightforward and it is quite generally accepted that using hydrogen as a fuel is one of the cleanest way to produce thermal energy (even if the fact that hydrogen is not found on planet earth in

relevant quantities and has to be *man made* should be pointed out). The improvement of combustion equipment in respect to thermal efficiency is a much more challenging task because the optimal design of most combustion equipment requires complete understanding and accurate predictive capability of turbulent flows.

Turbulence is a very complex physical process that some fluids under certain conditions experience and can involve a range of different time and length scales (from a few to several hundred thousands), it has proven difficult to study in great detail and describe turbulent flows with mathematical models. The Navier-Stokes equations (see Chapter 2 for details) describe mathematically the behaviour of flowing fluids but, in spite of the fact that they come in a relatively simple and closed form (the number of equations equals the number of unknown independent variables), an analytic solution of this system of partial differential equations, even for the simplest turbulent flows, does not exist. In order to accurately determine the variables describing the flow (for example the velocity and pressure fields) the Navier-Stokes equations have to be solved numerically.

The ratio of the flowing fluid's inertia to its viscosity is a non-dimensional quantity, named Reynolds number, and its value is of fundamental importance in characterizing the flow that is being investigated

$$Re = \frac{U \cdot L \cdot \rho}{\mu} \tag{1.1}$$

where U and L are, respectively, a characteristic bulk velocity and macroscopic length scale associated with the flow while ρ is the density and μ the viscosity of the flowing fluid. For homogeneous isotropic turbulent flow the range of different length and time scales contained in the solution of the Navier-Stokes equations is (roughly) proportional to the third power of the Reynolds number associated with that flow. As independently observed by Kolmogorov (1941a) and Onsager (1945) the velocity field of a fluid is characterized by an infinite number of Fourier modes, whose mutual interaction redistributes the energy among more and more modes of increasingly higher wavenumber: a *cascade* of mechanical energy takes places, in a stepwise process where each Fourier mode interacts with modes of comparable wavenumber magnitude, from the large energy-containing scales of motion to the small scales where viscosity dissipates mechanical into thermal energy (chaotic molecular motion). The numerical solution of the Navier-Stokes equations where *all* the scales of the flow are accurately represented is called Direct Numerical Simulation (DNS). Today's most power-

ful parallel computers allow (within a reasonable time span) DNS of flows characterized by Reynolds numbers in the order of a few thousands.

If providing an accurate description of turbulent flows is difficult because of the large range of scales involved even more challenging becomes the description of the interaction between turbulence and combustion, where the range of scales which characterize the physical processes is enlarged to include chemical time scales and nonlinear coupling and feedback effects between convection, diffusion, acoustics and heat release. This complex picture is not very well understood as of yet but more accurate laboratory experiments and computations with increasingly more powerful and capable computer help the research community to improve the understanding of the physics of combustion.

1.2 Objective And Motivation

The present work aims at improving the understanding of the interaction between turbulence and combustion in the vicinity of a solid surface. This, in turn, will hopefully result in better estimates of the wall heat flux characteristic values and spatial patterns and also in improvements to turbulent combustion models that, to date, seem to perform poorly in the near-wall region. An important factor behind this poor performance is to be found in the fact that turbulence combustion models often rely on the assumption of isotropy of the turbulent field while turbulence quantities close to the wall are strongly anisotropic: the turbulent velocity fluctuations in the wall-normal direction are damped by the presence of the solid surface (wall-normal anisotropy) and the effect of main shear creates near-wall quasi-streamwise structures elongated in the flow direction (streamwise anisotropy).

The near-wall region of the flow, usually described as *boundary layer*, is where the flame extinguishes (or quenches) because of the heat loss into the solid material. The near-wall quenching process and the associated wall heat flux are believed to be the cause behind an important part of the total thermal conversion inefficiencies and pollutant emissions (as unburned fuel) from combustion equipment. Also, the boundary layer is responsible for the total convective heat transfer from the fluid to the solid material: being able to correctly estimate the maximum wall heat fluxes and their spatial pattern is of great importance in obtaining realistic lifetime estimates and improved design of combustion equipment that is subject to extreme

temperatures and thermal stresses.

The novel research field of micro and nano gas turbines development demands particular attention to and better understanding of both turbulence-flame interaction and flame-wall interaction processes because of the tiny spatial dimensions of the combustor (low volume to surface ratio). This often results in poor mixing, incomplete combustion, frequent flame-wall interactions and high wall heat fluxes, in short: low combustion efficiency and short lifetime of the combustor. In the next Section a description (by no means complete) is given of the available tools, methods and previous experiences in the investigation of turbulence, turbulent flames and flame-wall interaction, special attention is devoted to earlier experiences in DNS.

1.3 Tools

1.3.1 Computational Fluid Dynamics

Computational Fluid Dynamics (CFD) has emerged in recent years as a useful tool in the prediction, design and running of engineering processes and equipment involving combustion: furnaces, reciprocating engines, gas turbines, just to name some examples, all results from CFD calculations at some point of their design process. In the research and development of almost every industrial production process today, costly full (or even small) scale laboratory experiments and measurements are replaced by computer simulations that quickly and inexpensively give the designer or analyst the information needed for the optimal performance of their equipment or process.

The Closure Problem

In order to solve problems of practical interest, the CFD-approach, as opposed to DNS, chooses *not* to resolve all the different time, length, velocity and chemical scales associated with turbulent reactive flows. Only the scales associated with the most energetic low-frequency modes are resolved while the high frequency modes at the smaller scales are not resolved but modeled or neglected. In the context of applied engineering problems this simplification is usually obtained through an averaging process (Reynolds averaging which gives the Reynolds Averaged Navier-Stokes equations or RANS) but it comes at a price: the averaged Navier-Stokes equations are

no longer in closed form but some new terms, averaged products of fluctuating velocities or Reynolds stress terms and other averaged products of fluctuating quantities (velocity, pressure, temperature, enthalpy, reaction rates), resulting from the averaging operations, are unknown and need to be modeled. The closure of the Reynolds Averaged Navier-Stokes equations is a fundamental problem of CFD and two main approaches can be pointed out[1]:

- If one chooses to address the problem by solving some transport equations for the unknown Reynolds stresses these in turn give rise to higher-order statistical quantities and so on. The modeling problem is therefore not really solved but only moved to higher order statistical terms, this comes at a considerable computational cost.
- On the other hand, the simpler approach of modeling the Reynolds stress term by means of an algebraic equation, usually a linear eddy-viscosity model, suffer of some deficiencies in the prediction of any (possibly) anisotropic characteristics of the turbulent flow (and therefore perform poorly in predicting near-wall processes which are characterized by strong anisotropy).

The closure problem is particularly challenging near wall boundaries because of the already mentioned anisotropy but also because in turbulent flows the boundary layer is characterized by very small length scales (the boundary layer thickness in common combustion equipment is usually of the order of millimeters or less). The fact that in CFD one has chosen not to resolve the small scales of the flow implies that some appropriate models are needed to take into account phenomena that are taking place at scales which are not resolved by several orders of magnitude.

The Boundary Specification Problem

Another fundamental problem of CFD is the proper treatment of the boundaries of a turbulent multidimensional compressible reactive flow. Wall (or closed) boundaries and open boundaries represent respectively the physical and the artificial limits of the region of interest in the flow configuration that is being simulated, one hopes that what is happening outside

[1] A third method uses a stochastic approach and *pdf*-transport to obtain some of the unknown terms in exact form, see Pope (2000) for details.

this region can be either neglected or represented in the specification of the boundary conditions using simple models. *The numerical simulation of the reactive flow problem can produce a reliable solution only if these boundary conditions are properly specified in the computational domain.*

The correct specification of an open boundary (non-physical or artificial border of the flow configuration in the computational domain) for a compressible turbulent reacting flow is a challenging task and ongoing research subject, this topic is briefly addressed in Chapter 3. This work focuses on walls and solid boundaries which represent the physical limit of the bulk flow: the boundary layer, located between the bulk flow and the wall, represent a sort of "transition zone" where, depending on the characteristics of the fluid and of the flow, the wall-normal gradients of momentum and energy are largest. Being able to correctly estimate these possibly very large gradients is crucial in the accurate prediction of wall bounded turbulent reactive flow.

1.3.2 Laboratory Experiments

Before the widespread use of digital computers for the numerical solution of the Navier-Stokes equations revolutioned the scientific approach to the investigation of turbulence, laboratory experiments represented the only means to understand these physical processes. These experiments involve direct measurements of key quantities for the characterization of turbulent and reactive flows, As Leonardo Da Vinci wrote in the 15th century: "L'Esperienza E' Madre Alla Scienza" (Empirical observation is the mother of science).

The structure of turbulent flows has been under experimental investigation for more than 40 years, over 2000 journal articles have been written and published about this topic! A complete review of the literature is therefore not attempted here but only some of the main contributions of such a huge research effort are mentioned.

In 1883 (circa) Osborne Reynolds on the one side develops the first experimental techniques for the characterization of laminar and turbulent flows using a dye streak in pipe flow. On the other side he initiates also the statistical approach to the theoretical investigation of turbulence introducing the idea of splitting the velocity field of a flowing fluid into a mean and a fluctuating part. While the former quantity is typically only a function of its location and could be used to successfully characterize and, to some extent, predict the large scale motions of the flow, the latter fluctuating quantity

has to be treated as a stochastic function of space and time and very few case-dependent assumptions could be made about it.

The measurement techniques of the early years use intrusive methods, like hot-wires and probe sampling, to record instantaneous values of velocity, temperature and species concentration. Averaged and fluctuating quantities of the relevant variables can be extracted from long-time sampling of instantaneous values but these intrusive measurement methods are not considered very accurate because they affect, sometimes to a large extent, the phenomena that are being observed.

Many of the experimental works from the 1950s attempt the investigation of the structure of near-wall turbulence measuring the root-mean square and spectra of the turbulent velocity fluctuations by hot-wire sampling: typically the results from different authors do not agree very well (with margins well above what can be considered acceptable), this fact is generally attributed to differences in the experimental setup, random disturbances in the bulk flow or low accuracy of the measuring methods. Nevertheless, in spite of the poor agreement between the various experiments, it is already established in the early days of modern turbulence research that the streamwise and spanwise root-mean square velocity fluctuations in the near-wall region of the turbulent plane channel were larger than the wall-normal ones and that they showed sharp maxima very close to the wall (see Chapter 5). Basing his analysis on these empirical observations and on the fact that mechanical energy dissipation into heat is believed to occur mostly at small scales, Townsend (1956) proposed a two-layer model for the boundary layer:

- Most of the turbulence energy production and dissipation take place very close to the wall for $y^+ \leq 100$ in the *inner layer* [2]
- The *inner layer* is dominated by elongated counter-rotating rollers inclined downstream and outward from the wall in the direction of the mean shear
- The turbulence level in the flow further away from the wall in the *outer layer* is maintained by transport of a fraction of the turbulent energy generated at the wall to the outer region where it is finally dissipated

[2] y is the wall-normal cartesian coordinate and the superscript + indicates a non-dimensional quantity which is scaled by a wall viscous length scale $\delta_\nu = \nu \cdot \sqrt{\rho/\tau_w}$; e.g. $y^+ = y/\delta_\nu = y u_\tau/\nu$, where ν is the fluid kinematic viscosity, $u_\tau = (\sqrt{\tau_w \rho})$ is the wall shear velocity, τ_w and ρ are the wall shear stress and the fluid density respectively.

– Mean-flow energy is continuously transferred to the *inner layer* at a rate controlled by the mean shear stresses

The research community realizes soon enough that pointwise knowledge of the averaged and fluctuating quantities is not sufficient to unravel the complex structure of the turbulent boundary layer, considerable effort is therefore devoted to the development of new techniques for the spatial representation of the instantaneous velocity field. Advanced visualization methods are developed in the 1960s in order to study complex configurations of inhomogeneously sheared flows that require a deeper understanding of the actual details of the turbulent motions in the boundary layer for reliable formulations of theories and models.

The pioneering works of Runstadler *et al.* (1963) and Kline *et al.* (1967) investigate the structure of turbulence in the near-wall region by visual observations using wire-generated hydrogen bubbles. These new visualizations techniques prove themselves to be very important in understanding the spatial structure of near-wall turbulence. They reveal previously unknown features of the turbulent boundary layer: far from being only two-dimensional (in the wall-normal and streamwise directions as initially thought) the turbulent boundary layer, when observed using detailed visualization methods, show relatively coherent three-dimensional near-wall quasi-streamwise vorticity structures, horseshoe- or hairpin-like vortices protruding into the outer layer and associated with low and high speed streaks alternating very close to the wall in the spanwise direction, see Figure 1.1 for a pictorial representation of the boundary layer vorticity structures and Figure 1.2 for a typical instantaneous vorticity field from DNS. Several important conclusions can be drawn from these early experiments:

– The non-dimensional *mean* spacing between these three-dimensional structures in the streamwise and spanwise directions follows a universal correlation for fully turbulent boundary layers. Smith and Metzler (1983) reports for the streamwise direction a mean spacing (in non-dimensional wall units) of $\Delta x^+ \simeq 440$ and $\Delta z^+ \simeq 100$ for the spanwise direction, these averaged values confirm the previous estimates of Kline *et al.* (1967). Also, this spanwise mean spacing observed experimentally was some years later related to a resonance frequency characteristic of the Navier-Stokes equations in the theoretical work of Jang *et al.* (1986)

– The near-wall vorticity structures observed experimentally are not sta-

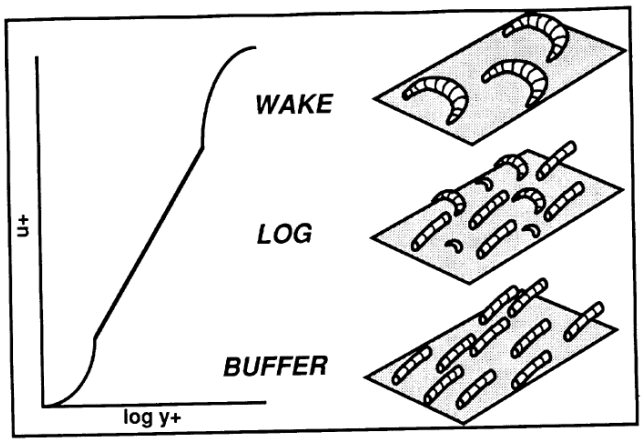

Figure 1.1: Pictorial representation of the boundary layer showing quasi-streamwise vortices in the near-wall region and horseshoe-like structures in the outer layer (from Robinson (1991)).

tionary in space but migrate and are characterized by a strong intermittency

– The near-wall vorticity structures are intrinsically three-dimensional in nature and they correlate with turbulent kinetic energy production

If a considerable number of experimental investigations about the turbulent structure of the boundary layer is present in the open literature, the same is not true for the fairly more complex configuration of a *reacting* flow in a turbulent boundary layer. An early measurement technique reported in Westenberg (1954) and Westenberg and Rice (1959) uses probe sampling to indirectly estimate transverse turbulence intensities by means of helium diffusion in ducted premixed flames. Even if this and other later probe sampling experiments allow the understanding of some general characteristic of flame behaviour, like flame spreading rate versus approaching turbulence level and mass fraction gradients as driving forces for diffusion[3], they do not yet contribute with a detailed description of the turbulent flame structure.

[3]See also Howe *et al.* (1963) about species measurements for turbulent diffusion estimates

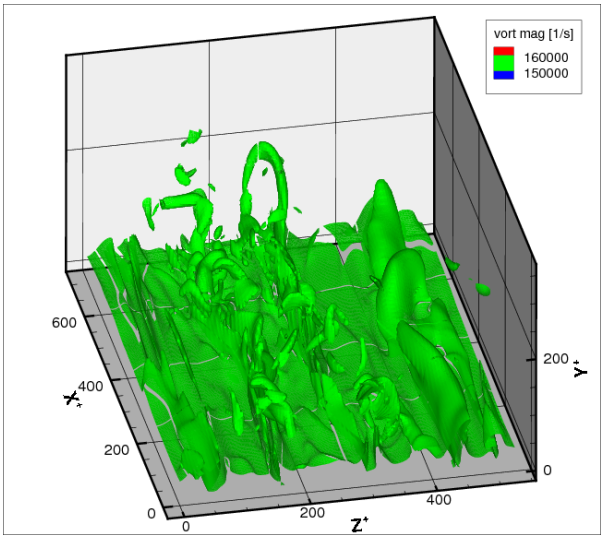

Figure 1.2: Isosurfaces of instantaneous vorticity magnitude in DNS of fully developed plane channel flow (see Chapter 5 for details about the simulation). The flow is in the positive x^+-direction, a large horseshoe-like structure protruding well into the outer layer is clearly visible.

More recent optical measurement techniques make extensive use of laser beams and advanced photography (Charged Coupled Device - or CCD - cameras) in order to extract detailed information about the flow and the combustion process without interfering (or doing so as little as possible) with the physical phenomena being studied.

In their investigations of v-shaped flames both in zero mean shear turbulent flow and reactive turbulent boundary layers Ng *et al.* (1982), Cheng and Ng (1982), Cheng and Ng (1983), Cheng and Ng (1984) and Cheng and Ng (1985) employ Schlieren photography for flame structures visualization, Rayleigh scattering for density measurements and Laser Doppler Velocimetry (LDV) for mean and rms fluid velocity distributions. They are able to reach some important conclusions at the end of their series of experiments:

- The combustion process in the boundary layer is dominated by its large-scale turbulent structures
- The thermal effects due to the presence of cold (unburnt) and hot (burnt) fluid pockets respectively rushing in (sweeps) or out (ejections) of the viscous layer change the turbulence intensities correlated to the large-scale structures respect to isothermal boundary layers (bursting less energetic probably because of higher viscosity in the hot gases)
- Combustion causes expansion of the boundary layer, large deflection of the mean streamlines away from the wall, acceleration and laminarization of the burnt gas
- Combustion increases the local wall friction coefficient C_f due to locally increased viscosity
- Conditional sampling techniques show that the Reynolds stress is reduced by combustion and the increase usually observed in the flame zone is due to the intermittency caused by the turbulent flame brush motion
- Due to the physical limitation of the cross-beam LDV system, the laser probe cannot be placed closer than 1 mm to the wall (measurements possible only outside the viscous sublayer)
- The turbulent v-shaped flame configuration is anisotropic with transverse velocity fluctuation larger than streamwise velocity fluctuations

In the early 1990s Ezekoye *et al.* (1992) combine experimental measurements and numerical simulations: they use thin film resistance thermometers to investigate wall heat flux in flame-wall interaction of premixed hydrocarbon flames for different equivalence ratios, Ξ, and wall temperatures, T_w, and run direct numerical simulations of flame quenching using a single-step chemistry approach. Comparison of the experimental results with the numerical simulations shows clearly the inadequacy of the single step chemical mechanism and simplified transport in describing the transient flame-wall interaction process, specifically the dependence of the wall heat flux on the wall temperature.

One problem often related to the experimental investigation of turbulent flames is that the range of scales (time, length, temperature etc.) that can be accurately measured by the instruments is somewhat limited by the hardware's calibration. In some cases, close contact with the flame and the associated high temperatures and heat fluxes have also negative effects on the accuracy of the equipment, it is therefore difficult to obtain very accurate measurements over the whole spectrum of scales that characterize a typical turbulent reactive flow. Also, while it is considered relatively straightforward to send a laser beam through a flame burning in a open space and observe the relevant quantities for a correct characterization of the combustion process, accurate laser experimental studies of boundary layer flows and of flame-wall interaction are very difficult to perform as reported by Barlow (2005):

- Velocity measurements performed with Laser Doppler Velocimetry (LDV) in the near wall region for $y^+ \leq 10$ are suspect because of the low signal to noise ratio
- Species measurements in the vicinity of a solid surface or confined in a small duct or chamber are also problematic because of spurious scattering of the laser beam by the solid material
- Optical access in boundary layer regions is often problematic due to the presence of the wall
- Intrusive measurements methods (hot-wires) are affected by the wall proximity and interfere with the boundary layer, *de facto* invalidating the results, as observed by Suzuki and Kasagi (2002)

The dispersion of maximum wall heat flux and quenching distance[4] mea-

[4]The distance from the wall at which the flame is extinguished or *quenched*

surements, resulting sometimes in *opposite* trends, proves clearly that the phenomenon of flame-wall interaction is very difficult to study experimentally and is not well understood as of yet, this is probably a consequence of the intrinsic difficulty in performing direct measurements of the quenching distance, especially important considering the small spatial scales of the phenomenon. Enomoto (2002) and Bellenoue *et al.* (2004) address the problem of measuring the typically very small quenching distances with advanced high definition photography (at a spatial resolution of $20\,\mu m$) and derive other quantities, such as the maximum wall heat flux, from adiabatic flame temperature estimates. Unfortunately the high definition cameras allow only one photograph during the $7\,ms$ long flame-wall interaction, leaving open some uncertainties about the accuracy of their measurements.

Because of the above mentioned difficulties in performing experimental measurements of near-wall flame behaviour, the present work pursues the DNS approach to investigate the details of the flame-wall interaction process. The Navier-Stokes equations are solved in their instantaneous form (as opposed to their Reynolds Averaged one) together with a detailed representation of the chemical kinetics of the premixed hydrogen-air flame, all the length and time scales of the reacting flow are resolved and very few assumption are made in the thermo-physical description of the simulated process: this is a so-called *numerical experiment*.

1.3.3 Numerical Experiments

Pope (2000) notes that the total resolution requirement and, consequently, the cost of a three-dimensional DNS scales with Re^3, most flows of practical interest are characterized by so large Reynolds numbers that direct simulations become intractable. As opportunely pointed out by Moin and Mahesh (1998) in their informative review work, direct numerical simulation should not be considered a brute force solution method of the Navier-Stokes equations for engineering problems but a new experimental method that can provide precious information and knowledge otherwise not obtainable in the laboratory. This knowledge can then be used to improve existing mathematical models or forge new ones that, implemented in CFD-codes, will try to represent the physical processes that are not resolved by the solution approaches usually adopted in these engineering codes. Turbulence models, for example, can be tested and evaluated directly just by comparing the modeled terms in the averaged equations with the DNS data representing those terms. Even laboratory experimental methods have been evaluated

and corrected basing the error analysis on DNS results as illustrated by Suzuki and Kasagi (2002) for hot-wire measurements.

Spectral Methods And Incompressible Isotropic Turbulence

The first direct simulations of turbulence are performed in the early 1970s but are limited by the computational power available in those days to flows characterized by modest turbulence levels. The concept of *novel numerical experiment* is introduced in the pioneering work conducted by Orszag and Patterson (1972) at the National Center for Atmospheric Research (Boulder, Colorado, USA). They report a 32^3 computation of incompressible homogeneous isotropic turbulence using a spectral method: the Navier-Stokes equations are Fourier-transformed from physical to wavenumber space and solved in wavenumber space as Galerkin equations, see Canuto *et al.* (1988) and Boyd (2001) for details about spectral methods. Given the limited amount of modes that can be adequately resolved on a 32^3 grid (the intermediate wavenumber - or inertial- range is not well resolved), nevertheless this important work confirms one of the main hypothesis of turbulence theory formulated 30 years earlier by Kolmogorov (1941b): the smallest scales of turbulence (named after the Russian scientist Kolmogorov scales η_κ, τ_κ etc.) get smaller compared to the large ones as the Reynolds number increases but their structure is independent of the Reynolds number.Mansour *et al.* (1978) attempt a Large Eddy Simulation[5] (LES) of shear flow turbulence and are among the first to report the presence in their numerical solution of large, organized structures comparable with those observed in experiments. Successive DNS attempts try to simulate incompressible isotropic homogeneous turbulent flows of increasing turbulence intensity, the most important being the work of Rogallo (1981) that opportunely modified the original Orszag & Patterson algorithm to achieve better time-stepping and reduction of the aliasing error. The spectral methods used in the early DNS are extremely efficient and accurate: Orszag and Patterson (1972) suggest that in order to obtain the same accuracy of their 32^3 computation using second-order finite difference stencils a 64^3 grid would be necessary. These methods, in their various forms, were therefore the preferred choice in times were computer memory was limited to few megabytes on the largest supercomputers and Fast Fourier Transform (FFT) algorithms were being

[5] Numerical solution of the instantaneous Navier-Stokes equations in which only the large scale are fully resolved by the grid, the small scales of turbulence are modeled

made available to the scientific computing community.

While achieving high accuracy at relatively low cost, Fourier series based spectral methods are characterized also by a few drawbacks: their applicability is limited to homogeneous directions along which the computational domain can be considered periodic and there is no need of imposing boundary conditions. Inhomogeneous directions (for example wall-normal or inflow/outflow directions) need some modifications of the method, usually involving for the wall-normal direction the use of Chebyshev polynomials as basis functions in the spectral approximation of the flow equations. Canuto *et al.* (1988) point out that imposing inflow and outflow boundary conditions on primitive variables of the flow as velocity, temperature, species concentrations or mass fractions in wavenumber space is often a daunting task that has not been resolved satisfactorily. Also, the nature of the spectral algorithms, which involves high order polynomials extending over the whole computational domain, makes these methods more appropriate for the simulation of incompressible *elliptic* problems in which correctly predicting acoustic waves propagation is not a fundamental issue: Choi and Moin (1990) extract the pressure power spectra from the DNS dataset of Kim *et al.* (1987) and report *artificial* numerical acoustic waves characterized by a very large sound speed of the order of $L/\Delta t$ where L is the computational box size and Δt is the time step used in the computation. Accordingly, the accuracy which characterize spectral methods is very likely to conserve and *instantaneously* spread eventual errors introduced in the boundary conditions specification.

Adding Complexity: The Turbulent Channel Flow

From the late 1970s toward the early 1980s the computational power available to scientists becomes large enough for Moin *et al.* (1978), Moin and Kim (1985) and Kim and Moin (1986) to perform LES of wall bounded fully developed turbulent plane channel flow. These are the first numerical simulations that reproduce, to some extent, the structure of near-wall turbulence: they employ a spectral method in the two homogeneous directions (stream- and spanwise) and a second-order finite difference method in the wall normal direction. The grid resolution used in these simulations is not adequate to resolve all the length and time scales of the flow but only the large ones (hence the name LES) and a sub-grid scale model has to be used to take into account the small scales of the turbulent flow. The LES from the Stanford group, even if not adequately resolving all time and length

scales (the spanwise resolution is very coarse), is able to reproduce some important aspects of wall turbulence:

- The largest vorticity vectors $\boldsymbol{\omega}$ outside the immediate vicinity of the wall ($y^+ > 50$) tend to have an inclination of 45 degrees from the wall in the flow direction (see Figures 1.3 and 1.4). This implies $\overline{\omega_x^2} = \overline{\omega_y^2}$
- Vortex stretching by mean shear is the dominant mechanism responsible for the formation of quasi-streamwise near-wall vorticity structures (see Figure 1.6)
- Two point correlations of the spanwise velocity component in the relevant directions (45 and 135 degrees) confirm the presence of vorticity structures tilted from the wall in the streamwise direction
- 70% of total turbulence production in boundary layers is caused by processes associated with near-wall vorticity structures
- The ejection of low-speed fluid from the wall at the end of the sweeping high-speed motion is associated to localized adverse pressure gradient by Kim (1983) using conditional sampling techniques

Although these first LES reproduce qualitatively the structure of near-wall turbulence, they are not able to do so also quantitatively and the relative spacing of vorticity structures in the span- and streamwise directions is overpredicted and do not agree with those observed in the laboratory experiments of Kline *et al.* (1967) and Smith and Metzler (1983).

The structure of the vorticity fields is also studied in several 128^3 DNS of homogeneous turbulent shear flow and various irrotational strained flows by Rogers and Moin (1987). In their numerical experiments they observe, early in the development of the shear layer and just above the main shear plane, vorticity vectors tilted 45 degrees *on average* in the streamwise direction: it is therefore concluded that inclined vorticity vectors are a common characteristic of all shear flows and not only of the wall bounded ones. In the same days Ashurst *et al.* (1987) perform a detailed statistical analysis of the dataset from Rogers and Moin (1987) and conclude that:

- The strain rate tensor eigenvectors relative magnitudes are 3:1:-4 (they sum to zero for incompressible flow)
- There is increased probability for the vorticity to point in the intermediate *extensive* strain direction (vortex stretching mechanism)

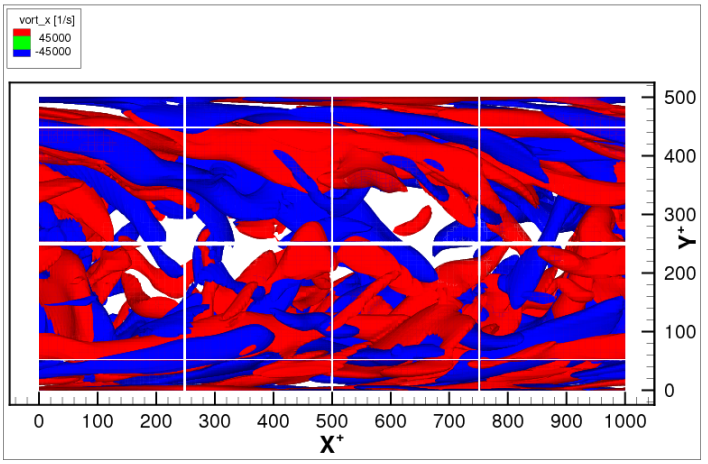

Figure 1.3: Isosurfaces of instantaneous streamwise component of vorticity vector in DNS of plane channel with mean flow in the positive x^+-direction.

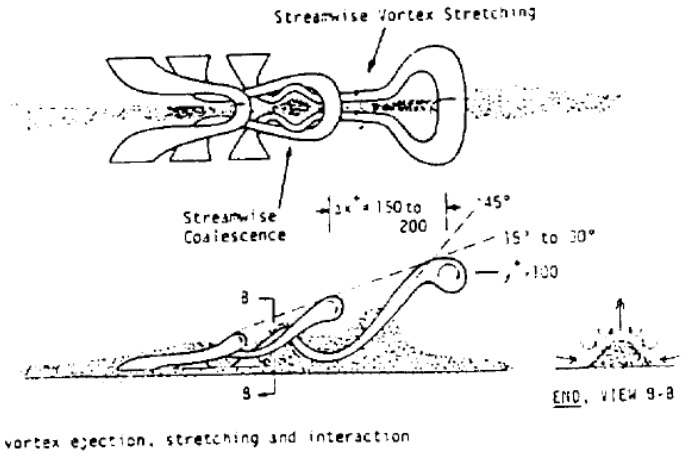

Figure 1.4: Pictorial representation of near-wall vortex stretching and its influence on quasi-streamwise vorticity structures (from Robinson (1991)).

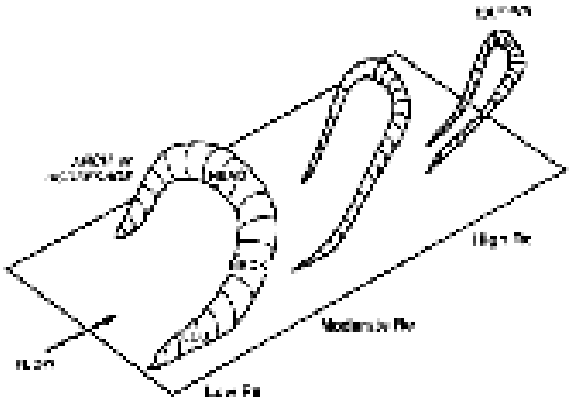

Figure 1.5: Pictorial representation of horseshoe-like vorticity structures for various Reynolds numbers (from Robinson (1991)).

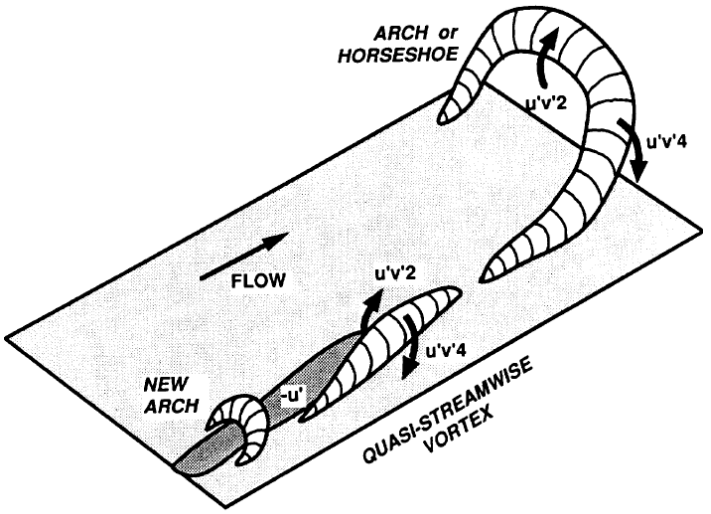

Figure 1.6: Pictorial representation of quasi-streamwise and horseshoe-like vorticity structures (from Robinson (1991)).

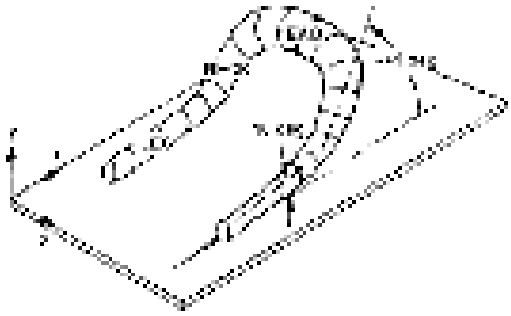

Figure 1.7: Nomenclature for schematic vorticity structure (from Robinson (1991)).

– There is increased probability for the scalar gradient to align in the *compressive* strain direction (vortex stretching mechanism)

thereby giving a more accurate quantitative proof of the vortex stretching mechanism and of its coupling with shear layer turbulence.

The first direct simulations of a fully developed turbulent channel flow are performed by Moser and Moin (1987) for a curved channel and by Kim *et al.* (1987) for a plane channel (Poiseuille flow). They employ a mixed spectral method using Fourier series in the homogeneous streamwise and spanwise (periodic) directions and Chebishev polynomials in the inhomogeneous wall normal direction. The simulations are performed on a $192 \times 128 \times 160$ grid for a Reynolds number of about 3200 based on the mean centerline velocity and channel half-width, this corresponds to a friction Reynolds number Re_τ based on the so called friction or wall shear velocity u_τ[6] and channel half-width H of about 180. The friction Reynolds number

$$Re_\tau = \frac{u_\tau \cdot H \cdot \rho}{\mu} \tag{1.2}$$

[6] $u_\tau = \left(\sqrt{\frac{\tau_w}{\rho}}\right)$ where τ_w is the wall shear stress

is the adimensional quantity that is commonly used to characterize wall-bounded turbulent flows. Even if at $Re_\tau \sim 180$ the database from this first turbulent channel flow simulation reveals the presence of low Reynolds Number effects (typically a very short or absent inertial range), the statistics extracted from it has since 1987 been used countless times to calibrate experimental equipment and measurements, validate other DNS-codes, forge, improve and test turbulence models implemented in RANS-codes, understand the mechanisms governing near-wall turbulence. In the streamwise and spanwise homogeneous directions Kim *et al.* (1987) assume homogeneous turbulence for their fully developed turbulent channel flow, this assumption eases considerably the numerical study of the turbulent channel allowing the use of periodic boundary conditions in the homogeneous directions. The fact that the DNS results match both turbulence theory and experimental data validates the above assumption.

However, few years later Jiménez and Moin (1991) show the dangers and limits of periodicity and that there are minimal domain dimensions below which periodicity of the homogeneous directions does not allow the turbulence to sustain itself and the simulated flow laminarizes. They report that the minimal box dimensions expressed in wall units are Reynolds number independent: $\Delta x^+_{min} \geq 350$ for the streamwise direction and $\Delta y^+_{min} \geq 100$ for the spanwise direction. These values are very close to the near-wall quasi-streamwise vorticity structures mean spacing measured experimentally and observed in numerical simulations, respectively in the streamwise and spanwise directions. The conclusions reached by Jiménez and Moin (1991) give important indications about the role of quasi-streamwise vorticity structures in the formation of the boundary layer, these represent a fundamental building block of wall-bounded turbulence and if not enough room is present for them to exist the turbulence is not able to sustain itself.

Several important numerical studies about the kinematics of the turbulent boundary layer structures by Robinson *et al.* (1989), Robinson (1991) and Chacín and Cantwell (1997) make extensive use of advanced computer visualization techniques in order to achieve a *visual representation* of the spatially coherent vorticity structures and indicate that the shape of the structures is subject to changes for increasing Reynolds number going from *fat* horseshoe-like to *slim* hairpin-like, see Figure 1.5. They also observe that these horseshoe- or hairpin-like vorticity structures, that are a combination of quasi-streamwise and spanwise vortices, are less common than the individual vortices and that the near-wall shear layers are closely related to quasi-streamwise and spanwise vortices.

Later direct simulations of fully developed turbulent plane channel by Andersson and Kristoffersen (1992), Moser *et al.* (1999) and Del Álamo *et al.* (2004) extract higher order statistics and scalings of the mean velocities, turbulent stresses and energy spectra profiles for increasingly high Reynolds numbers up to $Re_\tau \simeq 1900$. Moser *et al.* (1999) suggest 13 grid points below $y^+ = 10$ as necessary and sufficient for a correct representation of the viscous wall layer up to $Re_\tau = 590$. The work of Kravchenko *et al.* (1993) investigates the relationship between near-wall vorticity structures and wall-friction in turbulent plane channel flow using conditional sampling techniques and reports the interesting observation that high-skin friction regions on the wall are strongly correlated with streamwise vortices located on the average at $y^+ \sim 20$ approximately 90 wall units downstream from the high skin-friction location. Kasagi *et al.* (1995) characterize the high-vorticity core of the near-wall vorticity structures in respect to their relationship to low-pressure regions, they also associate the production of Reynolds (normal and shear) stress to the near-wall vortices. They reach these important conclusions by visual inspection of DNS datasets using a 3D computer graphics technique and prove once more the importance of advanced visualization methods in the understanding of turbulence phenomena. Some authors slightly change the channel flow configuration to study various other aspects of wall-turbulence: Kristoffersen and Andersson (1993) introduce rotation of the plane channel in order to determine the effect of rotational forces on wall-turbulence (a situation relevant in gas turbines rotors), Bech *et al.* (1995) study turbulent flow between moving walls (Couette flow) while Lygren and Andersson (2001) put these two effects together in a DNS of the flow between a stationary and a rotating disk.

DNS Of Wall Heat Transfer

In order to understand the influence of turbulence on wall heat transfer Kim and Moin (1989) numerically simulate the turbulent transport of a passive scalar in a $Re_\tau \simeq 180$ channel flow imposing a mean scalar gradient by keeping the wall temperature constant. They confirm experimental observations of streamwise thermal streaky structures and of large correlation (~ 0.95) of streamwise velocity fluctuations and temperature fluctuations. Kasagi *et al.* (1992) use a constant heat flux (isoflux) wall boundary condition and substantially confirm the statistics from Kim and Moin (1989): the close agreement observed between the Reynolds shear stress and the

wall normal turbulent heat flux suggest that these are generated by similar mechanisms. Kasagi *et al.* (1992) report also that the isothermal wall boundary condition is a valid assumption for an air flow, being the wall temperature fluctuations very small for most wall materials. Passive scalar transport and wall heat transfer is the subject of several other studies by Kawamura *et al.* (1999), Johansson and Wikström (1999), Kong *et al.* (2000) and Abe *et al.* (2004) that perform direct simulations of channels characterized by increasingly high Reynolds number up to $Re_\tau = 1020$ and for different Prandtl numbers[7]: results suggest that the effect of quasi-streamwise near-wall vorticity structures extends also to the wall heat-flux fluctuations and represent an important indication for the conclusion reached in Chapter 7 about flame-wall interaction.

Compressibility

All the direct simulations mentioned so far are performed by solving the Navier-Stokes equations for incompressible fluids, with constant density and a solenoidal velocity field. However, few real fluids are fully incompressible and the importance of compressibility effects increases under certain conditions, especially in fast flowing gases and in the presence of large density fluctuations, moreover the interactions between the flame and acoustic waves can only be captured in a compressible formulation. Supersonic and hypersonic airplanes, re-entry problem for space vehicles, subsonic turbulence in molecular clouds are typical applications for the study of compressible turbulence. Nevertheless the amount of studies in which the compressible formulation is adopted for numerical simulations of turbulence is somewhat limited compared to the incompressible case. Also very little experimental data is available on compressible turbulent flows due to the difficulties in measuring (traditionally with hot-wire probes) the fluid velocities and thermodynamic state variables when velocity, pressure, density and temperature fluctuations in the flow are of the same order of magnitude and intricately connected.

If a fully compressible formulation represent a very general approach that can be applied to a large range of flow problems, its use is also largely constrained by the need to resolve both large time scales associated to the fluid convection velocities and short time scales associated to fast acoustic

[7] The Prandtl number $Pr = \frac{\nu}{\alpha}$ is the adimensional quantity that represents the ratio of momentum diffusivity (ν is the kinematic viscosity) versus thermal diffusivity (α is the coefficient of thermal diffusivity)

waves: a very short time step is required to capture the fast acoustics and a long integration time is needed for complete representation of the large scale fluid motions. In the case of nearly incompressible low Mach number[8] problems characterized by widely different convective and acoustic speeds, this problem is particularly serious and leaves the incompressible approach often as the only practicable alternative.

In the case of a nearly incompressible low Mach number *reactive* flow, where detailed flame modelling involves fast chemical reactions and fast mass diffusion, other factors than the resolution of acoustic waves can limit the time step: in the solution of the equation system represented by the compressible Navier-Stokes equations coupled to a detailed chemical kinetics mechanism, the time step, when using a fully explicit time integration approach, is more often limited by chemistry and diffusion than by acoustics. Consequently, for the low Mach number simulations presented in this report the author adopt the more general compressible approach safely into the nearly incompressible limit ($M < 0.3$): for the ducted hydrogen-air flame modelled here, both the accurate representation of fastly diffusing radicals and the use of a detailed chemical kinetics mechanism present limitations on the time step often more strict than the acoustic ones.

Concerning the choice of a compressible versus an incompressible formulation, in a landmark paper Zank and Matthaeus (1991) use perturbative techniques to study the relationship between low Mach number compressible and incompressible fluids and the influence of fast and slow time scales on numerical solution of the Navier-Stokes equations. About the correct initial conditions for direct simulations they show that, following Kreiss' principle on the order of time derivatives, a smooth initial condition, giving solutions on the slow time scale only, is very important in suppressing initial acoustic transients (initial noise that pollutes the solution). This suggestion is adopted in the simulations reported in Chapter 7 by assigning as smooth initial conditions as possible especially along the flame front and in the flame anchor region. They also show that the *passive scalar* equation for heat transfer typically used in studies of incompressible turbulent flow should be derived and interpreted as an equation for a *nearly* incompressible fluid and not for an incompressible one! Doing otherwise results in

[8]The Mach number $M = |\boldsymbol{u}|/c$ represent the ratio of a characteristic convective velocity $|\boldsymbol{u}|$ to the speed of sound c. A turbulent Mach number M_t can also be defined when the characteristic convective velocity is substituted by the rms value of the velocity fluctuation $< \sqrt{u'^2} >$

an inconsistent formulation[9]. Zank and Matthaeus (1991) derive two sets of equations that describe the flowing fluid in two different states, a heat conduction dominated and a heat conduction modified hydrodynamics:

- In the heat conduction dominated state density and temperature fluctuations are anticorrelated and dominate pressure fluctuations
- In the heat conduction modified state none of the thermodynamic variables fluctuations dominate the others and pressure, temperature and density are weakly correlated

since these two formulations give such different density and temperature correlations, it is most critical to choose the formulation that correctly applies to the assumptions and and dominant processes of the physical problem being solved. These considerations, together with the availability of a state-of-the-art parallel compressible DNS code (see Section 1.3.4), motivated the adoption of the compressible formulation in the present work.

Compressible turbulence is studied by Moyal (1952) that proposes a decomposition of compressible turbulence in spectral space into a longitudinal component (random noise) parallel to the wave vector and a transversal component (eddy turbulence) normal to it. These components are also known as acoustic or dilatation component and solenoidal or incompressible component respectively. The interaction between these components are due to nonlinear effects and increase in importance with increasing Reynolds number. Kovásznay (1953) individuates three *modes* of disturbance fields applying perturbation theory to the Navier-Stokes equations for compressible, viscous and heat-conductive fluids: the vorticity mode, the entropy mode and the acoustic mode. From his hot-wire measurements (among the first) of a supersonic boundary layer flow Kovásznay (1953) concludes that the three modes are independent for small fluctuations but they interact for large fluctuations when linearization is not admissible, basically confirming the conclusions of Moyal (1952) in spite of the different decomposition adopted.

[9] From Zank and Matthaeus (1990): "*In deriving the incompressible heat-transfer equation it is argued that a non uniformly heated fluid is not incompressible in the usual sense because density varies with temperature and so should not be regarded as constant. Instead, it is necessary to hold the pressure constant. Thereafter, however, the density is assumed constant, in both the reduced thermal-transfer equation and the continuity equation. Furthermore, the pressure is no longer constant, satisfying instead the Poisson equation*"

The computational approach to the study of compressible turbulence starts with the work of Feiereisen *et al.* (1981) that run a three-dimensional DNS of compressible homogeneous turbulent isotropic and shear flow at low Reynolds and Mach number and applies a Helmotz decomposition on the dataset. Setting up the initial conditions for the direct simulation with a solenoidal velocity field (divergence free) and zero pressure fluctuations, the solution acquires velocity divergences (they remain small) but it does not differ much from a typical incompressible solution. Passot and Pouquet (1987) and Erlebacher *et al.* (1990) also adopt a Helmotz decomposition in order to separate the compressible and incompressible effects on the turbulence but increase the amount of compressibility. They show, in their two-dimensional DNS of homogeneous turbulence of increasingly high Reynolds number, that the evolution of the flow toward the formation of shocks is dependent on the initial conditions. Disequilibrium of initial conditions is necessary (not sufficient) to shock formation: an initial turbulent Mach number $M_t \sim 0.3$ leads to the formation of *shocklets*, the shocklets compressibility effects steepen the inertial spectra beyond the estimate of k^{-2} predicted analytically by Moiseev *et al.* (1981), for $M_t > 0.3$ the shocklets become strong shocks and transfer energy from mechanical to internal (heat) and partially back to mechanical with the formation of vortices (at the expenses of internal energy, the compressible spectrum is unchanged). Lee *et al.* (1991) investigate compressibility effects in fully three-dimensional isotropic turbulence and conclude that three-dimensional turbulence is less prone to shock formation than two-dimensional turbulence, however shocks will form at sufficiently high turbulent Mach number M_t. In a later work Lee *et al.* (1992) examine the applicability of Taylor's *frozen turbulence* hypothesis for compressible flows and conclude that vorticity and entropy (solenoidal) modes are correctly represented in the transfer between temporally and spatially evolving turbulence while Taylor's hypothesis is not applicable to the acoustic (dilatation) mode. This fact together with the conclusions of Piomelli *et al.* (1989) on the applicability of Taylor's hypothesis in wall-bounded flow suggest the validity of one of the approaches adopted in the present work for the turbulent inflow boundary specification, see Section 7.2.1 for details.

Concluding this brief review of compressible turbulence research, the existence of few studies about high speed (supersonic) wall-bounded flows should be mentioned. Direct simulations of fully compressible supersonic boundary layer flows are reported by Coleman *et al.* (1995), Huang *et al.* (1995), Maeder *et al.* (2001), Pantano and Sarkar (2002), Sandham *et al.*

(2002), Morinishi *et al.* (2004) for Mach numbers in the range 1.5 to 6.0 and viscous Reynolds numbers Re_τ in the order of the few hundreds. The turbulent statistics from these supersonic flows compare well with the incompressible cases given that the Van Driest transformation for the velocity is adopted, see Huang and Coleman (1994) for details. Pantano and Sarkar (2002) report a decreasing turbulence intensity production for increasing Mach number, in fact the pressure-strain correlation exhibits monotone decrease and they explain this trend with a possibly reduced communication [10] between disturbances and damped nonlinear interactions. Morinishi *et al.* (2004) examines the mean spanwise spacing between the near-wall vorticity structures for supersonic turbulent channel flow and confirm the value of 100 non-dimensional wall units already observed experimentally and in direct simulations of incompressible turbulent boundary layers.

Reactive Flows

The already large computational requirements that are typical of a DNS of non-reacting turbulent flows are considerably increased in the case that the flowing fluid is composed by a reacting mixture: transport equations for energy and species must be solved together with the Navier-Stokes equations and the system of ordinary differential equations that describe an eventual detailed chemical kinetics reaction mechanism has to be integrated to obtain the reaction rates for all species (source terms in the transport equations). Several DNS of both premixed and non-premixed, laminar and turbulent flames are found in the open literature from the last 15 years, for comprehensive (but fairly aged) reviews see Poinsot *et al.* (1996) and Vervisch and Poinsot (1998).

DNS of reactive flows has a shorter history if compared with the non-reactive case and starts in the early 1990s. Premixed flame propagation in isotropic turbulence is studied by Poinsot *et al.* (1990) and Haworth and Poinsot (1992) in a two-dimensional approximation with variable fluid properties and single-step chemistry, detailed chemical kinetics is included by Baum *et al.* (1994a) for hydrogen-air flame. Rutland *et al.* (1990) and El Tahry *et al.* (1991) choose to study the same physical problem in a more realistic three-dimensional flow configuration but make some simplification on the fluid properties assuming low heat release (constant density), con-

[10] Because of finite speed of sound and comparable convective velocities the disturbances interact less easily than in incompressible turbulence

stant unity Lewis number[11] and single-step chemical kinetics. Gran *et al.* (1996) examine the effects of differential diffusion in highly curved flames and their relative importance compared to chemistry effects. Veynante and Poinsot (1997) investigate the effects of favorable and adverse pressure gradients on propagation and wrinkling of turbulent premixed flames and report that a pressure decrease from unburnt to burnt gases, a situation common in ducted flames such those modelled in the present work, is found to decrease flame wrinkling, thickness and speed. Cant (1999) examines the statistical geometry of the flame surface and its interaction with a three-dimensional turbulence field. Chen *et al.* (1999) and more recently Im and Chen (2002), Echekki and Chen (2003) and Hawkes and Chen (2004) conduct fundamental investigations of flame-turbulence interaction in two-dimensional turbulent fields and study preferential diffusion effects, autoignition of hydrogen-air flames, and pollutant emissions of hydrogen-enriched methane flames with both detailed and reduced chemical kinetics. In another recent paper Guichard *et al.* (2004) report direct simulations of an anchored v-shaped premixed flame propagating in decaying isotropic turbulence and illustrate the most advanced turbulent injection procedure to date, combining a spectral and a finite-difference solver for inflow turbulence generation and turbulent flame simulation respectively. From the literature mentioned above it can be concluded that a two-dimensional approximation of the turbulent flow field is reasonably successful in representing premixed flame propagation in isotropic turbulence, being the flame geometry approximately two-dimensional, this is not the case for flame propagation in highly anisotropic turbulent fields like wall boundary layers and three-dimensional direct simulations are necessary in this context.

DNS Of Flame-Wall Interaction

Experimental investigations of near-wall flame propagation and quenching are complicated to set up and results are not very reliable because of serious difficulties in performing accurate measurements. On the computational side, one-dimensional and two-dimensional approaches for direct simulation of *laminar* flame-wall interaction are relatively inexpensive from the computational point of view and allow the use of detailed chemical kinetics mechanisms for the description of the combustion process. Already in

[11] The Lewis number $Le = \alpha/D$ is the adimentional quantity that represent the relative importance of thermal and mass diffusivity

the early 1980s Westbrook *et al.* (1981), Hocks *et al.* (1981) and a decade later Ezekoye *et al.* (1992) perform direct simulations of premixed laminar hydrocarbon flames propagating perpendicular to the wall and stagnating on it: this configuration is also known as head-on quenching (HOQ), see Figure 1.8 for a schematic representation of possible flame-wall interaction configurations. While Westbrook *et al.* (1981) employ detailed chemical kinetics to model the chemical reactions in the flame, Hocks *et al.* (1981) and Ezekoye *et al.* (1992) use simplified chemistry approaches, respectively two-step and single-step: however, *all* agree on the fact that radical recombination at the wall, characterized by low activation energy reactions, plays an important role in the flame-wall interaction process and that single-step chemistry, lacking detailed information about radical reactions, fails to predict flame-wall interactions correctly. Later studies of wall quenching for laminar hydrocarbon-air flames by Popp *et al.* (1996) and Popp and Baum (1997) focus on the effects of surface reactions and cross-diffusion on wall heat flux, flame heat release and quenching distance: at high wall temperatures, radical absorption by the catalytic surface reduces the amount of highly exothermic radical recombination reactions at the wall thereby reducing heat release and consequently wall heat flux. Wall quenching of hydrogen-oxygen premixed and non-premixed laminar flames is numerically simulated in de Lataillade *et al.* (2002) and Dabireau *et al.* (2003): once more the importance of radical recombination reactions at the wall is stressed and the authors report for hydrogen flames the same qualitative quenching behaviour as in hydrocarbon-air flames but quantitatively different adimensional wall heat flux and quenching distance parameters.

Multidimensional direct simulations of turbulent flame-wall interactions are very expensive computationally so very few studies of this configuration are reported in the literature. Poinsot *et al.* (1993), Bruneaux *et al.* (1996) and Bruneaux *et al.* (1997) study premixed flame head-on-quenching in a constant density and constant viscosity fluid. Using single-step chemistry first in a two-dimensional domain and later in a fully three-dimensional turbulent channel flow configuration (although limited to the minimal box of Jiménez and Moin (1991) in the homogeneous directions), they clearly show the inadequacy of the two-dimensional turbulence approach to study the wall-quenching process. The maximum wall heat flux predicted by the two-dimensional simulations is of the same order of the one observed experimentally and computed numerically for *laminar* flames, on the other side the three-dimensional simulation gives values of wall heat flux larger than the laminar value by a factor of two. This significant difference is attributed

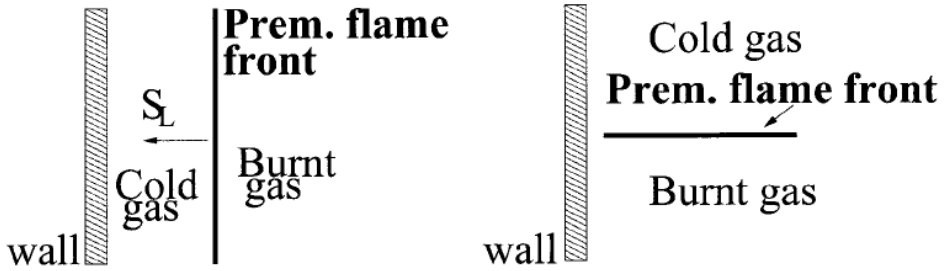

Figure 1.8: Schematic representation of head-on quenching (left) and side-wall quenching (right) configurations (from Dabireau *et al.* (2003)).

to the existence of the near-wall structures of intense quasi-streamwise vorticity in three dimensions that are absent in two dimensions.

The only numerical investigation, known to the author, of turbulent premixed flame side-wall quenching (SWQ) is reported in Alshaalan and Rutland (1998) and Alshaalan and Rutland (2002): they perform direct simulations of an anchored, premixed v-shaped flame modelled with single-step chemistry and propagating in three-dimensional, variable density, turbulent Couette flow for the minimal channel dimensions of Jiménez and Moin (1991), in this configuration statistically stationary results are obtained with averaging in the spanwise direction and in time and used in a modeling attempt. However, the data post-processing and modeling approach of both Bruneaux *et al.* (1996) and Alshaalan and Rutland (1998) are based on the flame surface density (Σ) analysis and assume flame propagation in the flamelet regime. This modeling approach relies then on the assumption that turbulent time scales are larger than chemical time scales (resulting in a continuous, wrinkled and thin flame surface) while near the wall, for certain Reynolds numbers and reacting mixture composition, turbulent length and time scales may decrease to values smaller than, respectively, flame thickness and chemical time scales and the flamelet approach may fail. Also, it

is not clear if the flame surface normal definition, characteristic of this approach, has any significance at the near-wall quenching position of a flame propagating parallel to the wall (SQW), see Figure 1.8, where the temperature and progress variable profiles are not parallel to each other because of the heat loss into the solid surface.

1.3.4 The DNS Code

A parallel fortran code, named S3D and developed at the Combustion Research Facility (Livermore, CA) under a research program of the United States Department of Energy, is used to perform the direct numerical simulations reported in this thesis. The code is programmed in FORTRAN 90, uses the Message Passing Interface (MPI) for interprocess communication in parallel execution, is portable to several different hardware and software architectures including Linux clusters, SGI Origin, IBM SP, Windows PC, Cray T3E and DEC Alpha clusters. The data presented here is obtained on Intel, DEC Alpha and Cray T3E hardware both at Sintef Energy Research in Trondheim, Norway, and Sandia National Laboratories in Livermore, California. The algorithm implemented in S3D solves the compressible Navier-Stokes equations in conservation form on a structured, Cartesian mesh in 1, 2 or 3 spatial directions. Chemical reactions coefficients are obtained from the CHEMKIN package, see Kee *et al.* (1999) for details. Scalar transport properties can be approximated in this code with a constant Lewis number for each species or mixture-averaged approach with or without thermal diffusion, all these approaches are compared in the context of the present work and used according to physical significance and practical feasibility, the transport coefficients for momentum (the mixture dynamic viscosity, μ), heat (the mixture thermal conductivity, λ_{mix}) and mass (the mixture averaged species diffusion and thermal diffusion coefficients, D_i^{mix} and D_i^T respectively) are computed from the TRANSPORT package, see Kee *et al.* (1999) for details. Spatial derivatives are computed with an eight-order[12] explicit finite difference scheme in conjunction with a tenth-order explicit spatial filter as in Kennedy and Carpenter (1994) in order to remove high frequency noise and reduce aliasing error. A fourth-order, five-stage explicit Runge-Kutta scheme developed by Kennedy *et al.* (2000) is used for time integration paired with a proportional-integral-derivative (PID) error controller to opti-

[12] On the domain boundaries one-sided third-order stencils are used for non homogeneous directions

mally adjust the time-stepping. A significant rewriting of S3D to improve its algorithm design and physical capabilities is exposed in Sutherland (2004): major updates provide a new formulation for the terms including derivatives of the transport coefficients in order to take into account transport property changes as a function of both fluid temperature and mixture composition (the effects of composition variations on the transport coefficients was previously neglected). As part of the present research work fluid-wall boundary conditions have been implemented in S3D for isothermal and adiabatic, non reacting and reacting solid nonporous surfaces[13], see Chapter 3; several alternative discretization of the convective terms in the Navier-Stokes equations have also been implemented in S3D and their mass and energy conservation and dealiasing properties tested and compared, see Chapter 4.

1.4 Research Strategy And Report Layout

In the present work DNS is used to study the evolution of an anchored premixed hydrogen-air v-shaped flame immersed in a low Reynolds number turbulent Poiseuille flow and characterized by a Damkohler number[14], Da, close to the value of 1/4. This turbulent reactive flow is simulated taking into account variable thermo-physical properties and detailed chemical kinetics, focus is on improving the understanding of the flame-wall interaction process in turbulent boundary layers. The wall surface is assumed inert. Ezekoye (1998) indicates water condensation at "cold" walls as a possibly important factor in reducing the wall heat flux, however, the multidimensional simulations reported in the present work assume isothermal channel walls at $750\,K$ and water condensation is neglected, together with surface reactions. According to Popp *et al.* (1996), "hot" ($> 400\,K$) solid surfaces, depending on the type of material they are made of, can act as a catalyst and, through radical absorption, desorption and recombination, can play an important role in the flame-wall interaction process: nevertheless in the present simulations the wall surface is considered as inert in order to make the conclusions reached here independent of some particular properties of the wall surface material.

Given the clear indications from studies available in the open literature

[13] The reacting wall approach is, at the time of the writing, still under testing and it is therefore not included in this report

[14] The Damkohler number is the ratio between a chemical and a turbulent time scale.

about one-dimenstional laminar flame-wall interactions, modelling of the combustion process with detailed chemical kinetics is adopted in this work since it is necessary for a proper representation of radical species diffusion and recombination at the wall: estimates of maximum wall heat flux and flame quenching distance are subject to considerable uncertainties in the single-step chemistry approximation of Bruneaux *et al.* (1996) and Alshaalan and Rutland (1998) and it is reasonable to assume that eventual *large* errors in these quantities spread to other physical quantities characterizing the flow and are convected downstream in the boundary layer.

The back-to-back flame configuration used by Bruneaux *et al.* (1996) does not allow statistically stationary analysis of the flame-wall interaction. Interesting quantities have to be averaged over several different realizations of the initial turbulence to insure their independence on the initial conditions and Bruneaux *et al.* (1996) use a statistical sample consisting of 30 interactions based on different realizations of the initial turbulent field. The v-shaped flame configuration adopted in this work is propagating in a turbulent plane channel flow characterized by considerably larger dimensions than the minimal channel of Jiménez and Moin (1991) used in Alshaalan and Rutland (1998): this allows statistically stationary results and the analysis of the correlation between the near-wall vorticity structures and the flame brush over a relatively large spanwise extension. No modeling attempt is considered in this report but the DNS database generated in the present work will be used in the formulation of a near-wall combustion model for CFD at a later stage.

The mathematical formulation of the general problem is derived in Chapter 2. The specific boundary conditions treatment and the assumptions made therein are exposed in Chapter 3. The numerical solution method is briefly discussed in Chapter 4. In Chapter 5 the flow solver is validated against previous numerical simulations of fully developed turbulent plane channel flow, the velocity fields from this validation database are also used to specify the turbulent inflow boundary condition in the flame-wall interaction simulation described in Chapter 7. The detailed chemical kinetics mechanism that is coupled with the flow solver is validated in Chapter 6 against previous numerical simulations of laminar flame-wall interaction and the effects of various assumptions about the fluid transport properties and wall temperatures are tested. Chapter 7 discusses the results from the three-dimensional turbulent flame-wall interaction and the physical insight gained from the simulations. Finally, a summary of the conclusions reached and suggestions for recommended future work are presented.

2 Mathematical Formulation

The system of partial differential equations governing compressible reactive viscous flow, also known as the Navier-Stokes equations, represent a set of hyperbolic partial differential equations that contains an incompletely elliptic perturbation. The unperturbed hyperbolic system describes the so-called *inviscid* Euler equations and is not considered in this work because of the importance of viscous effects in reactive wall-bounded flows.

The Navier-Stokes equations may be written in several different but mathematically equivalent forms. Because of the non-linearities that they contain, a general analytic solution of the Navier-Stokes equations does not exists and the numerical solution of this system of coupled partial differential equations is quite a formidable task. The formulation adopted for numerical solution in the S3D code is the conservative form of the equations, this choice is motivated by the compactness of the formulation that results in a minimal number of derivative operations at each time step of the time integration procedure. The mathematical formulation of the problem and some details about the assumptions and simplifications made in the present context are reported in the following Sections.

2.1 The Continuum Assumption

The realm of validity of the mathematical description of a flowing fluid through the Navier-Stokes equations relies on the *continuum assumption*: the molecular *mean free path*[1] is several times smaller than a characteristic length scale of the flow. This assumption implies that the smallest element of fluid considered contains a sufficient number of molecules to allow statistical averages of the fluid thermo-physical properties and their smooth variation, making them differentiatiable. In the present DNS of reactive boundary layers the length scale of the tiniest fluid volumes considered is of the order of $10\,\mu m$ and, even if very small, it is well within the limit of validity of the continuum assumption. The fundamental theory underlying

[1] The mean distance covered by a molecule between collisions

the continuum assumption is the Chapman-Enskog kinetic theory of dilute gases, see Hirshfelder *et al.* (1964) for details.

2.2 Conservation Equations

2.2.1 System Of Equations

The compressible Navier-Stokes equations are expressed in dimensional conservative form as[2]:

$$\frac{\partial(\rho \boldsymbol{u}_\alpha)}{\partial t} = -\boldsymbol{\nabla}_\beta \cdot (\rho \boldsymbol{u}_\alpha \boldsymbol{u}_\beta) + \boldsymbol{\nabla}_\beta \cdot (-p\delta_{\alpha\beta} + \tau_{\beta\alpha}) + \rho \sum_{i=1}^{\mathrm{N_g}} Y_i \boldsymbol{f}_{i\alpha} \tag{2.1}$$

$$\frac{\partial \rho}{\partial t} = -\boldsymbol{\nabla}_\beta \cdot (\rho \boldsymbol{u}_\beta) \tag{2.2}$$

$$\frac{\partial(\rho e_t)}{\partial t} = -\boldsymbol{\nabla}_\beta \cdot (\rho e_t \boldsymbol{u}_\beta) + \boldsymbol{\nabla}_\beta \cdot (-p\boldsymbol{u}_\beta + \tau_{\beta\alpha} \cdot \boldsymbol{u}_\alpha - \boldsymbol{q}_\beta) + \rho \boldsymbol{u}_\beta \cdot \sum_{i=1}^{\mathrm{N_g}} Y_i \boldsymbol{f}_{i\beta} + \sum_{i=1}^{\mathrm{N_g}} \boldsymbol{f}_{i\beta} \cdot \boldsymbol{J}_{i\beta} \tag{2.3}$$

$$\frac{\partial(\rho Y_i)}{\partial t} = -\boldsymbol{\nabla}_\beta \cdot (\rho Y_i \boldsymbol{u}_\beta) - \boldsymbol{\nabla}_\beta \cdot \boldsymbol{J}_{i\beta} + W_i \dot{\omega}_i \tag{2.4}$$

where, ρ is the fluid density, p is the fluid pressure, e_t is total specific internal energy of the fluid, i and j are species indexes, $\mathrm{N_g}$ is the total number of gas phase species, Y_i is the mass fraction of species i, W_i is the molecular weight of species i, t is the time, α and β are spatial direction indexes[3], $\delta_{\alpha\beta}$ is the Kronicker delta, $\boldsymbol{u}_\alpha$ is the velocity vector in direction α[4], $\boldsymbol{f}_{i\alpha}$ is the body force per unit mass of species i in direction α, $\boldsymbol{J}_{i\alpha} = \rho Y_i \boldsymbol{V}_{i\alpha}$ is the diffusive flux of species i in direction α with $\sum_{j=1}^{\mathrm{N_g}} \boldsymbol{J}_{i\alpha} = 0$, $\boldsymbol{V}_{i\alpha}$ is the diffusion velocity of species i in direction α, $\boldsymbol{q}_\alpha$ is the heat flux vector in direction α, $\tau_{\beta\alpha}$ is the viscous stress tensor for directions α and β, $\dot{\omega}_i$ is

[2] The Einstein notation is adopted in this report meaning that repeated spatial indexes, α and β, within the same term imply summation over their range of values

[3] Note that the Cartesian coordinates in the three spatial directions will be indicated indifferently with the symbols x_1, x_2, x_3 or x, y, z in the remaining of this report while the components of the velocity vector $\boldsymbol{u}$ will be indicated indifferently with u_1, u_2, u_3 or u, v, w.

[4] Note that vector quantities will always be indicated with **bold** fonts in the remaining of this report.

the molar reaction rate of species i per unit volume, and ∇_α is the gradient operator in direction α.

Alternatively, the convective non-linear terms in the conservation equations (first term on the right-hand side of 2.1-2.4) can be solved in skew-symmetric form because of the useful dealiasing properties of this formulation (see Section 2.2.2). The diffusive terms are evaluated by first computing the flux terms (viscous stress tensor $\tau_{\beta\alpha}$ in 2.1, heat flux vector $\boldsymbol{q}_\beta$ in 2.3, species diffusion velocity $\boldsymbol{J}_{i\beta}$ in 2.4) and then taking their respective divergences, this approach eases the use of realistic transport coefficients.

Numerical integration of the system of partial differential equations 2.1-2.4 gives the conserved variables solution vector $\mathbf{U}$ as:

$$\mathbf{U} = (\rho \boldsymbol{u}_\alpha, \rho, \rho e_t, \rho Y_i)^t \quad \alpha = 1,2,3 \quad i = 1, \cdots, \mathrm{N_g} \tag{2.5}$$

from which the primitive variables solution vector $\mathscr{U}$ is computed:

$$\mathscr{U} = (\boldsymbol{u}_\alpha, \rho, p, Y_i)^t \quad \alpha = 1,2,3 \quad i = 1, \cdots, \mathrm{N_g} \tag{2.6}$$

Note that only $\left(N_g - 1\right)$ species transport equations 2.4 need to be solved since the mass fraction of the last specie is determined from the constraint:

$$\sum_{i=1}^{\mathrm{N_g}} Y_i = 1 \tag{2.7}$$

and that the temperature T is extracted by iterative procedure from the total specific internal energy e_t and knowledge of the species mass fractions Y_i, finally the primitive variable pressure p is obtained from an *equation of state*. According to the theory of thermodynamics the state of a single-phase mixture is uniquely determined by the mixture composition and by two other independent intensive thermodynamic properties as density and temperature, see Moran and Shapiro (1998) for details. Consequently, the ideal gas equation of state completes the system of equations 2.1-2.4, providing the fluid pressure p, and is assumed to correctly describe the fluid mixture under investigation with the law:

$$p = \rho R T \tag{2.8}$$

where R is the specific gas constant for the mixture. On mass basis R is obtained from the mixture composition, the species molecular weights W_i and the universal gas constant $\mathscr{R}$:

$$R = \mathscr{R} \sum_{i=1}^{\mathrm{N_g}} \frac{Y_i}{W_i} = \frac{\mathscr{R}}{W} \tag{2.9}$$

in this last expression W is the mixture molecular weight defined as:

$$W = 1/\sum_{i=1}^{N_g}(Y_i/W_i) = \sum_{i=1}^{N_g}(X_i W_i) \tag{2.10}$$

and the species mole fractions X_i and mass fractions Y_i are related by:

$$\frac{Y_i}{X_i} = \frac{W_i}{W} \tag{2.11}$$

Some additional thermodynamic relations are derived in the remaining of this section while details of the convective, diffusive and source terms are discussed in the following sections.

The *total* specific internal energy in equation 2.3 is defined as:

$$e_t = \frac{\boldsymbol{u}_\alpha \boldsymbol{u}_\alpha}{2} + e \tag{2.12}$$

and represents the sum of kinetic and specific internal energy. The specific internal energy of a mixture is only dependent on its temperature and composition:

$$e = e(T, Y_i) = \sum_{i=1}^{N_g}(h_i Y_i) - \frac{p}{\rho} \tag{2.13}$$

and the equation of total specific internal energy becomes then:

$$e_t = \frac{\boldsymbol{u}_\alpha \boldsymbol{u}_\alpha}{2} + \sum_{i=1}^{N_g}(h_i Y_i) - \frac{p}{\rho} \tag{2.14}$$

The quantity h_i represents the partial specific enthalpy of specie i and is related to the temperature T by the isobaric variable specific heat of specie i $c_{p,i}$ in the following expression:

$$h_i = h_i^0 + \int_{T_0}^{T} c_{p,i} dT \tag{2.15}$$

where the isobaric specific heat is usually obtained from experimental measurements of:

$$c_{p,i} = \left(\frac{\partial h_i}{\partial T}\right)_p \tag{2.16}$$

and h_i^0 represent the formation enthalpy of specie i at the reference temperature T_0. The *mixture* isobaric specific heat can be approximated in common combustion processes by the formula:

$$c_p = \sum_{i=1}^{N_g} (c_{p,i} Y_i) \tag{2.17}$$

and is related to the *mixture* isochoric specific heat by the specific gas constant for the mixture R:

$$c_p = c_v + R \tag{2.18}$$

2.2.2 Convective Terms

The problem of unstable behaviour in the numerical solution of non-linear conservation laws such as the Navier-Stokes equations in the context of high order numerical methods (highly accurate both in space and time) is discussed in Mansour *et al.* (1978). Artificial generation of conserved flow-field quantities by the numerical method is reported together with the consequent destruction of the solution. Making use of a proof given by Mansour *et al.* (1978) about conservation of kinetic energy and extending it to compressible flow, Feiereisen *et al.* (1981) suggest that the adoption of *skew-symmetric* formulations of the convective terms contributes in conserving total energy by ensuring that the numerical method is incapable of artificially generating kinetic energy and results in improved overall stability and accuracy. DNS of homogeneous compressible turbulence by Blaisdell (1991) show by spectral analysis the effects of the skew-symmetric formulation in reducing aliasing errors and the associated growth of high-frequency energy. The effects of alternative convective formulations on numerical simulations of incompressible flows are also presented in Zang (1991) and Blaisdell *et al.* (1996) confirming the conclusions of earlier studies about the energy-conserving properties of the skew-symmetric formulation.

It is evident from this brief review that previous experiences with high-order numerical methods strongly suggest the adoption of the mathematically equivalent skew-symmetric form of the convective terms in place of the conservative one. There are however few other factors to be considered in choosing the convective formulation that best applies to a given problem. Following the compact notation suggested by Blaisdell (1991) the convective terms on the right-hand side of equations 2.1-2.4 are expressed

in the general *conservative* form as:

$$\frac{\partial(f g_\beta)}{\partial x_\beta} \tag{2.19}$$

where f represent the convected variable (in conservative form), as $\rho \boldsymbol{u}_\alpha$ or ρY_i, and g_β its convection velocity $\boldsymbol{u}_\beta$ in direction β. Alternative formulations of the convective terms are given in Blaisdell (1991) using the following general notation:

$$\frac{\partial(f g_\beta)}{\partial x_\beta} = \tilde{\alpha}\frac{\partial(f g_\beta)}{\partial x_\beta} + (1-\tilde{\alpha})\left(f\frac{\partial g_\beta}{\partial x_\beta} + g_\beta\frac{\partial f}{\partial x_\beta}\right) \tag{2.20}$$

where the parameter $\tilde{\alpha}$ is set to 1, 1/2 or 0 for the *conservation*, *skew-symmetric* and *convection* form respectively. In the context of the present research work the general formulation 2.20 and a new formulation of the convective terms are implemented in the S3D code by the author and tested, see Section 4.4, results are being organized in a journal article and scheduled for later publication. Applying 2.20 to the convective terms in the momentum equation and in the general scalar (ϕ) equation for $\tilde{\alpha} = 1/2$ one has:

$$\frac{\partial\left(\rho \mathbf{u}_\alpha \mathbf{u}_\beta\right)}{\partial x_\beta} = \frac{1}{2}\left[\nabla_\beta \cdot \left(\rho \mathbf{u}_\alpha \mathbf{u}_\beta\right) + \rho \mathbf{u}_\alpha \cdot \left(\nabla_\beta \mathbf{u}_\beta\right) + \mathbf{u}_\beta \nabla_\beta \cdot (\rho \mathbf{u}_\alpha)\right] \tag{2.21}$$

$$\frac{\partial\left(\rho \phi \mathbf{u}_\beta\right)}{\partial x_\beta} = \frac{1}{2}\left[\nabla_\beta \cdot \left(\rho \phi \mathbf{u}_\beta\right) + \rho \phi \cdot \nabla_\beta \mathbf{u}_\beta + \mathbf{u}_\beta \nabla_\beta \cdot (\rho \phi)\right] \tag{2.22}$$

As it is apparent in equations 2.21 and 2.22, adopting a skew-symmetric formulation implies additional derivative operations and is computationally more expensive than the original conservative formulation.

In the present context full-scale DNS are run using the cheaper conservative formulation in conjunction with a tenth-order explicit filter. This filter is only applied every 10 (up to 50 in the inert cases) global time steps and exclusively introduces artificial dissipation at the high wave-numbers to eliminate numerically generated high-frequency energy[5], the usefulness of the skew-symmetric formulation is recognized especially in running the many poorly resolved *test cases* for which full resolution is not affordable

[5] Finite difference stencils have only marginal resolution near the highest frequency allowed by the grid, see Section 4.2.2

and the high-order filter does not manage to contain the growth of aliased energy.

The following considerations should be taken into account in the treatment of the non-linear convective terms:

- The tendency to generate artificial high-frequency energy is typically a sign of poorly resolved calculations[6]: this alarm-bell should be listened to, addressing the problem by increasing grid resolution, instead of *silencing* it with a better dealiasing formulation
- Adoption of the skew-symmetric instead of the conservative formulation increases the number of derivative operations to be performed at each time step of the integration procedure and it is therefore computationally more expensive, this is especially true if a large number of species is present
- In variable density flows where the density has a non-trivial spectrum and the convective terms are characterized by cubic non-linearities, it is unclear whether the convective term may be treated as only quadratically non-linear
- Even if the original formulation of Blaisdell (1991) is computationally expensive and implicitly assumes only quadratic non-linearities of the form $\partial(fg)/\partial x_\beta$ in the convective terms, it is fairly easy to derive an alternative, more general and computationally cheaper[7] approach for treatment of eventual cubic non-linearities $\partial(fgh)/\partial x_\beta$.

2.2.3 Diffusive Terms

Dispensing with the spatial indexes to ease the notation, for dilute, multicomponent, polyatomic, reacting gases the mass flux of the specie i is equal to:

$$\boldsymbol{J}_i = \rho Y_i \boldsymbol{V}_i \tag{2.23}$$

where the diffusion velocity $\boldsymbol{V}_i$ is given as:

$$\boldsymbol{V}_i = -\sum_{j=1}^{N_g} D_{ij}^M \boldsymbol{d}_j - D_i^T \boldsymbol{\nabla}(\ln T) = -\sum_{j=1}^{N_g} D_{ij}^M \left[\boldsymbol{d}_j + k_j^T \boldsymbol{\nabla}(\ln T)\right] \tag{2.24}$$

[6] Non-linear interactions of modes correctly represented on the grid result in modes that cannot be represented on it and are incorrectly aliased to high frequency modes

[7] This statement applies in the context of the S3D code and not in general, see Chapter 4 for details

or, as the Stefan-Maxwell equation:

$$\sum_{j=1,j\neq i}^{\mathrm{N_g}} \frac{X_i X_j}{\mathscr{D}_{ij}} \left(\boldsymbol{V}_j - \boldsymbol{V}_i \right) = \boldsymbol{d}_i + k_i^T \boldsymbol{\nabla} (\ln T) \tag{2.25}$$

likewise, the heat flux vector can be computed with the expression:

$$\begin{aligned} \boldsymbol{q} &= \sum_{i=1}^{\mathrm{N_g}} h_i \boldsymbol{J}_i - \lambda \boldsymbol{\nabla} T - p \sum_{i=1}^{\mathrm{N_g}} D_i^T \boldsymbol{d}_i \\ &= \sum_{i=1}^{\mathrm{N_g}} h_i \boldsymbol{J}_i - \left(\lambda - \frac{p}{T} \sum_{i=1}^{\mathrm{N_g}} D_i^T k_i^T \right) \boldsymbol{\nabla} T + p \sum_{i=1}^{\mathrm{N_g}} k_i^T \boldsymbol{V}_i \end{aligned} \tag{2.26}$$

where radiative heat transfer is not included. Also, $X_i = WY_i/W_i$ is the mole fraction of species i, λ is the partial thermal conductivity, $D_{ij}^M = D_{ji}^M$ is Waldmann's symmetric multicomponent diffusion coefficient, D_i^T is Waldmann's thermal diffusion coefficient, k_i^T is Waldmann's thermal diffusion ratio, $\mathscr{D}_{ij}$ is the binary diffusion coefficient, and $\boldsymbol{d}_i$ is the diffusion driving force vector:

$$\boldsymbol{d}_i = \boldsymbol{\nabla} X_i + (X_i - Y_i) \boldsymbol{\nabla} (\ln p) + \frac{\rho Y_i}{p} \left[\boldsymbol{f}_i - \sum_{j=1}^{\mathrm{N_g}} Y_j \boldsymbol{f}_j \right], \quad i = 1, \cdots, \mathrm{N_g} \tag{2.27}$$

where $\sum_{i=1}^{\mathrm{N_g}} \boldsymbol{d}_i = 0$. The driving force vector includes thermodynamic forces generated by concentration gradients (first term on the right-hand side of 2.27), pressure gradients (second term, also called *barodiffusion*) and body forces (two rightmost terms in the equation), including the eventuality of different body forces on each specie. Note that while the functional forms of the heat flux vector and diffusion velocity are independent of whether the dilute gas mixture is polyatomic or reacting, the transport coefficients may be very sensitive to whether inelastic or reactive collisions take place.

In order to simplify the notation, the mixture thermal conductivity, λ_{mix}, and the diffusion impedance matrix, $\mathscr{R}_{ij}$, can be defined as:

$$\lambda_{mix} = \lambda - \frac{p}{T} \sum_{i=1}^{\mathrm{N_g}} D_i^T k_i^T, \qquad \mathscr{R}_{ij} = \frac{X_i X_j}{\mathscr{D}_{ij}}, \; i, j = 1, \cdots, \mathrm{N_g} \tag{2.28}$$

where the mixture and partial thermal conductivities become identical in the absence of thermal diffusion. The Stefan-Maxwell equation becomes:

$$\sum_{j=1,j\neq i}^{\mathrm{N_g}} \mathscr{R}_{ij}\left(\boldsymbol{V}_j - \boldsymbol{V}_i\right) = \boldsymbol{d}_i + k_i^T \boldsymbol{\nabla}(\ln T) \quad i = 1, \cdots, \mathrm{N_g} \tag{2.29}$$

This allows the heat flux vector and the mass flux vector of specie i to be written as:

$$\boldsymbol{q} = \sum_{i=1}^{\mathrm{N_g}} \left(\rho Y_i h_i + p k_i^T\right) \boldsymbol{V}_i - \lambda_{mix} \boldsymbol{\nabla} T, \tag{2.30}$$

$$\boldsymbol{J}_i = \rho Y_i \boldsymbol{V}_i = -\rho Y_i \sum_{j=1}^{\mathrm{N_g}} D_{ij}^M \left[\boldsymbol{d}_j + k_j^T \boldsymbol{\nabla}(\ln T)\right] \tag{2.31}$$

while the symmetric stress tensor for Newtonian fluids, representing diffusion of momentum, is given by:

$$\tau_{\alpha\beta} = \tau_{\beta\alpha} = \mu\left(\nabla_\alpha \boldsymbol{u}_\beta + \nabla_\beta \boldsymbol{u}_\alpha\right) + \left(\mu_B - \frac{2}{3}\mu\right)\left(\nabla_\gamma \boldsymbol{u}_\gamma\right)\delta_{\alpha\beta} \tag{2.32}$$

where μ is the molecular viscosity and μ_B is the bulk viscosity. This last quantity expresses the fluid resistance to rapid volume changes and it is identically zero for mono-atomic gases while it has non-zero value for poly-atomic gases. Equations 2.30-2.32 derived here for the diffusive fluxes in the general case are simplified, to some extent, in Section 2.3.2. This simplification is achieved by making some assumptions on the thermo-physical characteristics of the fluid considered.

2.2.4 Chemical Source Terms

The term $\dot{\omega}_i$ represents the chemical source term for specie i in the transport equations 2.4 and is computed from the *law of mass action* as:

$$\dot{\omega}_i = \frac{W_i}{\rho} \sum_{n=1}^{\mathrm{N_r}} \left(\nu_{in}^{''} - \nu_{in}^{'}\right) k_n \prod_{i=1}^{\mathrm{N_g}} c_i^{\nu_{in}^{'}} \tag{2.33}$$

This expression results from a detailed H_2-Air chemical kinetics mechanism, given in Li *et al.* (2003) and recalled in Table 2.1, involving N_g species

and N_r elementary reactions[8]. The quantity c_i is the molar concentration of specie i in the mixture, ν'_{in} and ν''_{in} are the stoichiometric coefficients for specie i in step n of the reaction system that is written in compact notation as:

$$\sum_{i=1}^{N_g} \nu'_{in} A_i \rightarrow \sum_{i=1}^{N_g} \nu''_{in} A_i \quad n = 1, \cdots, N_r \tag{2.34}$$

where the A_i represent the chemical symbol for specie i and the velocity coefficient k_n of each reaction step n in 2.34 is obtained from the modified Arrhenius expressions:

$$k_n(T) = B_n T^{a_n} exp\left(\frac{E_{an}}{\mathscr{R}T}\right) \tag{2.35}$$

the pre-exponential and exponential factors, B_n and a_n, and the activation energy E_{an} for step n are listed in Table 2.1.

2.3 Simplifications And Nondimensionalization

2.3.1 Assumption And Simplifications

In order to simplify the numerical solution of equations 2.1-2.4 the following assumptions are adopted in the present work:

- The flowing reactive fluid obeys the ideal gas law
- Mixture averaged transport coefficients D_i^{mix} represent correctly the multicomponent diffusion processes
- Body forces are neglected and the effect of buoyancy is not considered
- The cross diffusional Soret[9] and Dufour effects are not included, this simplification implies $\lambda_{mix} = \lambda$
- Barodiffusion is neglected
- Radiative heat transfer is not considered assuming optically thin flame
- Bulk viscosity is neglected for polyatomic gases

[8] For this specific mechanism $N_g = 9$ and $N_r = 19$

[9] The importance of the Soret effect on the propagation and wall-quenching of a laminar flame is evaluated in Chapter 6

Table 2.1: The 9-species and 19-reactions H_2-Air chemical kinetics mechanism of Li *et al.* (2003).

n	Reaction	B	a	E_a
1	O2 + H <-> OH + O	3.547e+15	-0.406	1.6599E+4
2	H2 + O <-> OH + H	0.508E+05	2.67	0.629E+04
3	OH + H2 <-> H + H2O	0.216E+09	1.51	0.343E+04
4	H2O + O <-> 2 OH	2.97e+06	2.02	1.34e+4
5	H2 + M <-> 2 H + M	4.577E+19	-1.40	1.0438E+05
6	2 O + M <-> O2 + M	6.165E+15	-0.50	0.000E+00
7	H + O + M <-> OH + M	4.714E+18	-1.00	0.000E+00
8	OH + H + M <-> H2O + M	3.800E+22	-2.00	0.000E+00
9	O2 + H (+M) <-> HO2 (+M)	1.475E+12	0.60	0.00E+00
10	H + HO2 <-> O2 + H2	1.66E+13	0.00	0.823E+03
11	H + HO2 <-> 2 OH	7.079E+13	0.00	2.95E+02
12	O + HO2 <-> OH + O2	0.325E+14	0.00	0.00E+00
13	OH + HO2 <-> O2 + H2O	2.890E+13	0.00	-4.970E+02
14	2 HO2 <-> O2 + H2O2	4.200e+14	0.00	1.1982e+04
15	H2O2 (+M) <-> 2 OH (+M)	2.951e+14	0.00	4.843E+04
16	H + H2O2 <-> OH + H2O	0.241E+14	0.00	0.397E+04
17	H + H2O2 <-> H2 + HO2	0.482E+14	0.00	0.795E+04
18	O + H2O2 <-> HO2 + OH	9.550E+06	2.00	3.970E+03
19	OH + H2O2 <-> H2O + HO2	5.800E+14	0.00	9.557E+03

the direct implications of these simplifying assumptions on the physical process under investigation are of so little importance that the numerical simulation can be considered as *model free*. The above mentioned assumptions ultimately result in the following simplified formulation of the diffusive fluxes:

$$\boldsymbol{q} = \sum_{i=1}^{\mathrm{N_g}} \rho Y_i h_i \boldsymbol{V}_i - \lambda \boldsymbol{\nabla} T, \tag{2.36}$$

$$\boldsymbol{J}_i = \rho Y_i \boldsymbol{V}_i = -\rho Y_i \frac{D_i^{mix}}{X_i} \nabla X_i = -\rho Y_i \frac{D_i^{mix}}{Y_i} \left(\nabla Y_i + \frac{Y_i}{W} \nabla W \right) \tag{2.37}$$

$$\tau_{\alpha\beta} = \mu \left(\nabla_\alpha \boldsymbol{u}_\beta + \nabla_\beta \boldsymbol{u}_\alpha \right) - \frac{2}{3} \mu \left(\nabla_\gamma \boldsymbol{u}_\gamma \right) \delta_{\alpha\beta} \tag{2.38}$$

where D_i^{mix} are *mixture-averaged* diffusion coefficients given in terms of the binary diffusion coefficients and the mixture composition as:

$$D_i^{mix} = \frac{1 - X_i}{\sum_{i=1, i \neq j}^{\mathrm{N_g}} X_j / \mathscr{D}_{ij}} \tag{2.39}$$

2.3.2 Nondimensionalization

Nondimensionalization is performed in S3D in order to achieve a certain degree of normalization of the terms in the dimensional equations 2.1-2.4. Once a specific state of the mixture is chosen, quantities relative to that state are represented by the subscript ∞. The variables are then nondimensionalized by the reference quantities listed in Table 2.2.

Note that $T_{\mathrm{ref}} \neq T_\infty$ so that the non-dimensional equation of state may be nondimensionalized as

$$p^*(\rho_{\mathrm{ref}} a_{\mathrm{ref}}^2) = \rho^*(\rho_{\mathrm{ref}}) R^*(c_{\mathrm{p},\infty}) T^*((\gamma_\infty - 1) T_\infty), \tag{2.40}$$

or

$$\frac{p^*}{\rho^* R^* T^*} = \frac{c_{\mathrm{p},\infty} T_\infty (\gamma_\infty - 1))}{a_{\mathrm{ref}}^2}. \tag{2.41}$$

Since $(\gamma_\infty - 1) = R_\infty / c_{\mathrm{v},\infty}$, $\gamma_\infty = c_{\mathrm{p},\infty} / c_{\mathrm{v},\infty}$, and $a_{\mathrm{ref}} = a_\infty = \gamma_\infty R_\infty T_\infty$, we find that the equation of state is given by $p^* = \rho^* R^* T^*$.

To nondimensionalize the governing equations, the path whereby one takes each of the flux terms and nondimensionalizes each elemental term is

Table 2.2: Reference variables and adimensional variables.

Variable	Reference Variable	Non-Dimensional Variable
velocity	$a_{\text{ref}} = a_\infty$	$u_i^* = u_i / a_{\text{ref}}$
length	L_{ref}	$x_\alpha^* = x_\alpha / L_{\text{ref}}$
		$\nabla_\alpha^* = \nabla_\alpha * L_{\text{ref}}$
time	$t_{\text{ref}} = L_{\text{ref}} / a_{\text{ref}}$	$t^* = t a_{\text{ref}} / L_{\text{ref}}$
density	$\rho_{\text{ref}} = \rho_\infty$	$\rho^* = \rho / \rho_{\text{ref}}$
energy	$e_{\text{t,ref}} = a_\infty^2$	$e_t^* = e_t / a_{\text{ref}}^2$
pressure	$\rho_{\text{ref}} a_{\text{ref}}^2 = \rho_\infty a_\infty^2$	$p^* = p / (\rho_{\text{ref}} a_{\text{ref}}^2)$
gas constant	$c_{\text{p},\infty}$	$R^* = R / c_{\text{p},\infty}$
temperature	$T_{\text{ref}} = (\gamma_\infty - 1) T_\infty$	$T^* = T / T_{\text{ref}}$
Molecular weight	W_{ref}	$W_i^* = W_i / W_{\text{ref}}$

avoided. Instead, the flux terms are nondimensionalized *externally* (as opposed to the more traditional internal nondimensionalization). The nondimensionalized governing equations then appear as,

$$\frac{\partial(\rho^* \boldsymbol{u}_\alpha^*)}{\partial t^*} = -\frac{\partial(\rho^* \boldsymbol{u}_\alpha^* \boldsymbol{u}_\beta^* + p^* \delta_{\alpha\beta})}{\partial x_\beta^*} + \left(\frac{\tau_{\text{ref}}}{\rho_{\text{ref}} a_{\text{ref}}^2}\right) \frac{\partial \tau_{\beta\alpha}^*}{\partial x_\beta^*} \tag{2.42}$$

$$\frac{\partial \rho^*}{\partial t^*} = -\frac{\partial(\rho^* \boldsymbol{u}_\beta^*)}{\partial x_\beta^*} \tag{2.43}$$

$$\frac{\partial(\rho^* e_t^*)}{\partial t^*} = -\frac{\partial\{(\rho^* e_t^* + p^*) \boldsymbol{u}_\beta^*\}}{\partial x_\beta^*} + \left(\frac{\tau_{\text{ref}}}{\rho_{\text{ref}} a_{\text{ref}}^2}\right) \frac{\partial(\tau_{\beta\alpha}^* \boldsymbol{u}_\alpha^*)}{\partial x_\beta^*} - \left(\frac{q_{\text{ref}}}{\rho_{\text{ref}} a_{\text{ref}}^3}\right) \frac{\partial \boldsymbol{q}_\beta^*}{\partial x_\beta^*} \tag{2.44}$$

$$\frac{\partial(\rho^* Y_i^*)}{\partial t^*} = -\frac{\partial(\rho^* Y_i \boldsymbol{u}_\beta^*)}{\partial x_\beta^*} - \left(\frac{J_{\text{ref}}^{(d)}}{\rho_{\text{ref}} a_{\text{ref}}}\right) \frac{\partial(\rho^* Y_i \boldsymbol{V}_{i\beta}^*)}{\partial x_\beta^*} + \left(\frac{\omega_{\text{ref}} W_{i,\text{ref}} L_{\text{ref}}}{\rho_{\text{ref}} a_{\text{ref}}}\right) W_i^* \dot{\omega}_i^*. \tag{2.45}$$

The idea here is that S3D will expect subroutines to return dimensional values of the three flux terms, $\tau_{\beta\alpha}$, $\boldsymbol{q}_\alpha$ and $\rho Y_i \boldsymbol{V}_{i\alpha}$ as well as $\dot{\omega}_i$ in c.g.s units. The modularity of the S3D code implies that, whatever constitutive relations the user solves, the dimensionality of these terms is promptly

nullified upon arrival. The most straightforward way to do this is to set

$$\tau_{\text{ref}} = \rho_{\text{ref}} a_{\text{ref}}^2, \quad q_{\text{ref}} = \rho_{\text{ref}} a_{\text{ref}}^3, \quad J_{\text{ref}}^{(d)} = \rho_{\text{ref}} a_{\text{ref}}, \quad \omega_{\text{ref}} = \frac{\rho_{\text{ref}} a_{\text{ref}}}{W_{i,\text{ref}} L_{\text{ref}}}, \tag{2.46}$$

thereby reducing all nondimensional groupings in parentheses to unity.

In addition to the adimensional Reynolds, Prandtl, Mach and Lewis numbers already introduced in Chapter 1 it is convenient to introduce another dimensionless quantity, the Schimdt number Sc that represent the relative importance of viscous and species diffusion:

$$Sc = \frac{\mu}{\rho D} \tag{2.47}$$

It is useful at this point to recall the dimensionless numbers introduced so far. The Reynolds number Re is the ratio of the inertial to the viscous forces in a flowing fluid and therefore indirectly represents its turbulence level:

$$Re = \frac{U \rho L}{\mu} \tag{2.48}$$

The Mach number M expresses the flow compressibility level and is the ratio of a characteristic convective velocity $|\boldsymbol{u}|$ to the speed of sound c:

$$M = \frac{|\boldsymbol{u}|}{c} \tag{2.49}$$

The Prandtl number Pr is the ratio of momentum to thermal diffusivity:

$$Pr = \frac{c_p \mu}{\lambda} \tag{2.50}$$

while the Lewis number Le describes the ratio of thermal to mass diffusivity:

$$Le = \frac{\lambda}{\rho c_p D} = \frac{Sc}{Pr} \tag{2.51}$$

that is often unity, being the Schmidt and Prandtl numbers close to unity for most gases. Hydrogen is an exception with a strong bias toward mass diffusivity and $Le \sim 0.3$.

3 Boundary Conditions

Boundary conditions have to provide knowledge to the equation solver about the surrounding world located outside the computational domain. The accuracy of the solution obtained from the numerical simulation will greatly depend on the information provided by the user about the surroundings through the boundary conditions. Assigning appropriate boundary conditions can be done in two successive steps.

3.1 Physical And Numerical Conditions

First it is necessary to specify the number of boundary conditions that are necessary to achieve well-posedness of the mathematical description of the problem and thus completely determine the flow solution in a given finite domain. The task of specifying these boundary conditions, that are called *physical* boundary conditions, should be independent of the numerical method used to solve the governing equations. A physical boundary condition specifies the known physical behaviour of one or more of the dependent variables at the boundary. The fact that one has properly assigned the physical boundary conditions is not a sufficient condition (it is though a necessary one!) for obtaining a numerical solution of the governing equations.

The second task in the boundary treatment consists in the specification of some additional *numerical* boundary conditions that have to be assigned in order to solve for variables that are not specified by the physical boundary conditions. The numerical boundary conditions or "soft" conditions can be seen as complementary relations required by the chosen particular numerical method and thus dependent on it. As noted by Gustafsson and Sundström (1978) it is important that these two tasks remain clearly distinct in order to obtain a well-posed problem description.

Among the different kinds of boundaries that limit a physical domain, two are particularly important due to their wide use in practical problems: open boundaries and close boundaries. The direct simulations of turbulent

reactive plane channel flow performed in the present work require specification of both open and close boundaries.

3.2 Open Boundaries

3.2.1 Infinite Domains

Many practical flows of interest are located in physical domains that are not bounded in one or more spatial directions. Gustafsson and Kreiss (1979) explain that when this is the case, the numerical method used to obtain a solution requires the specification of an artificial boundary in order to make the computational domain finite. The artificial boundary represents a connection between the computational domain and the surrounding non-calculated far field. Care must be taken in the definition of this *open boundary*. As explained in Rian (2003) an under-specification or over-specification of physical boundary conditions would lead to an ill-posed problem and are a classical cause of instability. An under-specification of boundary conditions leads to problems in obtaining a unique solution for the system of equations. On the other side an over-specification often produces flow solutions that show unphysical behaviour near the boundary where the boundary conditions are applied. A simple (but expensive in terms of computational time) solution to this problem is to extend the computational domain and locate the outlet or far-field boundaries far enough away from the region of interest. By doing this it is possible to get physically meaningful results, but at the expense of higher computational costs and the already high costs of DNS make this approach practically unfeasible.

3.2.2 Well-Posedness of The Navier-Stokes Equations

The first general treatment of initial boundary value problem for incomplete parabolic systems is conducted by Strikwerda (1977) who individuates a norm-bounding inequality that can be used to assess the well-posedness of a system for the assigned boundary conditions. The correct number of boundary conditions which should be imposed on the Navier-Stokes equations to obtain a well-posed problem is derived by Strikwerda (1977) and shown in Table 3.1. Still today there seems to be general agreement on the numbers listed in Table 3.1, see Svärd and Nordström (2005) for very recent work on this subject.

Table 3.1: Number of physical boundary conditions required for a three-dimensional flow to ensure well-posedness: N_{dim} is the number of spatial directions and N_g is the number of species

Boundary Type	Euler	Navier-Stokes
Supersonic Inflow	$N_{dim} + 2 + (N_g - 1)$	$N_{dim} + 2 + (N_g - 1)$
Subsonic Inflow	$N_{dim} + 1 + (N_g - 1)$	$N_{dim} + 2 + (N_g - 1)$
Supersonic Outflow	0	$N_{dim} + 1 + (N_g - 1)$
Subsonic Outflow	1	$N_{dim} + 1 + (N_g - 1)$

Gustafsson and Sundström (1978) find the well-posedness definition by Strikwerda (1977) not restrictive enough, giving some counter-examples and showing its weakness. They use the so-called *energy method* to derive well-posed boundary conditions for the linearized Navier-Stokes equations. The method they develop consisted in finding global energy estimates for the governing system of equations: the well-posedness criteria are satisfied if the growth of the "energy norm" (an L^2-equivalent norm) is appropriately bounded. They also find that for fluid flows between solid walls this requirement is always satisfied.

The problem of the non-linearity in equations 2.1-2.4 is later addressed by Dutt (1988). Using the fact that the Navier-Stokes equations at high Reynolds numbers are an incomplete elliptic perturbation of the Euler equations, he suggests the use of the entropy function for the Euler equations as a measure of the "energy" associated with the Navier-Stokes equations. He obtains in this way nonlinear "energy" estimates for the initial boundary problem and these estimates can then be used to derive boundary conditions that ensure energy growth or L^2 boundedness (well-posed boundary conditions).

The general method proposed by Dutt (1988) to check the well-posedness of Navier-Stokes equations does not address several practical problems related to the numerical solution. For example Poinsot and Lele (1992) point out the fact that the existence of acoustic waves crossing the boundaries is not been considered in Dutt's article.

3.2.3 The Problem of Spurious Reflections

The fact that one has to employ an artificial boundary may also lead to spurious numerical wave reflections that can seriously pollute the solution. As a result, less accurate solutions are produced, if any: the generation of spurious fluctuations that travel back and forth in the computational domain may cause the calculation to diverge and then crash as reported in Rudy and Strikwerda (1981).

In fluid flows, information about the flow conditions is transmitted across the open boundaries by physical waves. These open boundaries should allow waves (especially pressure waves or acoustic waves) to travel freely in and out of the computational domain. If the flow speed is supersonic all acoustic signals cannot travel upstream, they will only propagate downstream: at a supersonic outflow boundary no information about the downstream exterior of the domain is required. Conversely for a subsonic flow situation information can travel both upstream and downstream implying that incoming waves at a subsonic outflow boundary must carry information on the flow conditions from the exterior, outside the calculation domain. However the knowledge about the exterior can often be unsure or absent, additional modelling or qualified guesses about these flow conditions may be necessary and the amplitudes of the outgoing waves may be used as a starting point for the modelling of the incoming ones, this approach is used by Poinsot and Lele (1989) and is discussed below. As a consequence, subsonic outflow conditions are generally more difficult to handle than supersonic outflow conditions. Even if physical waves are not able to propagate upstream from the outlet, numerical waves may do so and Vichnevetsky (1986) shows that strong numerical coupling mechanisms between inlet and outlet boundaries can lead to non-physical oscillations for the one-dimensional advection equations. From this discussion it becomes clear that the overall accuracy and performance of numerical algorithms, as well as the interpretation of the results, strongly depend on the proper treatment of the open boundaries with non-reflecting schemes.

In general there is no unique "correct" choice of an artificial boundary for a given problem on an unbounded domain, this results in a boundary conditions treatment that is at times case dependent, but the resulting numerical solution should in any case be close to the solution of the original (unbounded) problem. There are basically two categories of methods found in the literature for handling artificial open boundaries, namely local and nonlocal (or global) boundary conditions. Global methods are nonlocal in

space or in time or both, and they are usually very accurate and robust. The derivation involves the use of integral transforms (Fourier and Laplace) along the boundary, see Gustafsson (1982), and therefore relates the boundary behaviour at a certain point to the situation of all the other points on the boundary (spatially nonlocal) and/or to their past situation (temporally nonlocal). From the viewpoint of the developers of numerical codes, nonlocal treatment of open boundary conditions have in general appeared to be computationally expensive and too cumbersome to implement. Local methods on the other hand are algorithmically simple, easier to implement, numerically cheap and geometrically universal but they are less accurate since they *often* assume local one-dimensionality of the propagating waves in the boundary-normal direction. Locally One Dimensional Inviscid -LODI- boundary equations are proposed in the work of Poinsot and Lele (1989).

Rudy and Strikwerda (1980) develop a non-reflecting boundary conditions technique for inert flow, this method uses the usual zero-th order extrapolation for the velocities and the density and a non-reflecting condition for the last variable (pressure or temperature) of the form:

$$\frac{\partial p}{\partial t} - \rho c \frac{\partial u}{\partial t} + \theta(p - p_\infty) = 0 \tag{3.1}$$

Here c is the speed of sound at the outflow, p_∞ is a far-field pressure value and θ is a coefficient varying with the flow. Rudy and Strikwerda (1981) compare their new method, applied to a subsonic outflow, with several traditional techniques including:

- Zero-th order extrapolation boundary conditions for all the variables
- Constant pressure boundary condition and zero-th order extrapolation for the remaining variables

The results of their comparison show much faster convergence and higher accuracy with the new non-reflecting boundary condition method, even if the non-reflecting condition is applied only to one variable, the pressure.

In their landmark paper about boundary conditions treatment, Poinsot and Lele (1992) confirm these results having developed a new and more complex procedure for specifying non-reflecting boundary conditions of higher precision and stability for *all* the independent variables in a viscous flow. The new method is named Navier-Stokes Characteristic Boundary Condition (NSCBC), is based on characteristic wave relations and improves a similar method reported earlier in Thompson (1987) and Thompson (1990) for the inviscid Euler equations. The emphasis in Poinsot and

Lele (1992) is on developing boundary conditions that are compatible with DNS. High-order schemes used in direct simulations do not introduce numerical dissipation and do not damp errors generated at the boundaries, they are therefore much more prone to instabilities when the boundary conditions are not accurate. Poinsot and Lele (1992) also compare their characteristic based method with the less sophisticate method suggested by Rudy and Strikwerda (1980), clearly showing the advantages of their (more complex) characteristic based approach. Especially in the case of simulations of transient flow problems, the numerical high-frequency waves (observed when using Rudy and Strikwerda's method) that propagate upstream and induce false inlet oscillations, are absent if the characteristic-based method is applied to the outflow boundary.

3.2.4 Oblique Waves And Turbulent Subsonic Inflows

Local boundary treatments like the NSCBC method are prone to introduce small amplitude reflected waves, usually in the direction tangential to the boundary, in the numerical solution. The issue of oblique waves is still today an open question in open boundary condition treatment and the problem is clearly "visible" when the outgoing waves reach the artificial boundary (or a corner) of the computational domain with a travel direction not normal to the same boundary: in this case the approximation of local one-dimensionality in the boundary-normal direction fails. Nicoud (1999) points out that transverse terms (parallel to the boundary) are necessary in multi-dimensional problems in order to reach an accurate and stable solution. In a recent paper Prosser (2005) tries to address the problem of oblique waves and seems to have obtained encouraging results but they are limited to the context of inviscid flows. Additional problems of spurious reflections are related to the specification of subsonic inflow conditions. As noted in Sutherland and Kennedy (2003), the fact that several primitive variables as velocity components, temperature, species mass fractions need to be imposed at the inflow boundary implicitly results in a constraint on the pressure gradient and thereby on the pressure. Requiring a full specification of the inflow boundary and at the same time its transparency to pressure waves emanating from within the computational domain is a tall order. To solve this problem Sutherland and Kennedy (2003) try the approach of a "soft" inflow specification by letting the inflow variables fluctuate in the immediate vicinity of the value to be imposed: this method appears to be fairly successful for viscous compressible reactive flows, it is implemented in the

S3D code and used in the simulations reported in the present work. Another modification of the NSCBC method is adopted by Guichard *et al.* (2004) in their coupled spectral/finite-differences direct simulations of a turbulent v-shaped flame and seems to eliminate unphysical boundary-generated acoustic waves. For the viscous reactive case Yoo *et al.* (2005) very recently suggest yet another approach to solve the problem of spurious reflections for subsonic inflow and oblique waves, it is based on the use of transverse terms tangential to the boundary and represents a promising alternative.

3.2.5 The NSCBC Method

Characteristic-based boundary conditions are extensively treated for the Euler equations and some general boundary formalism is developed for most kinds of boundary conditions, reflecting and non-reflecting. In the viscous case, for the Navier-Stokes equations, the Euler boundary conditions are also applied to obtain estimates of the wave amplitudes even if a rigorous theoretical proof for the acceptability is still to be given. The reasoning behind this extension to Navier-Stokes problems of boundary conditions techniques developed for Euler problems seems to rely on the following assumptions:

- Wave phenomena are associated with the hyperbolic (Eulerian) terms in the Navier-Stokes equations
- The "diffusion waves" associated with the viscous/diffusive terms in the Navier-Stokes equations can be neglected

The removal of *artificial numerical reflections* of physical waves at open boundaries is the main purpose of the Navier-Stokes Characteristic Boundary Conditions method developed by Poinsot and Lele (1992). In the NSCBC method, the Locally One-Dimensional Inviscid (LODI) characteristic-based equations are used, together with the physical boundary conditions specified on some primitive variables, to obtain amplitude estimates of waves travelling out of the domain and also to control the waves entering it. These boundary LODI equations are later modified to include the effects of diffusive and viscous terms and finally they are solved to obtain boundary values of the remaining primitive variables not yet assigned. Baum *et al.* (1994b) bring further this approach and extend it to the case of reactive flow with detailed chemical kinetics and more realistic thermodynamic relations, but it is unclear if the proposed method is stable for the case of a flame passing

through the open boundary. Almost a decade later, in a modified version of the NSCBC method Sutherland and Kennedy (2003) suggest the inclusion of the source terms in the LODI relations and report considerable improvements in respect to stability, especially in the problematic issue of a reaction zone crossing the boundary. Details about the modified version of the NSCBC method developed by Sutherland and Kennedy (2003) are briefly derived below since this method is implemented in the S3D code and used in the direct simulations reported in the present work. For additional details about the method formulation and performance in numerical tests the reader is advised to refer to the original paper of Sutherland and Kennedy.

3.2.6 Details Of The NSCBC Method

At the end of this section, after a brief general introduction to the NSCBC method, a more specific description is given of the boundary conditions actually imposed by the S3D code for the inflow and outflow boundaries in the two- and three-dimensional calculations of Chapter 7. These, plus the details about wall boundary conditions exposed in the next Section, are given in order to put the reader in the position of reproducing the numerical experiments reported in this report.

The conservative transport equations 2.1-2.4 may be written in compact form as:

$$\frac{\partial \mathbf{U}}{\partial t} + \frac{\partial \mathbf{F}}{\partial x_1} = \mathbf{S_U} \tag{3.2}$$

where the x_1-direction is assumed normal to the boundary, $\mathbf{U}$ is the solution vector in conservative form as in equation 2.5 while the vector $\mathbf{F}$ is defined as $\mathbf{F} = (\rho \boldsymbol{u}_1^2 + p \ , \ \rho \boldsymbol{u}_1 \boldsymbol{u}_2 \ , \ \rho \boldsymbol{u}_1 \boldsymbol{u}_3 \ , \ \rho \boldsymbol{u}_1 \ , \ (\rho e_t + p)\, \boldsymbol{u}_1 \ , \ \rho \boldsymbol{u}_1 Y_i)^t$ for $i = 1, \cdots, \mathrm{N_g}$. The vector term $\mathbf{S_U}$ includes all diffusion, source and convective terms tangential to the boundary. Poinsot and Lele (1992) neglect the right-hand side of equations 3.2 and use the one-dimensional Eulerian part of these equations in its characteristic form

$$\frac{\partial \mathbf{W}}{\partial t} + \tilde{l} \frac{\partial \mathbf{W}}{\partial x_1} = 0 \tag{3.3}$$

to obtain inviscid estimates for the wave amplitude variations. The elements of vector $\mathbf{W}$ are the *Riemann invariants* of the characteristic problem and the diagonal matrix $\tilde{l}$ contains the wave velocities associated to each invariant (the eigenvalues $l_1 = \boldsymbol{u}_1 - c$, $l_2 = \boldsymbol{u}_1$, $l_3 = \boldsymbol{u}_1$, $l_4 = \boldsymbol{u}_1$, $l_5 = \boldsymbol{u}_1 + c$,

$l_{5+i} = \boldsymbol{u}_1$). As mentioned above, Sutherland and Kennedy (2003) suggest the inclusion in equations 3.3 of the source terms resulting in:

$$\frac{\partial \mathbf{W}}{\partial t} + \mathcal{L} = \mathfrak{s}_{\mathbf{U}} \tag{3.4}$$

where $\mathcal{L} = l(\partial \mathbf{W}/\partial x_1)$ and $\mathfrak{s}_{\mathbf{U}}$ represents the source terms at the characteristic level. The LODI relations are then given in terms of the $\mathcal{L}$'s as shown in the table below. The rightmost column in the table lists the source terms (in the absence of body forces) as they appear when included on the right-hand side of the LODI equations, the quantity $\mathfrak{h}_i = [h_i - (c_{p,mix} TW/W_i)]$ is introduced to ease the notation. Recall that, in this report, the Cartesian coordinates in the three spatial directions are indicated indifferently with the symbols x_1, x_2, x_3 or x, y, z while the components of the velocity vector $\boldsymbol{u}$ are indicated indifferently with u_1, u_2, u_3 or u, v, w.

$\frac{\partial \mathbf{W}}{\partial t}$	*LODI*	$\mathfrak{s}_{\mathbf{U}}$
$\frac{1}{2}\left(\frac{\partial p}{\partial t} - \rho c \frac{\partial u_1}{\partial t}\right)$	$\frac{\partial u_1}{\partial t} + \frac{1}{\rho c}(\mathcal{L}_5 - \mathcal{L}_1) = 0$	$\frac{1-\gamma}{2}\sum_{i=1}^{N_g-1}\left(\mathfrak{h}_i - \mathfrak{h}_{N_g}\right) W_i \dot{\omega}_i$
$\frac{-1}{c^2}\frac{\partial p}{\partial t} + \frac{\partial \rho}{\partial t}$	$\frac{\partial \rho}{\partial t} + \frac{1}{c^2}\left[c^2\mathcal{L}_2 + (\mathcal{L}_5 + \mathcal{L}_1)\right] = 0$	$\frac{\gamma-1}{c^2}\sum_{i=1}^{N_g-1}\left(\mathfrak{h}_i - \mathfrak{h}_{N_g}\right) W_i \dot{\omega}_i$
$\frac{\partial u_2}{\partial t}$	$\frac{\partial u_2}{\partial t} + \mathcal{L}_3 = 0$	0
$\frac{\partial u_3}{\partial t}$	$\frac{\partial u_3}{\partial t} + \mathcal{L}_4 = 0$	0
$\frac{1}{2}\left(\frac{\partial p}{\partial t} + \rho c \frac{\partial u_1}{\partial t}\right)$	$\frac{\partial p}{\partial t} + (\mathcal{L}_5 + \mathcal{L}_1) = 0$	$\frac{1-\gamma}{2}\sum_{i=1}^{N_g-1}\left(\mathfrak{h}_i - \mathfrak{h}_{N_g}\right) W_i \dot{\omega}_i$
$\frac{\partial Y_i}{\partial t}$	$\frac{\partial Y_i}{\partial t} + \mathcal{L}_{5+i} = 0$	$W_i \dot{\omega}_i / \rho$

The $\mathcal{L}$'s are either computed from interior data (if they represent outgoing waves) or estimated from knowledge about the exterior (for incoming waves). The complete equations are retrieved using linear combinations of the $\mathcal{L}$'s (the d's in the table below) and the previously neglected $\mathbf{S}_{\mathbf{U}}$ terms.

$\mathcal{L}_1 =$	$\frac{(u_1-c)}{2}\left[\frac{\partial p}{\partial x_1} - \rho c \frac{\partial u_1}{\partial x_1}\right]$	$d_1 =$	$\frac{1}{c^2}\left[c^2\mathcal{L}_2 + (\mathcal{L}_5 + \mathcal{L}_1)\right]$
$\mathcal{L}_2 =$	$\frac{u_1}{c^2}\left[c^2\frac{\partial \rho}{\partial x_1} - \frac{\partial p}{\partial x_1}\right]$	$d_2 =$	$(\mathcal{L}_5 + \mathcal{L}_1)$
$\mathcal{L}_3 =$	$u_1\frac{\partial u_2}{\partial x_1}$	$d_3 =$	$\frac{1}{\rho c}(\mathcal{L}_5 - \mathcal{L}_1)$
$\mathcal{L}_4 =$	$u_1\frac{\partial u_3}{\partial x_1}$	$d_4 =$	$\mathcal{L}_3$
$\mathcal{L}_5 =$	$\frac{(u_1+c)}{2}\left[\frac{\partial p}{\partial x_1} + \rho c \frac{\partial u_1}{\partial x_1}\right]$	$d_5 =$	$\mathcal{L}_4$
$\mathcal{L}_{5+i} =$	$u_1\frac{\partial Y_i}{\partial x_1}$	$d_{5+i} =$	$\mathcal{L}_{5+i}$

The equation system solved on the boundary is summarized in the following table:

Continuity	$\frac{\partial(\rho)}{\partial t}$	$-d_1^{(x_1)} + \mathbf{S}_{\mathbf{U}_\rho}$
x_1 – Momentum	$\frac{\partial(\rho u_1)}{\partial t}$	$-u_1 d_1^{(x_1)} - \rho d_3^{(x_1)} + \mathbf{S}_{\mathbf{U}_{\rho\mathbf{u_1}}}$
x_2 – Momentum	$\frac{\partial(\rho u_2)}{\partial t}$	$-u_2 d_1^{(x_1)} - \rho d_4^{(x_1)} + \mathbf{S}_{\mathbf{U}_{\rho\mathbf{u_2}}}$
x_3 – Momentum	$\frac{\partial(\rho u_3)}{\partial t}$	$-u_3 d_1^{(x_1)} - \rho d_5^{(x_1)} + \mathbf{S}_{\mathbf{U}_{\rho\mathbf{u_3}}}$
Energy	$\frac{\partial(\rho e_t)}{\partial t}$	$-\rho u_1 d_3^{(x_1)} - \rho u_2 d_4^{(x_1)} - \rho u_3 d_5^{(x_1)}$ $-\sum_{i=1}^{N-1}\rho d_{5+i}^{(x_1)}(\mathfrak{h}_i - \mathfrak{h}_N)$ $-(e_t - c_v T)d_1^{(x_1)} - \frac{d_2^{(x_1)}}{(\gamma-1)} + \mathbf{S}_{\mathbf{U}_{\rho\mathbf{e_t}}}$
i – Specie	$\frac{\partial(\rho Y_i)}{\partial t}$	$-Y_i d_1^{(x_1)} - \rho d_{5+i}^{(x_1)} + \mathbf{S}_{\mathbf{U}_{\rho\mathbf{Y_i}}}$

In the context of the present work two kinds of open boundary conditions are used in the direct simulations of turbulent reactive channel flow: a *non-reflecting subsonic inflow* and a *non-reflecting subsonic outflow*. It should be stressed that the process of assigning a value to the $\mathcal{L}$'s is a dynamic one that depends on fluctuating quantities and their *label* can change from incoming to outgoing even on the same boundary or for different times.

Non-reflecting Subsonic Inflow

For a subsonic inflow located on the left boundary ($l_1 = \boldsymbol{u}_1 - c$ is leaving the domain) Table 3.1 shows that the Euler equations require $N_{dim} + 1 + (N_g - 1)$ conditions while the Navier-Stokes equations $N_{dim} + 2 + (N_g - 1)$. One viscous condition should then be imposed to avoid under- or over-specification in the limit of vanishing viscosity. As discussed in Sutherland and Kennedy (2003), the following viscous condition on the gradient of the stress tensor is strongly advised:

$$\left(\nabla_\gamma \tau_{\beta\alpha}\right) \boldsymbol{n}_\gamma \boldsymbol{n}_\beta \boldsymbol{n}_\alpha = 0 \tag{3.5}$$

The remaining inviscid conditions are imposed on the amplitude variations of the characteristic waves by setting:

$$\mathcal{L}_1 = \frac{(u_1 - c)}{2}\left[\frac{\partial p}{\partial x_1} - \rho c \frac{\partial u_1}{\partial x_1}\right] \tag{3.6}$$

$$\mathcal{L}_2 = \frac{\gamma - 1}{c^2}\left(\mathcal{L}_5 + \mathcal{L}_1\right) + \frac{\rho}{T}\frac{\partial T}{\partial t} + \rho W \sum_{i=1}^{N_g - 1}\left[W_{iN_g}\frac{\partial Y_i}{\partial t}\right] - \frac{\rho}{p}\mathbf{S}_{\mathscr{U}_p} \tag{3.7}$$

$$\mathcal{L}_3 = 0 \tag{3.8}$$

$$\mathcal{L}_4 = 0 \tag{3.9}$$

$$\mathcal{L}_5 = \frac{\mathbf{S}_{\mathscr{U}_p}}{2} - \rho c \mathscr{B}\left(\frac{\partial u_1}{\partial t}\right) \tag{3.10}$$

$$\mathcal{L}_{5+i} = W_i \dot{\omega}_i / \rho \tag{3.11}$$

where $W_{iN_g} = W\left(W_i^{-1} - W_{N_g}^{-1}\right)$, $\mathscr{B}$ is a relaxation coefficient for the time derivative of the inflow velocity and $\mathbf{S}_{\mathscr{U}_p}$ is the pressure source term at the primitive level:

$$\mathbf{S}_{\mathscr{U}_p} = (1 - \gamma) \sum_{i=1}^{N_g - 1}\left(\mathfrak{h}_i - \mathfrak{h}_{N_g}\right) W_i \dot{\omega}_i \tag{3.12}$$

Non-reflecting Subsonic Outflow

For a subsonic outflow located on the right boundary ($l_1 = \boldsymbol{u}_1 - c$ is entering the domain) one Euler condition and $N_{dim} + 1 + (N_g - 1)$ Navier-Stokes conditions are required according to Table 3.1. The number of independent viscous conditions to be imposed to avoid under- or over-specification in the limit of vanishing viscosity is $N_{dim} + (N_g - 1)$. This is achieved by imposing the following two conditions on the stress tensor:

$$\left(\nabla_\gamma \tau_{\beta\alpha}\right) \boldsymbol{n}_\gamma \boldsymbol{n}_\beta \boldsymbol{t}_{1,\alpha} = 0, \quad \left(\nabla_\gamma \tau_{\beta\alpha}\right) \boldsymbol{n}_\gamma \boldsymbol{n}_\beta \boldsymbol{t}_{2,\alpha} = 0, \tag{3.13}$$

and similar conditions on the heat and mass fluxes:

$$\left(\nabla_\beta \boldsymbol{q}_\alpha\right) \boldsymbol{n}_\beta \boldsymbol{n}_\alpha = 0, \quad \left(\nabla_\beta \boldsymbol{J}_{i,\alpha}\right) \boldsymbol{n}_\beta \boldsymbol{n}_\alpha = 0, \tag{3.14}$$

The remaining inviscid condition is imposed on the amplitude variations of the only incoming characteristic wave by setting:

$$\mathcal{L}_1 = \frac{\mathbf{S}_{\mathscr{U}_p}}{2} + \left[\sigma c \left(1 - \mathfrak{M}^2\right)(p - p_\infty)\right] / 2L \tag{3.15}$$

In this last expression $\sigma = 0.287$, $\mathfrak{M}$ is a Mach number associated with the boundary, L is the computational domain length and p_∞ is some far field value of pressure from which the pressure p in the domain should not drift too far.

3.3 Wall Boundaries

3.3.1 Closed Domains

In many devices (car and jet engines, turbines and compressors in general) and in industrial large scale equipment (pipelines, separators, furnaces) the flow of liquids and gases (both reactive or inert) is contained in some kind of solid structure. If one wants to simulate the behaviour of a device and precisely predict the flow resulting in certain conditions, one very important task is to model accurately the interaction between the solid walls and the flow itself. A correct description of the solid wall assume special importance in the case of combustion equipment as noted earlier in this report: heat loss, radical absorption, turbulence production and dissipation, fluid strain rate and flame stretch are all very important phenomena taking place

in the immediate vicinity of the wall and greatly influencing the combustion process.

A solid wall can, in respect to the adjacent flow, be characterised by its thermal properties (is the wall temperature constant or is it quickly assuming the fluid temperature?), its surface roughness (is the wall surface smooth or corrugated?), its chemical properties (is the wall undergoing surface chemical reactions?), its material properties (is the wall allowing flow normal to its surface?). The list below is a summary of wall characteristics that should be correctly described by the boundary conditions:

- Isothermal: constant wall temperature
- Adiabatic[1]: zero temperature gradient between wall and flow
- No-slip: zero flow velocity parallel to the wall
- Slip: non-zero flow velocity parallel to the wall
- Inert: no chemical surface reactions
- Reactive: surface reactions are taking place
- Solid: zero flow velocity normal to the wall
- Porous: non-zero flow velocity normal to the wall

In their work about thermal boundary layers Kong *et al.* (2000) note that wall boundary conditions usually implemented in direct simulations are limited to the no-slip and isothermal (or alternatively adiabatic) conditions and are not exact in general: in order to accurately solve any thermal boundary layer it is necessary to model and solve for the conjugate heat-transfer problem by specifying the thickness and thermal properties of the solid wall. Kasagi *et al.* (1989) study this problem and conclude that in the case of inert air flow ($Pr \sim 0.7$) over a metal, plastic or glass wall, the wall temperature fluctuations are almost zero independently of wall thickness.

In the present investigation of flame-wall interaction processes the conjugate heat transfer problem into the solid wall material is *not* coupled to the DNS of the turbulent reactive flow, but the *no-slip*, *inert* wall is also assumed *isothermal*, characterized by infinite thickness and heat capacity. This approach is chosen because it describes correctly relevant situations in many combustion devices:

[1] Phase changes and surface reactions at the wall are also considered negligible here.

– The no-slip condition at the solid surface generates the shear that in turn creates the turbulent boundary layer

– Metallic surfaces can be considered as inert in a wide range of temperatures without introducing large errors (eventual surface reactions would, to some extent, modify low-temperature exothermic radical recombinations at the wall)

– The solid surface in contact with the flow reaches locally isothermal conditions after an initial thermal transient

Also, the assumption of an isothermal wall, decoupled from the conjugate heat conduction problem in the solid material, allows the conclusions reached in this report to be as general as possible and independent from the details of the technical implementations of specific combustion devices.

3.3.2 Wall Boundary Conditions in DNS

A literature review on the subject of wall boundary conditions in direct simulations of turbulent flows revealed that at least three different approaches have been followed by researchers in the subject.

As recently noted by Svärd and Nordström (2005) solid walls *have to be considered as a special case in the characteristic-based boundary treatment* that in general assumes $|\boldsymbol{u}_\alpha| \neq 0$, in their paper Svärd and Nordström repeat the usual derivation for the Navier-Stokes equations in the special "no-flow" case assuming $|\boldsymbol{u}_\alpha| = 0$ and conclude that *a "no-flow" boundary should be considered as an outflow boundary.* This fact implies that for viscous multicomponent three-dimensional flows $4 + (N_g - 1)$ physical conditions have to be assigned, see Table 3.1.

According to the reviewed literature, in most numerical simulations the no-slip condition is applied to the velocity components, the isothermal wall conditions to energy conservation and the zero-flux condition to species

conservation[2], resulting in the following equations:

$$\boldsymbol{u}_1 = 0 \tag{3.16}$$

$$\boldsymbol{u}_2 = 0 \tag{3.17}$$

$$\boldsymbol{u}_3 = 0 \tag{3.18}$$

$$T = T_w \tag{3.19}$$

$$\frac{\partial Y_i}{\partial x_n} = 0 \tag{3.20}$$

Once equations 3.16-3.20 are enforced on the boundary, the problem of assigning the other independent thermodynamic variable, either pressure or density, has to be faced. The three approaches to wall boundary conditions found in the literature differ in the way this last problem of *wall pressure specification*[3] is addressed, in the following sections their differences and similarities are described and some comparative tests are reported in Section 3.4.

A: Continuity Equation

The simplest approach to the wall pressure problem, and seemingly the most used one, is basically not to solve any "special" expression at the wall. Once conditions 3.16-3.20 are imposed on the boundary, the continuity equation in conservative form (equation 2.2) gives ρ_w, the value of density *at the wall*, solving for[4]:

$$\frac{\partial \rho}{\partial t} = -\frac{\partial (\rho u_1)}{\partial x_1} = -\rho \frac{\partial u_1}{\partial x_1} \tag{3.21}$$

while the mixture composition at the wall, $Y_{i,w}$, is obtained from the species conservation equations 2.4, where the diffusive flux term is neglected[5]:

$$\frac{\partial (\rho Y_i)}{\partial t} = -\frac{\partial (\rho Y_i u_1)}{\partial x_1} + W_i \dot{\omega}_i \tag{3.22}$$

[2] This assumption is reportedly valid only for "low" wall temperatures $300 - 600\,K$, but remains still valid for higher temperatures if the wall can be considered inert, see Popp *et al.* (1996) for a detailed discussion

[3] The problem of assigning a value to the last independent thermodynamic variable, being it density or pressure, is referred as the *wall pressure problem* in the remaining of this report

[4] x_1 is the wall-normal direction and the gradients tangential to the wall are zero

[5] Because of condition 3.20 the diffusive contribution to the transport equation is assumed to be very small

which are solved for the conservative variables ($\rho Y_{i,w}$), division by density gives composition. The wall pressure value p_w is finally extracted from the equation of state 2.8 given that ρ_w, T_w and $Y_{i,w}$ are known. It should be noted that the first terms on the right-hand side of equations 3.21 and 3.22 are evaluated with one-sided differences.

B: NSCBC

The NSCBC method derived in Poinsot and Lele (1992), see Sections 3.2.5 and 3.2.6, treats wall boundary conditions in the same framework discussed above for the open boundaries and explicitly consider the case of isothermal and adiabatic no-slip wall together with adiabatic slip wall. Also this method is widely used in the open literature for inert and reactive flows and with good results, the procedure described here is reported in detail in Poinsot and Veynante (2001). At an isothermal wall located on the right x_1-boundary the wall pressure is extracted first by setting[6] $\mathcal{L}_1 = \mathcal{L}_5$, where $\mathcal{L}_5$ is estimated from interior values with one-sided differences. Subsequently the density value at the wall, ρ_w, is computed by substituting[7] for $\mathcal{L}_1$ and $\mathcal{L}_5$ in $d_1^{(x_1)}$ and solving the continuity equation listed in the Table on page 56 as:

$$\frac{\partial \rho}{\partial t} = -d_1^{(x_1)} = -\left(\frac{1}{c}\frac{\partial p}{\partial x_1} + \rho\frac{\partial u_1}{\partial x_1}\right) \tag{3.23}$$

while the mixture composition at the wall $Y_{i,w}$ is obtained from knowledge of ρ_w and solution of the species equations in conservation form (last equation listed in the Table on page 56, also in this case the diffusive contribution is neglected):

$$\frac{\partial (\rho Y_i)}{\partial t} = -Y_i d_1^{(x_1)} + W_i \dot{\omega}_i = -Y_i\left(\frac{1}{c}\frac{\partial p}{\partial x_1} + \rho\frac{\partial u_1}{\partial x_1}\right) + W_i \dot{\omega}_i \tag{3.24}$$

Also here, as in method A of the previous section, the wall pressure value p_w is then extracted from the equation of state once ρ_w, T_w and $Y_{i,w}$ are known, but, from comparison of equations 3.21 and 3.22 with equations 3.23 and 3.24, it is clear that these expression do not necessarily lead to the same values of p_w.

[6] The incoming wave amplitude variation is set equal to the outgoing one for perfect reflection, this is suggested by the first LODI relation from the top in Table 55

[7] $\mathcal{L}_2$, $\mathcal{L}_3$, $\mathcal{L}_4$ and $\mathcal{L}_{5+i}$ are all zero because the associated eigenvalue or wave velocity is zero

C: Wall Pressure Gradient

The third approach to the wall pressure problem has been suggested in the field of Computational Aero-Acoustics (CAA) by Tam and Dong (1994) for the *linearized* Navier-Stokes equations in Cartesian meshes and extended by Kurbatskii (1997) to complex meshes. Tam and Dong, to avoid notorious stability problems connected to one-sided high-order finite-difference stencils, use ghost points inside the wall together with centered stencils, normally used in the interior domain, to nullify the time derivative of momentum at the wall and achieve a perfectly reflecting no-flow boundary.

A similar formulation is developed in the context of the present work for reacting walls and is is scheduled for publication, Gruber and Kennedy (2006a). Ghost points into the solid wall are not used to avoid complications, instead third-order one-sided finite-difference stencils, that proved to be stable and accurate with the grid refining adopted at the wall, are employed to obtain the near-wall spatial gradients. The procedure for obtaining the wall pressure boundary condition starts by imposing the usual no-slip, isothermal and species zero-gradient conditions 3.16-3.20. Then, instead of computing ρ_w with some form of continuity equation as in methods A and B, the implications on the wall-normal momentum equation of the no-flow condition $\boldsymbol{u}_\alpha = 0$ are used to infer a viscous condition on the wall-normal pressure gradient.

Considering x_1 still as the wall-normal direction, the wall-normal momentum equation is given as:

$$\frac{\partial(\rho \boldsymbol{u}_1)}{\partial t} = -\boldsymbol{\nabla}_\beta \cdot (\rho \boldsymbol{u}_1 \boldsymbol{u}_\beta) + \boldsymbol{\nabla}_\beta \cdot (-p\delta_{1\beta} + \tau_{\beta 1}) \tag{3.25}$$

enforcing no-slip, $\boldsymbol{u}_\alpha = 0$ and $\frac{\partial(\rho \boldsymbol{u}_\alpha)}{\partial t} = 0$, the previous equation reduces to:

$$\boldsymbol{\nabla}_\beta \cdot (-p\delta_{1\beta} + \tau_{\beta 1}) = 0 \tag{3.26}$$

and the wall-normal pressure gradient is readily obtained as:

$$\frac{\partial p}{\partial x_1} = \boldsymbol{\nabla}_\beta \cdot (\tau_{\beta 1}) \tag{3.27}$$

At this point it is important to stress that:

- Equation 3.27 is *not* an independent condition on pressure but merely a consequence of no-slip

- Equation 3.27 includes the effects of viscosity
- Equation 3.27 is *not* strictly one-dimensional because it estimates the wall pressure gradient on the basis of multi-dimensional information included in the wall-tangential components of $\nabla_\beta \cdot (\tau_{\beta 1})$

This procedure to obtain the wall pressure seems to rely on a *locally multi-dimensional viscous* approach, as opposed to the LODI assumption of approach B. Once a value for $\frac{\partial p}{\partial x_1}$ is estimated, the pressure p_w at the wall can be computed simply inverting the one-sided finite-difference derivative operator, see Section 4.2.1 for details. The species mass fractions at the wall, $Y_{i,w}$, are obtained in the same manner, by inverting the one-sided finite-difference derivative operator, where condition 3.20 is also used. Finally, the density value at the wall, ρ_w, is computed from the equation of state once temperature T_w, pressure p_w and composition $Y_{i,w}$ are known.

Note

Approaches A, B and C (in the formulation of Tam and Dong) to the wall pressure problem are widely used and with considerable success in the vast literature on inert turbulent flows, for recent reviews in the field of computational aeroacoustics see Colonius and Lele (2004) and Hixon (2004). Approach C is developed aiming at a more general formulation for *reactive wall boundary conditions* where the other two approaches seem to be less appropriate to a consistent boundary specification, see Gruber and Kennedy (2006a). In this context, for inert walls, approach C seems also to be more self-consistent than approaches A and B since it is not clear if the solution of equations 3.22 or 3.24 *at the wall* is compatible with condition 3.20. Direct simulations of test cases for comparison of methods B and C are reported in Section 3.4 and some differences emerge in the reacting case. However, the full-scale DNS of the ducted v-shaped flame reported in Chapter 7 is run using approach B. The reason for this choice is twofold: a large level of confidence in approach B is built through numerous direct simulations reported in the literature, additionally, at the time of the full scale computations, approach C was still in the early stages of development.

3.3.3 Edges and Corners

Special attention must be devoted to the accurate treatment of boundary conditions at the edges and corners of the computational domain. A gen-

eral definition of possible combinations of boundary conditions for edges and corners remains to be given and appears to be even more difficult than the usual assessment of well-posedness. The boundary conditions to be imposed simultaneously on edges and corners according to the adjacent boundaries can be incompatible and this fact could result in a ill-posed boundary specification. A possible solution to this problem is to consider corners and edges as belonging only to one of the two or three adjacent boundaries: in the present work the edges between the solid walls boundaries and the inflow or outflow non-reflecting boundaries are considered as belonging to the wall only.

3.4 Numerical Tests

In this Section several comparison of the above mentioned B and C approaches to the wall pressure problem are reported. Further details and several test runs analyzing the behaviour of the non-reflecting inflow and outflow boundaries implemented in the S3D code are available in Sutherland (2004).

3.4.1 1-D Wall Bounded Pressure Wave

A one-dimensional DNS of a "pressure bomb" configuration is run with S3D. The one-dimensional physical domain of length L is bounded on both ends by solid isothermal walls, on the left side, for $x = 0$, approach B is used to specify the pressure boundary condition and on the right side, for $x = L$, approach C is used instead. The initial conditions are characterized by quiescent non-reacting single-component fluid, constant temperature and a gaussian peak in the pressure as shown is Figure 3.1. A uniform mesh consisting of 300 grid points is chosen for $L = 3.0e^{-03}\ m$ resulting in a spatial resolution of $10\,\mu m$. This level of resolution may seem unnecessary for the conditions of this simple test case but it is recommended for correct representation of premixed flame propagation: in order to maintain the same level of resolution for comparative purposes throughout the test sessions, the resolution required by the reacting cases is applied to the inert ones as well. The time step for the ERK integrator is also set according to the reacting case requirements to $\Delta t = 1.0e^{-08}\,s$. The violent initial transient produces reflections from both walls that travel forward and backward in the computational domain a large number of times due to the very low arti-

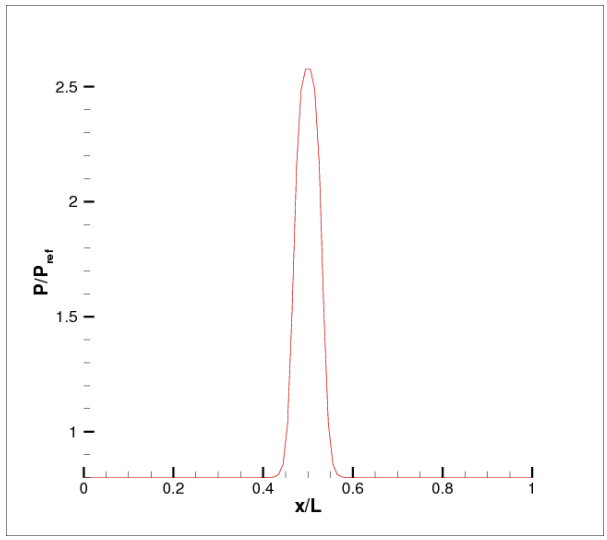

Figure 3.1: 1-D Bomb: Initial pressure field in the one-dimensional *pressure bomb* test at time $t = 0.0\,s$.

ficial dissipation of the numerical scheme, eventually, after a sufficient time span, the fluid viscosity slowly reduces the wave amplitudes. However, the the velocity, pressure, density, dilatation, and temperature profiles maintain their initial symmetry even at large times as illustrated in Figure 3.2 for the one-dimensional pressure field. In fact, the values of *all* variables at $x = 0$ and $x = L$ are identical for *all* times. This fact is an indication that the two different approaches for representation of solid wall boundaries, given that the correct number of conditions is specified in respect to well-posedness, describe well the same physical problem at least in one dimension.

3.4.2 2-D Wall Bounded Pressure Wave

A different pictures emerges from a two-dimensional direct simulation of the *pressure bomb* in a square domain bounded by two opposite walls in the y-direction and by non-reflecting open boundaries in the x-direction. Approach C is applied at the lower boundary for $y = 0$ while approach B is applied at $y = L$. At $t = 0.0\,s$ the gaussian pressure peak is placed in the geometric center of the domain ($x = L/2$ and $y = L/2$) in a quiescent single-

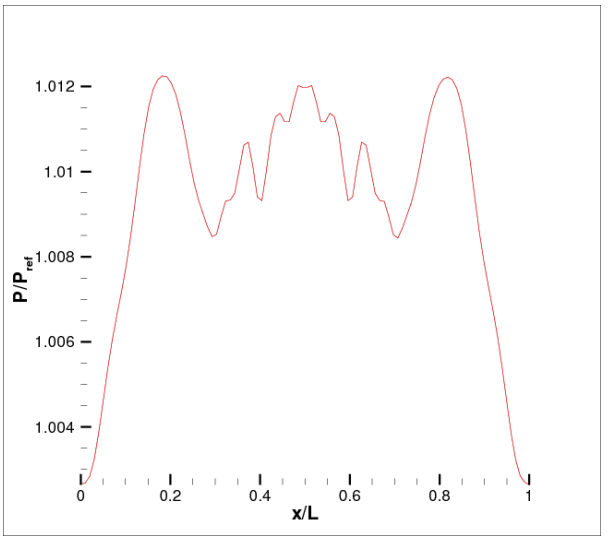

Figure 3.2: 1-D Bomb: Long time evolution of the pressure field in the one-dimensional *pressure bomb* test at time $t = 1.0 \cdot e^{02}\, s$.

component fluid. The spatial and temporal resolutions are the same as in the one-dimensional case resulting in a 300^2 uniform mesh with $\Delta x = \Delta y = 10\,\mu m$ and $\Delta t = 1.0e^{-08}$. Pressure and dilatation wave patterns travelling through the domain maintain some degree of symmetry as shown in Figure 3.3, *a perfectly symmetric wave pattern would imply that approaches B and C result in equal values for the density and pressure fluctuations at the wall.* However, a closer look to dilatation and pressure profiles at the wall reveals some differences of increasing magnitudes toward the open boundaries of the domain (at $x = 0$ and $x = L$), see Figures 3.4 and 3.5.

The wall pressure values obtained using the two different approaches seem to show better agreement in the geometrical center of the two opposite wall boundaries for $x = L/2$, in this point most incident waves are normal to the wall boundary because of the centered initial positioning of the pressure source. As one moves left or right along the walls from $x = L/2$ toward the open boundaries located at $x = 0$ and $x = L$, the angle of the incident waves deviates from the normal to the solid surface and acquires a tangential component, at the same time the agreement between $p_w(y = 0)$ and $p_w(y = L)$ seems to worsen. This fact may suggest that the differences

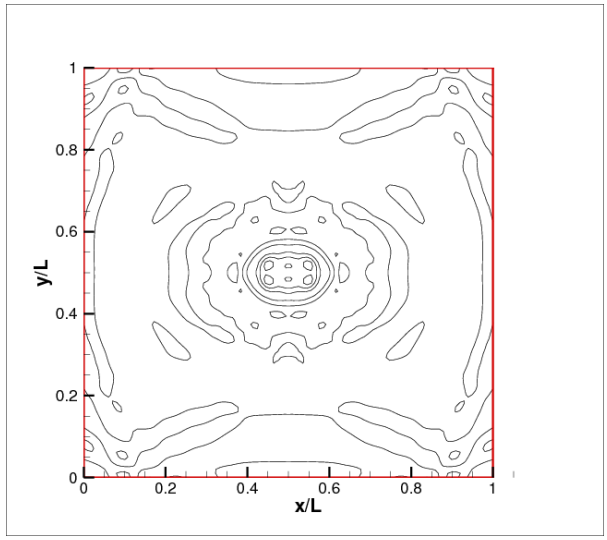

Figure 3.3: 2-D Bomb: Isocontours of dilatation field show symmetric patterns in the computational domain at time $t = 1.0 \cdot e^{-05}\, s$.

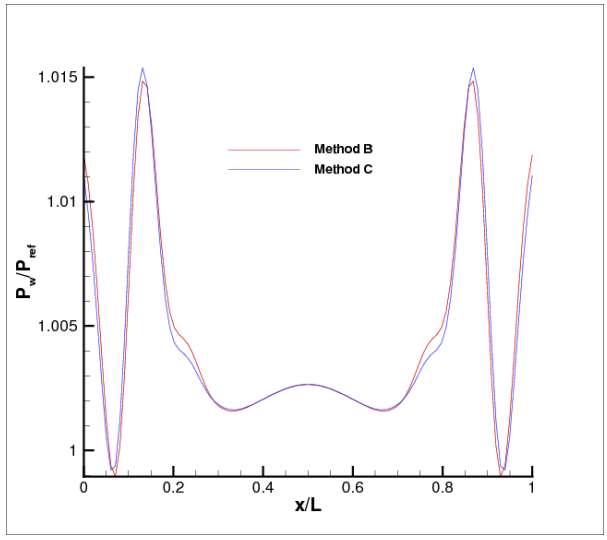

Figure 3.4: 2-D Bomb: Detail view of pressure profiles on the two opposite walls at time $t = 1.0 \cdot e^{-05}\, s$.

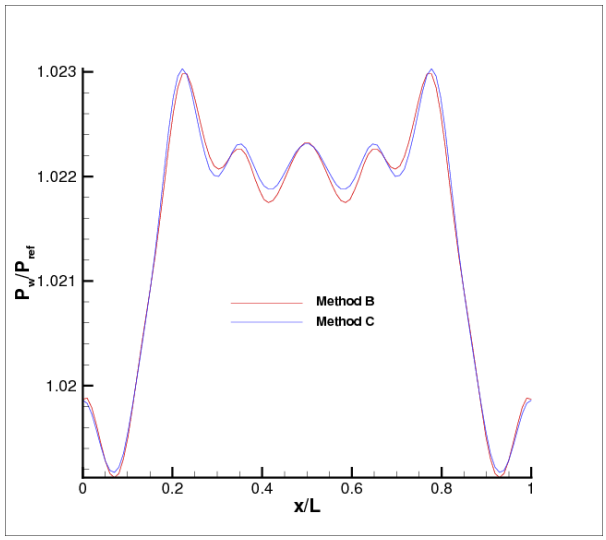

Figure 3.5: 2-D Bomb: Detail view of pressure profiles on the two opposite walls at time $t = 3.0 \cdot e^{-05}\, s$.

in p_w observed in Figures 3.4 and 3.5 are possibly a result of the locally one-dimensional inviscid assumption of approach B compared to the multi-dimensional viscous approach C, the absence of differences in the values of p_w for the simpler one-dimensional test configuration supports this conclusion.

3.4.3 1-D Wall Bounded Laminar Flame

A third numerical test is run for a reactive case placing a region of hot products[8] in the geometrical center of the same one-dimensional computational domain of the previous 1-D inert test and letting the laminar premixed flame propagate in the quiescent reactive stoichiometric mixture of hydrogen in air. This test is performed in order to investigate the behaviour of the different wall boundary conditions approaches B and C in the case of varying mass fractions Y_i. The physical dimensions of the computational domain are the same as in the previous inert test, so are the spatial and

[8] Smooth mass fractions and temperature profiles are used in order to avoid *large* initial acoustic disturbances

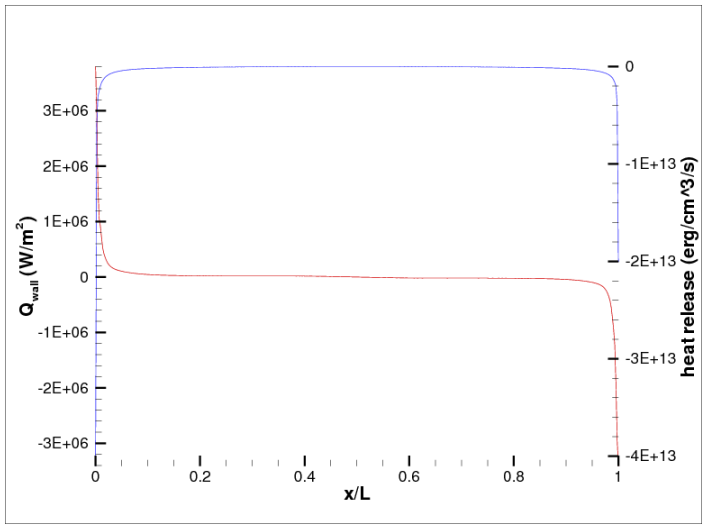

Figure 3.6: 1-D Laminar flame: Wall heat flux (red line) and heat release (blue line) profile in the computational domain at the time of quenching $t_Q = 4.6 \cdot e^{-05}\, s$.

temporal resolutions.

As in the inert case of Section 3.4.1 the two different formulations B and C are used on the opposite walls: in this case on the left side of the domain, for $x = 0$, approach C is used to specify the pressure boundary condition while on the right side, for $x = L$, approach B is used instead. The symmetry of the initial conditions is conserved until the laminar flame fronts propagating in opposite directions simultaneously reach the walls, then the resulting flame-wall interactions are characterized by different wall heat fluxes and heat release rates as shown in Figure 3.6 for the instant of maximum wall heat flux.

Note that the absolute value of the maximum wall heat flux is higher than those reported in Chapter 6 for similar flames. The reason for this discrepancy is to be found in the fact that the one-dimensional domain simulated in this boundary conditions test is *closed* between two walls and the domain pressure rises rapidly to values of about three times its initial (reference) value. Higher domain pressure implies both increasing unburnt gas temperature and higher reaction rates for the exothermic (and highly sensitive to third body concentration) recombination reactions at the wall,

finally resulting in higher wall heat flux.

3.4.4 2-D Wall Bounded Laminar Flame

A fourth numerical test is run for another reactive case, placing a circular spot of hot products[9] in the geometrical center of the same two-dimensional square computational domain of the previous 2-D inert test and letting the laminar premixed flame propagate in the quiescent reactive stoichiometric mixture of hydrogen in air. This test is performed in order to investigate the behaviour of the different wall boundary conditions approaches B and C in the case of varying mass fractions Y_i. The physical dimensions of the computational domain are the same as in the previous inert 2-D test, so are the spatial and temporal resolutions.

The laminar flame propagating in the reactive mixture is visualized in Figure 3.7 and 3.7 through the dilatation associated to heat release in the reaction zone. A certain degree of symmetry is still observed in these plots for $t = 5.0 \cdot e^{-05}\, s$ before the flame reaches the wall. At later times, when the laminar flame-wall interaction starts, considerable differences[10] in the values of p_w at the two opposite walls is clearly shown in Figure 3.10. A discrepancy in the values of all species mass fractions between the two opposite walls seems to be associated to the wall pressure difference in the flame-wall interaction zone, the mass fraction profiles at the two opposite walls are shown in Figure 3.10 for the radical specie H_2O_2. The reason of the diverging trend for the wall pressure values between approach B and C in the reacting case is still to be established. However it seems reasonable to assume that, being the opposite walls pressure values very similar in the inert test cases, the strong variations in the Y_i due to chemical reactions in the near-wall region[11] result in different behaviours of the boundary treatments. Further testing and analysis is required to establish which one of the two wall boundary treatments better represents the physics of fluid-wall interaction processes.

[9] Also in this case smooth mass fractions and temperature profiles are used in order to avoid *large* initial acoustic disturbances

[10] Large compared to the two inert test cases

[11] Together with the smaller effects due to the locally one-dimensional inviscid versus multi-dimensional viscous issue mentioned earlier

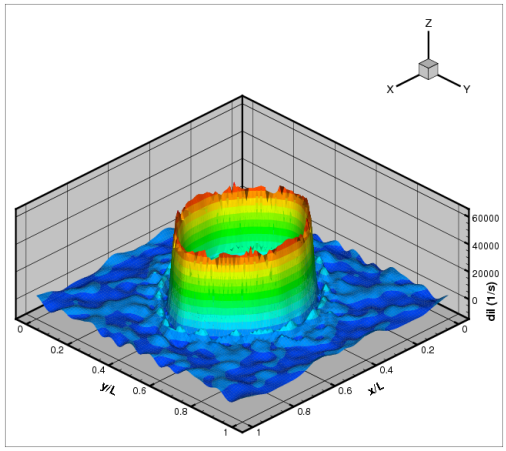

Figure 3.7: 2-D Laminar flame: The laminar flame is visualized by the dilatation associated to the heat release in the reaction zone as it propagates in low amplitude dilatation "noise" at time $t = 5.0 \cdot e^{-05}\, s$.

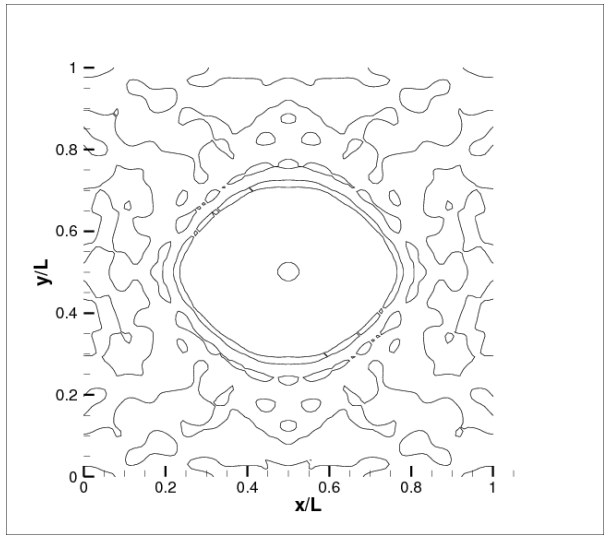

Figure 3.8: 2-D Laminar flame: Isocontours of dilatation show clearly the centered elliptic flame front and the degree of symmetry that still characterize the dilatation field at time $t = 5.0 \cdot e^{-05}\, s$.

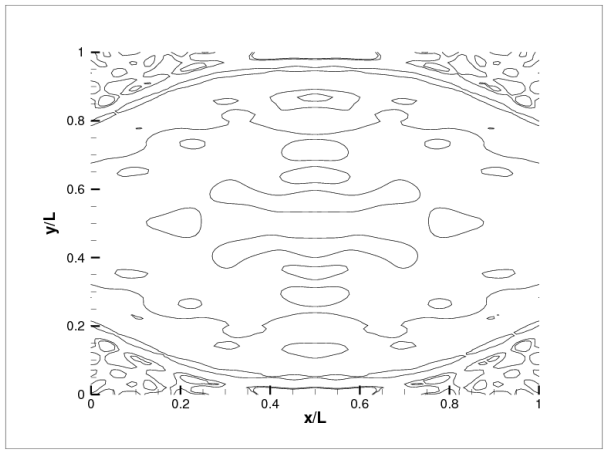

Figure 3.9: 2-D Laminar flame: Isocontours of dilatation show some degree of asymmetry in the dilatation field when the laminar flame reaches the walls at time $t = 1.2 \cdot e^{-054}\, s$.

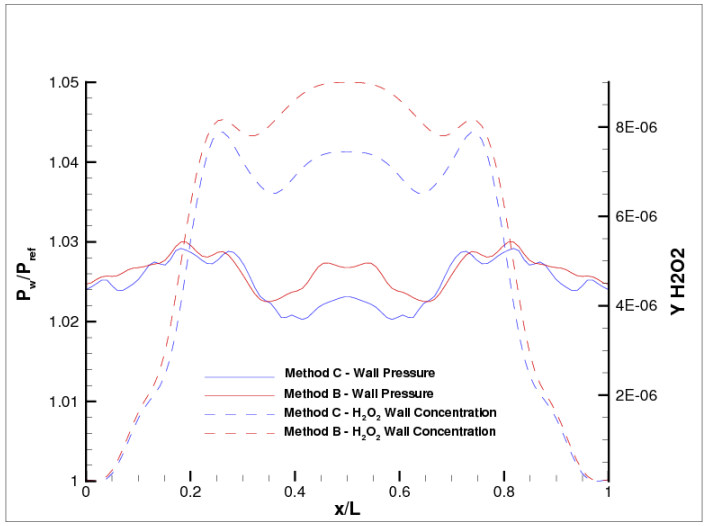

Figure 3.10: 2-D Laminar flame: Large differences in wall pressure and H_2O_2 mass fraction after the laminar flame has reached the opposite walls at time $t = 1.2 \cdot e^{-04}\, s$.

4 Numerical Method

4.1 Choice Of The Method

Direct simulation of turbulence sets high requirements on the numerical method. Turbulence is characterized by a very large range of time and length scales, representing a turbulent field on a mesh described by a finite number of grid points is equivalent to apply a low pass filter to the field's frequency spectrum: all frequencies higher than the those supported by the grid are removed. The high frequency modes at which viscous dissipation takes place at the smallest scales of turbulence have to be correctly represented by the grid, additional resolution requirements, often more stringent, are imposed in the direct simulations of turbulent *reactive* flows by rapidly varying spatial gradients in mass fraction profiles of the radical species. Fulfilling minimum grid resolution requirements is not enough, a numerical method characterized by low accuracy and large artificial dissipation would destroy all high frequency modes even if they were correctly represented by the grid at the beginning of the computation. Therefore the numerical scheme has to be *accurate* to correctly represent the smallest fluctuations, numerically stable, and at the same time computationally cheap, this last property is important to allow long time integration in domains large enough for representation of the largest time and spatial turbulent scales.

The best numerical method for any given situation is the one that is most computationally efficient for the relevant configuration: the one requiring the smallest computational effort for a given formal accuracy. However, other considerations play an important role in the choice of a numerical method, such as implementation issues, memory requirements, parallelization efficiency. For example, spectral methods are computationally cheap because derivative operators reduce to simple multiplications in spectral space and very accurate because of the high order of the interpolation polynomials that represent the solution vector in spectral space. Low computational cost and high accuracy are the reasons for the wide use of spectral methods in the early years of DNS, yet they are also more complicate

to parallelize and implement in non-homogeneous directions than finite-difference methods. The balance between all of these considerations has resulted in finite-difference methods as the best alternative and the majority of late DNS studies makes use of these numerical schemes. Note that, due to the large number of symbols needed in this Chapter, not all of these are listed in the nomenclature, however their significance should be clear and their understanding easy in present context.

4.2 Spatial Discretization And High Order Finite-Differences

The finite-difference approximation in discrete form of the first derivative of a continuous function $f = f(x)$ is derived here for a uniform mesh described by the nodes[1] $x_i = h(i-1)$ where $i = 1, \cdots, N$, h is the grid spacing and N is the number of nodes. In order to ease the notation in the following discussion the functional values at the grid nodes are designated as $f_i = f(x_i)$ and their first derivative as $f_i^{'} = \frac{\partial f}{\partial x}(x_i)$, the finite-difference stencil is then written as:

$$\begin{aligned} \beta[f_{i-2}^{'} + f_{i+2}^{'}] \quad &+ \quad \alpha[f_{i-1}^{'} + f_{i+1}^{'}] + \\ f_i^{'} \quad &= \\ a\frac{f_{i+1} - f_{i-1}}{h} \quad &+ \quad b\frac{f_{i+2} - f_{i-2}}{h} + \\ c\frac{f_{i+3} - f_{i-3}}{h} \quad &+ \quad d\frac{f_{i+4} - f_{i-4}}{h} + \\ e\frac{f_{i+5} - f_{i-5}}{h} \quad &+ \quad f\frac{f_{i+6} - f_{i-6}}{h} + \cdots + O(h^n) \end{aligned} \tag{4.1}$$

The function $O(h^n)$, the "Landau gauge symbol", denotes that in order-of-magnitude the errors in the above approximation are proportional to h^n. If the coefficients $\alpha = \beta = 0$ the above equation gives $f_i^{'}$ *directly* and the differencing method is named *explicit*. Otherwise the solution of an equation *system* is required to compute the derivatives simultaneously at all nodes and the differencing method is *implicit* or *compact*, see Lele (1992). For the direct simulations performed with the S3D code and presented in this report eight-order accurate explicit stencils (8E) are used in the interior domain and their coefficients are listed in Table 4.2. Spectral

[1] In the context of the present chapter indices α and β are not spatial indices and i and j are not species indices as elsewhere in this report

Table 4.1: Central difference stencils coefficients for $\left[\frac{\partial f}{\partial x}\right]$ on uniform meshes.

Accuracy	α	β	a	b	c	d	e	f
2^{nd} - (2E)	0	0	$\frac{1}{2}$	0	0	0	0	0
4^{th} - (4E)	0	0	$\frac{2}{3}$	$-\frac{1}{12}$	0	0	0	0
4^{th} - (4T)	0	$\frac{1}{4}$	$\frac{3}{4}$	0	0	0	0	0
6^{th} - (6E)	0	0	$\frac{3}{4}$	$-\frac{3}{20}$	$\frac{1}{60}$	0	0	0
6^{th} - (6T)	0	$\frac{1}{3}$	$\frac{7}{9}$	$\frac{1}{36}$	0	0	0	0
6^{th} - (6P)	$\frac{17}{57}$	$-\frac{1}{114}$	$\frac{15}{19}$	0	0	0	0	0
8^{th} - (8E)	0	0	$\frac{4}{5}$	$-\frac{1}{5}$	$\frac{4}{105}$	$-\frac{1}{280}$	0	0
8^{th} - (8T)	0	$\frac{3}{8}$	$\frac{25}{32}$	$\frac{1}{20}$	$-\frac{1}{480}$	0	0	0
8^{th} - (8P)	$\frac{4}{9}$	$\frac{1}{36}$	$\frac{20}{27}$	$\frac{25}{216}$	0	0	0	0
10^{th} - (10E)	0	0	$\frac{5}{6}$	$-\frac{5}{21}$	$\frac{5}{84}$	$-\frac{5}{504}$	$-\frac{1}{1260}$	0
10^{th} - (10T)	0	$\frac{2}{5}$	$\frac{39}{50}$	$\frac{1}{15}$	$-\frac{1}{210}$	$\frac{1}{4200}$	0	0
10^{th} - (10P)	$\frac{1}{2}$	$\frac{1}{20}$	$\frac{17}{24}$	$\frac{101}{600}$	$\frac{1}{600}$	0	0	0
12^{th} - (12E)	0	0	$\frac{6}{7}$	$-\frac{15}{56}$	$\frac{5}{63}$	$-\frac{1}{56}$	$\frac{1}{385}$	$-\frac{1}{5544}$
12^{th} - (12T)	0	$\frac{5}{12}$	$\frac{7}{9}$	$\frac{5}{63}$	$-\frac{5}{672}$	$\frac{1}{1512}$	$-\frac{1}{30240}$	0
12^{th} - (12P)	$\frac{8}{15}$	$\frac{1}{15}$	$\frac{154}{225}$	$\frac{91}{450}$	$\frac{2}{525}$	$-\frac{1}{12600}$	0	0

error analysis shows that centered stencils like those described by equation 4.1 when applied to linear hyperbolic problems *disperse* but do not dissipate the Fourier components of the solution. A non-dissipative dispersive solution conserves wave amplitudes but allows different phase speeds for different Fourier components, this implies that waves consisting of superposition of many different modes do not conserve their shape because of the nonzero relative speed between modes. "Dispersion Relation Preserving" or DRP schemes are used in the field of computational aero acoustics where a correct representation of the shape of superposed modes is of extreme importance but are not treated in this context since acoustic waves propagation is not at the focus here. However, they should be seriously considered in detailed studies of flame-acoustics interaction.

4.2.1 Boundary Closure With Finite-Difference Stencils

When derivatives have to be computed near the boundaries, equation 4.1 cannot be used and ad-hoc formulas have to be applied instead. Stability analysis of one-sided asymmetric stencils, see Carpenter *et al.* (1993), shows that long-time stable behaviour becomes difficult to achieve for boundary closures if they have high-order formal accuracy and the first-derivative operators have eigenvalues in the right half-plane. Grid refining toward the boundary has a positive effect on the stability of high-order one-sided stencils but, on the downside, impose low CFL stability limits, see Section 4.3 for details. The appropriate one-sided stencils for explicit methods are:

$$f_1' = \frac{1}{6\Delta x}\left(-11f_1 + 18f_2 - 9f_3 + 2f_4\right) \tag{4.2}$$

$$f_2' = \frac{1}{6\Delta x}\left(-2f_1 - 3f_2 + 6f_3 - f_4\right), \tag{4.3}$$

where both stencils are third-order accurate. For implicit tridiagonal and pentadiagonal schemes:

$$f_1' + 2f_2' = \frac{1}{2\Delta x}\left(-5f_1 + 4f_2 + f_3\right), \tag{4.4}$$

where the stencil is also third-order accurate. Using these one-sided stencils together with lower-order centered-difference stencils, all boundary derivative values may be computed. For instance, $(8E)$ would need four boundary points closed on each end of the domain. We would close it as $(3, 3, 4E, 6E - 8E - 6E, 4E, 3, 3)$ where the two outermost boundaries are closed as above

Order (n)	α_0	α_1	α_2	α_3	α_4	α_5
3	$\frac{-11}{6}$	$\frac{18}{6}$	$\frac{-9}{6}$	$\frac{2}{6}$	0	0
4	$\frac{-25}{12}$	$\frac{48}{12}$	$\frac{-36}{12}$	$\frac{16}{12}$	$\frac{-3}{12}$	0
5	$\frac{-137}{60}$	$\frac{300}{60}$	$\frac{-300}{60}$	$\frac{200}{60}$	$\frac{-75}{60}$	$\frac{12}{60}$

Table 4.2: Stencil coefficients for backward differences on uniform meshes

and the adjacent points are closed using the fourth- and sixth-order centered difference stencils. Assuming the grid composed by $N = 10$ points, at the opposite end of the domain the appropriate stencils are:

$$f'_{10} = \frac{-1}{6\Delta x}(-11f_{10} + 18f_9 - 9f_8 + 2f_7) \tag{4.5}$$

$$f'_9 = \frac{-1}{6\Delta x}(-2f_{10} - 3f_9 + 6f_8 - f_7), \tag{4.6}$$

Inversion Of One-Sided Stencils At The Wall

As mentioned in Section 3.3.2, the wall pressure p_w and composition $Y_{i,w}$ need to be estimated from the wall-normal pressure and species gradients at the left (L) and right (R) boundaries of a uniform grid. Designated as ϕ the variable whose value has to be "extracted" from knowledge of its boundary normal gradient, either of the following general expressions for $\phi'_i = (\boldsymbol{n}\cdot\boldsymbol{\nabla})\phi$ have to be solved:

$$\phi_i^L = \frac{1}{\alpha_0}\left(\Delta_g\phi'_i - \sum_{j=1}^{n}\alpha_j\phi_{i+j}\right), \qquad \phi_i^R = \frac{1}{\alpha_0}\left(\Delta_g\phi'_i + \sum_{j=1}^{n}\alpha_j\phi_{i-j}\right). \tag{4.7}$$

to find ϕ_i where Δ_g is the grid spacing in the wall-normal direction. Stencil coefficients are listed in table 4.2 for various orders of accuracy. Defining $S(\phi)$, the wall value of ϕ, $\phi_{(w)}$, is given by

$$S(\phi) \equiv \pm\sum_{j=1}^{n}\alpha_j\phi_{i\mp j}, \qquad \phi_{(w)} = \frac{1}{\alpha_0}\left[\Delta_g(\boldsymbol{n}\cdot\boldsymbol{\nabla})\phi + S(\phi)\right] \tag{4.8}$$

where $\boldsymbol{n}$ is the outward facing boundary normal. This strategy may be readily extended for implicit finite-difference stencils, however, certain high-order, time-stable formulations may prove cumbersome to apply in these contexts due to the large boundary blocks of the derivative matrices.

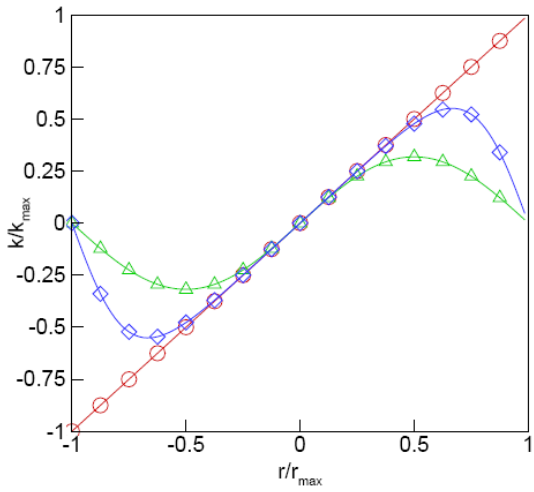

Figure 4.1: Modified wave-numbers for finite-difference stencils of increasing accuracy.

4.2.2 Filtering

In well-resolved computations, numerical errors are still present being introduced primarily at high wave-numbers. This can be seen by plotting the Fourier image of the finite-difference first derivative versus the spectral derivative or, alternatively, modified wave number k versus mode number r, see Lele (1992) for details. Figure 4.1 shows the wave-number of the exact spectral derivative (circles) and the modified wave-numbers of increasingly accurate (second and fourth-order, triangles and squares respectively) centered difference first derivatives relative. All of the finite-difference derivative operators have no resolution at $r = r_{max}$, where $r_{max} = N/2$ is the highest frequency mode that can be represented on the grid, and have only marginal resolution for wave-numbers near r_{max}. Nonlinear interaction of these marginally resolved waves of various wave-numbers results in higher wave-number information: interaction of wave-numbers k_1 and k_2 generates wave-number $k_3 = k_1 + k_2$ that may not be representable on the grid. When the grid is unable to resolve this high wave-number information, the error is introduced or "aliased" into lower wave-numbers, and eventually

contaminates the solution by a self-sustaining excitation process that produces high-wavenumber energy content growth over time. Additionally, successive application of the first derivative operator to obtain a second-order derivative[2] results in artificial energy growth at r_{max} for centered finite-difference operators, which facilitates what is commonly referred to as *odd-even* decoupling.

In order to suppress the growth of this non-physical high-frequency energy generated by both non-linear interactions and odd-even decoupling, S3D uses a numerical filter that creates artificial viscosity. Several criteria exist for a useful filter: eigenvalues that correspond to resolved low wavenumber information are virtually untouched, the relatively unresolved, high wave-number information is removed. The filter should possess a formal accuracy high enough not to filter resolved wave-numbers and it should be purely dissipative. Either an explicit or implicit filter can be chosen. In the direct simulations reported in this study a 10^{th}-order explicit filter is used because it is computationally more efficient, its design is more conceptually straightforward and it is purely dissipative (the implicit filters of Lele (1992) are also dispersive).

The filter function is implemented on the solution vector $\mathbf{U}$ as:

$$\mathbf{U}^f = (1 + \alpha_D \mathbf{D})\mathbf{U} \tag{4.9}$$

where $\mathbf{U}^f$ is the filtered vector, $\mathbf{D}$ is a symmetric dissipation matrix and α_D must be given by $(-1)^{n+1}2^{-2n}$ for a $(2n)^{th}$-order filter. For the 10^{th} order explicit filter used here, the top-left boundary sub-block $\mathbf{D}_B$ that completely describes the symmetric dissipation matrix $\mathbf{D}$ is given by the following coefficients:

$$\mathbf{D}_B = \begin{bmatrix} +1 & -5 & +10 & -10 & +5 & -1 \\ -5 & +26 & -55 & +60 & -35 & +10 \\ +10 & -55 & +126 & -155 & +110 & -45 \\ -10 & +60 & -155 & +226 & -205 & +120 \\ +5 & -35 & +110 & -205 & +251 & -210 \\ -1 & +10 & -45 & +120 & -210 & +252 \end{bmatrix} \tag{4.10}$$

[2] As mentioned in Chapter 2 the diffusive terms are evaluated in S3D by first computing the flux terms and then taking their respective divergences, this procedure results in two successive applications of the first derivative operator

4.3 Temporal Discretization And Explicit Runge-Kutta Schemes

As spatial discretization methods, also temporal discretization time marching schemes can be divided in *explicit*, *implicit* or mixed depending on how the solution vector **U** is obtained at the new time level:

$$\frac{d\mathbf{U}}{dt} = \mathbf{F}(\mathbf{U}, t) \tag{4.11}$$

If only values of **U** at previous time levels are used to obtain the new ones, then the time integration scheme is named *explicit*, otherwise, *implicit*. In the presence of *stiff* terms on the right-hand side of the equations it is also possible to integrate these terms implicitly and the other terms explicitly, an example of such mixed schemes is the *additive* Runge-Kutta (RK) time marching reported in Kennedy and Carpenter (2003). A particularly interesting special class of explicit Runge-Kutta methods, used in most modern codes, are those for which the coefficient have a special structure known as First Same As Last (FSAL). The advantage of FSAL methods is that the function value at the end of one integration step is the same as the first function value at the next integration step.

The details of implementing a five-stage explicit Runge-Kutta method, using the van der Houwen (vdH) methodology for the integration of equation 4.11 from time step n to time step $n+1$ with only two storage registers, are explained below, U is understood to be comprised of R variables. Third and fourth registers may be used to store an error estimator and the starting U-vector.

Assume register 1 (R1) contains the U-vector at time $t^{(n)} = t^{(1)}$, $U^{(n)} = U^{(1)}$. The function $F(U^{(n)}, t^{(n)}) = F^{(n)} = F^{(1)}$ is evaluated and the result is placed in register 2 (R2). The following operations are now performed the (error estimation and retention of $U^{(n)}$ are optional):

$$\begin{aligned} R_{old} &= R1 \\ R_{err} &= (b_1 - \hat{b}_1)(\Delta t)R2 \\ R1 &= R1 + a_{21}(\Delta t)R2 \\ R2 &= R1 + (b_1 - a_{21})(\Delta t)R2, \end{aligned} \tag{4.12}$$

which translates to:

$$\begin{aligned} R_{old} &= U^{(n)} \\ R_{err} &= (b_1 - \hat{b}_1)(\Delta t)F^{(n)} \\ U^{(2)} &= U^{(n)} + a_{21}(\Delta t)F^{(n)} \\ X^{(2)} &= U^{(2)} + (b_1 - a_{21})(\Delta t)F^{(n)} \\ &= U^{(n)} + b_1(\Delta t)F^{(n)}, \end{aligned} \tag{4.13}$$

where the X-vector is an intermediate vector that is used to pass information from one stage to the next. Boundary conditions for the $U^{(i)}$-vector are evaluated at $t^{(i)} = t^{(n)} + c_i(\Delta t)$. This constitutes the end of stage 1. The function is now evaluated with the contents of R1 and the result is then overwritten onto R1. Using this, the following is computed:

$$\begin{aligned} R_{err} &= R_{err} + (b_2 - \hat{b}_2)(\Delta t)R1 \\ R2 &= R2 + a_{32}(\Delta t)R1 \\ R1 &= R2 + (b_2 - a_{32})(\Delta t)R1, \end{aligned} \tag{4.14}$$

or

$$\begin{aligned} R_{err} &= R_{err} + (b_2 - \hat{b}_2)(\Delta t)F^{(2)} \\ &= (b_2 - \hat{b}_2)(\Delta t)F^{(2)} + (b_1 - \hat{b}_1)(\Delta t)F^{(n)} \\ U^{(3)} &= X^{(2)} + a_{32}(\Delta t)F^{(2)} \\ &= U^{(n)} + a_{32}(\Delta t)F^{(2)} + b_1(\Delta t)F^{(n)} \\ X^{(3)} &= U^{(3)} + (b_2 - a_{32})(\Delta t)F^{(2)} \\ &= U^{(n)} + b_2(\Delta t)F^{(2)} + b_1(\Delta t)F^{(n)}. \end{aligned} \tag{4.15}$$

Stage two is complete. Stage 3 begins with the evaluation of the function using the contents of R2. Overwriting the contents of R2 with the result of the function evaluation:

$$\begin{aligned} R_{err} &= R_{err} + (b_3 - \hat{b}_3)(\Delta t)R2 \\ R1 &= R1 + a_{43}(\Delta t)R2 \\ R2 &= R1 + (b_3 - a_{43})(\Delta t)R2, \end{aligned} \tag{4.16}$$

gives:

$$\begin{aligned}
R_{err} &= R_{err} + (b_3 - \hat{b}_3)(\Delta t)F^{(3)} \\
&= (b_3 - \hat{b}_3)(\Delta t)F^{(3)} + (b_2 - \hat{b}_2)(\Delta t)F^{(2)} + (b_1 - \hat{b}_1)(\Delta t)F^{(n)} \\
U^{(4)} &= X^{(3)} + a_{43}(\Delta t)F^{(3)} \\
&= U^{(n)} + a_{43}(\Delta t)F^{(3)} + b_2(\Delta t)F^{(2)} + b_1(\Delta t)F^{(n)} \\
X^{(4)} &= U^{(4)} + (b_3 - a_{43})(\Delta t)F^{(3)} \\
&= U^{(n)} + b_3(\Delta t)F^{(3)} + b_2(\Delta t)F^{(2)} + b_1(\Delta t)F^{(n)}. \qquad (4.17)
\end{aligned}$$

To begin stage 4, the function is now evaluated with the contents of R1 and the result is then overwritten into R1. Hence:

$$\begin{aligned}
R_{err} &= R_{err} + (b_4 - \hat{b}_4)(\Delta t)R1 \\
R2 &= R2 + a_{54}(\Delta t)R1 \\
R1 &= R2 + (b_4 - a_{54})(\Delta t)R1, \qquad (4.18)
\end{aligned}$$

or

$$\begin{aligned}
R_{err} &= R_{err} + (b_4 - \hat{b}_4)(\Delta t)F^{(4)} \\
&= (b_4 - \hat{b}_4)(\Delta t)F^{(4)} + (b_3 - \hat{b}_3)(\Delta t)F^{(3)} \\
&+ (b_2 - \hat{b}_2)(\Delta t)F^{(2)} + (b_1 - \hat{b}_1)(\Delta t)F^{(n)} \\
U^{(5)} &= X^{(4)} + a_{54}(\Delta t)F^{(4)} \\
&= U^{(n)} + a_{54}(\Delta t)F^{(4)} + b_3(\Delta t)F^{(3)} + b_2(\Delta t)F^{(2)} + b_1(\Delta t)F^{(n)} \\
X^{(5)} &= U^{(5)} + (b_4 - a_{54})(\Delta t)F^{(4)} \\
&= U^{(n)} + b_4(\Delta t)F^{(4)} + b_3(\Delta t)F^{(3)} \\
&+ b_2(\Delta t)F^{(2)} + b_1(\Delta t)F^{(n)}. \qquad (4.19)
\end{aligned}$$

Stage four is finished. On the final stage, stage five, the evaluation of the function is done using the contents of R2. Overwriting the contents of R2 with the result of the function evaluation, finally:

$$\begin{aligned}
R_{err} &= R_{err} + (b_5 - \hat{b}_5)(\Delta t)R2 \\
R1 &= R1 + b_5(\Delta t)R2, \qquad (4.20)
\end{aligned}$$

or

$$\begin{aligned} R_{err} &= R_{err} + (b_5 - \hat{b}_5)(\Delta t)F^{(5)} \\ &= (b_5 - \hat{b}_5)(\Delta t)F^{(5)} + (b_4 - \hat{b}_4)(\Delta t)F^{(4)} + (b_3 - \hat{b}_3)(\Delta t)F^{(3)} \\ &+ (b_2 - \hat{b}_2)(\Delta t)F^{(2)} + (b_1 - \hat{b}_1)(\Delta t)F^{(n)} \\ U^{(n+1)} &= X^{(5)} + b_5(\Delta t)F^{(5)} \\ &= U^{(n)} + b_5(\Delta t)F^{(5)} + b_4(\Delta t)F^{(4)} \\ &+ b_3(\Delta t)F^{(3)} + b_2(\Delta t)F^{(2)} + b_1(\Delta t)F^{(n)}. \end{aligned} \tag{4.21}$$

where $t^{(n+1)} = t^{(n)} + (\Delta t)$. It may be desirable to write $U^{(n+1)}$ back into the register that contained $U^{(n)}$ at the beginning of the time step in cases where the scheme has an even number of stages. If a FSAL scheme is being used then $U^{(n+1)}$ is used to compute $F^{(n+1)}$ and

$$R_{err} = R_{err} + (0 - \hat{b}_6)(\Delta t)R1 \tag{4.22}$$

or

$$\begin{aligned} R_{err} &= R_{err} + (0 - \hat{b}_6)(\Delta t)F^{(n+1)} \\ &= (0 - \hat{b}_6)(\Delta t)F^{(n+1)} + (b_5 - \hat{b}_5)(\Delta t)F^{(5)} + (b_4 - \hat{b}_4)(\Delta t)F^{(4)} \\ &+ (b_3 - \hat{b}_3)(\Delta t)F^{(3)} + (b_2 - \hat{b}_2)(\Delta t)F^{(2)} + (b_1 - \hat{b}_1)(\Delta t)F^{(n)} \end{aligned} \tag{4.23}$$

Note that register 1 has $F^{(n+1)}$ and that if the step is accepted then $F^{(n+1)} = F^{(1)}$ in the new step. To control solution error in a vdH scheme, first some appropriate solution error tolerance is chosen, $\epsilon \approx 10^{-3} - 10^{-5}$. Then $(\Delta t)^{(n+1)}$ may be determined based on either the I- or PI-controller step controller. If $U^{(n+1)}$ and $\hat{U}^{(n+1)}$ are computed to $q = (p+1)$-th and p-th order accuracy, respectively, then $\delta^{(n+1)}$ at time $n+1$ may be defined as $\delta^{(n+1)} = U^{(n+1)} - \hat{U}^{(n+1)} = R_{err}$. $\delta^{(n+1)}$ is then a local truncation error estimate for the lower-order formula. Experience teaches that it is also wise to place a limit on how quickly the time step is allowed to increase, factors of between 2 to 5 being the maximum.

A unique problem of the vdH schemes is that if R_{old} is not employed, when a step size is taken that exceeds the error tolerance it is too late to correct matters. In this case more conservative values of the "safety factor,"

κ might be advised. Normally $\kappa = 0.9$ is chosen but this might be reduced slightly here. Alternatively the error tolerance, ϵ, could be reduced so that any transgressions of the reduced tolerance might not be a transgression of the original tolerance. It should also be remembered that this procedure makes no sense if the U-vector is not normalized in some way so that meaningful comparisons may be made between, say, the energy equation and the momentum equations. One choice is:

$$\delta^{(n+1)*} = \frac{\delta^{(n+1)}}{U^{(n+1)}}, \tag{4.24}$$

in cases where $|U^{(n+1)}|$ is greater than, say 10^{-8} (depending on machine precision) and where $\delta^{(n+1)*}$ replaces $\delta^{(n+1)}$.

In the direct simulations reported here a fourth-order, five-stages, two-registers Explicit Runge-Kutta (ERK) scheme with PID error controller is used. The time step is set between 10 and 100 times lower than the anticipated CFL (Courant-Freidricks-Levy) limit that in the context of compressible low Mach number flows is an acoustic one dictated by the speed of sound a_0 as follows from the expression $CFL = (a_0 + u) \cdot (\Delta t/\Delta x) = a_0 \cdot (1 + M) \cdot (\Delta t/\Delta x)$. The method coefficients are listed in Table 4.3.

	RK3(2)4[2R+]C	RK4(3)5[2R+]C	RK5(4)9[2R+]S	RK5(4)9[2R+]C	RK5(4)9[2R+]M
a_{21}	$+\frac{11847461282814}{36547543011857}$	$+\frac{970286171893}{4311952581923}$	$+\frac{1107026461565}{5417078080134}$	$+\frac{2756167973529}{16886029417639}$	$+\frac{5573095071601}{11304125995793}$
a_{32}	$+\frac{3943225443063}{7078155732230}$	$+\frac{6584761158862}{12103376702013}$	$+\frac{38141181049399}{41724347789894}$	$+\frac{11436141375279}{13592993952163}$	$+\frac{315581365608}{4729744040249}$
a_{43}	$-\frac{346793006927}{4029903576067}$	$+\frac{2251764453980}{15575788980749}$	$+\frac{493273079041}{11940823631197}$	$+\frac{88551658327}{2352971381260}$	$+\frac{8734064225157}{30508564569118}$
a_{54}	-	$+\frac{26877169314380}{34165994151039}$	$+\frac{1851571280403}{6147804934346}$	$+\frac{1882111988787}{5590444193957}$	$+\frac{6457785058448}{14982850401353}$
a_{65}	-	-	$+\frac{11782306865191}{62590030070788}$	$+\frac{846820081679}{4754706910573}$	$+\frac{5771559441664}{18187997215013}$
a_{76}	-	-	$+\frac{9452544825720}{13648368537481}$	$+\frac{4475289710031}{6420120086209}$	$+\frac{1906712129266}{6681214991155}$
a_{87}	-	-	$+\frac{4435885630781}{26285702406235}$	$+\frac{1183947748311}{9144450320350}$	$+\frac{311585568784}{2369973437185}$
a_{98}	-	-	$+\frac{2357909744247}{11371140753790}$	$+\frac{3307377157135}{13111544596386}$	$-\frac{4840285693886}{7758383361725}$
b_1	$+\frac{1017324711453}{9774461848756}$	$+\frac{1153189308089}{22510343858157}$	$+\frac{2274579626619}{23610510767302}$	$+\frac{1051460336009}{14326298067773}$	$+\frac{549666665015}{5899839355879}$
b_2	$+\frac{8237718856693}{13685301971492}$	$+\frac{1772645290293}{4653164025191}$	$+\frac{693987741272}{12394497460941}$	$+\frac{930517604889}{7067438519321}$	$-\frac{548816778320}{9402908589133}$
b_3	$+\frac{57731312506979}{19404895981398}$	$-\frac{1672844663538}{4480602732383}$	$-\frac{347131529483}{15096185902911}$	$-\frac{311910530565}{11769786407153}$	$+\frac{1672704946363}{13015471661974}$
b_4	$-\frac{101169746363290}{37734290219643}$	$+\frac{2114624349019}{3568978502595}$	$+\frac{1144057200723}{32081666971178}$	$-\frac{410144036239}{7045999268647}$	$+\frac{1025420337373}{5970204766762}$
b_5	-	$+\frac{5198255086312}{14908931495163}$	$+\frac{1562491064753}{11797114684756}$	$+\frac{16692278975653}{83604524739127}$	$+\frac{1524419752016}{6755273790179}$
b_6	-	-	$+\frac{13113619727965}{44346030145118}$	$+\frac{3777666801280}{13181243438959}$	$-\frac{10259399787359}{43440802207630}$
b_7	-	-	$+\frac{393957816125}{7825732611452}$	$+\frac{286682614203}{12966190094317}$	$+\frac{4242280279850}{10722460893763}$
b_8	-	-	$+\frac{720647959663}{6565743875477}$	$+\frac{3296161604512}{22629905347183}$	$+\frac{1887552771913}{6099058196803}$
b_9	-	-	$+\frac{3559252274877}{14424734981077}$	$+\frac{2993490409874}{13266828321767}$	$-\frac{453873186647}{15285235680030}$
$\hat{b}_1$	$+\frac{15763415370699}{46270243929542}$	$+\frac{1016888040809}{7410784769900}$	$+\frac{266888888871}{3040372307578}$	$+\frac{3189770262221}{35077884776239}$	$+\frac{330911065672}{9937126492277}$
$\hat{b}_2$	$+\frac{514528521746}{5659431552419}$	$+\frac{11231460423587}{58533540763752}$	$+\frac{34125631160}{2973680843661}$	$+\frac{780043871774}{11919681558467}$	$-\frac{872991930418}{11147305689291}$
$\hat{b}_3$	$+\frac{27030193851939}{9429696342944}$	$-\frac{1563879915014}{6823010717585}$	$-\frac{653811289250}{9267220972999}$	$-\frac{483824475979}{5387739450692}$	$+\frac{2575378033706}{14439313202205}$
$\hat{b}_4$	$-\frac{69544964788955}{30262026368149}$	$+\frac{606302364029}{971179775848}$	$+\frac{323544662297}{2461529853637}$	$+\frac{1306553327038}{9528955984871}$	$+\frac{3046892121673}{11013392356255}$
$\hat{b}_5$	-	$+\frac{1097981568119}{3980877426909}$	$+\frac{1105885670474}{4964345317203}$	$+\frac{6521106697498}{22565577506855}$	$+\frac{1780184658016}{8929499316295}$
$\hat{b}_6$	-	-	$+\frac{1408484642121}{8758221613943}$	$+\frac{1400555694605}{19784728594468}$	$+\frac{10265149063}{2098741126425}$
$\hat{b}_7$	-	-	$+\frac{1454774750537}{11112645198328}$	$+\frac{1183541508418}{13436305181271}$	$+\frac{1643090076625}{4891294770654}$
$\hat{b}_8$	-	-	$+\frac{772137014323}{4386814405182}$	$+\frac{3036254792728}{15493572606329}$	$+\frac{116106750067}{3955800826265}$
$\hat{b}_9$	-	-	$+\frac{277420604269}{1857595682219}$	$+\frac{638483435745}{4187244659458}$	$+\frac{866868642257}{42331321870877}$

Table 4.3: Coefficients for several two-registers ERK methods

4.4 Convective Formulations

In Chapter 2 the advantages of a skew-symmetric formulation for the convective terms in the Navier-Stokes equations are briefly discussed. The main problem related to the use of this alternative formulation is the additional computational cost that it involves, mostly by increasing the number of derivatives that have to be evaluated at each time step. For chemically reacting mixtures described by a large number of species N_g, an associated large number $(N_g - 1)$ of species conservation equations has to be solved. In the context of the S3D code, assuming three spatial dimensions, each one of these $(N_g - 1)$ species conservation equations contains three convective terms, the energy and mass conservation equations contain three convective terms each and so do each of the three momentum equations. The total number of derivative operators N_d involved in the computation of the convective terms in their conservative formulation ($\tilde{\alpha} = 1$ in equation 2.20) is therefore:

$$N_d = 3 \cdot 3 + 3 + 3 + 3 \cdot (N_g - 1) = 15 + 3 \cdot (N_g - 1) \tag{4.25}$$

where N_g is the number of species. If $\tilde{\alpha} = 1/2$, it is readily seen from equations 2.21 and 2.22 that an extra cost, because of the additional derivatives, is involved and, for large N_g, the "heaviest" increase in cost, of $3+(N_g-1)\cdot 3$ *extra* derivatives, is related to the last term in equation 2.22. While the additional gradients in equation 2.21 are needed elsewhere to compute $\tau_{\beta\alpha}$ and the right-hand side of the continuity equation, the three extra gradients in each of the scalar equations (ρe_t,ρY_i) are not needed anywhere else in the solution algorithm of S3D and represent therefore a large extra cost associated exclusively to the skew-symmetric formulation. For the present simulations $N_g = 9$, the cost in terms of derivative operators N_d goes from the $N_d = 39$ in the conservative formulation to $N_d = 72$ in the skew-symmetric, almost a *doubling*!

If, following an alternative approach, the non-linearity of the convective terms in equations 2.1-2.4 is assumed *cubic*, characterized by a non-trivial density spectrum, the skew-symmetric form of these terms can be written, still assuming $\tilde{\alpha} = 1/2$, as:

$$\nabla_\beta \cdot (\rho \boldsymbol{u}_\alpha \boldsymbol{u}_\beta) = \frac{1}{2}\nabla_\beta \cdot (\rho \boldsymbol{u}_\alpha \boldsymbol{u}_\beta) + \frac{1}{2}\left[\boldsymbol{u}_\alpha \boldsymbol{u}_\beta \cdot \nabla_\beta \rho + \rho \boldsymbol{u}_\beta \cdot \nabla_\beta \boldsymbol{u}_\alpha + \rho \boldsymbol{u}_\alpha \nabla_\beta \cdot \boldsymbol{u}_\beta\right] \tag{4.26}$$

$$\nabla_\beta \cdot (\rho \phi \boldsymbol{u}_\beta) = \frac{1}{2}\nabla_\beta \cdot (\rho \phi \boldsymbol{u}_\beta) + \frac{1}{2}\left[\phi \boldsymbol{u}_\beta \cdot \nabla_\beta \rho + \rho \boldsymbol{u}_\beta \cdot \nabla_\beta \phi + \rho \phi \nabla_\beta \cdot \boldsymbol{u}_\beta\right] \tag{4.27}$$

All gradients in these equations are needed elsewhere in the solution algorithm and their evaluation in relation to the skew-symmetric convective formulation does not imply *any* extra cost. This new cubic skew-symmetric formulation can be also characterized by a second parameter $\tilde{\beta}$ in addition to the already mentioned $\tilde{\alpha}$, in the above equations $\tilde{\beta} = 0$. More details about the parameter $\tilde{\beta}$ and about the performance of this alternative skew-symmetric formulation in respect to anti-aliasing and energy conservation properties are presented in a series of tests reported in detail in Gruber and Kennedy (2006b). Direct simulations of decaying isotropic compressible turbulence for inert and reactive mixtures are run on several *poorly* resolved grids (the ratio of the Kolmogorov length scale to the grid scale is set to 0.2) for a turbulent Mach number, M_t, of 0.2 and 0.1 respectively. The number of modes r available in the computational box is intentionally limited to values that do not allow correct representation of the smallest scales of turbulence. This is done to compare the response of the different convective formulations to aliased energy. The test results seem to suggest similar (in the inert cases) or even better (in the reactive cases) de-aliasing properties for the new, and computationally much cheaper, *cubic* skew-symmetric formulation compared to the original *quadratic* formulation of Feiereisen *et al.* (1981) and Blaisdell (1991).

Figure 4.2 shows the typical time-evolution of the energy spectrum in a poorly resolved *unfiltered* direct simulation: energy is transferred from the low wave-number modes on the left of the spectrum to high wave-number modes on the right. In the absence of filtering, the initial violent energy transfer (red, yellow and orange lines) which takes place on a time scale comparable to an eddy turnover (ET), often causes such a rapid growth of aliased energy that the simulation crashes. This is the case especially when the conservative formulation ($\tilde{\alpha} = 1$) is used for the convective terms. However, even if the simulation survives, as it is often the case when employing de-aliased skew-symmetric convective formulations ($\tilde{\alpha} = 1/2$), in the long "decaying" transient, shown in the Figure up to 4 eddy turnovers, it does not produce a meaningful result: peaks in the green, light blue and dark blue lines show clearly that energy is unphysically accumulated at the characteristic modes of the grid. The time history of a filtered solution is shown in Figure 4.3 up to 4 eddy turnovers: the filter contains the growth of the energy "peaks" but does not completely eliminate them.

The energy spectra in Figure 4.4 show the different aliasing properties of several convective formulations in inert decaying isotropic turbulence after one-third characteristic eddy time (recall that the *only* difference between

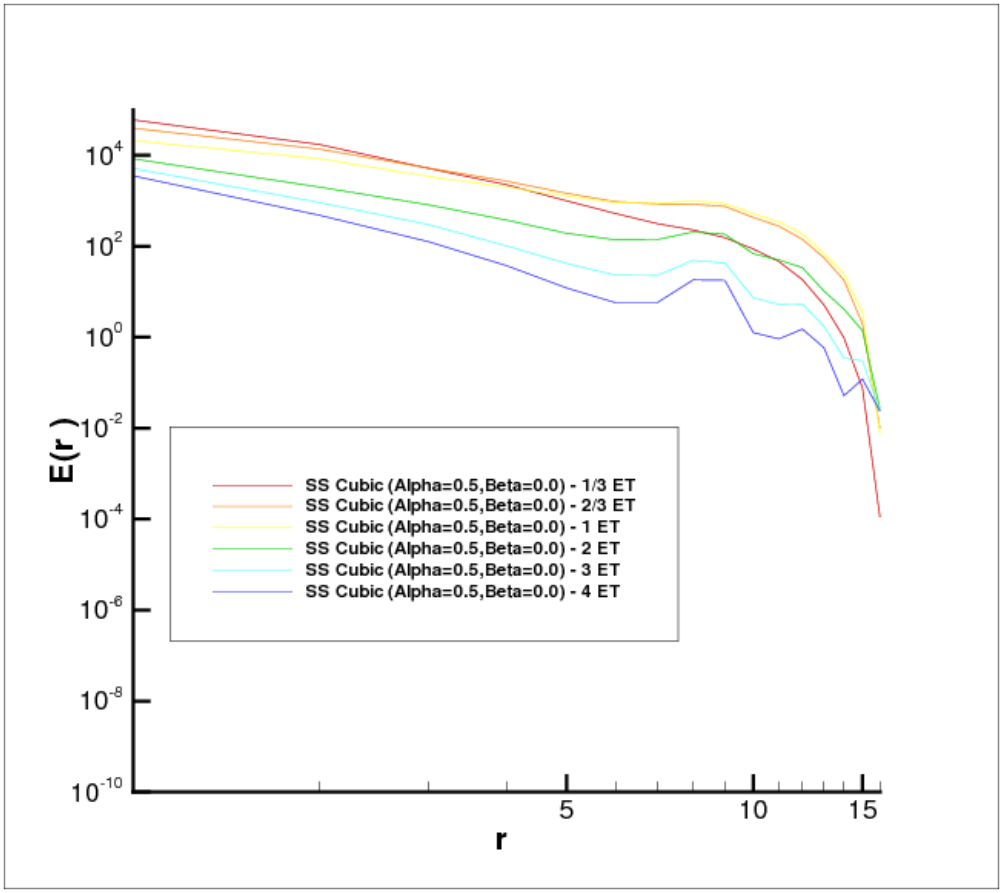

Figure 4.2: Inert case: typical time evolution of the energy spectrum $E(r)$ in *unfiltered* poorly resolved direct simulation of decaying isotropic turbulence on a 32^3 grid for $\tilde{\alpha} = 1/2$ and $\tilde{\beta} = 0$. The different times are non-dimensionalized by the characteristic eddy turnover time (ET) and r is the mode number.

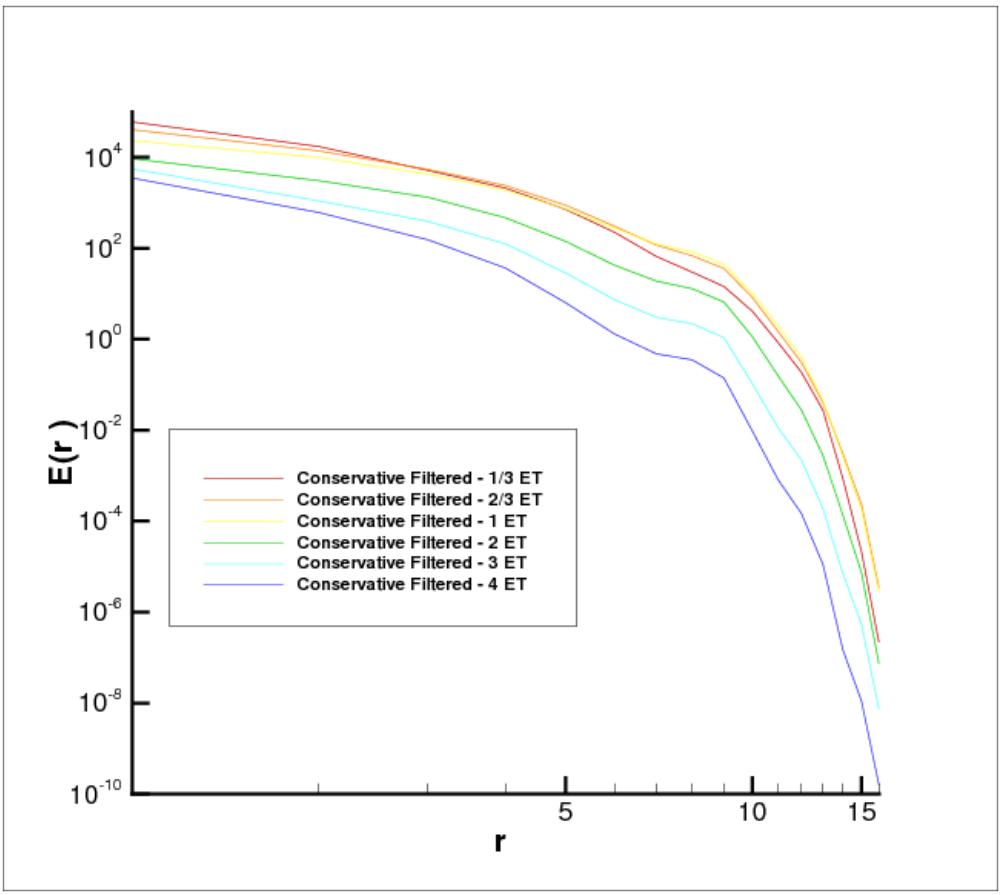

Figure 4.3: Inert case: typical time evolution of the energy spectrum $E(r)$ in *filtered* poorly resolved direct simulation of decaying isotropic turbulence on a 32^3 grid for $\tilde{\alpha} = 1$ and $\tilde{\beta} = 0$. The different times are non-dimensionalized by the characteristic eddy turnover time (ET) and r is the mode number.

these numerical tests is the convective formulation). The strong influence of the high-order explicit spatial filter on the energy spectrum of the conservative formulation is evident. The skew-symmetric formulations (dot-dashed lines) perform better than the unfiltered conservative formulation (dotted line) having accumulated less aliased energy at high wave-numbers, but considerably worse than the filtered solution (solid line). Figure 4.5 zooms in the high wave-numbers region and compares the different skew-symmetric formulations after one-third characteristic eddy time. An explanation of the parameter $\tilde{\beta}$ is given in Gruber and Kennedy (2006b) but details of the many alternative formulations is not relevant at this point, it is only important to note that the computationally expensive quadratic skew-symmetric formulation of Blaisdell (blue dashed line) and the much cheaper cubic formulation with $\tilde{\alpha} = 1/2$ and $\tilde{\beta} = 0$ (red dot-dashed line) perform *identically* in respect to the accumulated aliased energy.

In *poorly* resolved direct simulations of reacting mixtures the trend toward improved performance of the cubic formulations is more marked than in the inert cases, suggesting that a stronger cubic non-linearity is present and that the cubic convective formulations could have a considerable potential for improvement of reactive flows LES, poorly resolved by definition.

Figures 4.6 and 4.7 show a typical density field in the reactive case, the back-to-back flame is initially placed in the middle of the computational domain and propagates both in the negative and positive x-direction. Large density oscillations can be noticed near the flame front in enclosure "A". The time evolution of the energy spectra for a quadratic and a cubic formulation are compared in Figures 4.8 and 4.9 up to 5 characteristic eddy times. Also in this case, as in the inert one, the strong "aliased" energy transfer from the low to the high frequencies is evident. The cubic formulation seems to improve its performance over the quadratic one as the rate of "aliasing" shown by the spectral evolution is lower.

Another way of evaluating the performance of the different formulations is to examine the energy content of the (most energetic) low-frequency mode. Figure 4.10 shows, in the reactive case and for several convective formulations, the time evolution over 2 characteristic eddy times of the most energetic mode and the decay in its energy content. Also in this case the cubic skew-symmetric formulations seem to perform better than the quadratic ones as illustrated by the rate at which the energy is lost toward higher wavenumbers.

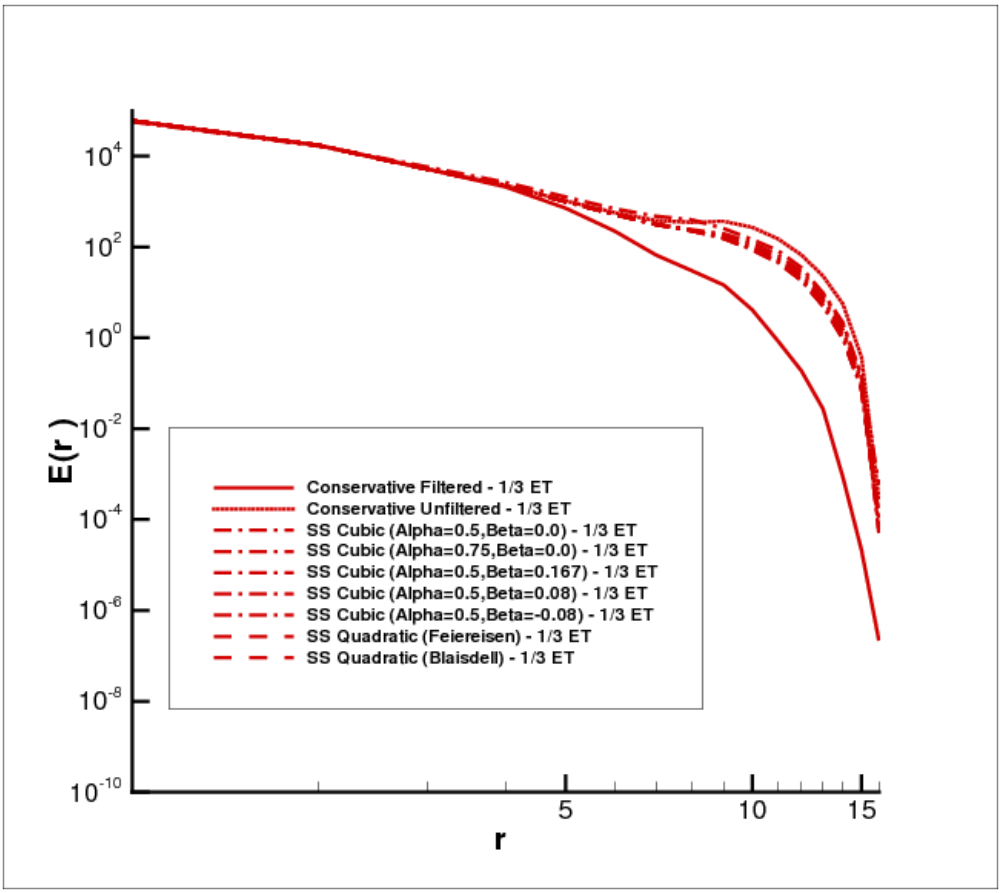

Figure 4.4: Inert case: comparison of anti-aliasing behaviour of different convective formulations after a simulation time comparable to $1/3$ eddy turnover time (ET).

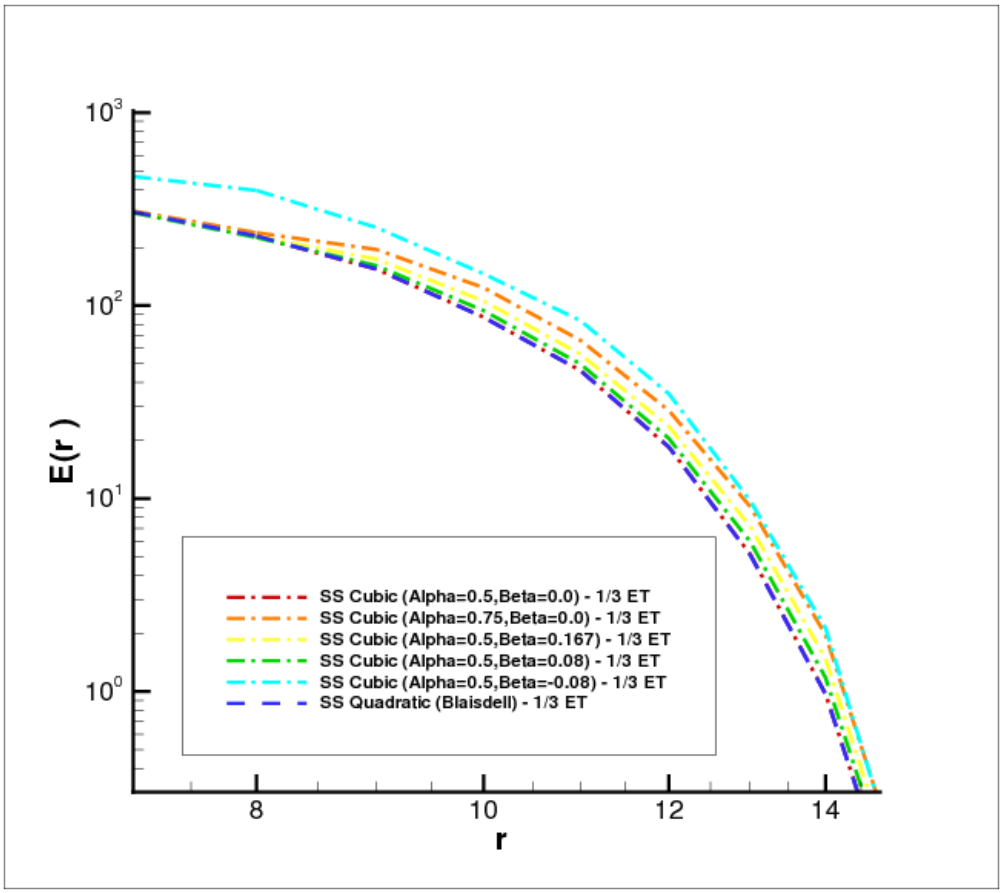

Figure 4.5: Inert case: comparison of anti-aliasing behaviour of different convective skew-symmetric formulations after a simulation time comparable to $1/3$ eddy turnover time (ET).

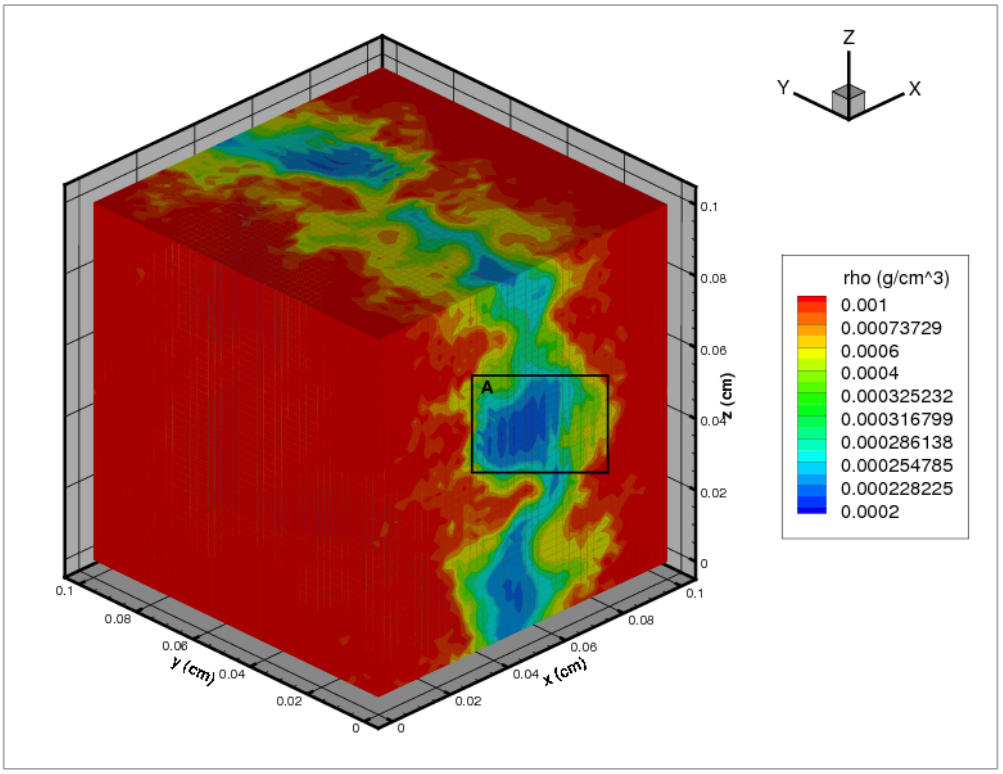

Figure 4.6: Reactive case: flooded isocontours of the density field showing the back-to-back flame propagating in the computational domain. Enclosure "A" show strong oscillations in density.

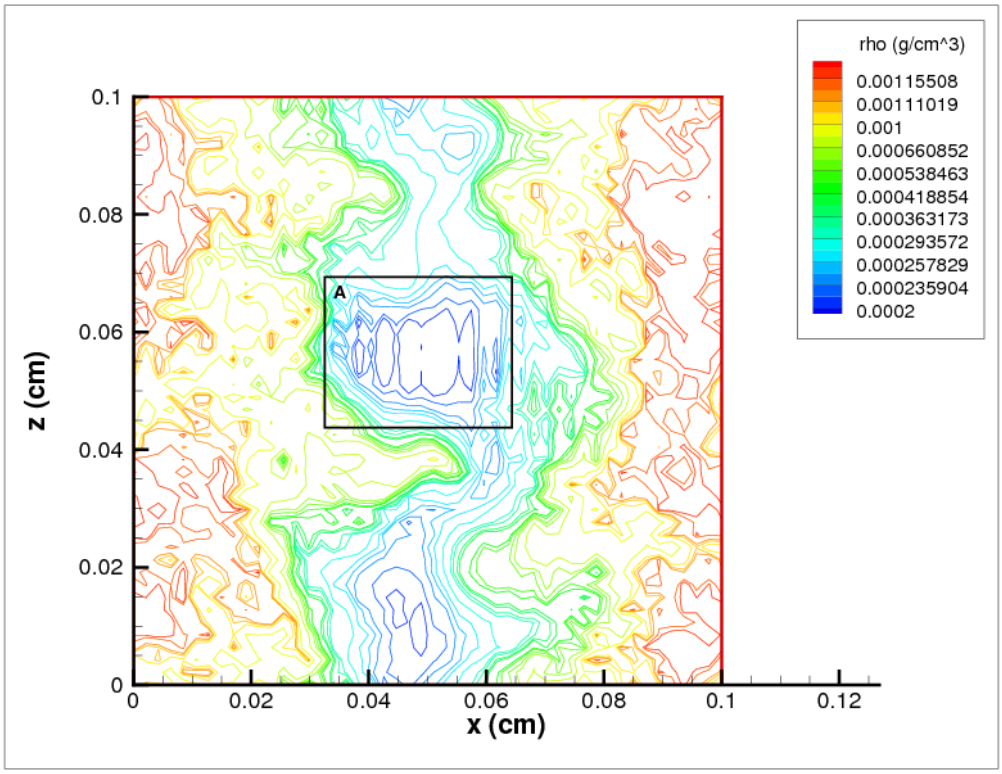

Figure 4.7: Reactive case: isolines of the density field showing the back-to-back flame propagating in the computational domain. Enclosure "A" show strong oscillations in density.

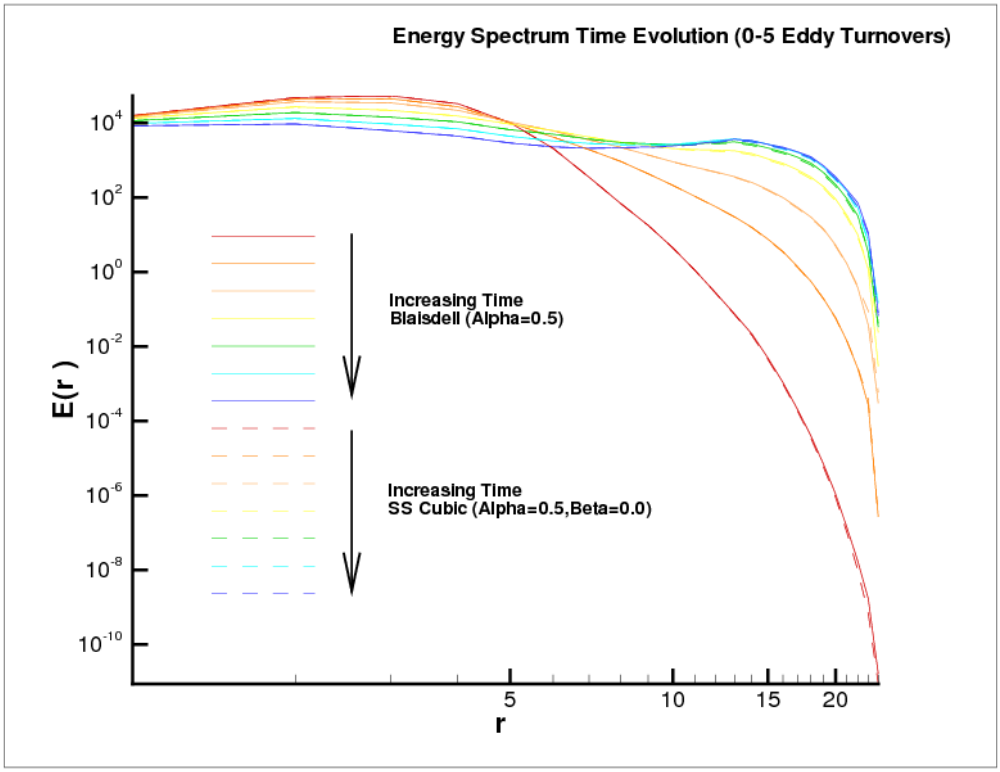

Figure 4.8: Reactive case: typical time evolution of the energy spectrum $E(r)$ in *unfiltered* poorly resolved direct simulation of decaying isotropic turbulence on a 48^3 grid for the quadratic skew-symmetric formulation of Blaisdell (solid lines) and for the cubic formulation with $\tilde{\alpha} = 1/2$ and $\tilde{\beta} = 0$ (dashed lines). The different times are non-dimensionalized by the characteristic eddy turnover time (ET) and r is the mode number.

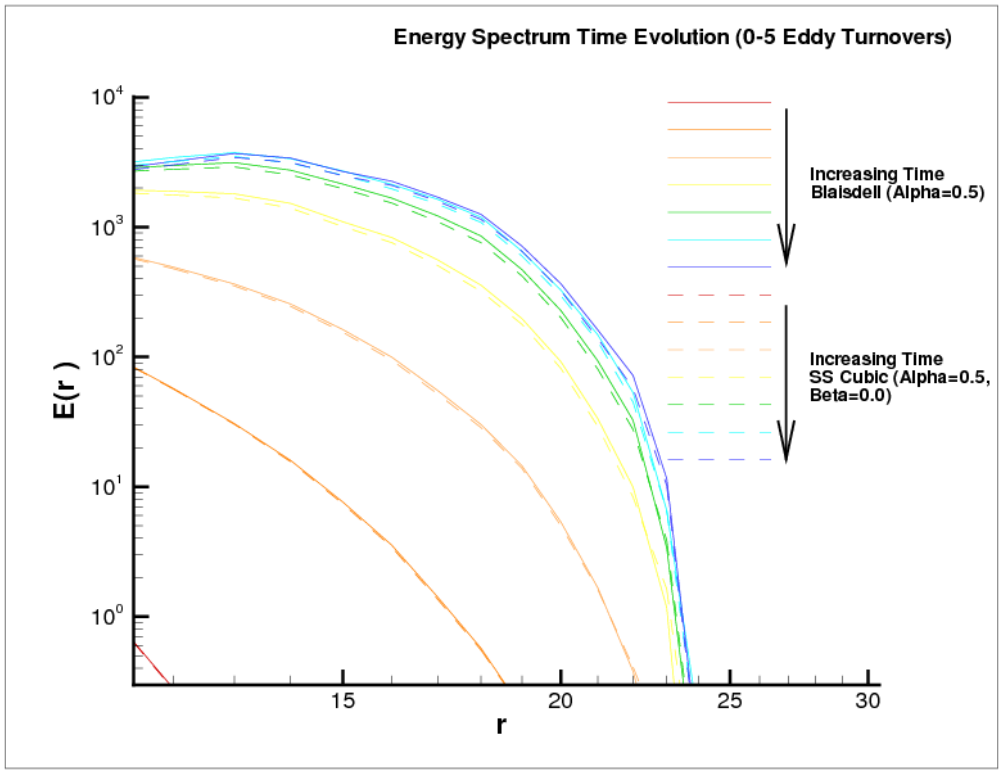

Figure 4.9: Reactive case (detail): typical time evolution of the energy spectrum $E(r)$ in *unfiltered* poorly resolved direct simulation of decaying isotropic turbulence on a 48^3 grid for the quadratic skew-symmetric formulation of Blaisdell (solid lines) and for the cubic formulation with $\tilde{\alpha} = 1/2$ and $\tilde{\beta} = 0$ (dashed lines). The different times are non-dimensionalized by the characteristic eddy turnover time (ET) and r is the mode number.

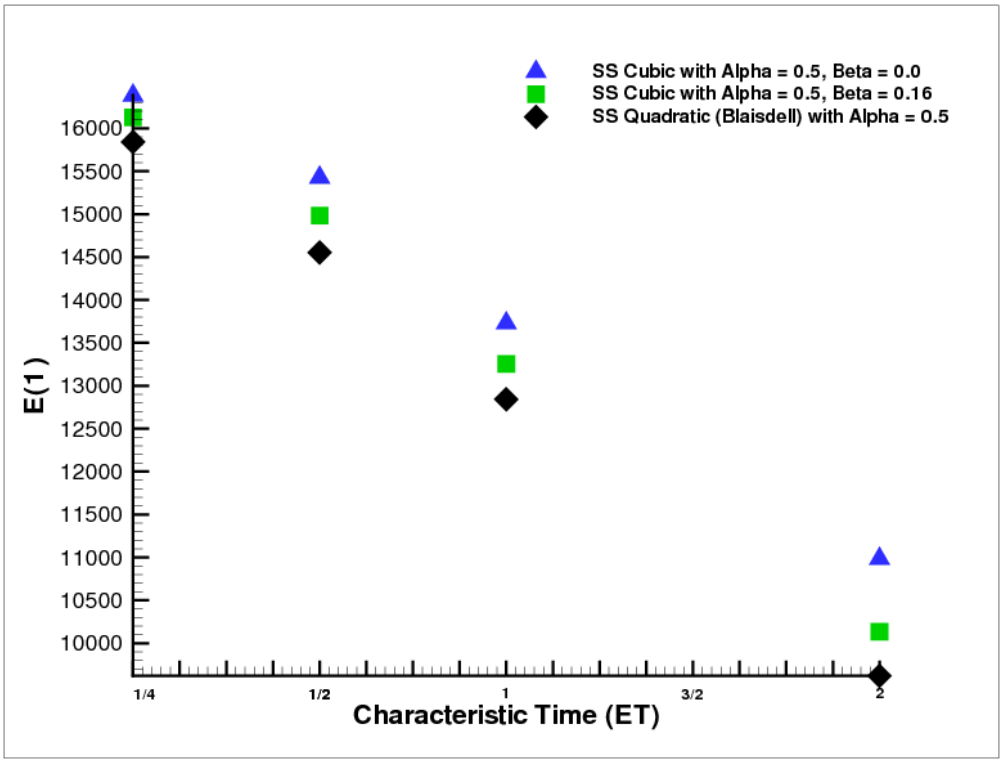

Figure 4.10: Reactive case: typical time evolution of the energy content at the lowest wavenumber $E(1)$ in *unfiltered* poorly resolved direct simulation of decaying isotropic turbulence on a 48^3 grid for the quadratic skew-symmetric formulation of Blaisdell and for the cubic formulations with $\tilde{\alpha} = 1/2$ and $\tilde{\beta} = 0$. The different times are non-dimensionalized by the characteristic eddy turnover time (ET).

Note

In conclusion of this brief discussion about the aliasing properties of different convective formulations it is important to point out that:

- The cubic approach to the skew-symmetric formulation of the convective terms proved to be computationally cheap and at least as good as the more expensive quadratic approach in *containing* the growth of aliased energy
- Poorly resolved test runs for which full DNS resolution is not affordable are conveniently performed using the cubic skew-symmetric convective formulation
- The results presented above seem to suggest that Large Eddy Simulations (poorly resolved by definition), especially in the case of reactive flows, could achieve considerable improvement by employing a cubic skew-symmetric formulation
- All full-scale direct simulations should be run with sufficient resolution, this reduces the growth of artificial aliased energy to minimal levels independently of the convective formulation used
- High-order filters are very effective in removing aliased energy and can mask, to some extent, the effects poorly resolved situations

5 Turbulent Channel Flow

DNS of fully developed inert turbulent plane channel flow is presented in this Chapter. The reason for this is twofold: the implementation of the wall boundary conditions in the S3D code has to be validated since the author of the present report is both the programmer and the first user of the code in a context of solid wall boundary conditions; in performing direct simulations of a premixed flame anchored in a turbulent channel the streamwise direction cannot be considered homogeneous, accordingly, generation of inflow data with realistic turbulent fluctuations has to be achieved with an auxiliary non-reacting simulation. It is important to note that the S3D code solves the fully compressible Navier-Stokes equations[1], in the case of nearly incompressible low-speed turbulent channel inert flow ($M \sim 0.1 - 0.2$), density and temperature fluctuations exhibit very small amplitudes and, as such, are relatively unimportant. The solution of the "cold" turbulent channel flow cases reported below is expected to be very similar to the results of Kim *et al.* (1987), this reference dataset is, in the remaining of this report, named KMM.

5.1 2D Turbulence

Before the availability to the author of a fully three-dimensional version of the S3D code, an older two-dimensional version of the same code was used for testing purposes. The feasibility of a two-dimensional turbulent channel flow simulation is investigated also with the aim of running 2-D vs 3-D comparison of near-wall flame behaviour.

The case, named 2DT in this report, is configured using the generally accepted resolution rules for the target Reynolds number. The parameters of the run are reported in detail in the next Section when a description of the 3-D cases is given. The *only* difference of the two-dimensional inert case in respect to the three-dimensional one is the absence of the spanwise direction.

[1] Although there is the limitation of not being able to resolve strong shocks!

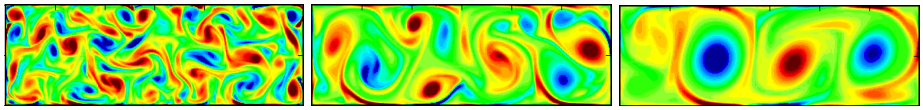

Figure 5.1: 2-D turbulence evolution

As the calculation is started, a compressible isotropic turbulent field (the velocity fluctuations are set to zero at the wall using a smooth spatial filter to enforce no-slip) is superimposed on a mean laminar velocity profile, a certain level of velocity fluctuations is present in the channel and the vortical motions are convected downstream by an imposed streamwise effective pressure gradient (in this case a body force). However, turbulence theory predicts, over time, the self organization of two-dimensional small eddies in larger ones: this is an *opposite* behaviour in respect to what happens in three-dimensional turbulence thanks to the action of the spanwise *vortex stretching* mechanism.

The *inverse energy cascade* acts unfortunately very quickly on the 2-D turbulence level and after only one channel transit time[2] the flow is nearly laminarized. Figure 5.1 clearly shows an example of the decay of fluctuation level and of the number of eddies. The flow ultimately does not laminarize entirely, leaving some large scale fluctuations (of the same characteristic length scale as the computational domain) act on the mean flow field.

In the case of the two-dimensional reactive channel flow simulations of Section 7.3.1 that are characterized by a non-homogeneous streamwise direction, it is common to artificially specify a "not-so-realistic"[3] fluctuations level at the inlet of the computational domain using one of the various techniques described in Section 7.2. This *forcing* of the inlet turbulence level allows the turbulent velocity fluctuations to reach an eventual flame placed downstream of the inlet and the interaction of it with the approaching (fairly unrealistic) turbulence can be studied. A serious problem related to this two-dimensional configuration is that, since 2-D channel turbulence is not able to sustain itself, turbulent fluctuations rapidly decay downstream of the inlet and the observed flame-turbulence interaction conditions are very likely very different from those wanted.

[2] The time necessary for a fluid particle to span the entire streamwise length of the computational domain

[3] See Section 7.2 for a detailed discussion of this notorious issue in DNS/LES

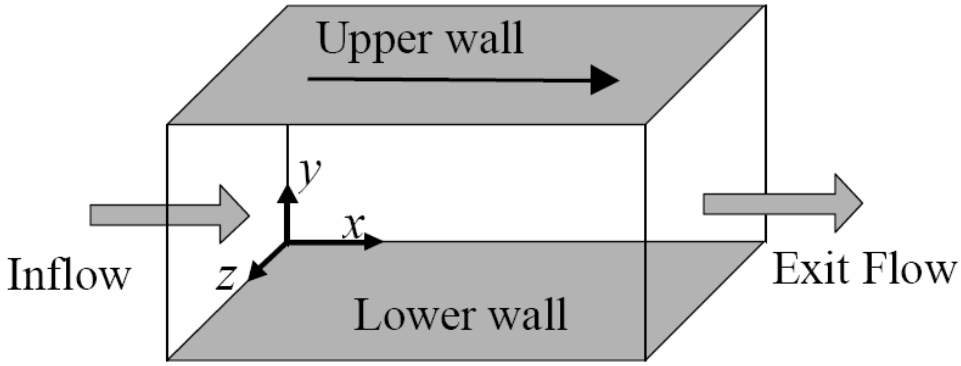

Figure 5.2: Pictorial representation of the plane channel, from Alshaalan (1997).

5.2 3D Channel Turbulence

The literature cited in Chapter 1 suggests that DNS of turbulent channel flow has a "long" and successful history. Direct simulations of channel flows characterized by increasingly high Reynolds numbers are being performed to study the scaling of the turbulent quantities for higher turbulence level. For a more complete picture of turbulent channel flows the reader is addressed to the vast literature on this subject. In the context of the present work, the focus is on DNS of premixed ducted flames and the "cold" turbulent channel case is briefly reported here for the sake of completeness.

5.2.1 Case Parameters

The parameters of the turbulent plane channel case, named 3DT, are set as follows:

- The target flow Reynolds number is $Re_0 = 3142$, based on the centerline velocity and the channel half-width, or $Re_\tau = 180$ if the friction velocity u_τ is used as reference.
- A computational box as in Figure 5.2 is built on a Cartesian $360 \times 200 \times 280$ grid. Moser *et al.* (1999) suggests that 13 or more grid

points are necessary and sufficient to fully resolve the inner viscous layer very close to the wall ($y^+ \leq 10$). The present grid is refined at the wall using a *tanh* mapping and the first point off the wall is at $y^+ = 0.5$. The grid resolution is expressed in wall units as $\Delta x^+ = 2.5$, $\Delta y^+ = 0.5 - 3.4$ and $\Delta z^+ = 2.0$. About these adimensional wall units, note that in a *nearly* incompressible and *nearly* isothermal context characterized by variable density and temperature there is no consistent and unique definition of the wall friction velocity u_τ that is valid everywhere in the computational domain. In the remaining of this report the *friction velocity*, u_τ, is therefore designated by a semi-local mean of its values averaged in the homogeneous directions. The grid is only stretched by a factor of 7 in the wall normal direction, the reason for this relatively "light" stretching (a factor of 100 is usual in other contexts) is to be found in the fact that the flame case reported in Section 7.3.2 requires high resolution also near the channel centerline and to simplify data transfer between the inert and reactive flow domains the same resolution is adopted in both cases.

– Periodic boundary conditions are imposed in the homogeneous directions and isothermal, inert, no-slip wall boundary conditions following Method B of Section 3.3.2 are set at the two opposite solid surfaces. In order to limit the cost of this *auxiliary* case[4], the relative dimensions of the box in the streamwise, wall normal and spanwise directions are $5H$, $2H$ and $3H$ respectively, where H is the channel half-width. This gives a box which is shorter than the "usual" one from KMM but considerably larger than the "minimal" box of Jiménez and Moin (1991), a certain low degree of periodicity in the streamwise direction should however be expected because of the large mean streamwise extension of the quasi-coherent near-wall vorticity structures. In the present context an eventual low degree of periodicity is not to be considered a serious issue since the streamwise vorticity structures "migrate" randomly (although on a relatively long time scale) in the spanwise direction and, moreover, the aim of these simulations is to generate reasonably realistic channel turbulence that can be fed into the reactive flow cases of Chapter 7 and not to perform a detailed study of the statistics of channel turbulence.

[4]The box dimensions in the reactive case will be reduced further in the streamwise direction to $4H \times 2H \times 3H$

- The flow is driven, instead of the usual pressure gradient, by an external body force of the form ρf_1 acting in the streamwise direction, this is done in order avoid non-zero streamwise gradients of mean density and pressure. This approach has been used earlier in DNS of compressible turbulent channel flows, see Huang *et al.* (1995).

- The initial turbulent field is set by superimposing a Passot-Pouquet isotropic compressible spectrum to a laminar mean flow profile, see Passot and Pouquet (1987). The flow gains a turbulent profile between 1 and 2 transit times.

- Pressure, density and temperature are set to uniform values (a "hot" wall temperature T_w is needed in the reactive cases and the density is chosen accordingly): $\rho = 0.47\,kg/m^3$, $p = 1\,atm$, $T = T_w = 750\,K$.

- The time step is fixed to a very low value ($\Delta t = 1.0e^{-09}\,s$) because of synchronization with the reactive case.

- The total integration time of the simulation is 12 transit times corresponding to $2.175\,ms$ or 535 wall time units[5].

5.3 Results

DNS results are conveniently presented here in two ways: one is a visual inspection of the three-dimensional instantaneous fields of several different variables in order to gain a qualitative (and to a certain extent quantitative) idea of the spatial characteristic of near-wall turbulence, the other is the extraction of first and second order statistical moments for single- and two-point correlations.

5.3.1 Instantaneous Fields

In this Section the instantaneous fields from the inert channel flow simulation are visually examined to investigate about the presence in the solution of the characteristic near-wall streamwise vorticity structures.

Figure 5.3 shows a pictorial representation of the wall layer and its characteristic structures elongated in the flow direction: large "bulges" in the

[5]The "inner" or wall time unit is defined as $t_w \sim \nu/u_\tau^2$ and equals $4.06\,\mu s$ under the present conditions.

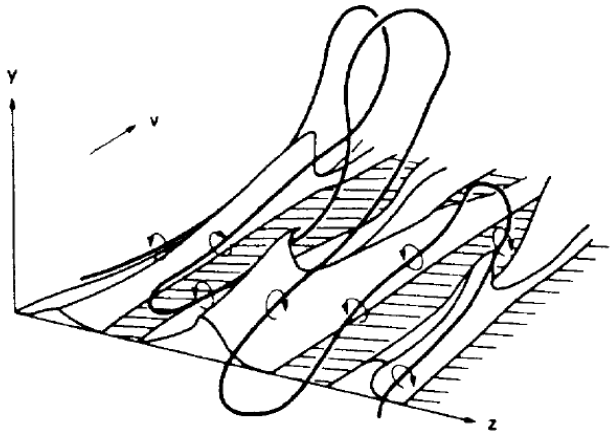

Figure 5.3: Conceptual model of the wall layer showing "bulges" in vorticity magnitude isosurface representing ejections of low speed fluid from the wall by counter rotating quasi-streamwise vorticity structures, from Robinson (1991).

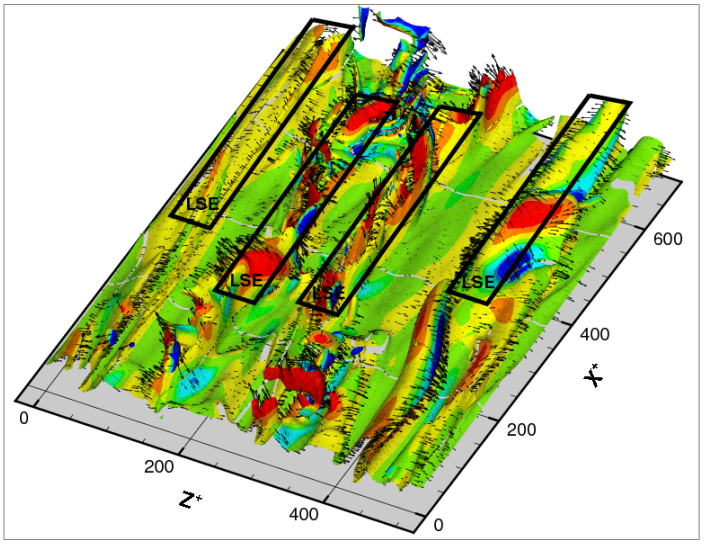

Figure 5.4: Turbulent channel flow at $Re_\tau = 180$: vorticity magnitude isosurface showing low speed ejections (LSE) regions.

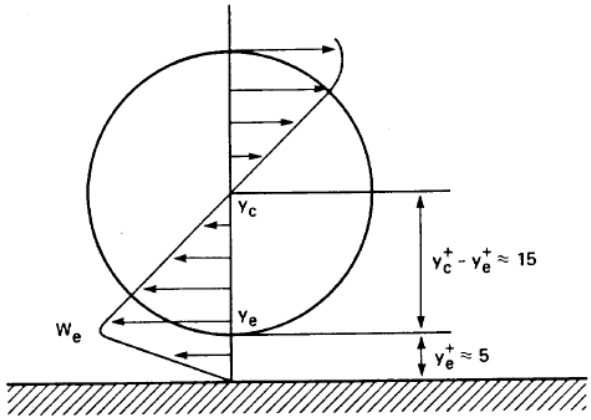

Figure 5.5: Schematic representation of quasi-streamwise vorticity structure, from Kim *et al.* (1987).

vorticity magnitude isosurfaces represent ejections of low speed fluid from the wall by counter rotating quasi-streamwise vorticity structures. This is only one of many (relatively similar) conceptual models proposed for the turbulent boundary layer, however velocity fields from the present DNS of turbulent plane channel flow seem to confirm qualitatively this conceptual model. Figure 5.4 shows an isosurface of vorticity magnitude ($|\boldsymbol{\Omega}| = |\boldsymbol{\nabla}\times\boldsymbol{u}| = 150000\,1/s$) and its relative velocity vectors (yellow-to-red colored regions represent wall-normal velocity fluctuations pointing away from the wall), low speed ejection (LSE) regions are marked by black rectangles. The LSE are separated in the spanwise direction by high speed fluid rushing toward the wall from the outer layer (the green regions in Figure 5.4) pushed by the wall-bound side of the quasi-streamwise roller, see Figure 5.5 for a schematic representation of the quasi-streamwise roller given by Kim *et al.* (1987). As it should be expected for the chosen spanwise domain dimension of 540 wall units, approximately four low- and four high-speed streaks can be individuated in Figure 5.4, in Chapter 7 the high speed fluid approaching the wall will be related to the maximum wall heat flux regions resulting from the flame-wall interaction.

Figures 5.6, 5.7 and 5.8 illustrate the relative position of several near-

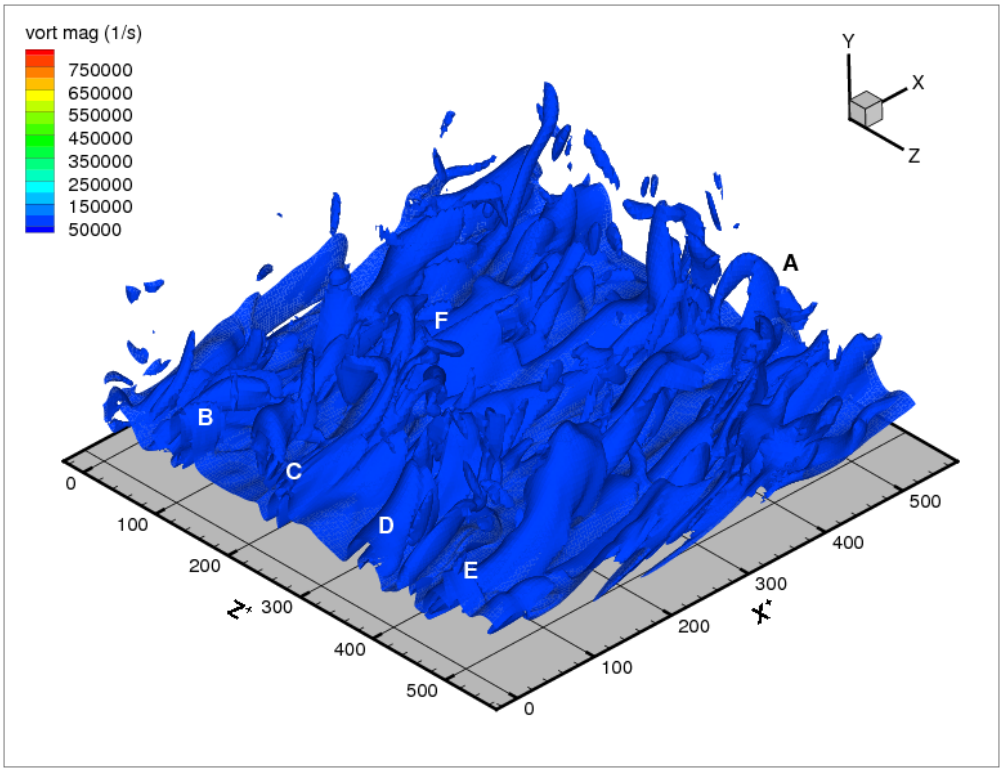

Figure 5.6: Turbulent channel flow at $Re_\tau = 180$: vorticity magnitude isosurface, tiny horseshoe-like vorticity structures are visible near "A" and "F", the spanwise spacing of the streamwise structures "B", "C", "D", "E" is about 100 wall units.

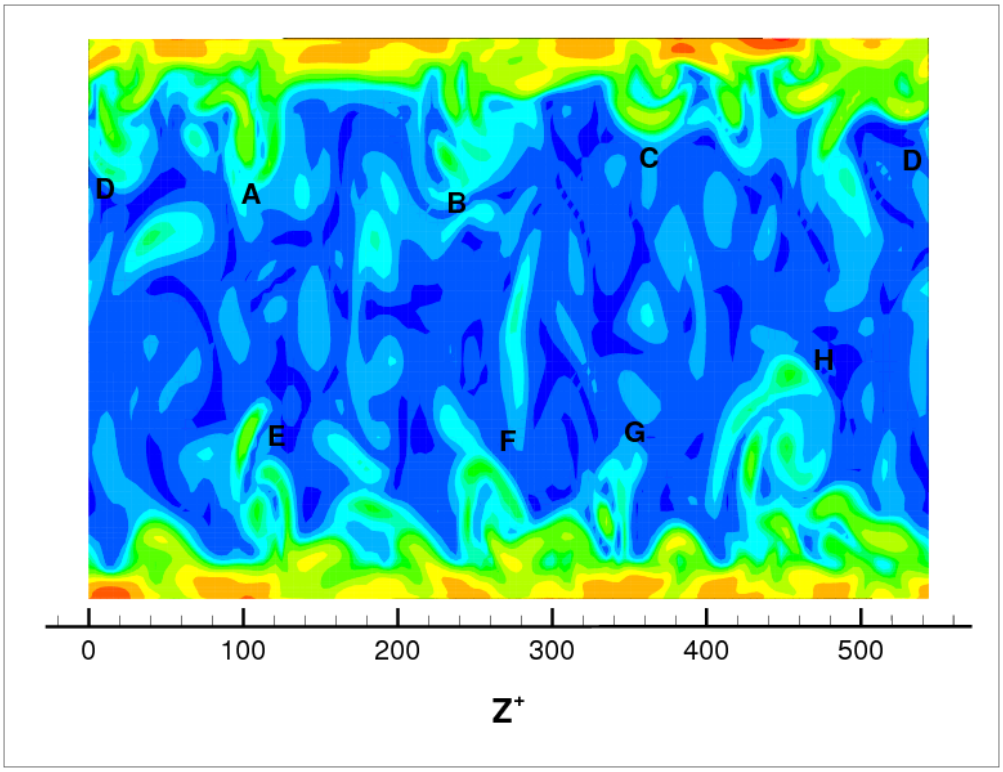

Figure 5.7: Turbulent channel flow at $Re_\tau = 180$: vorticity magnitude isocontours, several vorticity structures are visible beside the letters "A", "B", "C", "D" near the top wall and beside "E", "F", "G", "H" near the bottom wall, the spanwise spacing of the structures is about 100 wall units.

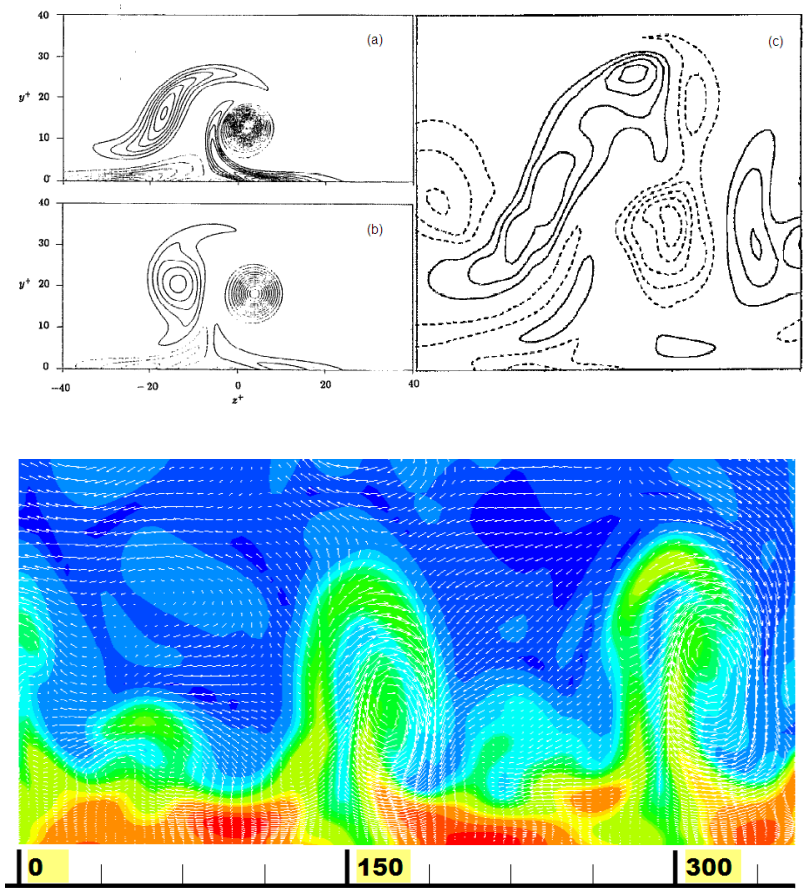

Figure 5.8: Turbulent channel flow at $Re_\tau = 180$: a two-dimensional streamwise vorticity evolution model in the z^+-y^+ plane by Orlandi and Jiménez (1994) is shown in the black and white figures (a) and (b), a typical near-wall streamwise vorticity field from a 3-D DNS calculation is shown in figure (c), the bottom color figure visualizes details of vorticity magnitude isocontours and white velocity vectors in the z^+-y^+ plane from the present simulation. The red contour regions represent "splats" of relatively fast moving fluid on the lower solid wall caused by the action of counter-rotating streamwise vorticity structures.

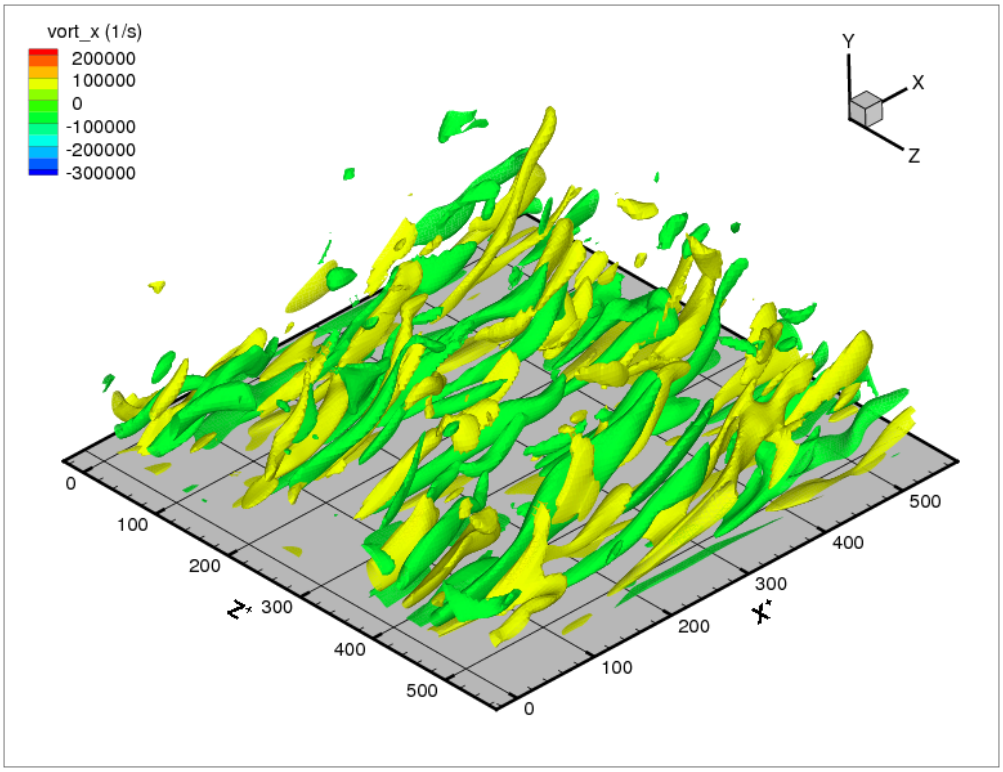

Figure 5.9: Turbulent channel flow at $Re_\tau = 180$: streamwise vorticity isosurfaces show the relatively good spatial correlation of counter-rotating fluid regions.

wall vorticity structures. In the first Figure, a typical instantaneous vorticity magnitude isosurface ($|\boldsymbol{\Omega}| = |\boldsymbol{\nabla} \times \boldsymbol{u}| = 100000\,1/s$) is visualized, only half of the computational domain streamwise length is shown. Note a tiny horseshoe-like vorticity structure near the letter "A" and an even smaller hairpin-like structure immediately to the left of the letter "F". Letters "B", "C", "D" and "E" are placed close to larger streamwise structures (note the bulges in the vorticity "sheet") elongated in the streamwise direction and separated by a spanwise spacing of about 100 wall units, these can be thought of as LSE between the quasi-streamwise "legs" of horseshoe-like structures: as mentioned earlier in Chapter 1, considerable experimental and computational (from direct simulations) evidence suggests that the "legs" of horseshoe-like vorticity structures represent regions of intense streamwise vorticity peaking at $y^+ = 20$ and separated on average by 100 wall units in the spanwise direction, see Kim *et al.* (1987). Most of the turbulent energy production in the boundary layer is associated to these intense streamwise vorticity structures that, in turn, due their origin to mean shear.

The isocontours of vorticity magnitude in Figure 5.7 and those complete of white velocity vectors in the more detailed Figure 5.8 show the instantaneous spacing of the vorticity structures: note the smaller streamwise vortex located just below $z^+ = 75$ and the larger one above $z^+ = 150$ rotating in opposite directions. The red contour regions (high vorticity magnitude) in the Figure represent "splats" of relatively fast downward moving fluid on the lower wall caused by counter rotating quasi-streamwise vortices. Visual inspection of several instantaneous fields confirms the characteristic spacing of 100 wall units.

Figure 5.9 illustrates the global pattern of streamwise vorticity (green and yellow isosurfaces represent streamwise vorticity with opposite sign), counter rotating vorticity structures are often paired in the spanwise direction with a marked tendency for inducing vorticity of the opposite sign also below the individual structures in the viscous sublayer ($y^+ < 5$).

As discussed later in Chapter 7 the quasi-streamwise vorticity structures have a strong influence on the near-wall flame behaviour and the presence of a spanwise row of these is important to observe the effect of adjacent vorticity structures on the flame brush[6].

[6]Previous DNS of turbulent flame-wall interactions are limited to the minimal box of Jiménez and Moin (1991) and this fact makes difficult the observation of the combined effects of two adjacent structures, see Bruneaux *et al.* (1996) and Alshaalan and Rutland (1998)

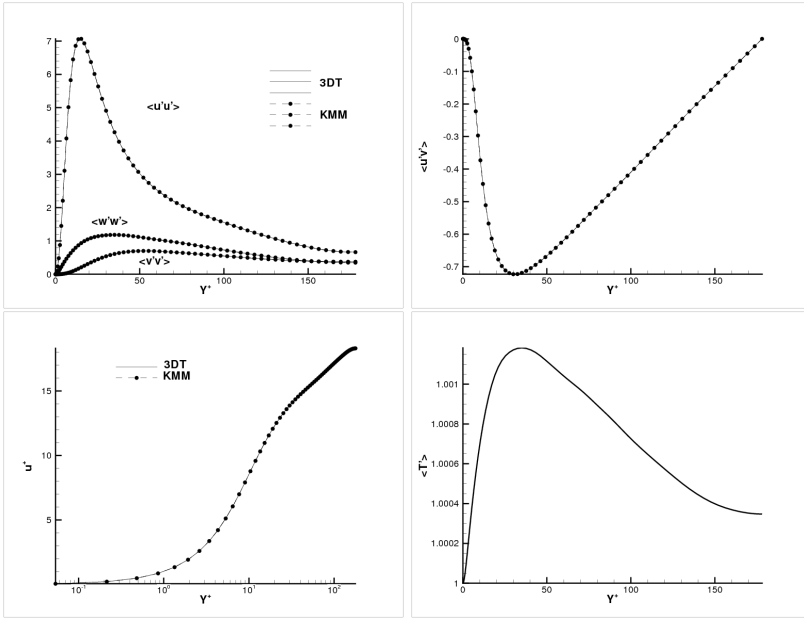

Figure 5.10: Turbulent channel flow at $Re_\tau = 180$: averaged Reynolds stresses, adimensional mean velocity profile (normalized by the shear velocity) and averaged temperature fluctuation (normalized by the wall temperature).

5.3.2 Statistical Analysis

Because of the relatively small box dimensions reliable statistics are obtained sampling the data at temporally uncorrelated "snapshots" of the turbulent field. Samples of the solution are collected with time intervals comparable with the "outer" or large structures time unit $t_{LE} = H/U_0$ or $36.25\,\mu s$, see Andersson and Kristoffersen (1992). A time interval of $18\,\mu s$ is chosen in the present case and this results in a total number of 120 samples available for the statistical analysis of the inert case.

Results from single-point time-averaged, spatially-averaged (in the homogeneous directions) correlations show good agreement with the reference KMM case and are presented in Figure 5.10.

Spatially and temporally averaged two-points correlations are also extracted from the DNS database in order to confirm the visual observations of the previous Section and are showed in Figures 5.11. All correlations of

fluctuating quantities are normalized by their maximum rms values. The negative local minimum at an average spanwise spacing of 35 wall units for the wall-normal velocity fluctuation correlation confirms the average streamwise vortex radius of about 15 wall units already observed in KMM. The weaker positive local maximum at a spanwise spacing of 100 wall units is also in good accordance with the visual observations mentioned in the previous Section and with the existing experimental and computational evidence about boundary layer turbulent flows. Finally, Figure 5.12 illustrates the fact that the streamwise correlation of the streamwise velocity fluctuation does not decay to zero within half of the computational domain length in that direction: this is due to the limited size of the computational box in the homogeneous streamwise direction, the relatively short time interval between samples and to the large streamwise extension of the near-wall vorticity structures.

5.4 Inert Turbulent Channel: Conclusions

Two-dimensional direct simulations of fully developed inert turbulent plane channel flow clearly show the inadequacy of the turbulent wall boundary layer representation in a 2-D domain where the mechanisms for near-wall turbulence production by quasi-streamwise vorticity structures located above the viscous sublayer are absent. Results from fully three-dimensional direct simulations of channel turbulence are in good agreement with the generally accepted knowledge about turbulent wall boundary layers and compare well with the statistics reported in the literature. On the basis of these results it is concluded that the present version of the S3D code is able to correctly represent wall bounded turbulent flows and the velocity fields computed in the inert case can be used to specify the velocity fluctuations at the inflow boundary of the reactive case, see Chapter 7 for a detailed discussion about this topic.

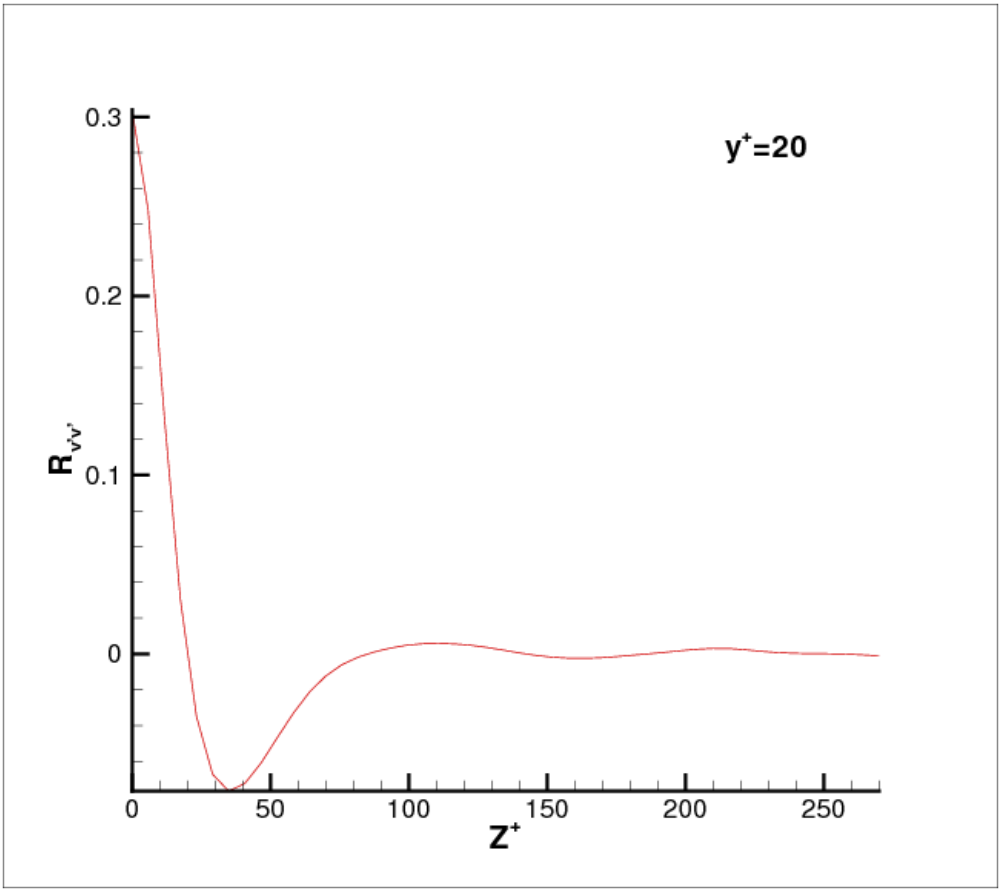

Figure 5.11: Turbulent channel flow at $Re_\tau = 180$: two-point spanwise correlation of wall-normal velocity fluctuation.

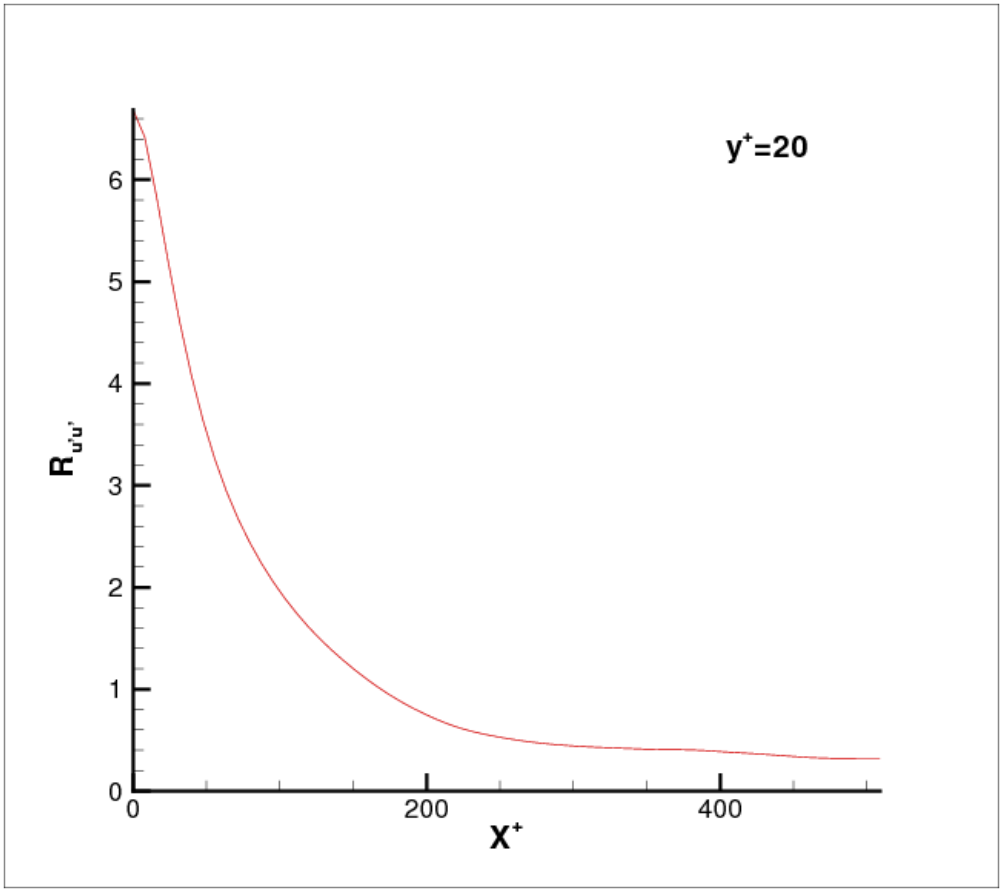

Figure 5.12: Turbulent channel flow at $Re_\tau = 180$: two-point streamwise correlation of streamwise velocity fluctuation.

6 Laminar Flame-Wall Interaction

The simplest configuration for the study of combustion processes is represented by the laminar flames. Laminar flames are classified in two groups: a laminar flame is named *premixed* when the combustion front propagates relative to a mixture containing both fuel and oxidant; *Non-premixed* or *diffusion* laminar flames are characterized instead by a stationary combustion zone where the reactants, previously separate, come in contact and react. In the context of this work, premixed flames, both laminar and turbulent, are studied, therefore only the physical characteristic of this type of flame configuration is briefly described in the following discussion. For a detailed description of diffusion flames see Warnatz *et al.* (1999).

6.1 Laminar Premixed Flames

In this section several important quantities usually employed in the characterization of premixed combustion processes are derived in the case a freely propagating premixed laminar flame. Some additional quantities, useful for the analysis of flame-wall interactions and quenching of a flame approaching a solid wall are also introduced.

6.1.1 Freely Propagating Flames

One important quantity in the description of freely propagating laminar premixed flames is the *laminar flame speed* that, for equal thermal and mass diffusivities ($Le \sim 1$), is defined as:

$$S_l = \sqrt{\frac{D_f}{\tau_c}} \tag{6.1}$$

where $\tau_c \sim 1/k$ is a chemical reaction time scale whose value is inversely proportional to the global reaction velocity k, the global analogous to the elementary reaction velocities of equations 2.35, while D_f is a diffusion velocity characteristic of the flame (representing either thermal or mass

diffusion, λ or D, assumed to be equal). A *laminar flame thickness* can now be estimated as:

$$\delta_l = \sqrt{\frac{\lambda_u}{\rho_u c_{p,u} S_l}} \tag{6.2}$$

the subscript u implies that the relevant quantities are evaluated in the unburnt mixture. The estimate δ_l for the flame thickness is a quite "crude" one, obtained from an order-of-magnitude approach. If the temperature profile across a laminar premixed flame is known from measurements or computations, a considerably better estimate of the flame thickness is obtained as:

$$\delta_l^0 = \frac{T_b - T_u}{max\left(\frac{\partial T}{\partial x}\right)} \tag{6.3}$$

where T_b and T_u are the temperatures in the burnt and unburnt gases respectively and x is the spatial direction of the laminar flame propagation.

Once characteristic flame velocity and length scales are defined, it is also convenient to introduce a characteristic flame time as follows:

$$t_l = \frac{\delta_l^0}{S_l} \tag{6.4}$$

6.1.2 Confined Flames

In the case of a laminar premixed flame propagating toward a solid "cold" wall, the distance of the flame from the wall x is usually adimensionalized by the characteristic flame thickness. This normalization results in the local *Peclet number*:

$$Pe = \frac{x}{\delta_l} \quad or \quad Pe = \frac{x}{\delta_l^0} \tag{6.5}$$

As the laminar flame approaches the solid wall, the large temperature difference between the combustion zone (assumed at or near $T_a \sim 2000\,K$, the adiabatic flame temperature) and the wall surfaces (T_w in the range 300 K - 800 K) induces a consequently large energy flux into the wall, the *wall heat flux*:

$$\Phi_w = -\lambda \left(\frac{\partial T}{\partial x}\right)_w \tag{6.6}$$

where the temperature gradient is evaluated at the wall and λ is the thermal conductivity of the gas mixture. A convenient normalization of the wall heat

flux is achieved by scaling it with the flame *flame power* (heat release per unit time and unit flame surface):

$$F = \frac{|\Phi_w|}{\rho_u S_l c_{p,mix}(T_b - T_u)} \tag{6.7}$$

The wall acts on the flame as a heat sink and depletes it of thermal energy, at a certain distance from the wall the flame *quenches* and the wall heat flux reaches its maximum. The quenching distance x_Q and the flame thickness at quenching δ_Q define a quenching Peclet number:

$$Pe_Q = \frac{x_Q}{\delta_Q} \tag{6.8}$$

and a dimensional quenching heat flux:

$$\Phi_Q = -\lambda \frac{T_a - T_w}{x_Q} \tag{6.9}$$

or in adimensional form:

$$F_Q = \frac{T_a - T_w}{T_a - T_u} \cdot \frac{1}{Pe_Q} \tag{6.10}$$

In the absence of a thermal boundary layer between the wall and the near-wall unburnt mixture $T_u \sim T_w$ and the adimensional quenching heat flux can be approximated by the inverse of the quenching Peclet number $F_Q \sim 1/Pe_Q$. The quenching time t_Q is commonly adimensionalized by scaling with the characteristic flame time obtaining $T_Q = t_Q/t_l$.

6.2 Direct Simulations of Laminar Flame-Wall Interaction

Direct simulations of premixed laminar flame-wall interaction are not considered any longer computationally very expensive on modern computers. The physical characteristics of the process are correctly represented by a one-dimensional approximation in the case of the flame front traveling toward the wall along the wall-normal direction, the head-on quenching (HOQ) configuration (see Figure 1.8). The intrinsic simplicity of the one-dimensional configuration allows detailed investigation and hopefully better understanding of the effects of different physical assumptions made in

the problem formulation: the impact of thermal diffusion and wall temperature, for example, on the transient process of flame quenching and on the wall heat flux Φ, is more easily evaluated when the complication of multi-dimensionality is avoided. Moreover, one-dimensional simulations are computationally "light" and allow the use of complicated chemical kinetic mechanisms characterized by many species and elementary reactions for a correct representation of combustion process.

6.2.1 Previous Work

As mentioned in Chapter 1, experimental investigation of flame-wall interaction is very challenging because of the tiny length and time scales of the transient phenomenon and reported results are characterized by a considerable spread. However, several numerical studies of laminar flame-wall interactions are found in the literature for both simple and detailed gas-phase chemical kinetics, inert and reacting wall surfaces; there seems to be wide agreement on a quenching Peclet number value for hydrocarbon flames of order 3, which implies a value of 0.3 for the adimensional wall heat flux $F_Q \sim 1/Pe_Q$, see Westbrook *et al.* (1981), Hocks *et al.* (1981), Vlachos *et al.* (1993), Popp *et al.* (1996), Popp and Baum (1997), Egolfopoulos *et al.* (1997), Ezekoye (1998), Hasse *et al.* (2000). Interestingly, Dabireau *et al.* (2003) reports quite different values of the characteristic parameters for hydrogen flames with values of $Pe_Q = 1.7$ and $F_Q = 0.129$ which are notably different from those obtained earlier for hydrocarbon flames quenching[1]. Wide agreement is also found in numerical simulations about the wall temperature effects on the maximum wall heat flux and quenching distance: the generally reported trend is that Pe_Q decreases and Φ_Q increases with increasing T_w, the flame manages to get closer to the wall before being quenched and this in turn produces a steeper temperature gradient that results in larger heat flux.

6.2.2 Case Description And Results

Eight cases characterized by three different wall temperatures and the inclusion (or lack of) transport cross effects are reported here. The one-dimensional domain in the simulations has a total length L of $2\,mm$. Conditions corresponding to an isothermal wall at fixed temperatures T_w equal

[1]Note also that the approximation $F_Q \sim 1/Pe_Q$ does not seem to hold for hydrogen flames and seems to fail with the reported values of F_Q and Pe_Q

to $300\,K$, $750\,K$ and $800\,K$ are enforced at its left boundary for $x = 0\,mm$ and an open non-reflecting boundary is placed on the right boundary at $x = 2\,mm$. 300 grid nodes are used, giving a spatial resolution of $6.6\,\mu m$ which is enough to resolve the flame structures with more than 10 grid nodes. The initial conditions are computed with CHEMKIN PREMIX for an hydrogen-air mixture characterized by *equivalence ratios* of $\Xi = 1$ and $\Xi = 1.5$. The PREMIX solution is then fed into the DNS code which solves the one-dimensional system of equations 2.1-2.4 coupled to the chemical kinetics mechanism of Table 2.1 and simulates the flame propagation toward the solid isothermal wall.

The table below summarize the assumptions adopted in the different test cases simulated and their effects on the characteristic quantities. Note that, since there is no single definition of flame position in a detailed chemistry context, the spatial position of the peak of the fuel reaction rate is assumed to be the "marker" for flame-wall distance estimates. On the bottom line, the results of Dabireau *et al.* (2003) for a $H_2 + O_2$ flame are listed for comparison:

$Case$	T_w	$Soret$	Ξ	Pe_Q	$\Phi_Q(MW/m^2)$	F_Q	T_Q
$LW1$	300 K	No	1.0	1.6	0.75	0.11	26.1
$LW7$	750 K	No	1.0	1.4	1.15	0.11	29.3
$LW5$	750 K	No	1.5	1.3	1.25	0.12	32.3
$LW2$	800 K	No	1.0	1.2	1.45	0.14	33.2
$LW3$	300 K	Yes	1.0	1.7	0.61	0.1	28.1
$LW8$	750 K	Yes	1.0	1.7	1.2	0.13	32.5
$LW6$	750 K	Yes	1.5	1.4	1.23	0.12	32.7
$LW4$	800 K	Yes	1.0	1.3	1.4	0.14	33.8
DAB	750 K	Yes	1.0	1.7	NA	0.13	32.7

The computed values that are reported on the above table for the various characterist quantities show good agreement with the generally observed trends of increasing wall heat flux and decreasing quenching distance for

increasing T_w. The effect of thermal diffusion together with the steep thermal gradient in the near-wall region contributes to depletion of radicals from the propagating flame increasing its quenching distance, decreasing its velocity and wall heat flux. Moreover, the values of the characteristic parameters (F_Q,Pe_Q etc.) reported in Dabireau *et al.* (2003) for hydrogen flames are confirmed by the present simulations, this fact strengthens the confidence in the results of both studies and also contribute to the generally accepted idea that hydrogen is a fuel with characteristics very different from those of other more common hydrocarbon fuels.

Figures 6.1-6.6 show the laminar flame structures, as the flame freely propagates in the center of the domain still "far" from the wall, through plots of the major, intermediate and radical species profiles of mass fraction and reaction rates. The global heat release rate (red line) is also plotted to mark the exothermic reaction zone. As it is evident from the plots both the species concentration profiles and the species reaction rates profiles are perfectly resolved on the grid.

In order to give some of the transient details of the flame quenching process, temperature profiles are shown for several times in Figure 6.7, the effect of thermal diffusion in reducing the flame propagation speed is clearly visible. The time evolution of all species mass fractions is shown in Figures 6.8-6.15, while Figures 6.16-6.18 show the time evolution of the reaction rates of fuel H_2 and radical species H and O. The large negative values of the radical reaction rates at quenching represent radical consumption by low activation energy exothermic recombination reactions that take place very close to the wall. They form the intermediate species HO_2 and H_2O_2 that, in turn, show positive peaks at the wall having several times larger values than in the free propagating flame front. This fact is also in agreement with the results of Dabireau *et al.* (2003) that also reports very high consumption of radicals at the wall and the consequent large production of intermediate species.

6.2.3 Summary of 1D HOQ Simulations

Results from one-dimensional simulations of flame-wall interaction with the S3D code are in agreement with the generally accepted theory about the wall-quenching process and compare well with analogous data for hydrogen flames from Dabireau *et al.* (2003). The capability of the S3D code to correctly represent flame-wall interactions in the one-dimensional configuration, resulting in values of the characteristic quantities that are close to

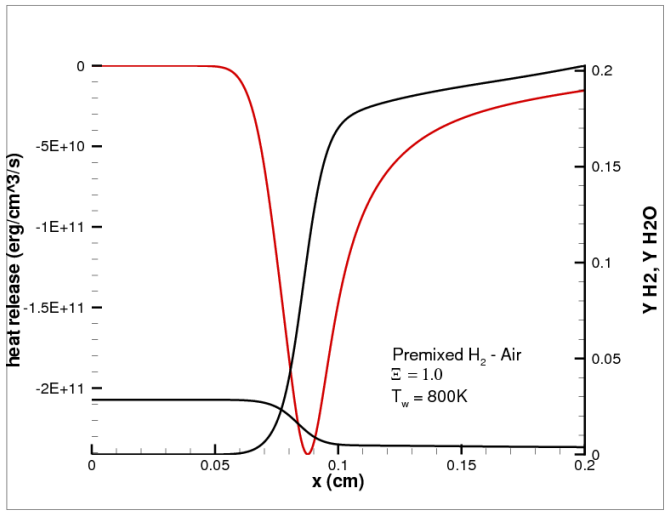

Figure 6.1: Structure of 1-D premixed laminar flame(LW2): heat release (red line) and major species (black lines).

those found in the literature, contributes to build confidence in the multi-dimensional simulations reported in the next Chapter.

The effects of thermal diffusion and of wall temperature appear to be important in respect to the quenching distance and maximum wall heat flux. Neglecting the Soret effect increases the heat flux into the wall by 10% and flame speed by $2-3\%$, at the same time decreasing the quenching distance by $5-10\%$. However, results also show that the process of flame-wall interaction is *qualitatively* unchanged by the inclusion (or lack) of the Soret effect. This fact partially justifies the approach chosen in the expensive three-dimensional calculations where the Soret effect is conveniently neglected (its inclusion is computationally very expensive). The maximum wall heat flux computed in the three-dimensional simulations can be adjusted to a lower value as suggested by the one-dimensional parametric study or, if high accuracy (less than 10% uncertainty) in the estimates of the maximum wall heat flux is necessary, a direct simulation that takes into account the Soret effect should be considered instead. In the present context focus is on observing the wall heat flux spatial pattern and its relation to the flame-turbulence interaction.

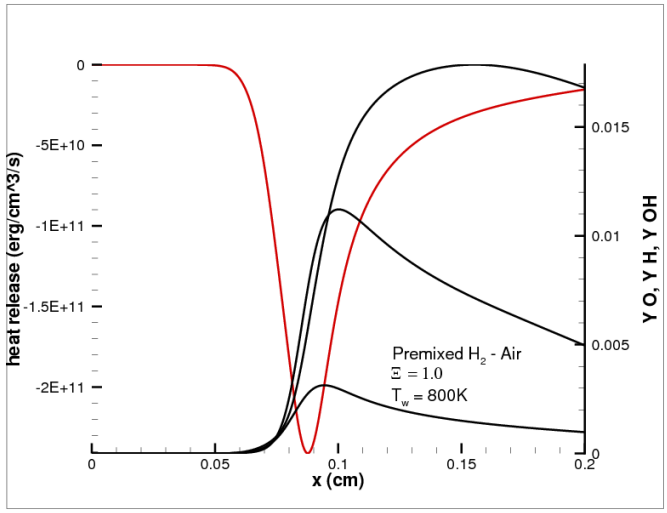

Figure 6.2: Structure of 1-D premixed laminar flame(LW2): heat release (red line) and radical species (black lines).

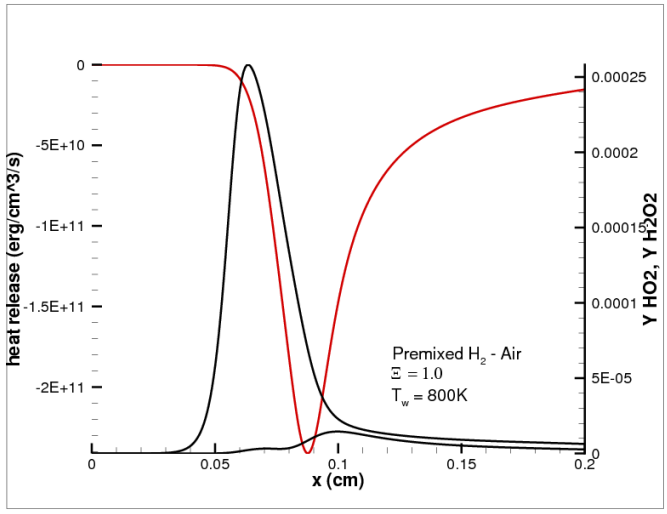

Figure 6.3: Structure of 1-D premixed laminar flame(LW2): heat release (red line) and intermediate species (black lines).

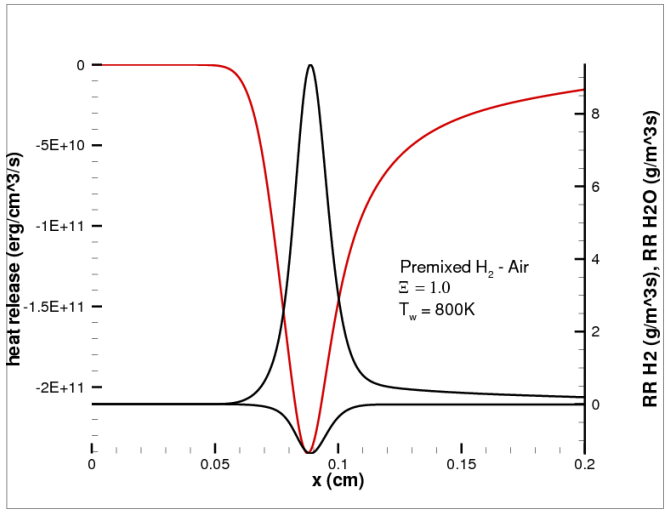

Figure 6.4: Structure of 1-D premixed laminar flame(LW2): heat release (red line) and major species reaction rates (Black Lines).

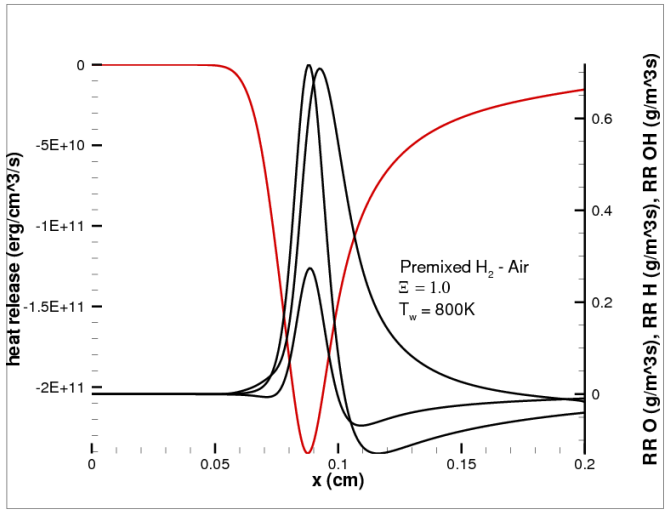

Figure 6.5: Structure of 1-D premixed laminar flame(LW2): heat release (red line) and radical species reaction rates (Black Lines).

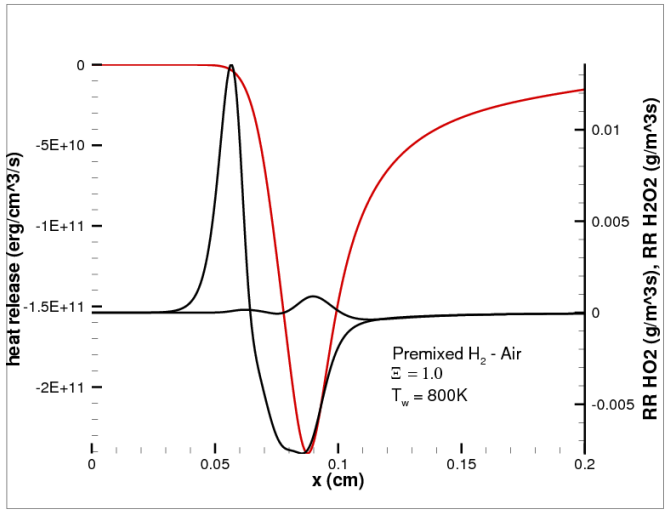

Figure 6.6: Structure of 1-D premixed laminar flame(LW2): heat release (red line) and radical species reaction rates (Black Lines).

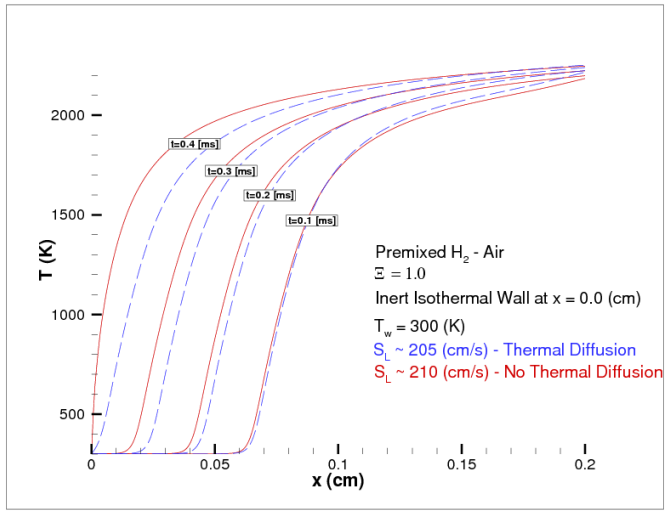

Figure 6.7: Flame propagation toward the wall(LW1,LW3): the effect of thermal diffusion on the laminar flame velocity is evident from the temperature profiles.

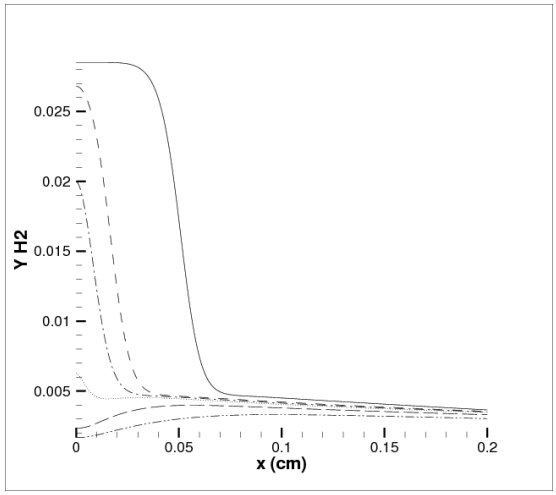

Figure 6.8: Head-on quenching(LW4): mass fraction profiles of H_2 at different times. Solid line $t = 7.4e^{-05}\,s$; Dash line $t = 1.0e^{-04}\,s$; Dash-Dot line $t = 1.05e^{-04}\,s$; Dot line $t = 1.1e^{-04}\,s$; Long-Dash line $t = 1.25e^{-04}\,s$; Dash-Dot-Dot line $t = 1.5e^{-04}\,s$.

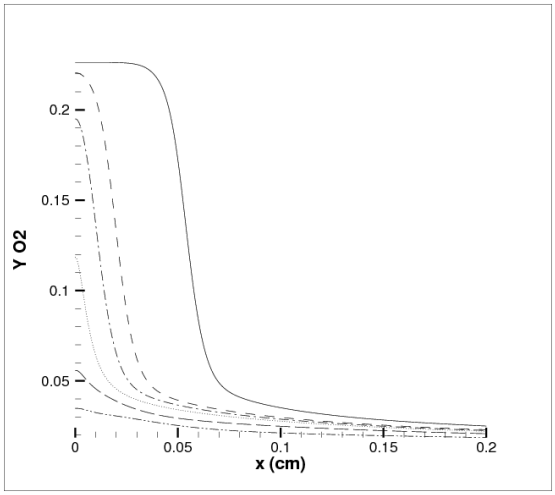

Figure 6.9: Head-on quenching(LW4): mass fraction profiles of O_2 at different times. Solid line $t = 7.4e^{-05}\,s$; Dash line $t = 1.0e^{-04}\,s$; Dash-Dot line $t = 1.05e^{-04}\,s$; Dot line $t = 1.1e^{-04}\,s$; Long-Dash line $t = 1.25e^{-04}\,s$; Dash-Dot-Dot line $t = 1.5e^{-04}\,s$.

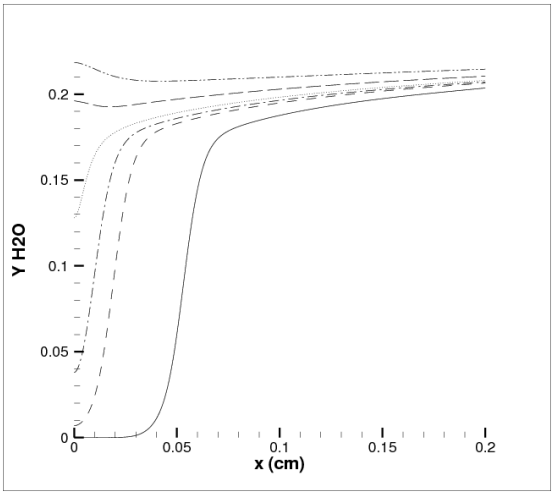

Figure 6.10: Head-on quenching(LW4): mass fraction profiles of H_2O at different times. Solid line $t = 7.4e^{-05}\,s$; Dash line $t = 1.0e^{-04}\,s$; Dash-Dot line $t = 1.05e^{-04}\,s$; Dot line $t = 1.1e^{-04}\,s$; Long-Dash line $t = 1.25e^{-04}\,s$; Dash-Dot-Dot line $t = 1.5e^{-04}\,s$.

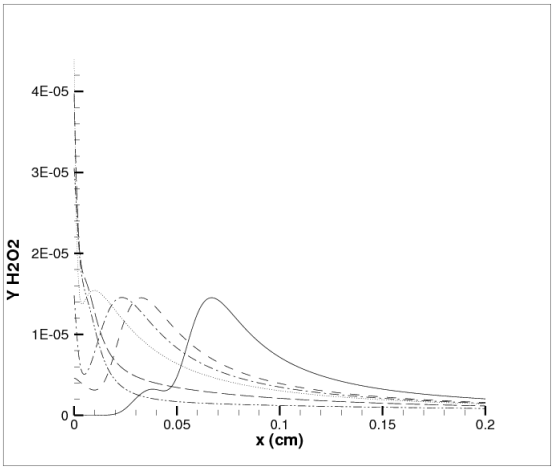

Figure 6.11: Head-on quenching(LW4): mass fraction profiles of H_2O_2 at different times. Solid line $t = 7.4e^{-05}\,s$; Dash line $t = 1.0e^{-04}\,s$; Dash-Dot line $t = 1.05e^{-04}\,s$; Dot line $t = 1.1e^{-04}\,s$; Long-Dash line $t = 1.25e^{-04}\,s$; Dash-Dot-Dot line $t = 1.5e^{-04}\,s$.

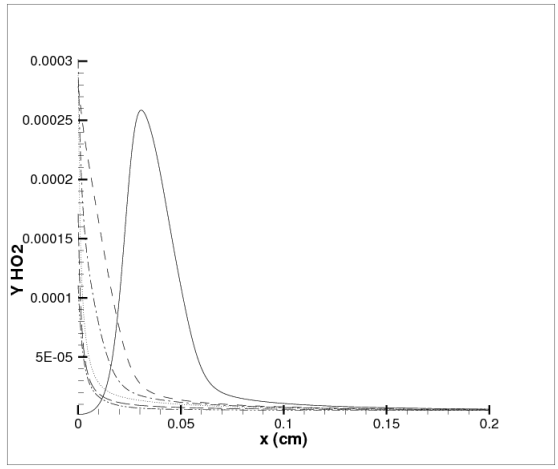

Figure 6.12: Head-on quenching(LW4): mass fraction profiles of HO_2 at different times. Solid line $t = 7.4e^{-05}\,s$; Dash line $t = 1.0e^{-04}\,s$; Dash-Dot line $t = 1.05e^{-04}\,s$; Dot line $t = 1.1e^{-04}\,s$; Long-Dash line $t = 1.25e^{-04}\,s$; Dash-Dot-Dot line $t = 1.5e^{-04}\,s$.

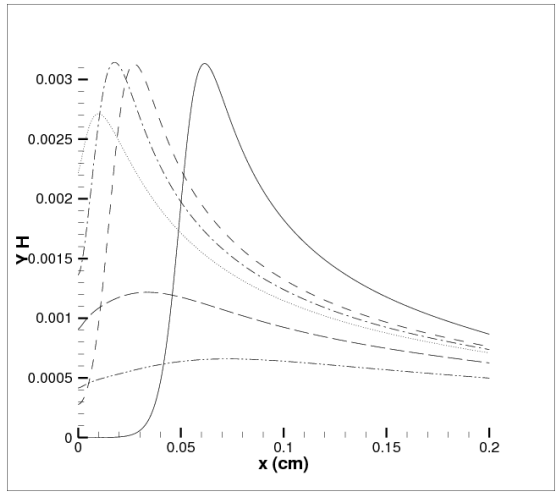

Figure 6.13: Head-on quenching(LW4): mass fraction profiles of H at different times. Solid line $t = 7.4e^{-05}\,s$; Dash line $t = 1.0e^{-04}\,s$; Dash-Dot line $t = 1.05e^{-04}\,s$; Dot line $t = 1.1e^{-04}\,s$; Long-Dash line $t = 1.25e^{-04}\,s$; Dash-Dot-Dot line $t = 1.5e^{-04}\,s$.

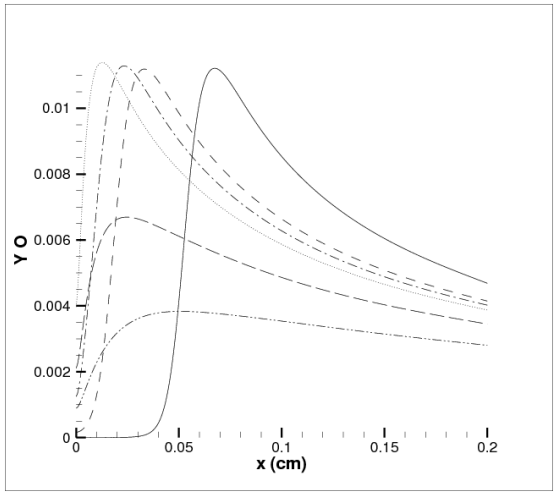

Figure 6.14: Head-on quenching(LW4): mass fraction profiles of O at different times. Solid line $t = 7.4e^{-05}\,s$; Dash line $t = 1.0e^{-04}\,s$; Dash-Dot line $t = 1.05e^{-04}\,s$; Dot line $t = 1.1e^{-04}\,s$; Long-Dash line $t = 1.25e^{-04}\,s$; Dash-Dot-Dot line $t = 1.5e^{-04}\,s$.

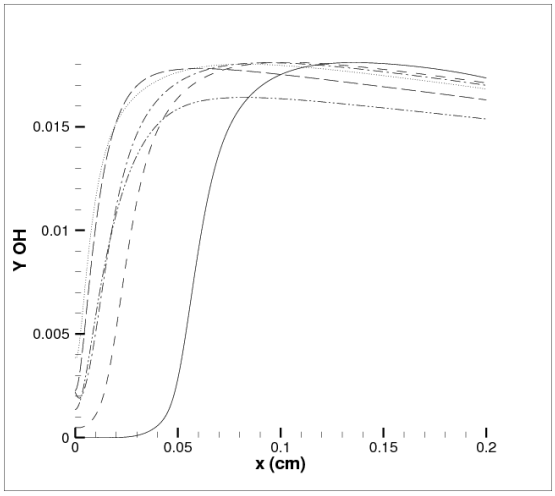

Figure 6.15: Head-on quenching(LW4): mass fraction profiles of OH at different times. Solid line $t = 7.4e^{-05}\,s$; Dash line $t = 1.0e^{-04}\,s$; Dash-Dot line $t = 1.05e^{-04}\,s$; Dot line $t = 1.1e^{-04}\,s$; Long-Dash line $t = 1.25e^{-04}\,s$; Dash-Dot-Dot line $t = 1.5e^{-04}\,s$.

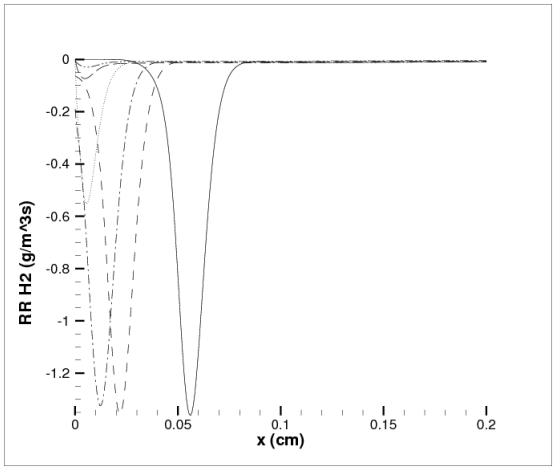

Figure 6.16: Head-on quenching(LW4): reaction rate profiles of H_2 at different times. Solid line $t = 7.4e^{-05}\,s$; Dash line $t = 1.0e^{-04}\,s$; Dash-Dot line $t = 1.05e^{-04}\,s$; Dot line $t = 1.1e^{-04}\,s$; Long-Dash line $t = 1.25e^{-04}\,s$; Dash-Dot-Dot line $t = 1.5e^{-04}\,s$.

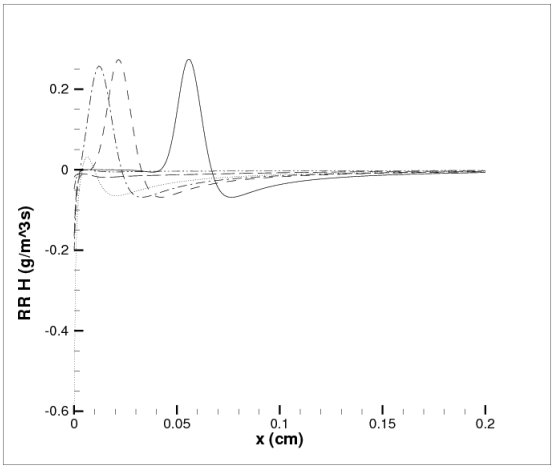

Figure 6.17: Head-on quenching(LW4): reaction rate profiles of H at different times. Solid line $t = 7.4e^{-05}\,s$; Dash line $t = 1.0e^{-04}\,s$; Dash-Dot line $t = 1.05e^{-04}\,s$; Dot line $t = 1.1e^{-04}\,s$; Long-Dash line $t = 1.25e^{-04}\,s$; Dash-Dot-Dot line $t = 1.5e^{-04}\,s$.

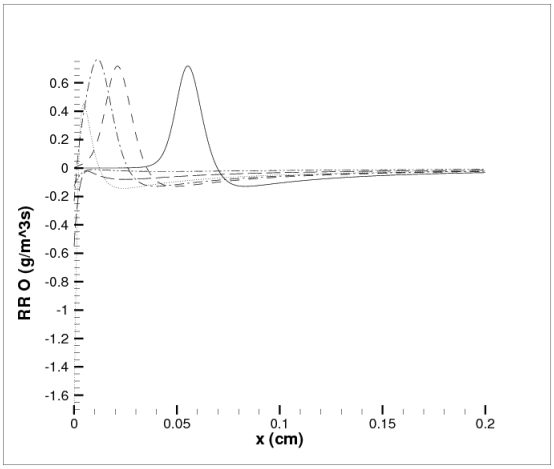

Figure 6.18: Head-on quenching(LW4): reaction rate profiles of O at different times. Solid line $t = 7.4e^{-05}\,s$; Dash line $t = 1.0e^{-04}\,s$; Dash-Dot line $t = 1.05e^{-04}\,s$; Dot line $t = 1.1e^{-04}\,s$; Long-Dash line $t = 1.25e^{-04}\,s$; Dash-Dot-Dot line $t = 1.5e^{-04}\,s$.

7 Turbulent Flame-Wall Interaction

The one-dimensional direct simulations of laminar flame-wall interaction described in Chapter 6 are relatively straightforward to perform and, because of the "low" computational cost of the flow solver in 1-D, detailed transport and chemistry models can be used for an accurate characterization of the transient process. Moreover, the laminar flame interaction with the wall is governed only by (almost completely separable) chemical and diffusion processes, this contributes to a relative ease in the understanding of this transient phenomenon. If the flame-wall interaction takes place in a turbulent flow, the problem becomes immediately much more difficult to understand because of the complex coupled effects of turbulence, combustion and presence of the wall. Each of these three phenomena feels the influence of the other two and also influence them!

7.1 Turbulence-Flame-Wall Coupling

Following the approach used in Poinsot and Veynante (2001), the complex picture can be summarized by describing the different effects separately:

- Turbulence acts on the flame by convective wrinkling and strain. Wrinkling improves the combustion rate by enhanced mixing of hot products and cold reactants and, by doing so, increases the flame propagation speed. Turbulence-induced flame strain "thins the flame out", increasing the heat loss, and may result in quenching and extinction for high strain levels. The *turbulent flame speed* S_t[1] increases almost linearly with increasing turbulent fluctuations u' (the wrinkling effect is positively acting on the flame) until the turbulence level becomes so high that excessive strain causes flame extinction "tearing it apart" (the heat loss to the surroundings is larger than the heat released by chemical reactions). Turbulence acts also on the wall because turbulent convection associated to the near-wall vorticity structures pushes

[1] Several models proposed to estimate the turbulent flame speed directly relate it with the mixture characteristic laminar flame speed and the turbulent fluctuations level of the flow, see Warnatz *et al.* (1999).

the flame toward the wall or away from it inducing strong spatial variations in the wall heat flux (these are in turn responsible for large thermal stresses that shorten the lifetime of the solid material).

- The flame modifies the turbulence level of the incoming flow to lower values by reducing its Reynolds number: this is due to the large increase in the fluid's viscosity caused by the high flame temperatures. The flame acts also on the wall usually by causing large thermal energy transfer into it that can change the wall material properties.

- The presence of the wall induces turbulent production by generating strain through the mean shear induced on the flow and at the same time damps the wall normal components of turbulent fluctuations resulting in the strong anisotropic character of boundary layer turbulence. The wall influence the flame too acting as a heat sink, depleting it of energy and quenching it.

Understanding the details of this intricate picture is not an easy task. Direct numerical simulation is a powerful tool that allows detailed reproduction of this complex interaction and creation of databases consisting of spatial and temporal evolution of all involved quantities. The information contained in the databases has to be extracted in convenient ways. In the present context two approaches to the analysis of DNS data are considered. One approach consists in examining the instantaneous reacting flow field through advanced visualization techniques in order to obtain qualitative and quantitative information about the transient character of the flame-wall interaction process; the second approach makes use of statistical correlations in order to obtain a quantitative picture of the cross effects between near-wall turbulence and flame propagation. Advanced visualization of complex three-dimensional data fields is a challenging task but its intensive use has demonstrated over the years the importance of visualization in understanding of the physics of three-dimensional phenomena as boundary layer turbulence, see Robinson (1991) for a relevant example.

This Chapter focuses on the visual analysis of instantaneous data fields from DNS of turbulent flame-wall interaction, some statistical correlations extracted from the database are also included. First, the challenges related to the specification of realistic inflow turbulence data for spatially evolving reactive flows are described. Then, results from two-dimensional direct simulations of a v-shaped premixed flame anchored in a plane channel and propagating in 2-D synthetic turbulence are presented; the following

section illustrates and discusses instantaneous and preliminary averaged data extracted from the database of a fully three-dimensional direct simulations of the same v-shaped premixed flame, anchored, this time, in realistic Poiseuille flow turbulence. Finally, some conclusions drawn from the data presented in this Chapter are discussed together with suggestions for further work.

7.2 Non-Homogeneous Turbulent Channel

The fully developed turbulent channel flow briefly described in Chapter 5 is characterized by two homogeneous directions (the streamwise, x, and the spanwise, z, directions) and one non-homogeneous direction (the wall normal one, y). This fact allows, in that case, the use of periodic boundary conditions in the x-direction under the assumption that the simulated boundary layer flow is fully developed. The z-direction is also treated with periodic boundary conditions under the assumption that the channel is also infinitely wide and that there are no "border" effects.

If a flame is placed in the channel, it propagates into the flowing fluid converting the mixture of reactants into products. The strong heating of the fluid associated to the chemical reactions modifies to great extent some of the fluid's properties like temperature, density and viscosity, thereby changing also some of the flow properties, as the turbulent fluctuation level and its characteristic Reynolds number. The flow can no longer be considered homogeneous in the streamwise direction because there is now a strong streamwise variation of many of its properties. This fact implies that periodic boundary conditions are not usable any longer in the streamwise direction but time-dependent turbulent inflow conditions have to be specified at the inflow boundary. The flow evolution downstream of the inlet greatly depends on the fluctuating velocity field specified at the boundary: it is therefore important to specify realistic turbulent fluctuations that represent as well as possible a *realistic* turbulent field.

7.2.1 Turbulent Subsonic Inflow for Reactive DNS

Specifying realistic turbulent fluctuations at the inflow boundary of the computational domain is a difficult task: computationally cheap random-noise generation methods produce unrealistic turbulent correlations and a long "development section" is necessary before realistic turbulence is

achieved in the channel (the overall cost of these methods is not *so* low after all!), more advanced methods generate more realistic turbulence but they are often costly, involving even expensive auxiliary direct simulations.

Several different approaches of varying efficacy are reported in the literature, see Lund *et al.* (2003) for a review. The accuracy requirements for the inlet turbulent fluctuations depend to a large extent on the configuration of the flow to be simulated: wall-bounded flows require very accurate specification of the inflow condition, the reason for this is to be found in the intrinsic complexity of near-wall turbulence. As already discussed in Chapters 1 and 5, near-wall turbulence consists of quasi-coherent three-dimensional organized vorticity structures, the complex spatial and phase relationship between velocity components cannot be obtained analytically and require an auxiliary direct simulation of the turbulent channel. For the present simulations with the S3D code, several approaches to generate inflow turbulence are tested and compared.

Random Fluctuations

Generation of de-correlated random fluctuations superimposed to the mean flow field is the simplest method of obtaining fluctuating inflow data, but it produces highly unrealistic turbulent conditions that need a development section of 50 or more boundary layer thicknesses to achieve a fluctuating field that vaguely *resembles* channel turbulence. This approach performs so poorly that it is not considered here.

Fourier Spectrum

More sophisticated is the method of artificially generating an isotropic turbulent field developed by Lee *et al.* (1992) that consists in specifying the fluctuations Fourier spectrum leaving the phase at random. Le *et al.* (1997) extend the method (without great success) to the case of anisotropic turbulence in their simulation of a backward-facing step, successive tests of the same configuration reveal that at least 20 boundary layer thicknesses are necessary before achieving realistic turbulent fields. Given the inaccuracy of this approach in representing turbulent inflow conditions for fully developed channel flow, the Fourier method is used, in the present context, together with the Taylor's hypothesis discussed below, only to generate the synthetic 2-D turbulent inflow field for the two-dimensional simulation of Section 7.3.1 named TW0.

Taylor's Hypothesis: Spatial Sampling

Taylor's hypothesis of *frozen turbulence* states that the temporal evolution of a fluctuating quantity can be related to its spatial evolution by a convection velocity. In mathematical form this relation can be expressed with the following formula:

$$\frac{\partial \xi}{\partial t} = -U_c \frac{\partial \xi}{\partial x} \tag{7.1}$$

where U_c is an appropriate streamwise convection velocity and x is the direction of the mean flow. Equation 7.1 is widely used in laboratory experiments to obtain estimates of the spatial derivatives of the quantity ξ in the direction of U_c from values of the time derivative of the same quantity measured at a fixed location. In determining turbulent velocity fluctuations for the specification of a turbulent inlet, the above formula is used to estimate the time derivatives of ξ needed at the boundary from knowledge of its spatial derivatives in a "frozen" realization of an instantaneous turbulent field, for example, one of those reported in Chapter 5. As already mentioned in Chapter 1, the applicability of Taylor's frozen turbulence hypothesis to compressible flows is studied by Lee *et al.* (1992), they conclude that vorticity and entropy (solenoidal) modes are correctly represented by the use of equation 7.1, the same is not true for the acoustic (dilatation) mode. Piomelli *et al.* (1989) investigate the applicability of Taylor's hypothesis in wall-bounded flows and confirm previous conclusions by Hussain *et al.* (1987) suggesting that the frozen turbulence hypothesis holds except very close to the wall where its failure is caused by the large value of mean shear. The problem of determining the "correct" convection velocity U_c for use in equation 7.1 is addressed in Choi and Moin (1990) while studying convection of pressure fluctuations. The authors suggest for the convection velocity:

$$0.6 \cdot U_0 \leq U_c \leq 0.8 \cdot U_0 \tag{7.2}$$

where U_0 is the channel mean centerline velocity.

The frozen turbulence approach is relatively "cheap" because makes use of only *one* stored turbulent field. It is tested with relative success by Na and Moin (1998) in their direct simulation of a spatially developing boundary layer: in order to reduce the effect of the temporal periodicity intrinsically characterizing the method, they introduce small random modulations of the velocity fluctuations amplitudes (leaving the phase angle unchanged to preserve the spatial structure of the turbulence) and observe that only a "short" development section of 10 boundary layer thicknesses is needed

before obtaining realistic turbulence conditions. Moreover, they report little influence of the chosen convection velocity for values of U_c between $4/5 \cdot U_0$ and U_0.

The relative ease of implementation and low computational requirements of this method balance its few well known drawbacks. The Taylor's hypothesis method is used to obtain turbulent fluctuations at the inflow boundary in one of the two three-dimensional DNS cases (TW1) reported in Section 7.3.2 (the other DNS case, named TW2, uses the more expensive approach described below).

Auxiliary Simulation: Temporal Sampling

The only way of obtaining the correct velocity fluctuations for realistic specification of turbulent inflow boundaries is computing them directly in an auxiliary temporally evolving DNS. This "parallel" DNS has to be configured to match the Reynolds number of the flow field that is wanted for feeding in the principal simulation. The auxiliary code has to store, for nearby time intervals (better if every time step, to reduce temporal interpolation errors), one "slice" of the turbulent field at a fixed streamwise location. Then, this time evolving sequence of slices has to be fed into the principal simulation. Guichard *et al.* (2004) show that, by coupling a spectral incompressible solver with the finite-difference main DNS code, the overhead resulting from the auxiliary simulation is limited to barely 10% of the total cost. This is due to the highly efficient spectral simulation. The S3D code is not coupled to any spectral solver, however, an efficient algorithm is developed for storing and feeding the time-slices from the auxiliary "cold" channel flow into the principal simulation resulting in a overhead of about 20% of the total cost.

7.2.2 Comparison Of Spatial And Temporal Sampling

In the present Section, the last two methods discussed above for generating a turbulent inlet are compared by inspection of the turbulent statistical quantities in the three-dimensional DNS solutions of cases TW1 and TW2: further details about the parameters of the simulations are available in the relative Section. In one of the two simulations (TW1) Taylor's hypothesis is used to specify the time-dependent fluctuating velocity components from spatially evolving data in a "frozen" turbulence box stored on disk, in the other case (TW2) instead, an auxiliary simulation provide a pure temporally

evolving turbulent field that is fed into the computational domain through the inflow boundary.

Figures 7.1-7.6 confirm the previous observation of Hussain *et al.* (1987) and Piomelli *et al.* (1989): applying Taylor's hypothesis to strongly sheared flow produces unrealistic fluctuation level in the near-wall region as clearly seen in the plots of the statistical quantities at $x^+ = 50$, few grid nodes downstream of the inlet boundary. The quantities most affected by the inaccuracy of the boundary specification are the streamwise component of the normal stress and the shear stress. All profiles improve considerably further downstream and already for $x^+ = 100$ all of the lines deviate marginally from the reference case KMM. However, even if at $x^+ = 100$ the turbulent fluctuations level in TW1 has recovered its correct values some uncertainty remains as to if the correct phase relationship in spectral space between the different Fourier modes of the solution has been achieved. Because of this uncertainty, results and conclusions from the first case (TW1 - the run is completed) will be in a later publication compared with data from the second case (TW2 - the run is still running at the time of the writing). Preliminary comparisons give good agreement between TW1 and TW2 in respect to the wall heat flux spatial distribution and maximum values.

7.3 Turbulence Effects On Flame-Wall Interactions

7.3.1 Two-Dimensional Simulations

As already discussed in Section 5.1, turbulence is not sustainable in a two-dimensional domain and a realistic boundary layer is not representable in two spatial dimensions. An inverse cascade transfers energy from higher to lower wave-numbers and small eddies "regroup" and merge into larger eddies until only few large eddies are left, characterized by length scales comparable to the domain size. Moreover, the intrinsic three-dimensional structure of near-wall turbulence, its effect on flame propagation and its interaction with the wall cannot be represented in a two-dimensional domain. However, two-dimensional cases are very useful as a "lightweight" testing platform for parameter studies and code optimization before the fully three-dimensional simulations are started and can, to some extent, provide useful information about the nearly two-dimensional physical processes (as vortex-flame interaction) that take place far from the walls in nearly isotropic conditions. In this Section some salient characteristics of

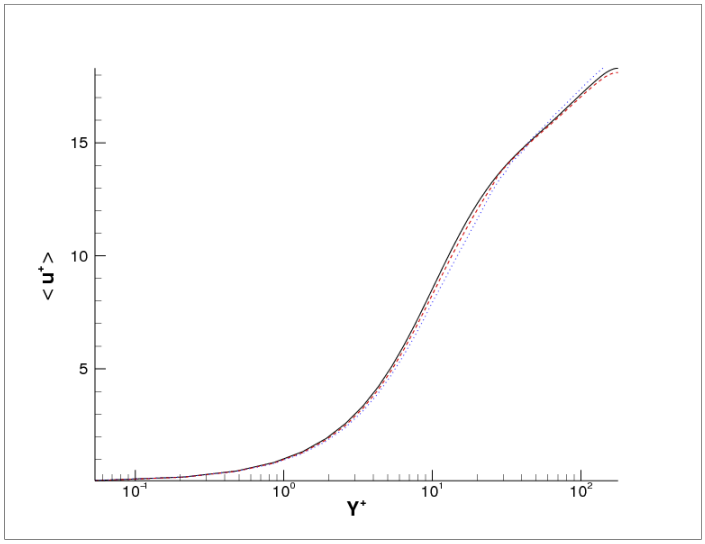

Figure 7.1: Reduced mean velocity profile at $x^+ = 50$: solid black line, KMM; dashed red line, TW2; dash-dot-dot blue line, TW1.

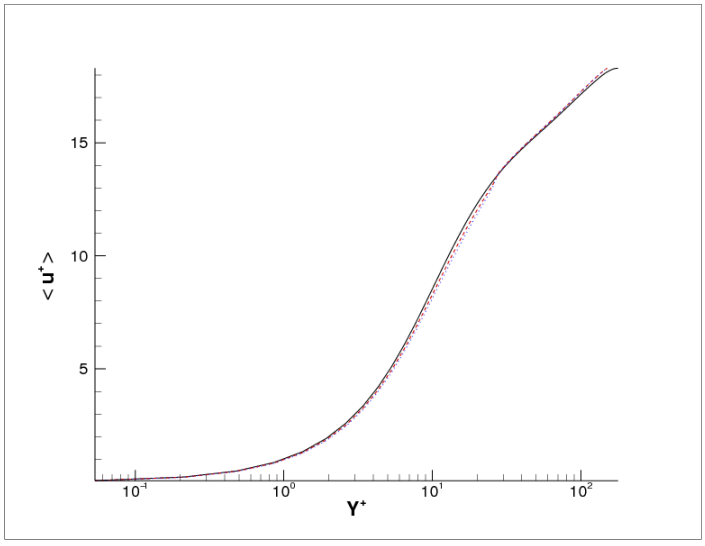

Figure 7.2: Reduced mean velocity profile at $x^+ = 100$: solid black line, KMM; dashed red line, TW2; dash-dot-dot blue line, TW1.

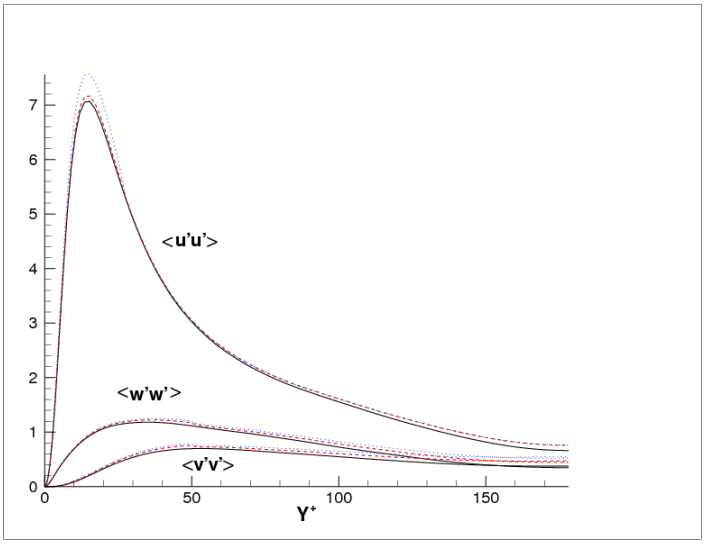

Figure 7.3: Reduced normal stress at $x^+ = 50$: solid black line, KMM; dashed red line, TW2; dash-dot-dot blue line, TW1.

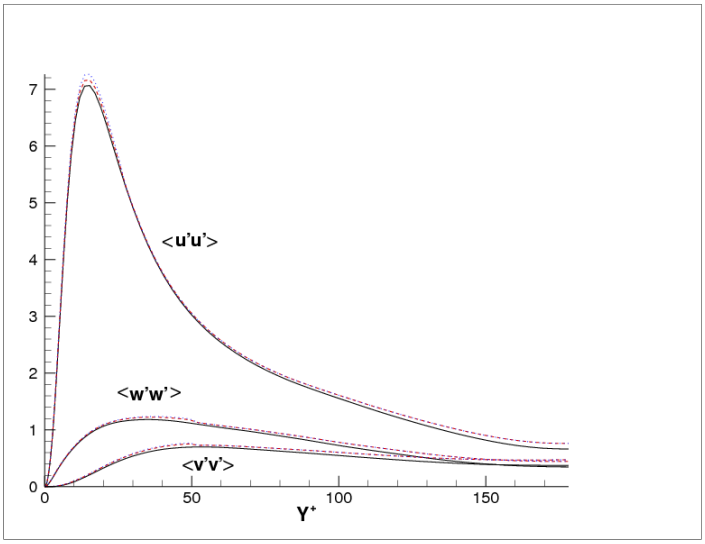

Figure 7.4: Reduced normal stress at $x^+ = 100$: solid black line, KMM; dashed red line, TW2; dash-dot-dot blue line, TW1.

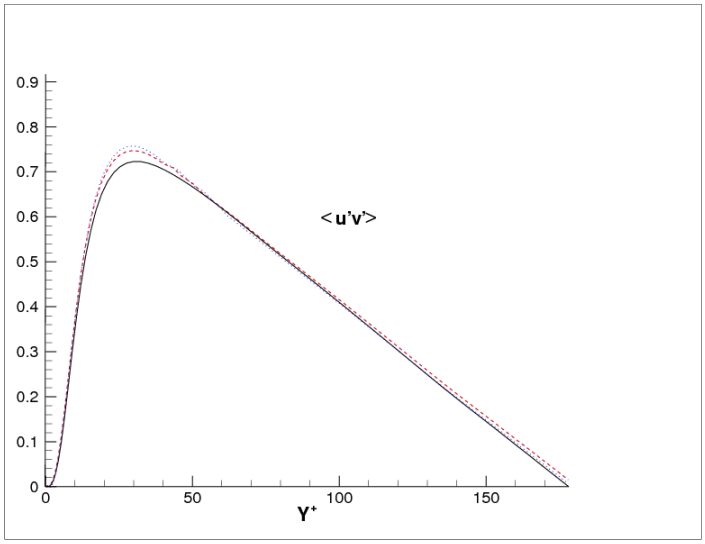

Figure 7.5: Reduced shear stress at $x^+ = 50$: solid black line, KMM; dashed red line, TW2; dash-dot-dot blue line, TW1.

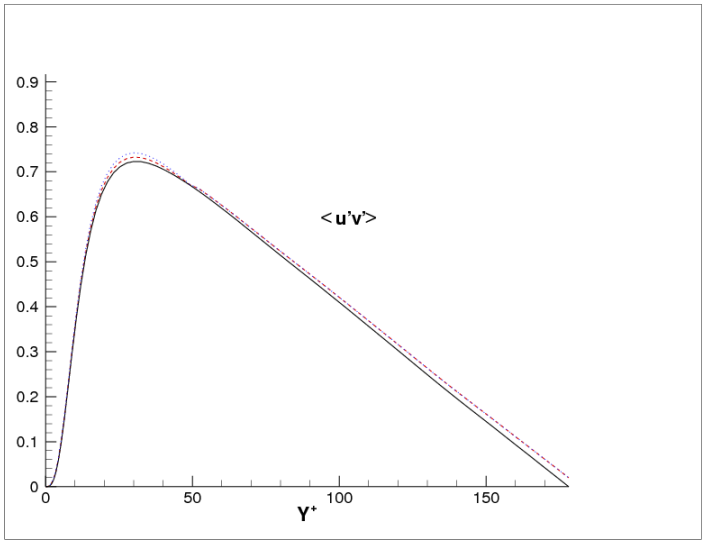

Figure 7.6: Reduced shear stress at $x^+ = 100$: solid black line, KMM; dashed red line, TW2; dash-dot-dot blue line, TW1.

the 2-D flame-wall interaction are briefly illustrated before proceeding to the 3-D simulations.

Case Description

The two-dimensional premixed flame simulation (TW0) is characterized by the same parameters of cases TW1 and TW2 described in Section 7.3.2, the only difference being the total length of the domain that is $8.7\,mm$ instead of $11.6\,mm$ as in the 3-D simulations and the flat 2-D domain not extending in the spanwise direction z of the plane channel. The channel is $5.8\,mm$ wide in the wall normal direction as in the 3-D cases. A turbulent Reynolds number equal to $Re_\tau = 180$ is assumed. This physical situation is approximated as follows in the 2-D computational domain: a compressible turbulent isotropic field obtained by translation of the Passot-Pouquet analytic spectrum to physical space, see Passot and Pouquet (1987), and characterized by zero mean velocity is superimposed on a typical turbulent channel mean velocity profile with the wanted channel centerline velocity. The newly computed velocity field is then passed through a smooth spatial filter to bring all velocity components to zero at the wall. The filtered turbulent velocity field obeys the no-slip condition at the wall and is used as initial condition for the velocity fluctuations in the domain, it is also stored as a "frozen" box from which the time-dependent turbulent inlet can be determined as explained in Section 7.2.1. This procedure for specifying the turbulent inlet gives a very *crude* representation of the turbulent channel (being the velocity fluctuations obtained from an isotropic assumption), which is in fact unrealistic; however, in the context of 2-D channel turbulence, being this unrealistic in itself, the use of computationally more expensive ways of specifying the initial and boundary conditions has little meaning. The centerline velocity is set to $U_0 = 80\,m/s$, this value, for a kinematic viscosity in the cold reactants equal to $\nu = \mu/\rho = 7.3e^{-05}\,m^2/s$ (at $T_u = 750\,K$) and a channel half-width of $2.9\,mm$, results in the target Reynolds number $Re_0 \sim 3200$. The Soret effect is neglected and the walls are assumed isothermal at $T_w = 750\,K$. The total number of grid nodes is $280 \times 200 = 56000$, the grid is stretched in the wall-normal direction with the usual *tanh* mapping. The chemical reactions are modeled by the mechanism of Table 2.1: premixed hydrogen and air burn in a v-shaped anchored flame characterized by an equivalence ratio $\Xi = 1.5$. Spatial resolution is $\Delta x = 32\,\mu m$ ($\Delta x^+ = 2.0$) in the streamwise direction and $54\,\mu m \geq \Delta y \geq 6.7\mu m$ ($3.4 \geq \Delta y^+ \geq 0.5$) in the wall normal direction. Note

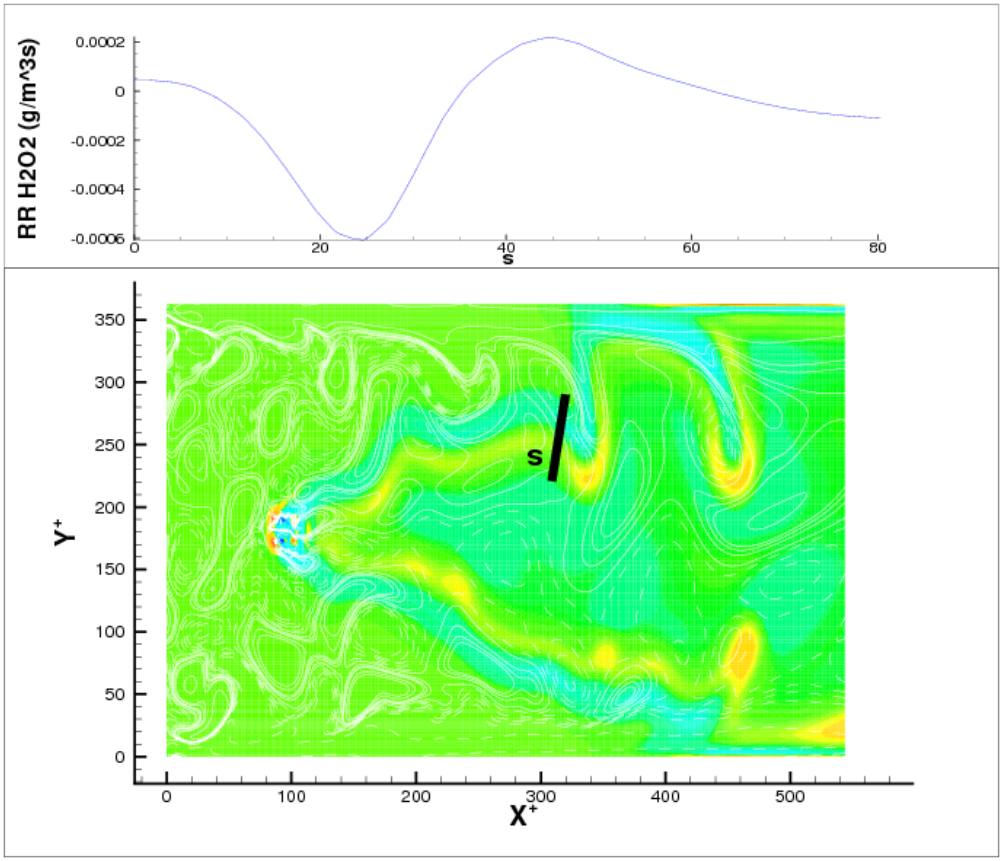

Figure 7.7: 2-D ducted flame: white isocontours of spanwise vorticity (dashed lines represent negative values) and flooded contours of H_2O_2 reaction rate. A one-dimensional profile of the H_2O_2 reaction rate is plotted along the black line **s**.

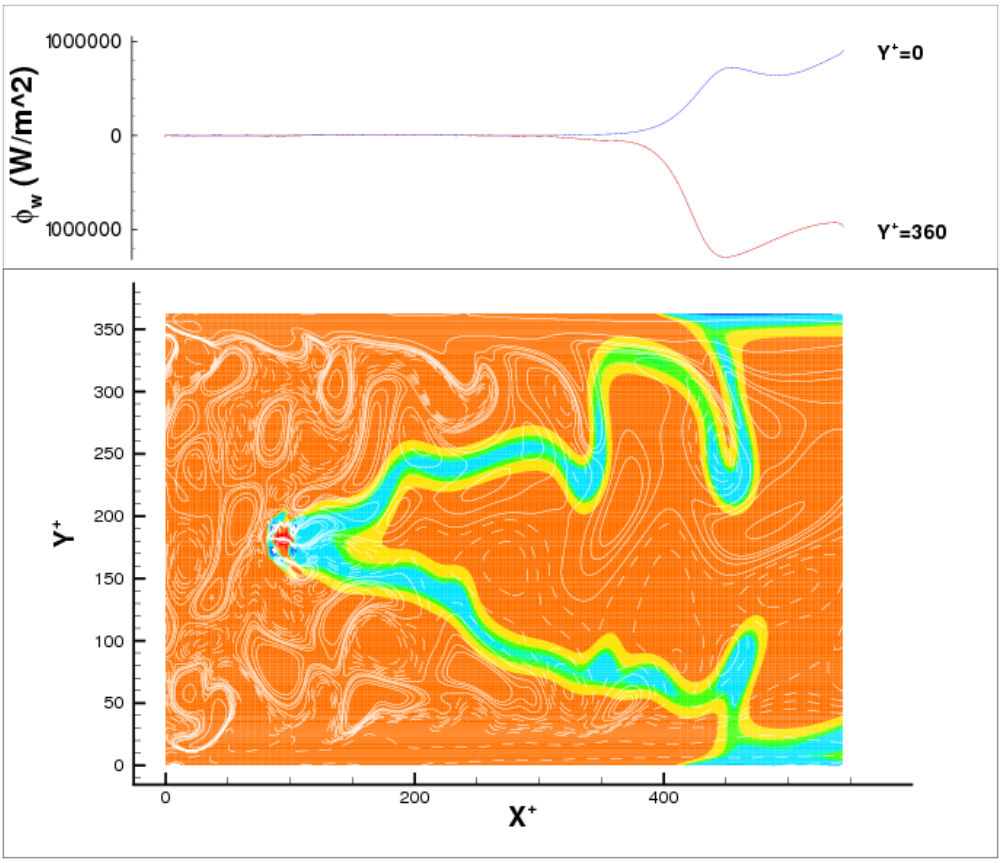

Figure 7.8: 2-D ducted flame: white isocontours of spanwise vorticity (dashed lines represent negative values) and flooded contours of heat release rate. The wall heat flux on both walls is clearly related to flame parts convected toward the wall by incoming eddies. Realization 1.

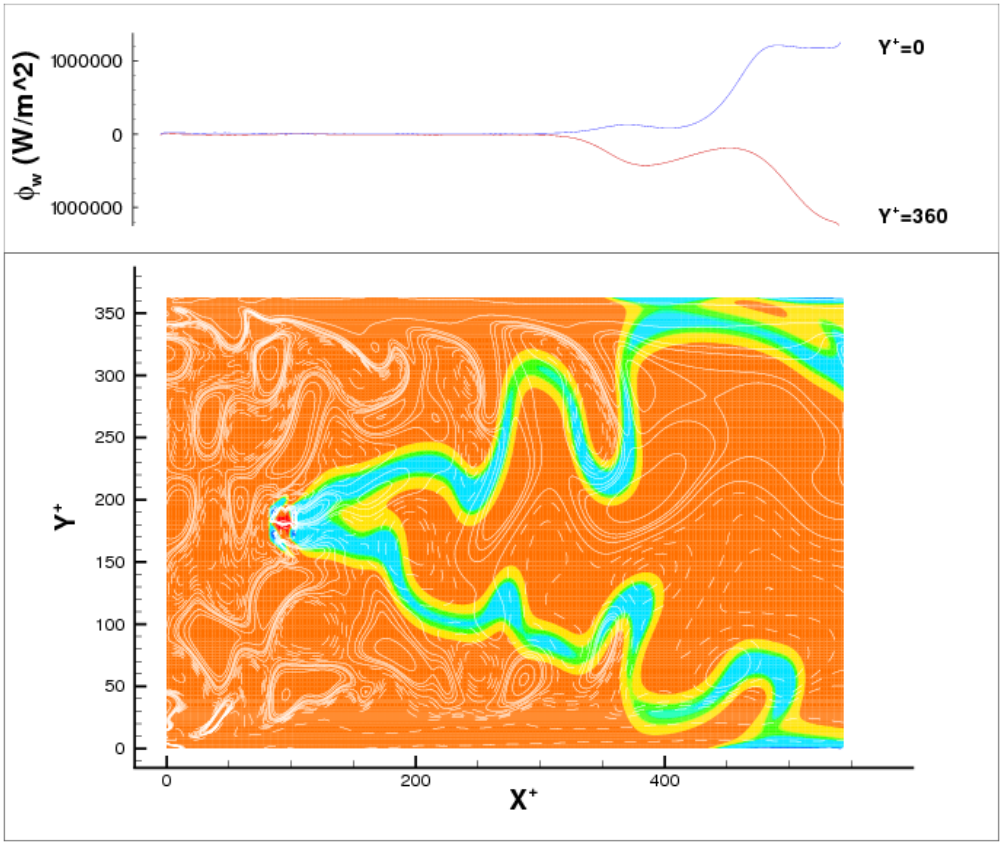

Figure 7.9: 2-D ducted flame: white isocontours of spanwise vorticity (dashed lines represent negative values) and flooded contours of heat release rate. The wall heat flux on both walls is clearly related to flame parts convected toward the wall by incoming eddies. Realization 2.

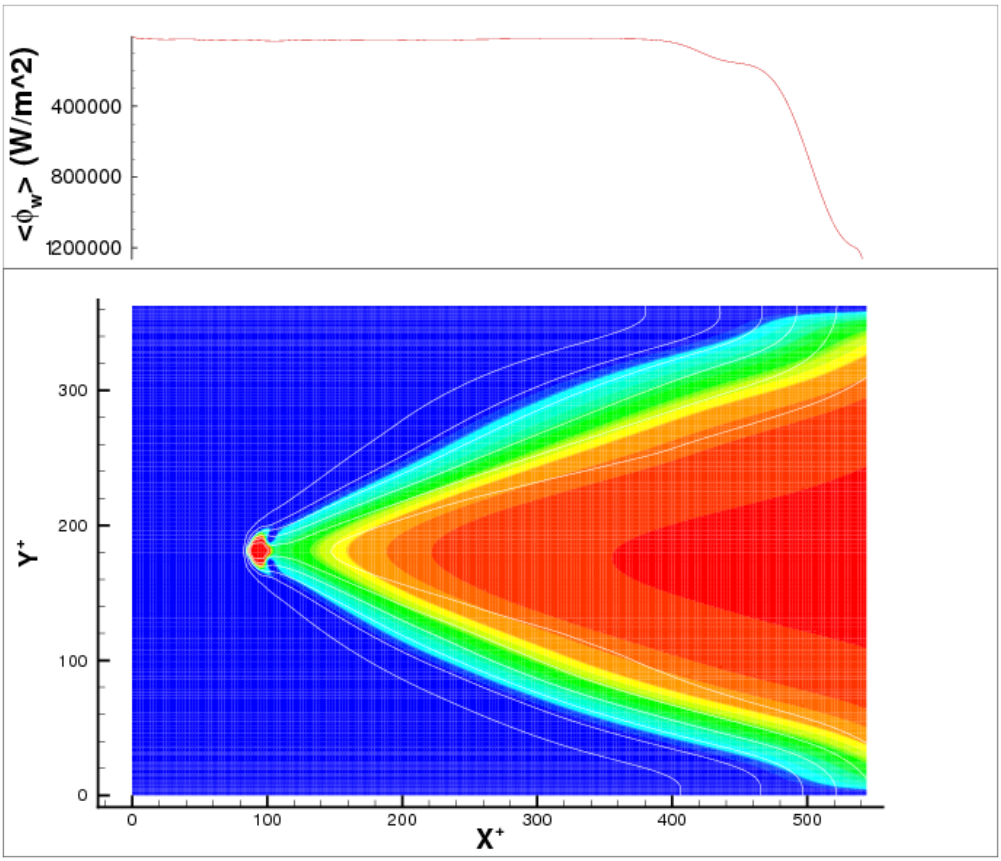

Figure 7.10: 2-D ducted flame: white isocontours of average fuel mass fraction and flooded contours of average temperature.

that the lowest resolution, encountered in proximity of the channel centerline in the wall normal direction, is too coarse to correctly resolve the flame structure, typically the reaction rates profiles of the intermediate species HO_2 and H_2O_2. However, because of the flame shape and position, only small regions of the flame propagate close to the channel centerline (those in the immediate vicinity of the anchor). Consequently, the coarse wall-normal resolution near the channel centerline does not seem to negatively affect the flame structure: the intermediate species reaction rates, notoriously prone to oscillations when the flame structure is under-resolved, behave smoothly as shown in Figure 7.7 for the H_2O_2 reaction rate profile. On the basis of these results from the two-dimensional case TW0, the same resolution of $\Delta y \sim 50\,\mu m$ is used near the channel centerline in the three-dimensional simulations described below.

Results

Qualitative analysis of the instantaneous wall heat flux pattern is attempted in Figures 7.8 and 7.9: strong effects of the spanwise vorticity on the flame wrinkling and flame-wall interaction are clearly visible. The two realization of the instantaneous fields show values of the maximum wall heat flux of the order of those observed in the one-dimensional laminar HOQ cases. Figure 7.10 shows the average temperature field and heat flux. In respect to the laminar HOQ configuration described in Chapter 6, the two-dimensional SWQ is characterized, on average, by comparable values of the maximum wall heat flux around $\sim 1.25\,MW/m^2$. Because of the effect of the anchor on its shape, the flame is not always impinging on the wall from the normal direction, as in HOQ, but at an angle: this fact, together with the passage of eddies past the reaction front, produces flame strain and stretching which, in turn, thin the flame out reducing the flame heat release and consequently the maximum wall heat flux. This is the reason behind the occurrence, from time to time and for different streamwise locations, of flame-wall interaction events characterized by lower maximum wall heat flux in the multi-dimensional case compared to the laminar one. Finally, it is important to note that the viscous sublayer, usually confined to $y^+ \leq 5$ in 3-D turbulent boundary layers, extends far out into the inner layer (up to $y^+ \sim 25$) in the 2-D simulations. This fact is a consequence of the 2-D approximation and is shown in Figures 7.8 and 7.9 by the white vorticity isolines running nearly parallel to the wall between $y^+ = 0$ and $y^+ \sim 25$. The absence, in the near-wall region, of intense streamwise vorticity structures that "push" the

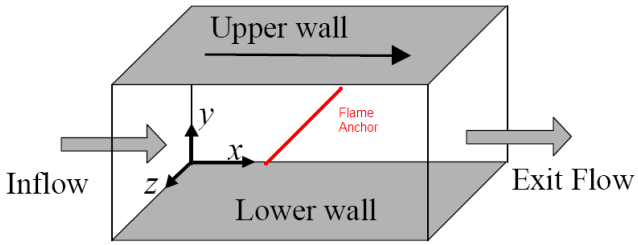

Figure 7.11: Pictorial representation of the plane channel with the anchor located near the channel centerline downstream of the inlet.

flame toward the wall is probably the main reason for the lower maximum wall heat fluxes observed in 2-D turbulent flame-wall interaction compared to 3-D as already pointed out in Bruneaux *et al.* (1996).

7.3.2 Three-Dimensional Simulations

In order to investigate the effects of realistic near-wall turbulence on flame-wall interaction a three-dimensional DNS is required. In the next two Sections results from case TW1 are reported and a comparison with preliminary results from case TW2 (still running at the time of the writing) indicates negligible differences in the flame-wall interaction spatial and temporal patterns, these two cases differ principally in the way the turbulent inlet velocity fluctuations are generated: the TW1 inlet boundary is fed with a spatially evolving turbulence sampled from a single "frozen" realization of a turbulent field using Taylor's hypothesis, TW2 is provided at the inlet boundary with temporally evolving turbulence at a fixed streamwise location from a parallel auxiliary run. While the former procedure is not very complicated to implement and computationally cheap the latter one is more "correct" but it is considerably more expensive from the computational point of view. There is some degree of uncertainty about the ability of the DNS fed using the "frozen" turbulence box to quickly recover in the near-wall region the correct phase relationship between the different Fourier modes of the velocity fluctuations. Because of this uncertainty, results and conclusions from case TW1 will, at a later stage, be compared with data from case TW2. The algorithm for a computationally efficient feeding

of the temporally evolving turbulence used in case TW2 was implemented in the S3D code while case TW1 was already running. At the time of the writing case TW1 has been stopped after 5 transit times, while case TW2 has reached 2 transit times. The availability of these two datasets gives the opportunity to compare near-wall flame behaviour and observe any eventual differences in the wall heat flux spatial patterns and their maximum values due to the two different approaches in the specification of inlet turbulence (as mentioned above, preliminary comparison indicates that differences in these quantities are indeed negligible).

Case Parameters

The parameters used in the three-dimensional reactive cases, named TW1 and TW2, are similar to those used in the inert turbulent channel case and are reported below:

- The target flow Reynolds number is $Re_0 = 3142$, based on the centerline velocity U_c and the channel half-width H, or $Re_\tau = 180$ if the friction velocity u_τ is used as reference speed.

- A computational box as in Figure 7.11 is built on a Cartesian $360 \times 200 \times 280$ grid ($316 \times 100 \times 140$ for case TW2). The present grid is refined at the wall using a *tanh* mapping and the first point off the wall is at $y^+ = 0.5$. The grid resolution is expressed in wall units[2] as $\Delta x^+ = 2.0$, $\Delta y^+ = 0.5 - 3.4$ and $\Delta z^+ = 2.0$. Note that the grid is only stretched by a factor of 7 in the wall normal direction, the reason for this relatively "light" stretching (a factor of 100 is usual in other contexts) is to be found in the flame resolution requirements near the channel centerline. The grid resolution values are doubled in case TW2, however, the near-wall resolution $\Delta y^+ = 0.5$ is conserved by increasing the stretch factor and reducing the resolution near the channel centerline to $\Delta y^+ = 7$.

- The relative dimensions of the box in the streamwise, wall normal and spanwise directions are $4H$, $2H$ and $3H$ respectively in case TW1 and $7H$, $2H$ and $3H$ in case TW2.

[2] Recall that wall units in this report are based on a semi-local definition of the friction velocity u_τ averaged in the approaching "cold" turbulence.

- Periodic boundary conditions are imposed in the spanwise direction and isothermal, inert, no-slip wall boundary conditions (according to Method B of Section 3.3.2) are set at the two opposite solid surfaces. At the inflow boundary a non-reflecting fluctuating inlet is imposed while at the outflow boundary a non-reflecting outlet is specified whose pressure is weakly coupled to a far field pressure p_∞ in order to avoid unrealistic pressure drift of the solution.

- In case TW1 the initial turbulent field is equal to one realization of the inert case 3DT and inlet turbulent fluctuations are specified using spatial sampling from a frozen realization of the same inert case (or by temporal sampling from a simultaneous auxiliary simulation in case TW2). The flame anchor is specified by imposing adiabatic flame temperature and burnt gas composition in a cylindrical domain that extends in the spanwise direction for the length of the computational box and is placed near the channel centerline ($y^+ \sim 100$) approximately 100 wall units downstream of the inflow boundary in case TW1. In case TW2 the flame anchor is placed at the centerline ($y^+ = 180$) approximately 180 wall units downstream of the inlet. In order to reduce acoustic emissions from the anchor the imposed values of temperature and mass fractions are smoothly blended into the solution using a gaussian spatial filter.

- Initial pressure is set to $1\,atm$, while density, temperature and composition fields are initialized in the shape of a V-flame. An auxiliary progress variable function c is used to associate all points in the three-dimensional domain to a one-dimensional PREMIX solution of the hydrogen-air flame under investigation ($\Xi = 1.5$). The temperature of the wall and of the cold reactants is set to $750\,K$.

- The target turbulent Reynolds number and chemical composition of the mixture result in a Damkohler number $Da \sim 0.26$ that is very similar to the one simulated by Alshaalan and Rutland (2002). This Damkohler number is based on the wall time scale ($t_w = \nu/u_\tau^2$) and on the flame time scale ($t_l = \delta_l/S_l$). As pointed out in a landmark paper by Poinsot *et al.* (1996), the present Damkohler number, even if outside the flamelet regime traditionally indicated by the Borghi diagram, for details see Borghi (1988), still implies flamelet-like regimes characterized by a slightly thickened continuous flame sheet embedding Kolmogorov-scale eddies. Poinsot *et al.* (1996) propose the Ex-

tended Flamelet Assumption (EFA) to model this turbulent combustion regime in which the flame is only quenched by eddies at least one or two order of magnitude larger (and faster) than the Kolmogorov eddies. Other relevant parameters of the simulation are: $S_l/U_c = 0.1625$, $u_\tau/S_l = 0.33$, $u_\tau/U_c = 0.053$ and $\delta_l/H = 0.069$.

- The time step is fixed to the value $\Delta t = 4.0e^{-09}\ s$ well within the acoustic CFL stability limits.
- The total integration time of the simulation is 5 transit times for case TW1 and corresponds to $0.725\,ms$. As mentioned above case TW2 is still running at the time of the writing and a target integration time of 12 transit times is considered.

The results presented below are obtained by the analysis of a DNS database consisting of five flow-through times of case TW1 and the discussion of these results focuses on the observed *spatial pattern* of the wall heat fluxes. Preliminary statistical analysis of case TW2 data is also included. The available datasets are believed to be sufficient to reach reliable conclusions about the spatial pattern of the flame-wall interaction. The influence of the near-wall quasi-streamwise coherent vorticity structures on flame-wall interaction events is confirmed to a great extent by visual observation of the instantaneous fields for both case TW1 and case TW2, and also by the statistical analysis of the DNS database from case TW2. However, as observed in Poinsot *et al.* (1996), a reliable statistical description of turbulent reactive flow from DNS data in general, and of the characteristic *temporal pattern* of the maximum wall heat fluxes in particular requires longer integration of the solution and a larger statistical sample than the one available at this time. Consequently, the temporal scaling aspects of the present FWI will be discussed at a later time in an already scheduled publication when a larger sample will be available.

Note

The temporal recurrence pattern of 120 outer time units ($\sim tU_c/H = t/t_{LE}$) between "wall heat flux bursting events" reported in Alshaalan and Rutland (2002) cannot be confirmed (or rejected) with the presently available time evolving sample of the solution for cases TW1 and TW2 being the sample too small. However, it is opportune to note at this point that, even if the temporal scaling suggested by Alshaalan and Rutland correlates well

with the average time interval between the "turbulent bursting events" reported by Jiménez and Moin (1991), it is a very large scaling indeed compared to the global statistical sample (extending over 210 outer time units only) available to Alshaalan and Rutland. Their conclusions about the nature of the temporal scaling for strong wall heat flux events (its relation to the turbulent bursting events) should therefore be checked, and eventually confirmed, with a long time integration of a similar configuration: this is a partial goal for the scheduled continuation of the present work.

7.3.3 Visualization Of The Instantaneous Fields

Visual analysis of the instantaneous fields is performed using the advanced capabilities of the visualization software ©TECPLOT and all Figures below are exported from this software tool to the postscript format. From visual inspection of Figures 7.12-7.16 it is possible to infer that:

- Figure 7.12: the approaching turbulent flow field (represented by the blue isosurface of vorticity magnitude) has a strong influence on the flame shape (represented by the orange flame temperature isosurface) producing a characteristic wrinkling of its surface. Note in the Figure the tongue of unburnt gases pushed away from the wall by a vorticity structure.

- Figure 7.12: the flame has a strong effect on the approaching turbulent flow field whose fluctuation level rapidly decay to nearly laminar levels in the burnt gases (flat vorticity isosurface).

- Figure 7.13: elongated quasi-streamwise vorticity structures (yellow and green isosurfaces) visually exhibit good spatial correlation with the locations where the temperature isosurface (blue-to-red isosurface of $T = 1000\,K$ marking the preheat zone) achieves the minimum distance from the wall. The blue-to-red coloring scale represent the isosurface's distance from the wall, the legend is in wall units).

- Figures 7.14: the red "hotspots" of maximum wall heat flux (marked with "H") exhibit a characteristic spatial pattern and a spanwise spacing of 100 wall units, the same spanwise spacing is characteristic of the quasi-streamwise vorticity structures of intense streamwise vorticity (marked with "A" and "B"). Visual observation of several instantaneous fields shows good spatial correlation between these vorticity

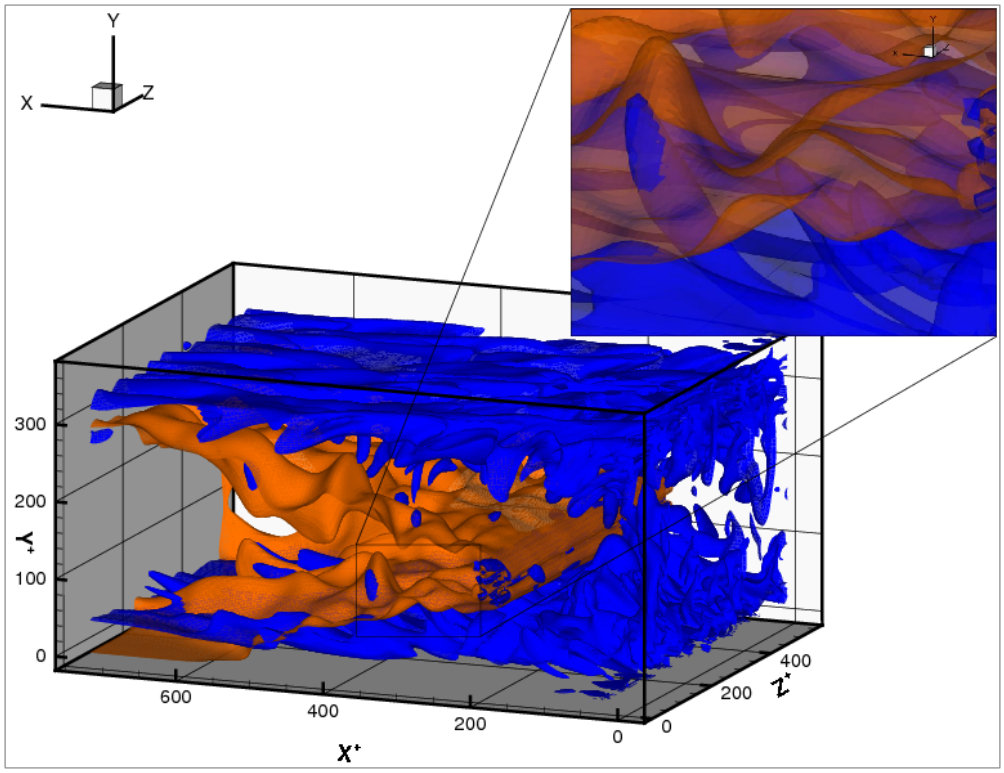

Figure 7.12: Instantaneous view of the computational domain: a vorticity magnitude isosurface (blue) visualized together with a flame temperature isosurface (orange) illustrates the effect of the turbulent field on the flame shape. A characteristic "tongue" of unburnt gases pushed away from the wall by near-wall vorticity motion is clearly visible in the zoomed enclosure.

structures and the locations of maximum wall heat flux, see also the near-wall detail in Figure 7.15.

- Figures 7.16: the red "hotspots" of maximum wall heat flux exhibit a characteristic spatial pattern and a spanwise spacing of 100 wall units, the same spanwise spacing is characteristic of the quasi-streamwise vorticity structures of intense streamwise vorticity. The yellow isolines represent intense wall-normal vorticity induced by the quasi-streamwise vorticity structures elongated in the flow directions and located just above the viscous sublayer at $y^+ = 5$, see Figure 5.5. The measured maximum wall heat flux normalized by the flame power, F_Q, in the 3-D simulation peaks to values ($F_{Q,max,t} \sim 0.3$) larger by a factor of two compared to the laminar cases ($F_{Q,max,l} \sim 0.12$).

- Figures 7.17 and 7.18: the figures show a typical occurrence of maximum wall heat flux induced by a quasi-streamwise vorticity structure, slightly lifted from the wall, "passing through" the flame front and pushing it toward the solid surface. The instantaneous wall-normal profile (along line "S" of Figure 7.17) of streamwise vorticity ω_x (dashed line) show a local maximum at $y^+ \sim 30$ (instead of $y^+ \sim 20$) and is zero at $y^+ \sim 15$ (instead of $y^+ \sim 5$) indicating that the streamwise vortex is slightly "tilted" from the wall at the "hotspot" location, this fact is confirmed by visual observation of Figure 7.17. The profile of wall-normal velocity v (solid line) peaks at $y^+ \sim 40$ and shows that there is a strong motion of fluid toward the wall (positive v is directed toward the upper wall).

The above considerations strongly suggest the existence of a correlation between the quasi-streamwise vorticity structures of the boundary layer and the locations of intense heat transfer between the flame and the wall. The use of detailed chemical kinetics in the present context ensures correct transient representation of the radical dynamics (even in the lack of the Soret effect) and of the instantaneous wall heat flux. The effect of the wall-normal velocity fluctuations seems to be important in pushing the flame toward the wall or away from it, thereby causing large variations in the instantaneous wall heat flux. For very thin wall thicknesses (this is often the situation in gas turbine combustors) and relatively long time scales (the quasi-streamwise vorticity structures are elongated in the flow direction) such spatially varying wall heat fluxes could imply large thermal stresses and shorten the combustor lifetime. However, it is important to clearly

state that the above conclusions on a possible correlation between quasi-streamwise vorticity and wall heat flux rely on the *visual observation* of a limited number of different realizations (~ 100) of the solution of cases TW1 and TW2. In order to obtain a more quantitative indication about the presence of such correlation the database accumulated so far is analyzed statistically in the next Section.

7.3.4 Statistical Analysis

In order to reduce the post processing computational cost samples of the solution are collected for case TW1 only in a sub domain limited to half of the streamwise, wall-normal and spanwise extension of the computational domain and with a time interval of 1.8 wall units as suggested by Alshaalan and Rutland (2002) for a similar configuration. The total integration time of case TW1 (5 transit times) amounts to 182 wall units allowing storage of 100 samples for statistical analysis. Samples are collected in the sub domain delimited by the following spatial dimensions $5.8\,mm \le x \le 1.16\,mm$, $0.0\,mm \le y \le 2.9\,mm$ and $0.0\,mm \le z \le 4.35\,mm$.

The correlation of wall heat flux, Q_w, sampled at $y^+ = 0$ and streamwise vorticity magnitude, $|\omega_x|$, sampled at various wall distances $y^+ \ge 0$ and normalized by the maximum values is extracted from the TW1-database using the following expression:

$$R\left(Q_w\left(x^+, y^+ = 0, z^+\right), |\omega_x\left(x^+, y^+, z^+\right)|\right) = \frac{\langle Q_w |\omega_x| \rangle}{Q_{w,m}\omega_{x,rms,m}} \tag{7.3}$$

where the subscript m is intended to designate the maximum values of the variables. A two-point spatial correlation in the spanwise direction, z^+, of the wall heat flux and of the wall-normal velocity is computed for case TW1 using the following expression:

$$R_{Qv} = \langle [\Phi_{w,max} v(z_0)] \cdot [\Phi_w v(z_0 + \Delta z)] \rangle \tag{7.4}$$

where the location $z_0 = z_{\Phi_{max}}$ is assigned to all points on the solid surfaces whose wall heat flux exceeds the maximum laminar value, $\Phi_{w,max,l}$, given in the table on page 121 (case LW5), v is the wall normal velocity at $y^+ = 20$ (a positive sign is assigned to a wall-normal velocity directed toward the wall). Normalization is performed by $\Phi_{w,max,l}$ and by the rms value at $y^+ = 20$ of the wall-normal velocity.

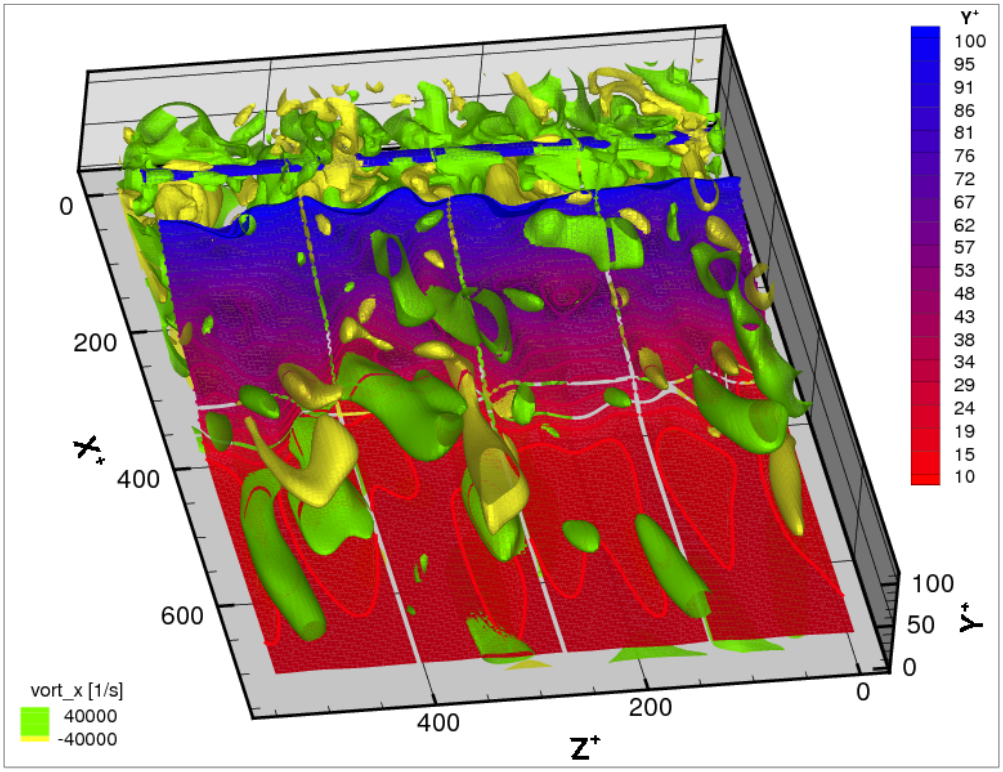

Figure 7.13: Instantaneous view of the lower wall: yellow and green isosurfaces show quasi-streamwise vorticity structures and their good spatial correlation with the locations in which the flame preheat-zone (blue-to-red isosurface describing $T = 1000\,K$) is closest to the wall.

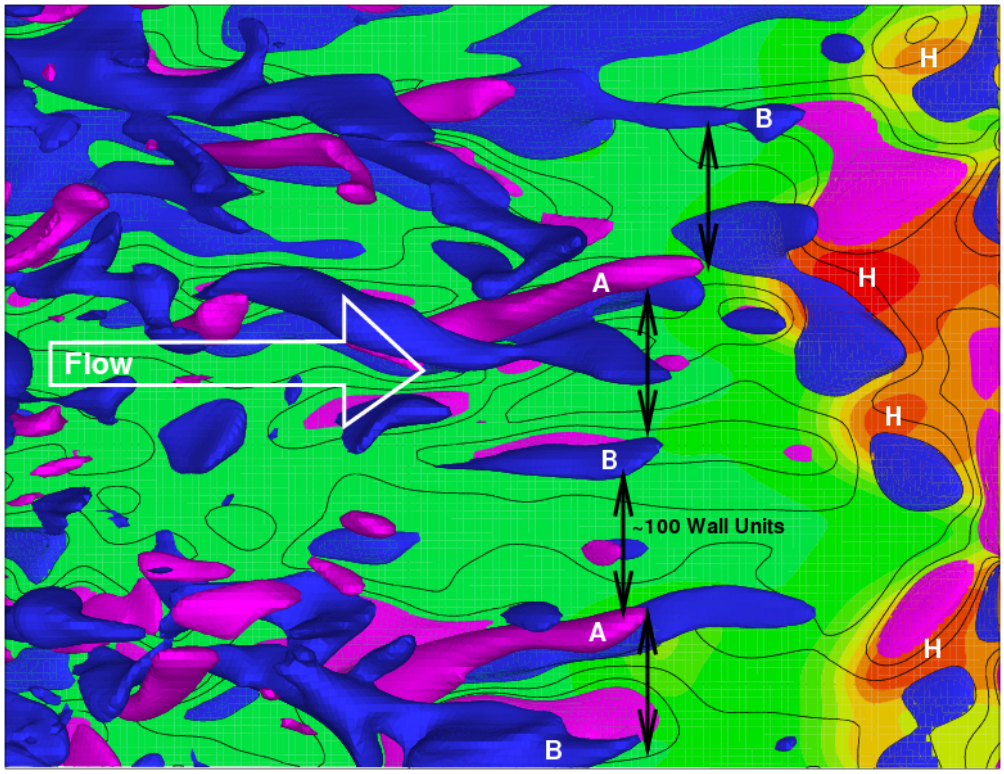

Figure 7.14: Instantaneous view of the lower wall: streamwise vorticity isosurfaces (blue=clockwise rotation, pink=counterclockwise rotation) show good spatial correlation between quasi-streamwise intense vorticity structures (designated by "A" and "B") and wall heat flux "hotspots" located further downstream (designated by "H").

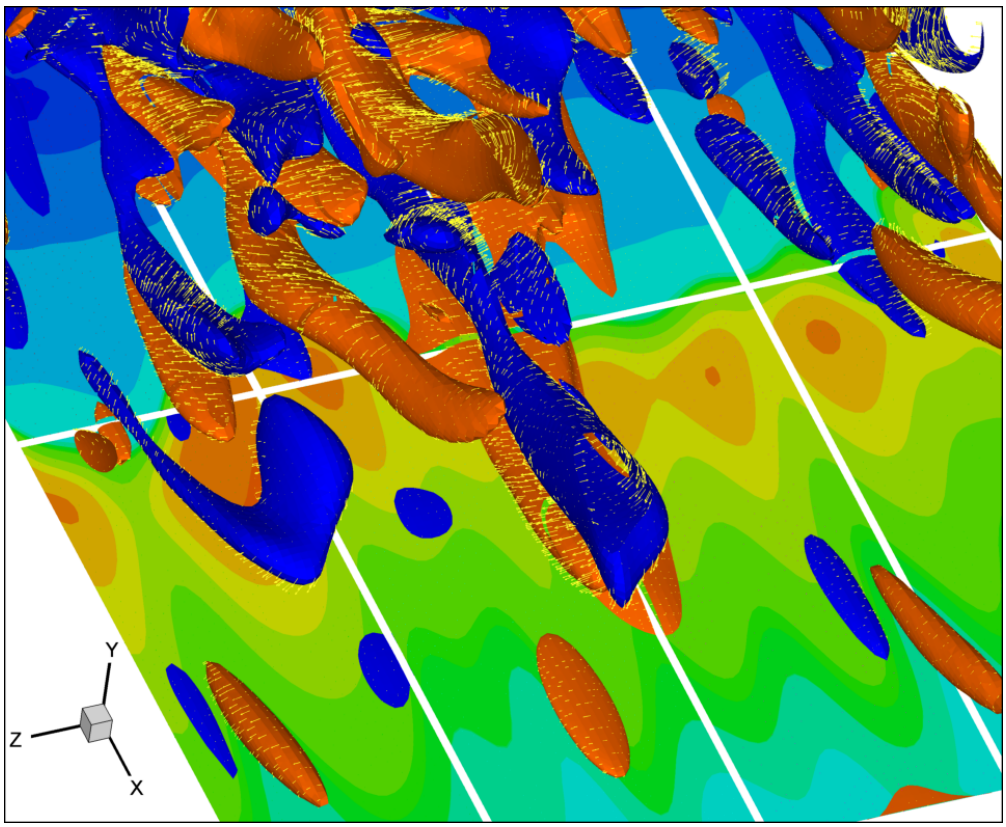

Figure 7.15: Instantaneous view of the lower wall (detail): streamwise vorticity isosurfaces (blue surfaces=clockwise rotation, orange surfaces=counterclockwise rotation) show good spatial correlation between quasi-streamwise intense vorticity structures and wall heat flux "hotspots" (blue-to-green-to-red isocontours), the yellow velocity vectors attached to the vorticity isosurfaces indicate the instantaneous direction of motion of the fluid.

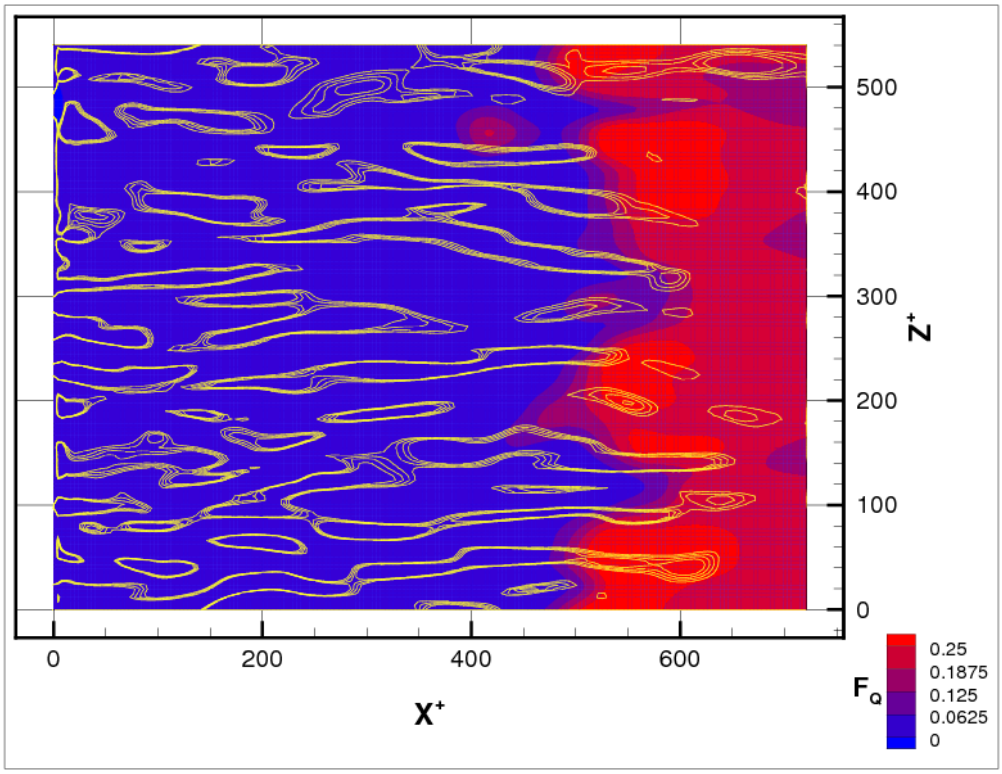

Figure 7.16: Instantaneous view of the lower wall: blue-to-red isocontours show the spatial pattern of the adimensional wall heat flux F_Q and its maximum values, yellow isolines represent wall-normal vorticity at $y^+ = 5$ and show a characteristic "streaky" pattern.

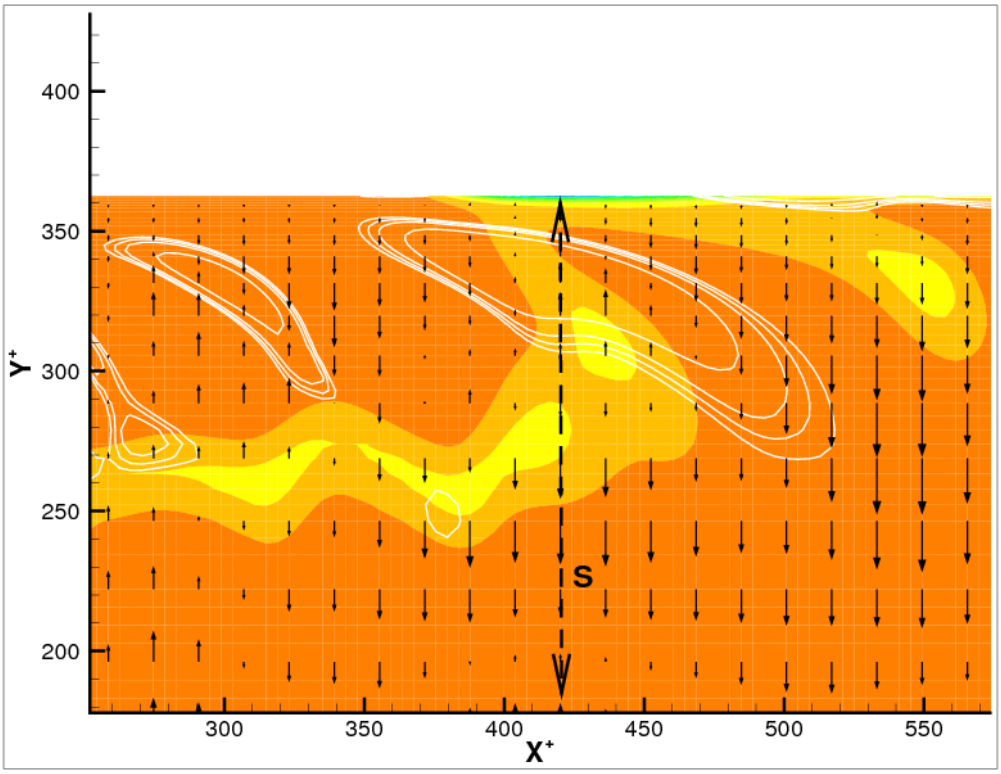

Figure 7.17: Side view of the upper wall: isocontours of heat release describing the flame front and white isolines of streamwise vorticity representing quasi-streamwise vorticity structures are shown in a vertical x^+-y^+ plane. The vertical plane corresponds to the spanwise position of instantaneous maximum wall heat flux (located at the top of the dashed line named "S").

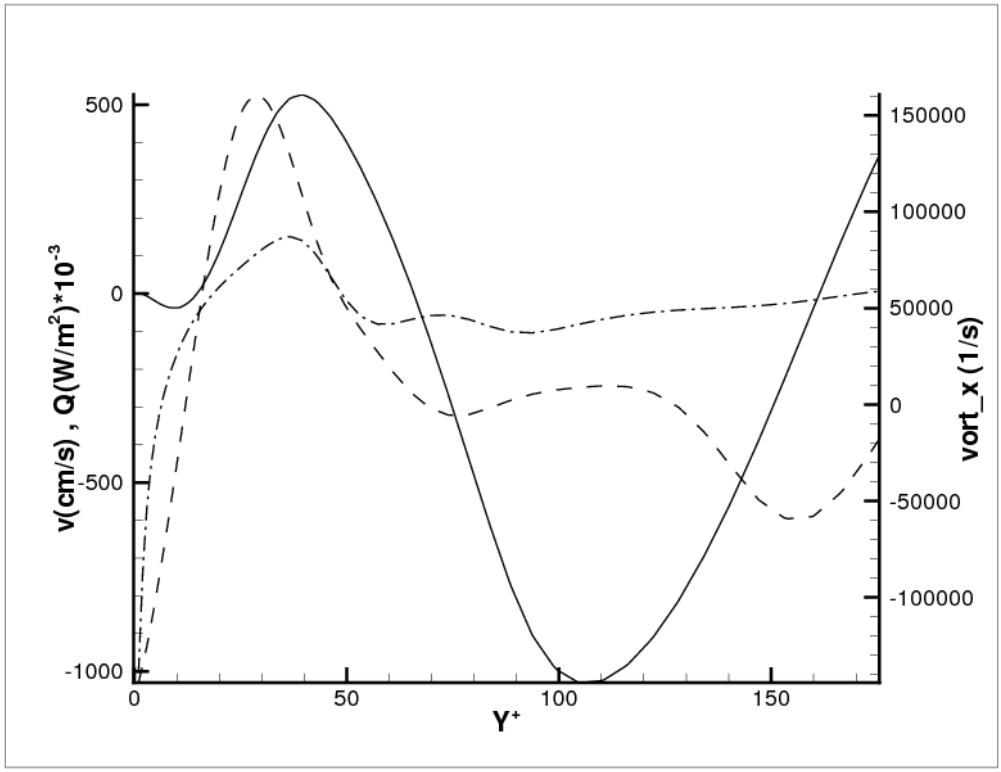

Figure 7.18: Instantaneous wall-normal profiles (along line "S" of Figure 7.17) of heat flux Q (dash-dot line), wall-normal velocity v (solid line) and streamwise vorticity ω_x (dashed line) starting ($y^+ = 0$) at the point of maximum wall heat flux on the wall and ending at the channel centerline ($y^+ = 180$).

- Figures 7.19-7.23 show the correlation 7.3 extracted from the TW1-database for several distances from the wall and confirm the visual observations of the previous Section suggesting the existence of a relation between streamwise vorticity and wall heat flux and of a characteristic spanwise interval of 100 wall units between peaks of maximum heat flux. The correlation 7.3 show maximum values at $y^+ = 22$ in Figure 7.21, this fact is in good accordance with the generally accepted theory of the turbulent boundary layer that wants the maximum in the streamwise vorticity and wall-normal velocity fluctuations (toward or away from the wall) also at $y^+ \sim 22$, see Figure 5.5 for reference. The local maxima located between the absolute maxima in the correlations are due to secondary "weaker" quasi-streamwise vorticity structures (see Figure 1.4) that have a minor influence on the wall heat flux.
- Figure 7.24 illustrates the spanwise correlation 7.4 extracted from the TW1-database of wall heat flux Q_w and wall-normal velocity v sampled at $y^+ = 20$ (positive velocity is assumed toward the wall). The correlation shows a clear negative local minimum at a spanwise distance of 50 wall units due to the ejection of fluid from the wall (negative fluctuation). This ejection of low speed fluid from the wall has the effect of pushing the flame surface away from the wall thereby reducing also the correlated wall heat flux. The weaker maximum further away represents a high-speed sweep located on average at a distance of 100 wall units from the absolute maximum and is only weakly correlated to it, this implies that adjacent "hotspots" are, on average, not aligned in the spanwise direction as illustrated by Figure 7.16. The fact that the correlation of Figure 7.24 shows a sharp gradient when moving away from its maximum both confirms the behaviour of the correlation in Figure 7.21 and suggests that the maximum wall heat flux events are highly localized in space, this implies large thermal stresses in the solid material.

Note that, at the time of the writing of this document, the amount of available samples and their total time span is limited to a time interval comparable with the characteristic lifetime of the longest quasi-streamwise structures. This fact is the cause of the "noise" still present in the correlations and leaves some uncertainty about the degree of temporal and spatial correlation between the different samples. However, as more samples become available from case TW2, results with improved statistics will be made

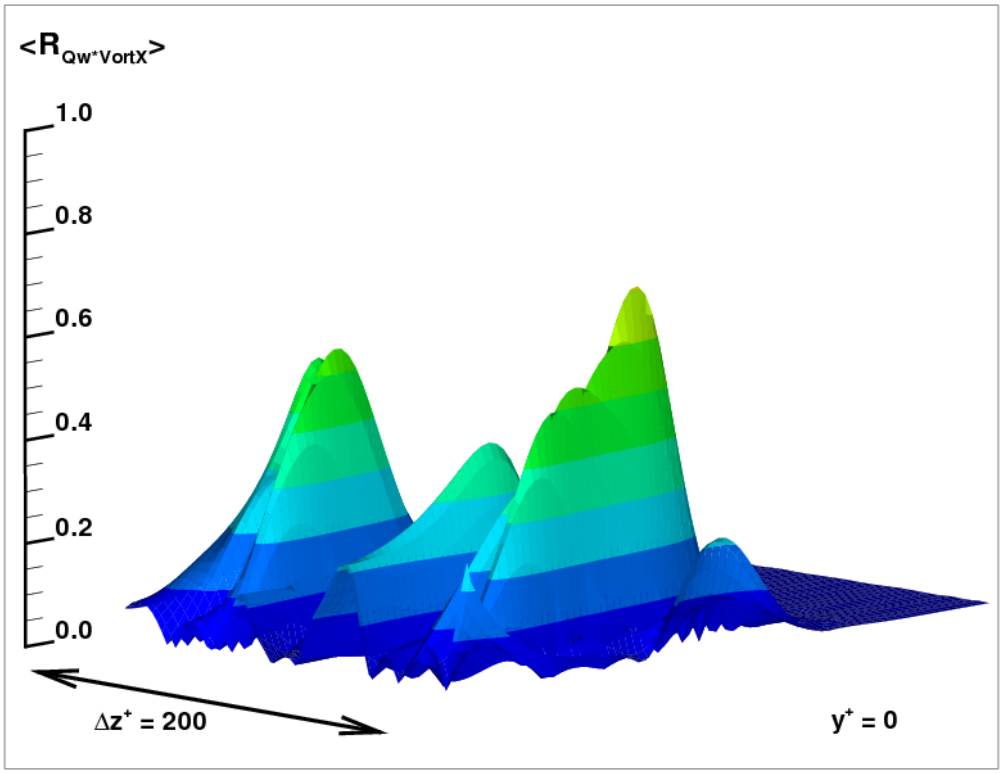

Figure 7.19: Spatial correlation of wall heat flux and streamwise vorticity at $y^+ = 0$.

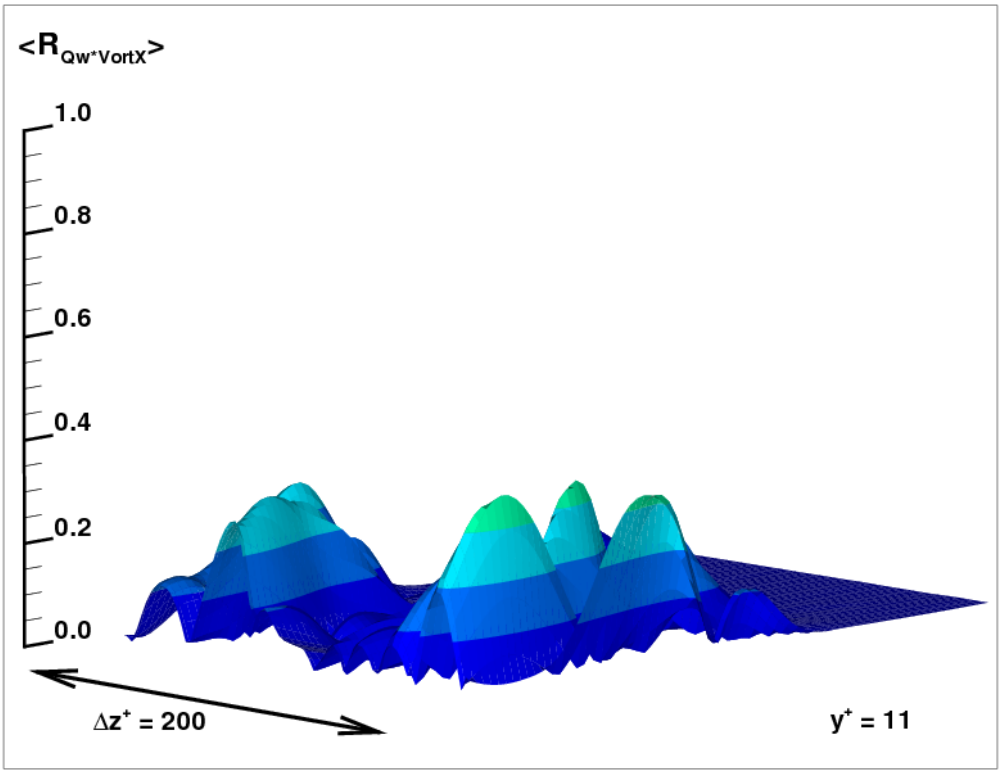

Figure 7.20: Spatial correlation of wall heat flux and streamwise vorticity at $y^+ = 11$.

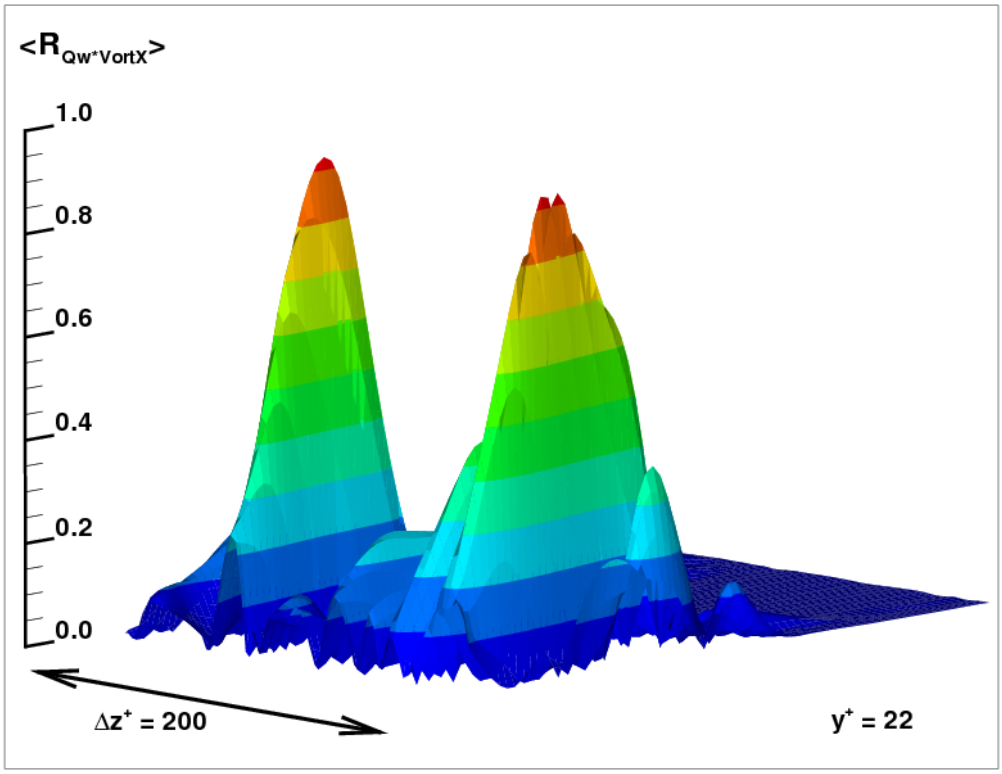

Figure 7.21: Spatial correlation of wall heat flux and streamwise vorticity at $y^+ = 22$.

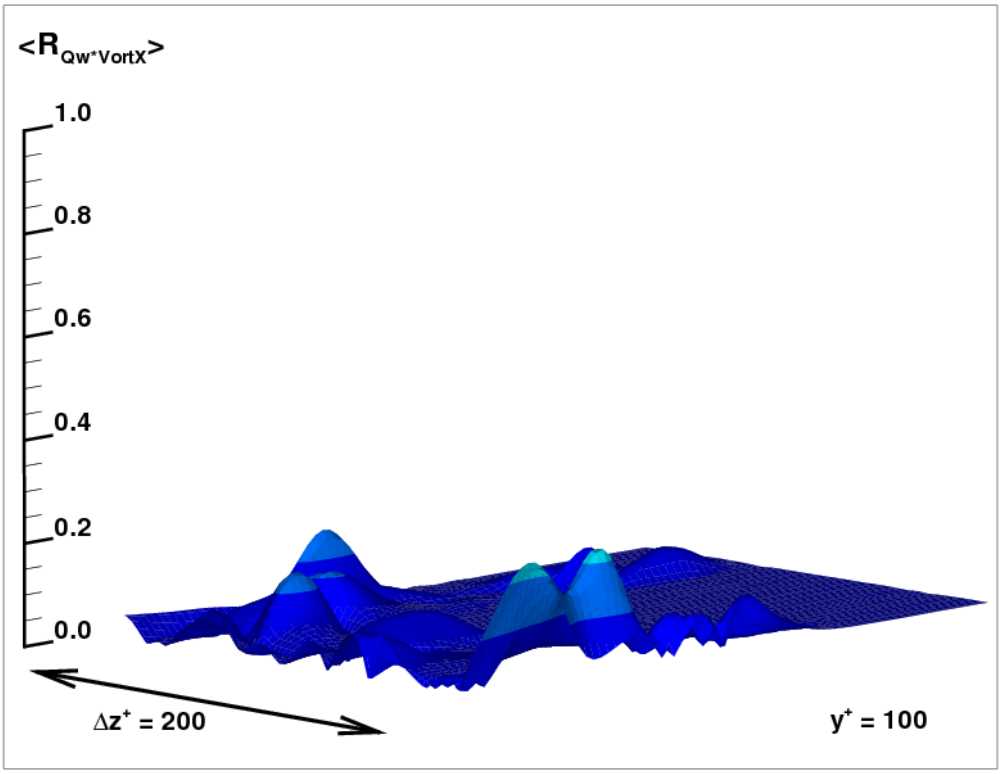

Figure 7.22: Spatial correlation of wall heat flux and streamwise vorticity at $y^+ = 100$.

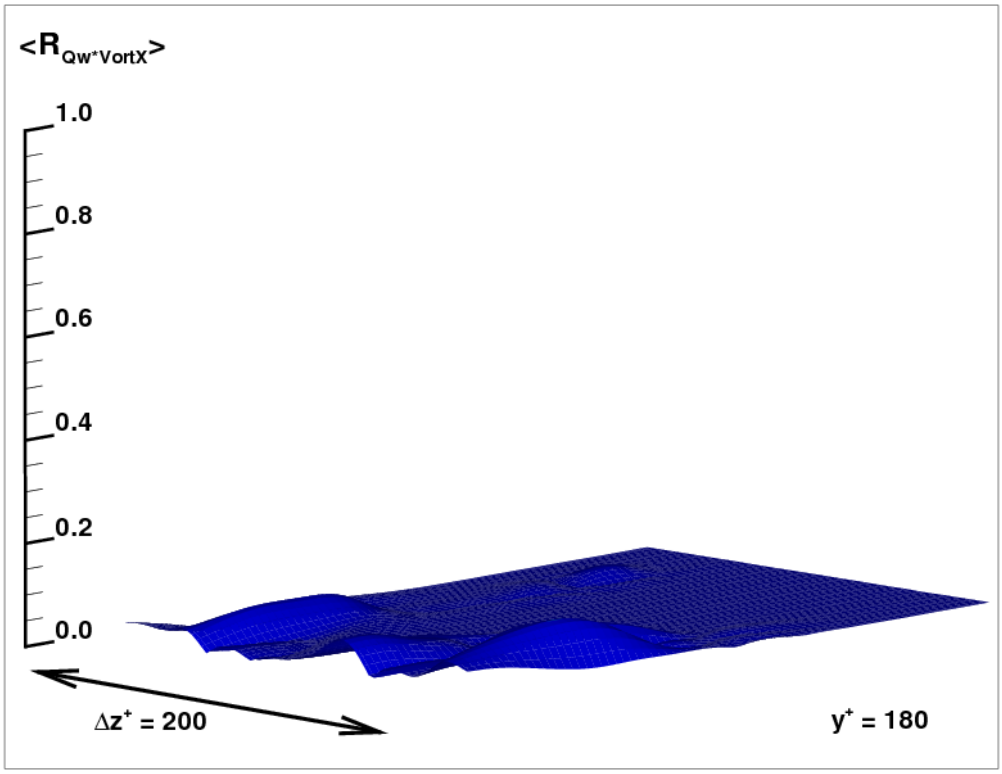

Figure 7.23: Spatial correlation of wall heat flux and streamwise vorticity at $y^+ = 180$.

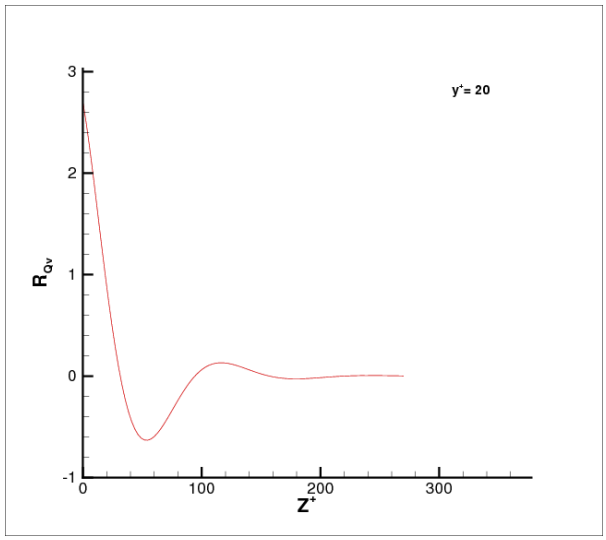

Figure 7.24: Spanwise correlation of the wall heat flux and wall-normal velocity fluctuation.

available in a future publication. Preliminary analysis of 88 realizations of the solution for case TW2 collected at different times is attempted here:

- Figure 7.25 shows the mean wall heat flux computed along the channel streamwise direction in case TW2, averaging is performed in the spanwise direction and in time for both the lower and the upper wall. The maximum value of $1.4\,MW/m^2$ for the mean wall heat flux is located 1043 wall units downstream of the inlet and is approximately coincident with the most probable location of flame-wall impingement/interaction. Immediately downstream of this location the averaged wall heat flux swiftly descend to a value $1.0\,MW/m^2$ induced by the hot burnt products.

- The spectral data in Figure 7.26 is sampled at the streamwise location of the maximum mean wall heat flux ($x^+ = 1043$) on both the lower and the upper wall in case TW2 and confirm the spatial pattern observed in the instantaneous fields: the peak marked with the black rectangle in the spatial frequency spectrum suggests that there is, on average, a spanwise interval of 100 wall units (characteristic frequency $l_e = 1/100$) between strong wall heat flux events.

- Figure 7.26 shows also that, for case TW2, the most significant temporal scales of the fluctuating wall heat flux are found to lie approximately in the spectral plateau between $0.037\,ms$ and $0.11\,ms$ or $9 < t^+ < 27$ in wall time units[3]. The black circle in Figure 7.26 approximately marks the temporal frequency $t_e \sim 27\,KHz$ at which the wall heat flux fluctuations become significant, note that this frequency t_e compares well the characteristic outer time scale $t_{LE} = H/U_c = 3.65e^{-05}\,s$. Although some uncertainties remain in the literature on the issue of the characteristic longitudinal dimension and temporal "life-span" of near-wall streamwise vorticity structures, Orlandi and Jiménez (1994) suggest, using an interesting simplified modeling approach, that the approximate near-wall eddy turnover time is $t^+ \sim 16$ wall units while Jiménez (1998) indicates a characteristic aspect ratio of 10 for these structures elongated in the streamwise direction. The latter indication implies that for a characteristic streamwise vortex diameter of 30 wall units (see Figure 5.5) the vorticity structure length can be estimated to $L^+ \sim 300$ wall units and the characteristic near-wall eddy "life-span" time scale to $t^+ \sim L^+/u^+ \sim 300/12 \sim 25$ where $u^+ \sim 12$ is assumed in the relevant region of the boundary layer (at $y^+ \sim 20$). The dimensional analysis above is based on what exposed in Orlandi and Jiménez (1994) and Jiménez (1998) suggesting that the characteristic near-wall eddy turnover time is $t^+ \sim 16$ and its characteristic "life-span" approximately $t^+ \sim 25$, these estimates are in good agreement with the observed range of temporal scales $9 < t^+ < 27$ wall time units between strong wall heat flux fluctuations.

- The pdf of the instantaneous wall heat flux sampled at $x^+ = 1043$ on both the lower and the upper wall in case TW2 is shown in Figure 7.27 and exhibits a long negative skewness, this indicates that the flame is often impinging onto the wall at the sampling location (or immediately upstream of it) being the occurrences of "low" heat transfer into the wall (in the range 0.2 - 1.0 [MW/m2]) relatively rare. This fact confirms that the chosen streamwise location for the wall heat flux sampling at $x^+ = 1043$ is well suited to study the effects of the flame-wall interaction on the wall heat transfer.

[3]Recall that the adimensional wall time unit is $t^+ = t_w \sim \nu/u_\tau^2$ and, as the spatial wall units, is based on quantities relative to the approaching turbulent flow.

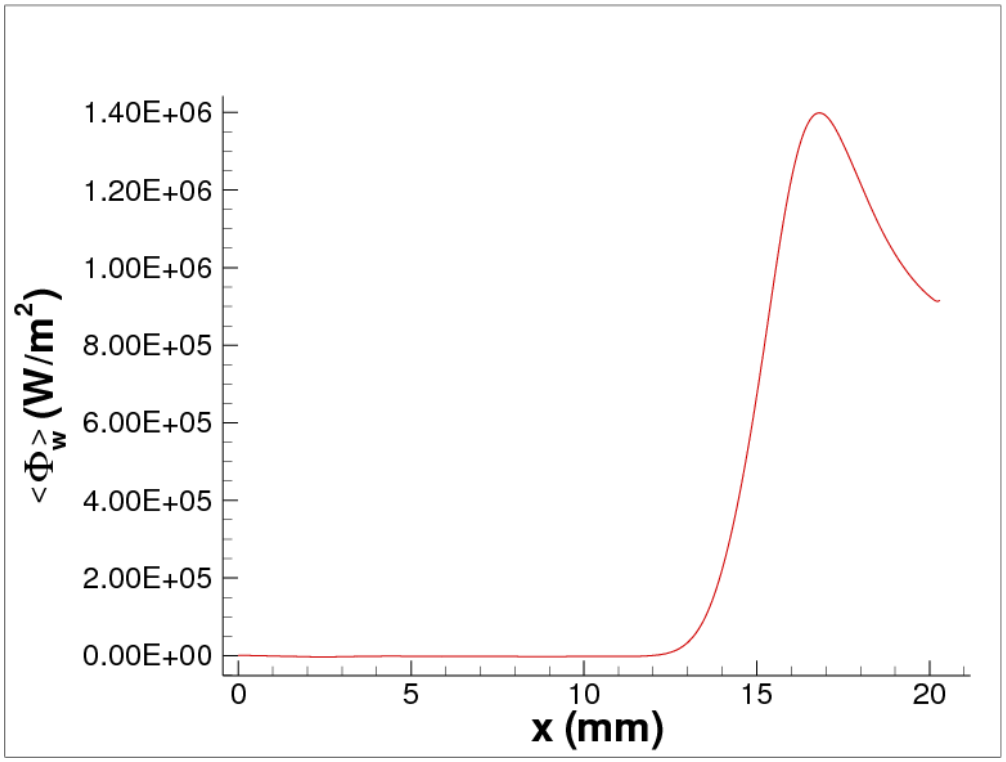

Figure 7.25: Mean value of the wall heat flux along the channel streamwise direction. The averaging is performed in time and in the spanwise direction for both the lower and the upper wall.

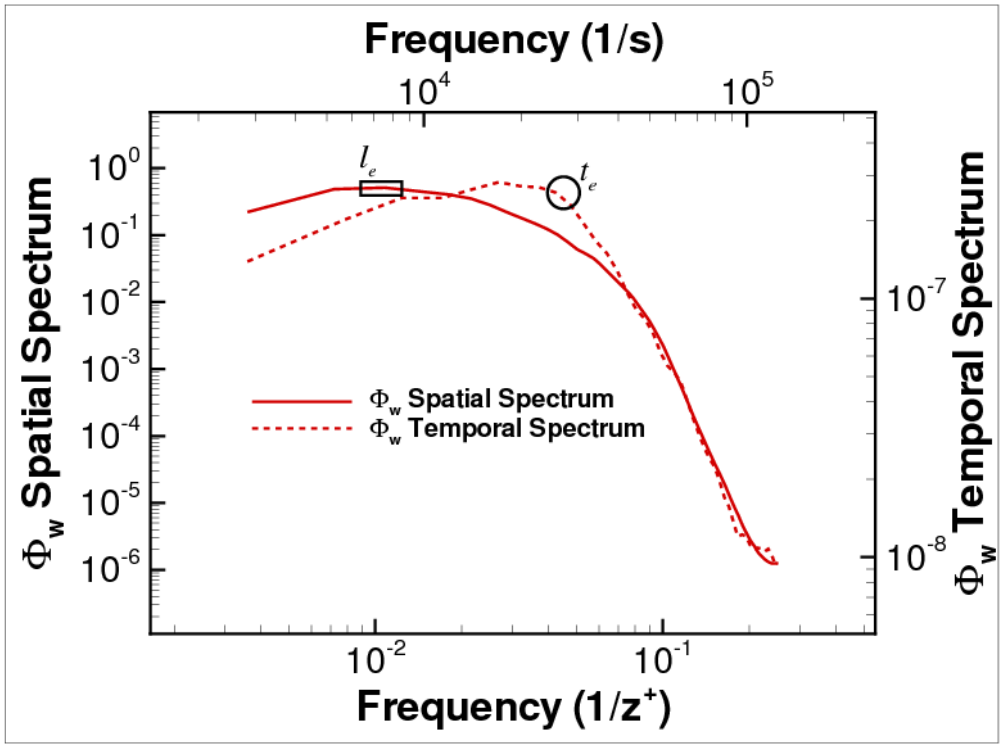

Figure 7.26: Spatial and temporal spectra of the wall heat flux sampled along a spanwise line at $x^+ = 1043$ for both the lower and the upper wall.

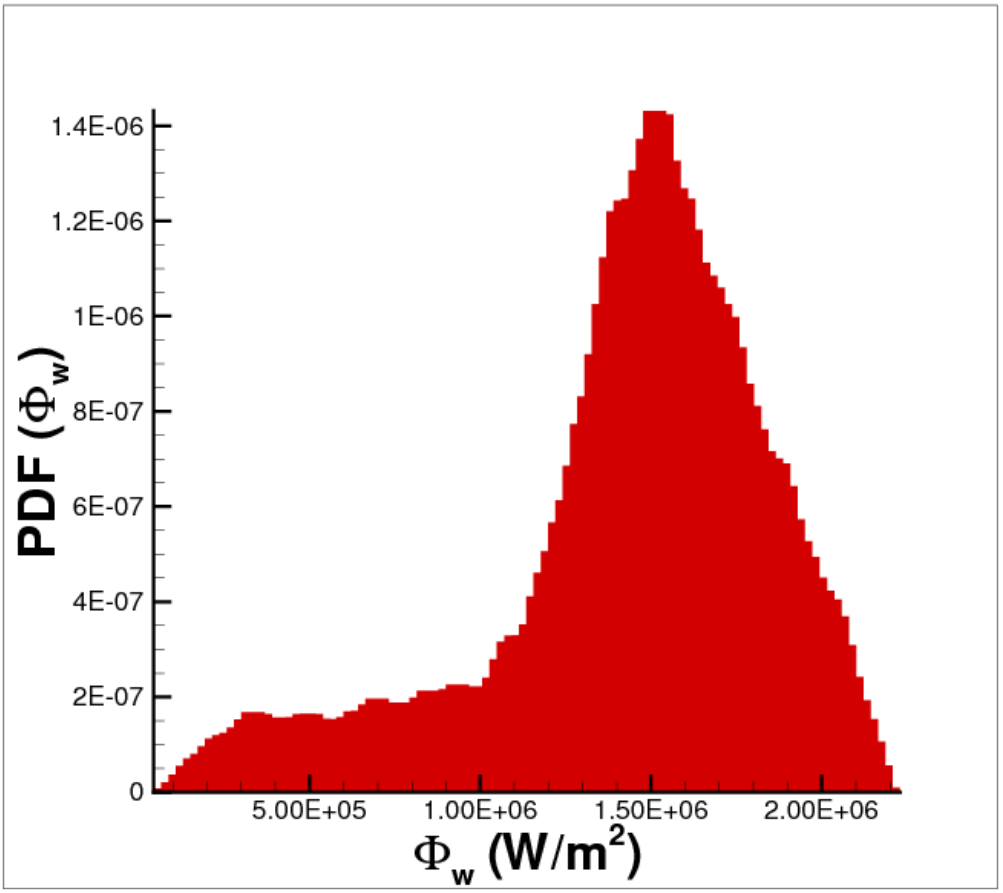

Figure 7.27: Probability density function for the wall heat flux sampled along a spanwise line at $x^+ = 1043$ for both the lower and the upper wall.

7.4 Conclusions And Further Work

Direct numerical simulation (DNS) of three-dimensional turbulent flame-wall interaction in plane channel flow is reported for premixed hydrogen-air flames at low Reynolds number $Re_\tau = 180$. The following conclusions can be drawn from the present work:

- The observed characteristic spatial pattern in the maximum wall heat flux seems to be highly correlated to the quasi-streamwise intense vorticity structures of the wall boundary layer and is in good agreement with earlier DNS results of Alshaalan and Rutland (1998) and Bruneaux *et al.* (1996)[4].
- Although the wall heat flux "hotspots" slowly migrate in the spanwise direction following the associated quasi-streamwise vorticity structures and also slightly change their streamwise location (following the flame brush "flapping"), the observed average spanwise spacing between these "hotspots" is 100 wall units.
- The characteristic time scales ($9 < t^+ < 27$) for the strong wall heat flux events are extracted from the DNS data and correlate well with the characteristic eddy turnover and "life-span" time scales confirming that vorticity structures have an important role in the wall heat flux fluctuations pattern.
- The maximum wall heat flux registered in the turbulent simulations TW1 and TW2 is larger than the one measured in the laminar HOQ case LW5 by a factor of two. This relatively large increase in the maximum wall heat flux is probably due to intense streamwise vorticity near-wall structures that, in the turbulent cases, push the flame very close to the wall thereby increasing the heat transfer into it.

The validity of the above mentioned scaling at higher Reynolds numbers cannot be assessed at this point and must be verified by far more expensive calculations. As pointed out in Abe *et al.* (2004), outer large-scale patterns become more significant than near-wall streaky streamwise vorticity structures for increasing Reynolds number: this trend may be responsible for an eventual modification of the scalings reported here at higher Re_τ. Therefore, it is unclear if the spatial and temporal pattern of the wall heat flux

[4] Since these are limited to the "minimal box" of channel turbulence and make use of simplified single-step chemistry a direct comparison of the results is difficult.

"hotspots" observed in the present study is still correctly describing the flame-wall interaction process at higher Reynolds numbers. A DNS of the same flame-wall interaction configuration at higher Reynolds numbers is therefore recommended to confirm the maximum wall heat flux spatial and temporal patterns reported in this work.

Knowledge about the characteristic wall heat flux spatial frequency l_e and temporal frequency t_e, if confirmed by the long-time integration of the solution and for higher Reynolds numbers can be used to estimate, at the microscale level, the thermal stresses acting on the (often very thin) walls of gas turbine combustion chambers and to obtain a more accurate estimate of the combustor lifetime. As an example, in a $2\,cm$ wide annular combustion chamber of a micro gas turbine operating at a Reynolds number $Re \sim 310$ under comparable pre-heating and stoichiometric conditions, the flame-wall interaction processes would induce a wall heat flux variation between $0.2\,MW/m^2$ and $2.2\,MW/m^2$ on a length scale $1/l_e \sim 1.6\,mm$ and on a temporal scale of $1/t_e \sim 1.0\,ms$. The issue of thermal stresses is especially important in micro and nano gas turbines in which, because of the tiny combustor dimensions, flame-wall interaction is very likely to occur. Thermal stresses are ultimately responsible for fatigue failure of combustors. More accurate methods for their estimation, based on turbulence characteristic of the reactive flow, could represent a starting point for the successful development of solid materials that are able to better handle thermal stresses.

As mentioned in Chapter 1, turbulent combustion models available to commercial CFD users suffer from several problems, these are especially serious in the near-wall regions of turbulent flows producing often unrealistic predictions. The Eddy Dissipation Concept (EDC) turbulent combustion model, to give an example known to the author, overpredicts to a large extent the burning rate in the near-wall region of a turbulent reactive flow and a near-wall, low Reynolds number modification of the model is seen as an important step in achieving more reliable and accurate CFD predictions. The database created in conjunction with the present research work represent an optimal starting point also for a modeling attempt in respect to improvement of turbulent combustion models that are relevant in applied engineering problems.

7.5 Acknowledgments

The author is very grateful to his principal advisor Professor Inge Gran and to Professor Ivar Ertesvag from NTNU for the interest shown in the present research work, for making it possible and for reading some parts of the manuscript. Funding from the Norwegian Research Council for the eight months overseas fellowship (Nov 2004 - Jun 2005) at the Combustion Research Facility (CRF) in Livermore, California, in the framework of an international collaboration between SINTEF Energy Research and the CRF, is gratefully acknowledged. The CRF's colleagues J. H. Chen, E. R. Hawkes and R. Sankaran have been of fundamental importance in the realization of the present work and will be in its future development. Invaluable help is acknowledged to J. H. Chen for making the S3D code available to the author. A very special thank goes to C. A. Kennedy for the many hours of productive work together in California and to S.T. Munkejord for his help in configuring and using LaTeX.

Bibliography

Abe, H., Kawamura, H., and Matsuo, Y. Surface heat-flux fluctuations in a turbulent channel flow up to $re_\tau = 1020$ with $pr = 0.025$ and 0.71. *Journal of Heat and Fluid Flow*, volume 25: pages 404–419, 2004.

Alshaalan, T. M. Studying reacting couette flow using direct numerical simulations. Doctoral thesis, University of Wisconsin-Madison, Department of Mechanical Engineering, May 1997.

Alshaalan, T. M. and Rutland, C. J. Turbulence, scalar transport, and reaction rates in flame-wall interaction. In: *Twenty-Seventh Symposium (International) on Combustion*, pages 793–799. The Combustion Institute, 1998.

Alshaalan, T. M. and Rutland, C. J. Wall heat flux in turbulent premixed reacting flow. *Combustion Science and Technology*, volume 174: pages 135–165, 2002.

Andersson, H. I. and Kristoffersen, R. Statistics of numerically generated turbulence. *Acta Applicandae Mathematicae*, volume 26: pages 293–314, 1992.

Ashurst, W. T., Kerstein, A. R., Kerr, R. M., and Gibson, C. H. Alignment of vorticity and scalar gradient with strain rate in simulated navier-stokes turbulence. *Physics of Fluids*, volume 30: pages 2343–2353, 1987.

Barlow, R. S. Personal communication, February 2005. Combustion Research Facility, Sandia National Laboratories, Livermore, CA, USA.

Baum, M., Poinsot, T., Haworth, D. C., and Darabiha, N. Direct numerical-simulation of $\mathbf{H}_2 - \mathbf{O}_2 - \mathbf{N}_2$ flames with complex chemistry in 2-dimensional turbulent flows. *Journal of Fluid Mechanics*, volume 281: pages 1–32, 1994a.

Baum, M., Poinsot, T., and Thévenin, D. Accurate boundary conditions for multicomponent reactive flow. *Journal of Computational Physics*, volume 116: pages 247–261, 1994b.

Bech, K., Tillmark, N., Alfredsson, P. H., and Andersson, H. I. An investigation of turbulent plane couette flow at low reynolds numbers. *Journal of Fluid Mechanics*, volume 286: pages 291–325, 1995.

Bellenoue, M., Kageyama, T., Labuda, S. A., and Sotton, J. Direct measurements of laminar flame quenching distance in a closed vessel. *Experimental Thermal and Fluid Science*, volume 27: pages 323–331, 2004.

Blaisdell, G. Numerical simulation of compressible homogeneous turbulence. Doctoral thesis, Stanford University, Department of Mechanical Engineering, Thermoscience Division, May 1991.

Blaisdell, G. A., Spyropoulos, E. T., and Qin, J. H. The effect of the formulation of nonlinear terms on aliasing errors in spectral methods. *Applied Numerical Mathematics*, volume 21: pages 207–219, 1996.

Borghi, R. Turbulent combustion modelling. *Progress in Energy and Combustion Science*, volume 14: pages 245–292, 1988.

Boyd, J. P. *Chebyshev and Fourier Spectral Methods*. Dover Publications, New York, second edition, 2001. ISBN 0-486-41183-4.

Bruneaux, G., Akselvoll, K., Poinsot, T., and Ferziger, J. H. Flame-wall interaction simulation in a turbulent channel flow. *Combustion and Flame*, volume 107: pages 27–44, 1996.

Bruneaux, G., Poinsot, T., and Ferziger, J. H. Premixed flame-wall interaction in a turbulent channel flow: Budget for the flame surface density evolution equation and modeling. *Journal of Fluid Mechanics*, volume 349: pages 191–219, 1997.

Cant, S. Direct numerical simulation of premixed turbulent flames. *Philosophical Transactions of The Royal Society of London*, volume 357, no. 1764: pages 3583–3604, 1999.

Canuto, C., Hussaini, M., Quarteroni, A., and Zang, T. *Spectral Methods in Fluid Dynamics*. Springer-Verlag, New York, 1988. ISBN 3-540-17371-4.

Carpenter, M. H., Gottlieb, D., and Arbanel, S. Stable and accurate boundary treatments for compact, high-order finite-difference schemes. *Applied Numerical Mathematics*, volume 12, no. 0: pages 55–87, 1993.

Chacín, J. and Cantwell, B. Study of turbulence structure using the invariants of the velocity gradient tensor. Doctoral thesis, Stanford University, Department of Mechanical Engineering, FPC Division, August 1997.

Chen, J. H., Echekki, T., and Kollmann, W. The mechanism of two-dimensional pocket formation in lean premixed methane-air flames with implications to turbulent combustion. *Combustion and Flame*, volume 116: pages 15–48, 1999.

Cheng, R. K. and Ng, T. T. Some aspects of strongly heated turbulent boundary layer flow. *Physics of Fluids*, volume 25: pages 1333–1341, 1982.

Cheng, R. K. and Ng, T. T. Velocity statistics in premixed turbulent flames. *Combustion and Flame*, volume 52: pages 185–202, 1983.

Cheng, R. K. and Ng, T. T. On defining the turbulent burning velocity in premixed v-shaped turbulent flames. *Combustion and Flame*, volume 57: pages 155–167, 1984.

Cheng, R. K. and Ng, T. T. Conditional reynolds stress in a strongly heated turbulent boundary layer with premixed combustion. *Physics of Fluids*, volume 28: pages 473–488, 1985.

Choi, H. and Moin, P. On the space-time characteristics of wall-pressure fluctuations. *Physics of Fluids*, volume 2: pages 1450–1460, 1990.

Coleman, G. N., Kim, J., and Moser, R. D. A numerical study of turbulent supersonic isothermal-wall channel flow. *Journal of Fluid Mechanics*, volume 305: pages 159–183, 1995.

Colonius, T. and Lele, S. K. Modeling artificial boundary conditions for compressible flow. *Progress in Aerospace Sciences*, volume 40: pages 345–416, 2004.

Dabireau, F., Cuenot, B., Vermorel, O., and Poinsot, T. Interaction of flames of $h_2 + o_2$ with inert walls. *Combustion and Flame*, volume 135: pages 123–133, 2003.

de Lataillade, A., Dabireau, F., Cuenot, B., and Poinsot, T. Flame/wall interaction and maximum wall-heat fluxes in diffusion burners. In: *Proceedings 29th International Symposium on Combustion*, pages 775–779. The Combustion Institute, 2002.

Del Álamo, J. C., Jiménez, J., Zandonade, P., and Moser, R. Scaling of the energy spectra of turbulent channels. *Journal of Fluid Mechanics*, volume 500: pages 135–144, 2004.

Dutt, P. Stable boundary conditions and difference schemes for navier-stokes equations. *SIAM Journal on Numerical Analysis*, volume 25(2): pages 245–287, 1988.

Echekki, T. and Chen, J. H. Direct numerical simulation of autoignition in non-homogeneous hydrogen-air mixtures. *Combustion and Flame*, volume 134: pages 169–191, 2003.

Egolfopoulos, F. N., Zhang, H., and Zhang, Z. Wall effects on the propagation and extinction of steady, strained, laminar premixed flames. *Combustion and Flame*, volume 109: pages 237–252, 1997.

El Tahry, S. H., Rutland, C. J., and Ferziger, J. H. Structure and propagation speed of turbulent premixed flames - a numerical study. *Combustion and Flame*, volume 83: pages 155–173, 1991.

Enomoto, M. Sidewall quenching of laminar premixed flames propagating along the single wall surface. In: *Proceedings 29th International Symposium on Combustion*, pages 781–787. The Combustion Institute, 2002.

Erlebacher, G., Hussaini, M. Y., Kreiss, H. O., and Sarkar, S. The analysis and simulation of compressible turbulence. *Theoretical and Computational Fluid Dynamics*, volume 2: pages 73–95, 1990.

Ezekoye, O., Greif, R., and Sawyer, R. F. Increased surface temperature effects on wall heat transfer during unsteady flame quenching. In: *Proceedings 24th International Symposium on Combustion*, pages 1465–1472. The Combustion Institute, 1992.

Ezekoye, O. A. Heat transfer consequences of condensation during premixed flame quenching. *Combustion and Flame*, volume 112: pages 266–269, 1998.

Feiereisen, W. J., Reynolds, W. C., and Ferziger, J. H. Numerical simulation of compressible, homogeneous, turbulent shear flow. Doctoral thesis, Stanford University, Department of Mechanical Engineering, Thermoscience Division, March 1981.

Gran, I. R., Echekki, T., and Chen, J. H. Negative flame speed in an unsteady 2-d premixed flame: A computational study. In: *Proceedings 26th International Symposium on Combustion*, pages 323–329. The Combustion Institute, 1996.

Gruber, A. and Kennedy, C. A. Boundary conditions to the navier-stokes equations for compressible gas mixtures at nonporous, reacting and nonreacting solid surfaces, November 2006a. To appear.

Gruber, A. and Kennedy, C. A. Reduced aliasing formulations of the convective terms within the compressible navier-stokes equations, December 2006b. To appear.

Guichard, L., Réveillon, J., and Hauguel, R. Direct numerical simulation of statistically stationary one- and two-phase turbulent combustion: A turbulent injection procedure. *Flow, Turbulence and Combustion*, volume 73: pages 133–167, 2004.

Gustafsson, B. The choice of numerical boundary conditions for hyperbolic systems. *Journal of Computational Physics*, volume 48: pages 270–283, 1982.

Gustafsson, B. and Kreiss, H. O. Boundary conditions for time dependent problems with an artificial boundary. *Journal of Computational Physics*, volume 30: pages 333–351, 1979.

Gustafsson, B. and Sundström, A. Incompletely parabolic problems in fluid dynamics. *SIAM Journal on Applied Mathematics*, volume 35(2): pages 343–357, 1978.

Hasse, C., Bollig, M., Peters, N., and Dwyer, H. A. Quenching of laminar iso-octane flames at cold walls. *Combustion and Flame*, volume 122: pages 117–129, 2000.

Hawkes, E. R. and Chen, J. H. Direct numerical simulation of hydrogen-enriched lean premixed methane-air flames. *Combustion and Flame*, volume 138: pages 242–258, 2004.

Haworth, D. C. and Poinsot, T. Numerical simulations of lewis number effects in turbulent premixed flames. *Journal of Fluid Mechanics*, volume 244: pages 405–436, 1992.

Hirshfelder, J. O., Curtiss, C. F., and Bird, R. B. *Molecular Theory of Gases and Liquids*. John Wiley & Sons, New York, second edition, 1964. ISBN 9-999-99999-9.

Hixon, R. Radiation and wall boundary conditions for computational aeroacoustics: A review. *International Journal of Computational Fluid Dynamics*, volume 18: pages 523–531, 2004.

Hocks, W., Peters, N., and Adomeit, G. Flame quenching in front of a cold wall under two-step kinetics. *Combustion and Flame*, volume 41: pages 157–170, 1981.

Howe, N. M., Shipman, C. W., and Vranos, A. Turbulent mass transfer and rates of combustion in confined turbulent flames. In: *Proceedings 9th International Symposium on Combustion*, pages 36–47. The Combustion Institute, 1963.

Huang, P. G. and Coleman, G. N. Van driest transformation and compressible wall-bounded flows. *AIAA Journal*, volume 32: pages 2110–2113, 1994.

Huang, P. G., Coleman, G. N., and Bradshaw, P. Compressible turbulent channel flows: Dns results and modelling. *Journal of Fluid Mechanics*, volume 305: pages 185–218, 1995.

Hussain, A. K. M. F., Jeong, J., and Kim, J. Studying turbulence using numerical simulation databases. In: *Proceedings of the 1987 Summer Program of the Center for Turbulence Research, Stanford University, CA*, pages 273–290. 1987.

IEA. *World Energy Outlook 2004*. International Energy Agency, 9 rue de la Fédération, 75739 Paris Cedex 15, France, first edition, 2004.

Im, H. G. and Chen, J. H. Preferential diffusion effects on the burning rate of interacting turbulent premixed hydrogen-air flames. *Combustion and Flame*, volume 131: pages 246–258, 2002.

Jang, P. S., Benney, D. J., and Gran, R. L. On the origin of streamwise vortices in a turbulent boundary layer. *Journal of Fluid Mechanics*, volume 169: pages 109–123, 1986.

Jiménez, J. The largest scales of turbulent wall flows. In: *Annual Research Briefs of the Center for Turbulence Research, Stanford University, CA*, pages 137–154. 1998.

Jiménez, J. and Moin, P. The minimal flow unit in near wall turbulence. *Journal of Fluid Mechanics*, volume 225: pages 213–240, 1991.

Johansson, A. V. and Wikström, P. Dns and modelling of passive scalar transport in turbulent channel flow with a focus on scalar dissipation rate modelling. *Flow, Turbulence and Combustion*, volume 63: pages 223–245, 1999.

Kasagi, N., Kuroda, A., and Hirata, M. Numerical investigation of near-wall turbulent heat transfer taking into account the unsteady heat conduction in the solid wall. *Journal of Heat Transfer*, volume 111: pages 385–393, 1989.

Kasagi, N., Sumitani, Y., Suzuki, Y., and Oaki, I. Kinematics of the quasi-coherent vortical structure in near-wall turbulence. *Journal of Heat and Fluid Flow*, volume 16: pages 2–10, 1995.

Kasagi, N., Tomita, Y., and Kuroda, A. Direct numerical simulation of the passive scalar field in a turbulent channel flow. *ASME Journal of Heat Transfer*, volume 14: pages 598–606, 1992.

Kawamura, H., Abe, H., and Matsuo, Y. Dns of turbulent heat transfer in channel flow with respect to reynolds and prandtl number effects. *Journal of Heat and Fluid Flow*, volume 20: pages 196–207, 1999.

Kee, R. J., Dixon-Lewis, G., Warnatz, J., Coltrin, M. E., Miller, J. A., and Moffat, H. K. A fortran chemical kinetics package for the analysis of gas-phase chemical kinetics. Technical Report Release 3.5, Reaction Design Inc., San Diego, CA, 1999.

Kennedy, C. A. and Carpenter, M. H. Several new numerical methods for compressible shear-layer simulations. *Applied Numerical Mathematics*, volume 14, no. 0: pages 397–433, 1994.

Kennedy, C. A. and Carpenter, M. H. Additive runge-kutta schemes for convection-diffusion-reaction equations. *Applied Numerical Mathematics*, volume 44, no. 0: pages 139–181, 2003.

Kennedy, C. A., Carpenter, M. H., and Lewis, R. M. Low-storage, explicit runge-kutta schemes for the compressible navier-stokes equations. *Applied Numerical Mathematics*, volume 35, no. 0: pages 177–219, 2000.

Kim, J. On the structure of wall-bounded turbulent flows. *Physics of Fluids*, volume 26: pages 2088–2097, 1983.

Kim, J. and Moin, P. The structure of the vorticity field in turbulent channel flow. part 2. study of ensemble-averaged fields. *Journal of Fluid Mechanics*, volume 162: pages 339–363, 1986.

Kim, J. and Moin, P. Transport of passive scalars in a turbulent channel flow. In: *Proceedings 6th International Symposium on Turbulent Shear Flow, 7-9 September, Tolouse, France*, pages 85–96. 1989.

Kim, J., Moin, P., and Moser, R. Turbulence statistics in fully developed channel flow at low reynolds number. *Journal of Fluid Mechanics*, volume 177: pages 133–166, 1987.

Kline, S. J., Reynolds, W. C., Schraub, F. A., and Runstadler, P. W. The structure of turbulent boundary layers. *Journal of Fluid Mechanics*, volume 30: page 741, 1967.

Kolmogorov, A. N. Dissipation of energy in locally isotropic turbulence [in russian]. *Dokl. Akad. Nauk. S.S.S.R.*, volume 32: pages 19–21, 1941a.

Kolmogorov, A. N. The local structureof turbulence in incompressible viscous fluid for very large reynolds number[in russian]. *Dokl. Akad. Nauk. S.S.S.R.*, volume 30: pages 299–303, 1941b.

Kong, H., Choi, H., , and Lee, J. S. Direct numerical simulation of turbulent thermal boundary. *Physics of Fluids*, volume 12: pages 2555–2568, 2000.

Kovásznay, L. E. G. Turbulence in supersonic flow. *Journal of the Aeronautical Sciences*, volume 20, no. 10: pages 657–674, 1953.

Kravchenko, A. G., Choi, H., and Moin, P. On the relation of near-wall streamwise vortices to wall skin friction in turbulent boundary layers. *Physics of Fluids*, volume 5: pages 3307–3309, 1993.

Kristoffersen, R. and Andersson, H. I. Direct simulations of low-reynolds-number turbulent flow in a rotating channel. *Journal of Fluid Mechanics*, volume 256: pages 163–197, 1993.

Kurbatskii, K. A. Solid wall boundary conditions for computational aeroacoustics problems. Doctoral thesis, Florida State University, College of Arts and Sciences, September 1997.

Le, H., Moin, P., and Kim, J. Direct numerical simulation of turbulent flow over a backward-facing step. *Journal of Fluid Mechanics*, volume 330: pages 349–374, 1997.

Lee, S., Lele, S. K., and Moin, P. Eddy shocklets in decaying compressible turbulence. *Physics of Fluids*, volume 3: pages 657–664, 1991.

Lee, S., Lele, S. K., and Moin, P. Simulation of spatially evolving turbulence and the applicability of taylor's hypothesis in compressible flow. *Physics of Fluids*, volume 4: pages 1521–1530, 1992.

Lele, S. K. Compact finite difference schemes with spectral like resolution. *Journal of Computational Physics*, volume 103: pages 16–42, 1992.

Li, J., Zhao, Z., Kazarov, A., and Dryer, F. L. An updated comprehensive kinetic model for h_2 combustion. In: *Proceeedings of the Fall Technical Meeting of the Eastern States Section of the Combustion Institute, Penn State University, University Park, PA*. The Combustion Institute, 2003.

Lund, T. S., Squires, K. D., and Wu, X. Turbulent inflow boundary conditions for les. In: *Proceeedings of the 41st Aerospace Sciences Meeting and Exhibit, 6-9 January 2003, Reno, Nevada*. American Institute of Aeronautics and Astronautics, 2003.

Lygren, M. and Andersson, H. I. Turbulent flow between a rotating and a stationary disk. *Journal of Fluid Mechanics*, volume 426: pages 297–326, 2001.

Maeder, T., Adams, N. A., and Kleiser, L. Direct simulation of turbulent supersonic boundary layers by an extended temporal approach. *Journal of Fluid Mechanics*, volume 429: pages 187–216, 2001.

Mansour, N. N., Ferziger, J. H., and Reynolds, W. C. Large eddy simulation of a turbulent mixing layer. Doctoral thesis, Stanford University, Department of Mechanical Engineering, Thermoscience Division, April 1978.

Moin, P. and Kim, J. The structure of the vorticity field in turbulent channel flow. part 1. analysis of istantaneous fields and statistical correlations. *Journal of Fluid Mechanics*, volume 155: pages 441–464, 1985.

Moin, P. and Mahesh, K. Direct numerical simulation: A tool in turbulence research. *Annual Review of Fluid Mechanics*, volume 30: pages 539–578, 1998.

Moin, P., Reynolds, W. C., and Ferziger, J. H. Large eddy simulation of incompressible turbulent channel flow. Doctoral thesis, Stanford University, Department of Mechanical Engineering, Thermoscience Division, May 1978.

Moiseev, S. S., Petviashvily, V. I., Toor, A. V., and Yanovsky, V. V. The influence of compressibility on the selfsimilar spectrum of subsonic turbulence. *Phisica D*, volume 2: pages 218–223, 1981.

Moran, M. J. and Shapiro, H. N. *Fundamentals of Engineering Thermodynamics*. John Wiley & Sons, New York, third edition, 1998. ISBN 9-99-999999-9.

Morinishi, Y., Tamano, S., and Nakabayashi, K. Direct numerical simulation of compressible turbulent channel flow between adiabatic and isothermal walls. *Journal of Fluid Mechanics*, volume 502: pages 273–308, 2004.

Moser, R., Kim, J., and Mansour, N. Direct numerical simulation of turbulent channel flow up to $re_\tau = 590$. *Physics of Fluids*, volume 11, no. 4: pages 943–945, 1999.

Moser, R. and Moin, P. The effects of curvature in wall-bounded turbulent flows. *Journal of Fluid Mechanics*, volume 175: pages 479–510, 1987.

Moyal, J. E. The spectra of turbulence in a compressible fluid: Eddy turbulence and random noise. *Mathematical Proceedings Cambridge Philosophical Society*, volume 48: pages 329–344, 1952.

Na, Y. and Moin, P. Direct numerical simulation of a separated turbulent boundary layer. *Journal of Fluid Mechanics*, volume 374: pages 379–405, 1998.

Ng, T. T., Cheng, R. K., Robben, F., and Talbot, L. Combustion-turbulence interaction in the turbulent boundary layer over a hot surface. In: *Proceedings 19th International Symposium on Combustion*, pages 359–366. The Combustion Institute, 1982.

Nicoud, F. Defining wave amplitude in characteristic boundary conditions. *Journal of Computational Physics*, volume 149: pages 418–422, 1999.

Onsager, L. The distribution of energy in turbulence. *Physical Review*, volume 68: page 286, 1945.

Orlandi, P. and Jiménez, J. On the generation of turbulent wall friction. *Physics of Fluids*, volume 6: pages 634–641, 1994.

Orszag, S. A. and Patterson, G. S. Numerical simulation of three-dimensional homogeneous isotropic turbulence. *Physical Review Letters*, volume 28: pages 76–79, 1972.

Pantano, C. and Sarkar, S. A study of compressibility effects in the high-speed turbulent shear layer using direct simulation. *Journal of Fluid Mechanics*, volume 451: pages 329–371, 2002.

Passot, T. and Pouquet, A. Numerical simulation of compressible homogeneous flows in the turbulent regime. *Journal of Fluid Mechanics*, volume 181: pages 441–466, 1987.

Piomelli, U., Balint, J. L., and Wallace, J. M. On the validity of taylor's hypothesis for wall-bounded flows. *Physics of Fluids*, volume 1: pages 609–611, 1989.

Poinsot, T., Candel, S., and Trouvé, A. Application of direct numerical simulation to premixed turbulent combustion. *Progress in Energy and Combustion Science*, volume 21: pages 531–576, 1996.

Poinsot, T., Haworth, D. C., and Bruneaux, G. Direct simulation and modeling of flame-wall interaction for premixed turbulent combustion. *Combustion and Flame*, volume 95: pages 118–132, 1993.

Poinsot, T. and Lele, S. K. Boundary conditions for direct simulations of compressible viscous reacting flow. Technical Report 102, Center for Turbulence Research, Bldg. 500, Stanford University, Stanford, CA 94305-3030, 1989.

Poinsot, T. and Lele, S. K. Boundary conditions for direct simulations of compressible viscous flow. *Journal of Computational Physics*, volume 101: pages 104–129, 1992.

Poinsot, T. and Veynante, D. *Theoretical and Numerical Combustion*. Edwards, Inc., Philadelphia, first edition, 2001. ISBN 1-93-021705-6.

Poinsot, T., Veynante, D., and Candel, S. Diagrams of premixed turbulent combustion based on direct simulation. In: *Proceedings 23th International Symposium on Combustion*, pages 613–619. The Combustion Institute, 1990.

Pope, S. B. *Turbulent Flows*. Cambridge University Press, Cambridge, second edition, 2000. ISBN 0-521-59886-9.

Popp, P. and Baum, M. Analysis of wall heat fluxes, reaction mechanisms, and unburnt hydrocarbons during the head-on quenching of a laminar methane flame. *Combustion and Flame*, volume 108: pages 327–348, 1997.

Popp, P., Smooke, M., and Baum, M. Heterogeneous/homogeneous reaction and transport coupling during flame-wall interaction. In: *Proceedings 26th International Symposium on Combustion*, pages 2693–2700. The Combustion Institute, 1996.

Prosser, R. Improved boundary conditions for the direct numerical simulation of turbulent subsonic flows i: Inviscid flows, January 2005. To appear.

Rian, K. E. Open boundaries in numerical simulations of compressible flows. Doctoral thesis, University of Trondheim, Norwegian Institute of Technology, Division of Thermodynamics, May 2003.

Robinson, S. K. Kinematics of turbulent boundary layer structure. Technical Report TM-103859, NASA, Moffet Field, 1991.

Robinson, S. K., Kline, S., and Spalart, P. A review of quasi-coherent structures in a numerically simulated turbulent boundary layer. Technical Report TM-102191, NASA, Moffet Field, 1989.

Rogallo, R. S. Numerical experiments in homogeneous turbulence. Technical Report TM-81315, NASA, Langley, 1981.

Rogers, M. M. and Moin, P. The minimal flow unit in near wall turbulence. *Journal of Fluid Mechanics*, volume 176: pages 33–66, 1987.

Rudy, D. H. and Strikwerda, J. C. A nonreflecting outflow boundary condition for subsonic navier-stokes calculations. *Journal of Computational Physics*, volume 36: pages 55–70, 1980.

Rudy, D. H. and Strikwerda, J. C. Boundary conditions for subsonic compressible navier-stokes calculations. *Computers and Fluids*, volume 9: pages 327–338, 1981.

Runstadler, P. W., Kline, S. J., and Reynolds, W. C. An investigation of the flow structure of the turbulent boundary layer. Technical Report 8, Department of Mechanical Engineering, Stanford University, Bldg. 500, Stanford University, Stanford, CA 94305-3030, 1963.

Rutland, C., Ferziger, J. H., and El Tahry, S. H. Full numerical simulations and modeling of turbulent premixed flames. In: *Proceedings 23th International Symposium on Combustion*, pages 621–627. The Combustion Institute, 1990.

Sandham, N. D., Li, Q., and Yee, H. C. Entropy splitting for high-order numerical simulation of compressible turbulence. *Journal of Computational Physics*, volume 178: pages 307–322, 2002.

Smith, C. R. and Metzler, S. P. The characteristics of low-speed streaks in the near-wall region of a turbulent boundary layer. *Journal of Fluid Mechanics*, volume 129: pages 27–54, 1983.

Strikwerda, J. C. Initial boundary value problems for incompletely parabolic systems. *Communications on Pure and Applied Mathematics*, volume 30: pages 797–822, 1977.

Sutherland, J. C. Evaluation of mixing and reaction models for large-eddy simulation of nonpremixed combustion using direct numerical simulation. Doctoral thesis, University of Utah, Department of Chemical and Fuels Engineering, May 2004.

Sutherland, J. C. and Kennedy, C. A. Improved boundary conditions for viscous, reactive, compressible flows. *Journal of Computational Physics*, volume 191: pages 502–524, 2003.

Suzuki, Y. and Kasagi, N. Evaluation of hot-wire measurements in wall shear turbulence using a direct numerical simulation database. *International Journal for Numerical Methods in Fluids*, volume 40: pages 487–496, 2002.

Svärd, M. and Nordström, J. Well posed boundary conditions for the navier-stokes equations, January 2005. To appear.

Tam, C. K. W. and Dong, Z. Wall boundary conditions for high-order finite-difference schemes in computational aeroacoustics. *Theoretical and Computational Fluid Dynamics*, volume 6: pages 303–322, 1994.

Thompson, K. W. Time dependent boundary conditions for hyperbolic systems, i. *Journal of Computational Physics*, volume 68: pages 1–24, 1987.

Thompson, K. W. Time dependent boundary conditions for hyperbolic systems, ii. *Journal of Computational Physics*, volume 89: pages 439–461, 1990.

Townsend, A. A. *The Structure Of Turbulent Shear Flow*. Cambridge University Press, Cambridge, first edition, 1956. ISBN 0-52-129819-9.

Vervisch, L. and Poinsot, T. Direct numerical simulation of non-premixed turbulent flames. *Annual Review of Fluid Mechanics*, volume 30: pages 655–691, 1998.

Veynante, D. and Poinsot, T. Effect of pressure gradients on turbulent premixed flames. *Journal of Fluid Mechanics*, volume 353: pages 83–114, 1997.

Vichnevetsky, R. Invariance theorems concerning reflection at numerical boundaries. *Journal of Computational Physics*, volume 63: pages 268–282, 1986.

Vlachos, D. G., Schmidt, L. D., and Aris, R. Ignition and extinction of flames near surfaces: Combustion of h_2 in air. *Combustion and Flame*, volume 95: pages 313–335, 1993.

Warnatz, J., Maas, U., and Dibble, R. W. *Combustion*. Springer, Berlin, second edition, 1999. ISBN 3-54-065228-0.

Westbrook, C. K., Adamczyk, A. A., and Lavoie, G. A. A numerical study of laminar flame wall quenching. *Combustion and Flame*, volume 40: pages 81–99, 1981.

Westenberg, A. A. Flame turbulence measurements by the method of helium diffusion. *Journal of Chemical Physics*, volume 22: pages 814–823, 1954.

Westenberg, A. A. and Rice, J. L. Further measurements of turbulence intensity in flame zones. *Combustion and Flame*, volume 3: pages 459–465, 1959.

Yoo, C. S., Wang, Y., Trouvé, A., and Im, H. G. Characteristic boundary conditions for direct simulations of turbulent counterflow flames, January 2005. To appear.

Zang, T. A. On the rotation and skew-symmetric forms for incompressible flow simulations. *Applied Numerical Mathematics*, volume 7: pages 27–40, 1991.

Zank, G. P. and Matthaeus, W. H. Nearly incompressible hydrodynamics and heat conduction. *Physical Review Letters*, volume 64: pages 1243–1246, 1990.

Zank, G. P. and Matthaeus, W. H. The equations of nearly incompressible fluids. 1. hydrodynamics, turbulence and waves. *Physics of Fluids*, volume 3: pages 3307–3309, 1991.